Spectral and Dynamical Observables in Disordered Open Quantum Systems

A Thesis

Submitted to the
Tata Institute of Fundamental Research, Mumbai
Subject Board of Physics
for the degree of Doctor of Philosophy

by

Sparsh Gupta

International Centre for Theoretical Sciences,
Bengaluru
Tata Institute of Fundamental Research
January, 2026

DECLARATION

This thesis is a presentation of my original research work. Wherever contributions of others are involved, every effort is made to indicate this clearly, with due reference to the literature, and acknowledgement of collaborative research and discussions.

The work was done under the guidance of Professor Manas Kulkarni at the International Centre for Theoretical Sciences, Tata Institute of Fundamental Research, Bengaluru.

Sparsh Gupta

In my capacity as supervisor of the candidate's thesis, I certify that the above statements are true to the best of my knowledge.

Manas Kulkarni

Date: Jan 30th, 2026

Dedicated to my parents and my family.

Acknowledgments

The last five years of my PhD have been a journey filled with joy, challenges, growth, and reflection. It has shaped me into a stronger and more patient person. Along the way, I have been fortunate to receive guidance, encouragement, and inspiration from many people. This thesis would not have been possible without their support. These acknowledgements are a small gesture to express my deepest gratitude to all of them.

First and foremost, I would like to express my deepest gratitude to my advisor, Prof. Manas Kulkarni, for being an exceptional mentor. His patience, positivity, and constant encouragement in the early years kept me on track, while his trust and freedom in the later years allowed me to develop as an independent researcher. His understanding nature and positive energy consistently inspired me. Even during times when he was away from India, he always made time to guide me through WhatsApp or Zoom whenever I needed help. His guidance has been invaluable throughout this journey.

I am also deeply grateful to my collaborators: Soumi Ghosh, Hari Kumar Yadalam, Prof. Bijay Kumar Agarwalla, Prof. Abhishek Dhar, Prof. Anupam Kundu, Prof. Camille Aron, and Prof. Sanjib Sabhapandit. It was a privilege to work with such inspiring researchers who taught me to look at problems from different perspectives. I fondly remember the impromptu visits to their offices that often led to enlightening discussions. In my early PhD days, Soumi and Hari, who were postdoctoral fellows at ICTS, played a key role in guiding me through my first research projects, and I learned immensely from them.

I would also like to thank Prof. Sthitadhi Roy and Prof. Subroto Mukherjee for being part of my thesis mentoring committee. Their constructive feedback over the years proved invaluable, and I also benefited from other interesting discussions with them.

I am deeply grateful to my family for their unconditional love, patience, and

understanding throughout these years. Their continuous support kept me going, even during the toughest times. I also owe heartfelt thanks to my best friends, Sachin and Rishabh, for always being there for me - for being unwavering sources of comfort and perspective, and helping me see things in perspective. I am equally grateful to Yash for his support and encouragement during this journey.

My heartfelt thanks go to my colleagues and friends at ICTS, who made these years both scientifically stimulating and personally enjoyable. I am grateful to Jitendra, Anup, Alan, Uddeepta, Ankush, Harshit, Saikat, Rajarshi, Dibyanandan, Shivam, Umesh, Bikram, Tamoghna, Mahaveer, Atharva, Prashant, Santhosh, Junaid, Rekha, and Mrinal for all the scientific discussions - whether serious or lighthearted, and for the many fun and memorable moments we shared outside of the academic sphere. I am also thankful to the postdoctoral fellows at ICTS - Dipankar, Madhumita, Shalabh, Sharath, and Rekha - with whom I had regular discussions that enriched both my work and perspective. Special thanks to Archak da, who always provided clarity and constructive insights on my research problems whenever I approached him.

Over these years, my circle of friends at ICTS truly became my second family. I am deeply thankful to Uddeepta, Anup, Sumi, Rajarshi, Tarang, Tamoghna, Jeetu, Saikat, Jigyasa, Dibyanandan, Ankush, Harshit, Shivam, Akash, Mahaveer, Shashank, Aditya Thorat and Aditya Rajput, Soummyadip, Bhanu, Prateek, Souvik, Kunal, and Ankur for filling my life with warmth, fun, and laughter. I will always cherish these moments and friendships. I would also like to acknowledge other friends and colleagues at ICTS who, in different ways, had an impact during my time here: Bibek, Priyadarshi, Sandip, Irshad, Harsh, Rishabh Kaushik, and Aishwarya.

I especially thank Dipankar and Tushar for our delightful cooking sessions in Hostel 4, often seasoned with engaging cricket discussions that brightened up daily life. Rajarshi deserves special mention for generously being my "code debugger" long before ChatGPT came into existence!

I am also very grateful to the ICTS community (faculty, staff, administrative members, and everyone else) for creating such a wonderful and supportive environment and working tirelessly behind the scenes to ensure our lives become as easy as possible. Their efforts to support students, whether in routine situations or in the midst of the pandemic, when they ensured our well-being by delivering food and services, were truly commendable and deeply appreciated.

My gratitude also extends to NCBS, our wonderful neighbor to the ICTS community. From working in their library or having long canteen conversations to playing in the sports complex or simply hanging out, NCBS became an integral

part of my PhD journey. Over the years, the basketball court, in particular, was my happy place that provided me with a quantum of solace whenever I needed some. I am especially thankful to my friends at NCBS - Vinod, Rajat, Arpit, Rakshan, Praveen, Vinay, and Reuben — for their friendship and shared moments outside work.

I am also grateful to Prof. Arnab Das and Prof. Aurelia Chenu for reviewing this thesis and for their valuable time and insightful suggestions.

Finally, apart from all the scientific discussions, I will always cherish the countless fun and sometimes silly moments that made PhD life meaningful — from long debates about cricket with ICTS friends, to NBA discussions with Alan, to endless conversations about movies and TV shows. These seemingly small things made my PhD life as memorable and precious as the academic journey itself.

There are too many people to thank individually, but every person I met has contributed to my journey in some way. The experiences, lessons, and friendships have shaped who I am today, and I will always be indebted to them.

I would also like to thank the developers of the NovaThesis template for their effort in making it so well-designed and accessible [1].

To all who walked alongside me in research and in life, I express my heartfelt gratitude.

Abstract

Understanding how quantum systems thermalize or localize remains a central challenge in modern physics, particularly in the presence of disorder and environmental interactions. While the phenomena of thermalization, chaos, and localization are comparatively well established in isolated Hermitian systems, their counterparts in open and non-Hermitian settings are less developed. This thesis addresses these issues by exploring the stability of localization phenomena when quantum systems are coupled to external environments through dissipation and driving. The central goal is to uncover how spectral and dynamical signatures of localized and delocalized phases, and transitions between them, are modified by environmental influence, and whether traces of localization can persist despite decoherence, in both one-dimensional interacting and non-interacting systems.

The first part of the thesis focuses on interacting disordered systems, analyzed through non-Hermitian Hamiltonians and Lindblad master equations. Using spectral tools such as complex spacing ratios and the dissipative spectral form factor, together with dynamical probes including imbalance and activity, we study the influence of dissipation and quantum jumps, both in the ergodic and many-body localized regimes. These studies reveal that although environmental coupling can destabilize localized phases, controlled suppression of quantum jumps can promote the emergence of localization, highlighting subtle mechanisms through which localization may survive in open quantum systems.

The second part of the thesis examines non-interacting system-environment setups through unitary dynamics, with the environment modeled microscopically as a thermal reservoir that injects particles (bosons or fermions) into the system. This setup enables a detailed study of particle injection, spreading, and equilibration in disorder-free and quasi-periodic lattices coupled to an environment. By analyzing observables such as spatial density profiles, total occupation, and entanglement entropy, we establish universal scaling features of ballistic transport

in clean lattices. In quasi-periodic lattices, by contrast, the dynamics strongly depend on the underlying phase, leading to distinct behavior across delocalized, critical, and localized regimes. Comparisons with quantum master equations further clarify the domains of validity and limitations of these approaches.

Together, these complementary approaches: dissipative system dynamics and explicitly modeled system-environment unitary evolution, provide a broad and nuanced understanding of localization stability. This work bridges idealized isolated models and realistic experimental conditions where environments are unavoidable, with direct implications for controlling and detecting localized quantum phases in modern experimental platforms.

Published Articles

1. Soumi Ghosh, **Sparsh Gupta**, and Manas Kulkarni, Phys. Rev. B 106, 134202 (2022), "Spectral Properties of Disordered Interacting Non-Hermitian Systems"

2. Akash Trivedi, **Sparsh Gupta**, Bijay Kumar Agarwalla, Abhishek Dhar, Manas Kulkarni, Anupam Kundu, and Sanjib Sabhapandit, Phys. Rev. A 108, 052204 (2023), "Filling an empty lattice by local injection of quantum particles"

3. **Sparsh Gupta**, H. K. Yadalam, Manas Kulkarni and Camille Aron, Phys. Rev. A 109, L050201 (2024), "Quantum jumps in driven-dissipative disordered many-body systems"

In-Preparation

1. **Sparsh Gupta**, Bijay Kumar Agarwalla, Abhishek Dhar, Manas Kulkarni, Anupam Kundu, and Sanjib Sabhapandit, "Local Injection of quantum particles in quasiperiodic lattice"

Contents

List of Figures

List of Tables

1 Introduction

1.1 Background

A cup of hot coffee gradually cools to room temperature, while a cold drink warms up, illustrating a basic principle: thermalization. As energy is exchanged between a system and its surroundings, both are driven toward thermal equilibrium. This universal process, described by statistical physics [2–6], explains how macroscopic properties emerge from microscopic dynamics, regardless of the system's initial state.

In isolated systems, this approach to equilibrium is called *thermalization*. Understanding how reversible microscopic laws give rise to irreversible macroscopic phenomena lies at the heart of statistical physics. During thermalization, systems lose memory of their initial conditions and display universal macroscopic behavior consistent with the second law of thermodynamics. This process explains the typical, equilibrium properties observed in nature, making the study of equilibration and thermalization a fundamental question in both classical and quantum physics.

In classical physics, thermalization (or lack thereof) is traditionally understood through ergodicity, chaos, and integrability [7–9]. The Ergodic Hypothesis [10–13] originally proposed by Boltzmann states that the time average of any observable equals its ensemble average, provided the system is allowed to evolve for long enough time. In other words, a single system will eventually visit all accessible microstates, spending an amount of time in each microstate, proportional to the probability of that state in the ensemble. This hypothesis has been rigorously established only for a few models, including Sinai billiards [14, 15], the Bunimovich stadium [16], and hard-sphere gases on a torus [17].

Ergodicity is often accompanied by chaos, and it arises due to the nonlinearity in equations of motion. Chaotic systems are typically characterized by exponential sensitivity to initial conditions, lack extensive conserved quantities, and they relax

to thermal ensembles. In contrast, integrable systems possess an extensive set of conserved quantities restricting their dynamics to regular, closed orbits in phase space, preventing ergodicity. As a result, they do not thermalize in the conventional sense but instead equilibrate to *Generalized Gibbs Ensembles* (GGE) [18–22], where the conserved quantities explicitly enter the statistical description. Thus, while chaotic systems forget their initial information, integrable systems may exhibit long-lived memory of initial conditions.

Whether ergodicity is truly necessary and sufficient for thermalization in non-integrable systems remains unclear despite large progress [23]. Rigorous proofs of Ergodicity for general systems are a challenging problem, especially in the thermodynamic limit, making classical equilibration a deep and subtle issue. This issue was famously exposed in the Fermi-Pasta-Ulam-Tsingou (FPUT) problem [24–26], where a numerical test on an anharmonic chain surprisingly revealed quasiperiodic motion rather than thermalization. This paradox showed that even simple non-linear systems can resist ergodicity and preserve information about their initial states. The FPUT discovery sparked decades of inquiry into the intricate links between non-linearity, chaos, and integrability in many-body physics [27].

Following these classical considerations, one can turn to the phenomenon of thermalization in quantum systems. Unlike classical dynamics, the notions of ergodicity and chaos do not straightforwardly apply, due to the lack of a clear analog of phase-space trajectories in quantum mechanics. Moreover, the unitary and linear nature of isolated quantum systems preserves all information, making it unclear at first whether the principles of statistical mechanics can sensibly be applied to isolated quantum systems. The key question becomes: how can interacting quantum many-body systems equilibrate despite their inherently reversible dynamics?

In 1929, von Neumann [28, 29] addressed this issue by emphasizing that thermalization should be understood at the level of macroscopic observables rather than the quantum state. He argued that expectation values of such observables relax to equilibrium values similar to those in classical systems. A key assumption in his formulation was that individual energy eigenstates within a microcanonical shell already encode thermal properties. This idea, later refined, evolved into what is now known as the Eigenstate Thermalization Hypothesis (ETH).

In the 1950s, Wigner [30] proposed modeling complex Hamiltonians, such as those of large nuclei, by random matrices. This crucial insight laid the groundwork for random matrix theory (RMT) [31–33] in quantum physics. The universal predictions of RMT, such as level repulsion, were found to match the spectral correlations of these complex nuclei. Berry and Tabor [34, 35] later conjectured

that the quantum systems whose corresponding classical dynamics are integrable, their energy levels exhibit Poissonian statistics, behaving like independent random variables without level repulsion. By contrast, Bohigas, Giannoni, and Schmit (BGS) [36] in 1984 proposed that quantum systems with corresponding classically chaotic dynamics display energy level statistics described by random matrix theory (RMT). Together, the Berry-Tabor and BGS conjectures established RMT and spectral statistics as defining tools for distinguishing between integrability and chaos in quantum systems. These results have since been extended to a wide range of many-body systems [21, 31, 32, 37–39], with spectral observables such as level-spacing distributions [40], adjacent gap ratios [41, 42], and the spectral form factor [43, 44] serving as key indicators of quantum chaos [21, 41, 42, 45–52].

Now, we understand the mechanism of thermalization in quantum systems, where the quantum mechanical evolution is compatible with the macroscopic irreversibility at the level of observables. A central paradigm here is the *Eigenstate Thermalization Hypothesis* (ETH) [21, 22, 53–62]. ETH states that in quantum chaotic systems, the expectation values of local observables in individual eigenstates coincide with thermal ensemble predictions. Consider the time evolution of the expectation value of an observable $\hat{O}$ is given by

$$O(t) = \langle\psi(t)|\hat{O}|\psi(t)\rangle = \sum_{m,n} C_m^* C_n e^{i(E_m - E_n)t} O_{mn} \tag{1.1}$$

where E_m and $|m\rangle$ are the eigenvalue and eigenstates of the Hamiltonian, respectively. $O_{mn} = \langle m|\hat{O}|n\rangle$ with $|\psi(0)\rangle = \sum_m C_m|m\rangle$. Separating into diagonal and off-diagonal parts at long times, the average is determined by the diagonal terms, $\sum_m |C_m|^2 O_{mm}$. Thermalization occurs when this matches the ensemble predictions. Deutsch [53] was the first to highlight the connection between such behavior and RMT, explaining how quantum statistical mechanics emerges in closed systems.

Srednicki [54] later formalized ETH by proposing the ansatz for local observables,

$$O_{mn} = O(\bar{E})\delta_{mn} + e^{-S(\bar{E})/2} f_O(\bar{E}, \omega) R_{mn} \tag{1.2}$$

where $\bar{E} = (E_m + E_n)/2$ is the mean energy, $\omega = E_m - E_n$ is their energy difference, $O(\bar{E})$ is the expectation value of O obtained from the microcanonical ensemble at energy $\bar{E}$. $O(\bar{E})$ and $f_O(\bar{E}, \omega)$ are smooth and slowly varying function of their arguments. $S(\bar{E})$ is the thermodynamic entropy, and R_{mn} is a random variable with zero mean and unit variance. This implies diagonal matrix elements of observables vary smoothly with energy and are described by a thermal ensemble, while

off-diagonal elements are exponentially suppressed with system size, ensuring thermalization.

This structure explains why observables in chaotic systems equilibrate: eigenstates themselves look thermal, so time averaging is not required. ETH thus bridges quantum chaos with statistical mechanics and has been verified in experiments in various setups [63–68].

Another perspective comes from considering subsystems [69–71]. Consider a quantum system with Hamiltonian H, partitioned into subsystem A and its environment B (see Fig. 1.1a). The reduced density matrix of A is $\rho_A(t) = \mathrm{Tr}_B[\rho(t)]$, where $\rho(t)$ is the state of the full system. If the reduced density matrix of A, $\rho_A(t)$ converges at long times to,

$$\rho_A^{(\mathrm{eq})} = \mathrm{Tr}_B[\rho^{(\mathrm{eq})}] \quad \text{where} \quad \rho^{(\mathrm{eq})} = \frac{e^{-\beta H}}{Z}, \tag{1.3}$$

for every subsystem A, then the system is said to thermalize. Here, β is the inverse temperature that comes from the average energy obtained from the microcanonical ensemble. In this case, the system effectively acts as its own reservoir. The underlying mechanism for this process lies in quantum entanglement. The unitary evolution scrambles initially local information into highly nonlocal correlations across the system. While all microscopic information is preserved globally, it becomes inaccessible locally, producing the effective loss of memory, which gives rise to the phenomenon of thermalization.

While ETH provides a powerful explanation for thermalization in isolated quantum many-body systems, it does not hold universally. A prominent class of exceptions is integrable systems. Rigol et al. [55] explicitly demonstrated this breakdown in one-dimensional hard-core bosons, showing that ETH fails to hold strictly, though a weaker form may apply, and they relax to a *Generalized Gibbs Ensemble* (GGE). Thermalization of integrable systems predicted by GGE has been experimentally confirmed [72, 73].

In non-interacting quantum systems, the concepts of eigenstate thermalization, quantum chaos, and random matrix theory do not apply in the same way as they do in generic interacting systems. This difference arises because non-interacting models are quadratic, with many-body dynamics reducible entirely to the evolution of single-particle modes. Such systems possess an extensive set of conserved quantities and do not develop the complexity and correlations typical of chaotic systems.

Another important class of ETH-violating systems is disordered quantum systems exhibiting localization. Anderson's pioneering work in 1958 [74] revealed

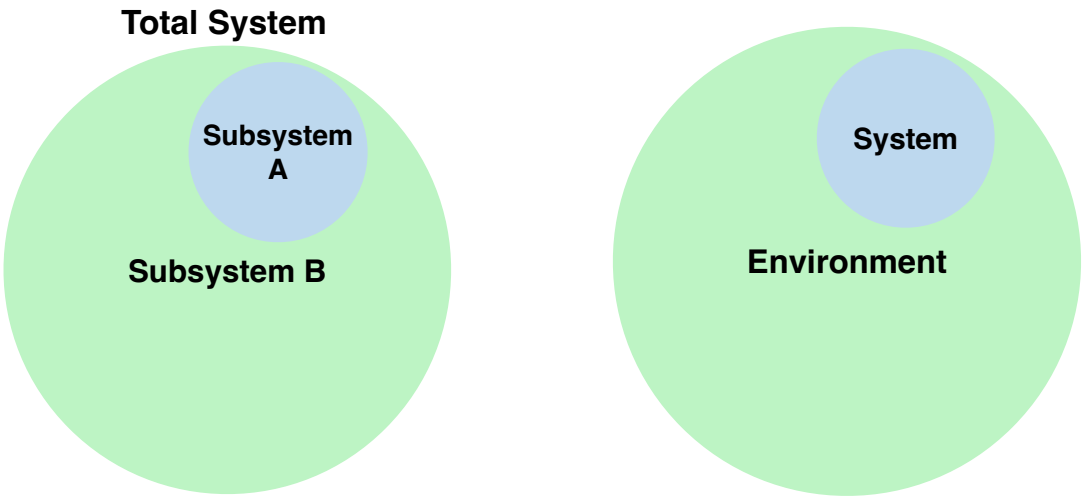

(a) Isolated Quantum System (b) Open Quantum System

Figure 1.1: (a) In conventional quantum statistical mechanics, a closed quantum system can be partitioned into a subsystem (A) and its complement (B), altogether undergoing unitary evolution. If the system thermalizes, region (B) effectively acts as a bath for subsystem (A). (b) For an open quantum system, the system of interest exchanges energy and particles with an external reservoir (or bath), introducing dissipation and decoherence in the system. The key difference between these setups is that, in practical scenarios, the environment's degrees of freedom are often inaccessible or difficult to manipulate and control.

that random potentials in a lattice can localize quantum particles spatially, leading to suppression of transport and breakdown of thermalization. This phenomenon, known as *Anderson localization*, is characterized by exponentially localized single-particle eigenstates and emerges prominently in one and two dimensions, while in higher dimensions it undergoes a disorder-induced transition [74–77]. It has been observed experimentally in ultracold atoms [78–83] and photonic experiments [84–89].

A central question, first raised by Anderson, is whether localization persists in the presence of interactions. This led to the concept of *many-body localization* (MBL) [52, 71, 90–93], which prevents thermalization even in interacting systems. In the MBL phase, long-time memory of the initial state is retained, in sharp contrast to thermalizing dynamics.

MBL exhibits several hallmark features: logarithmic growth of entanglement entropy [94, 95], area-law scaling of eigenstate entanglement even at finite energy density [96–98], absence of transport [52, 99], and quasi-local conserved operators known as local integrals of motion (LIOMs) [98, 100]. LIOMs naturally explain ETH breakdown, as they constrain dynamics and preserve memory of initial conditions [101]. Experimental realizations of MBL and localization transitions

have been reported across multiple platforms, including cold atoms, trapped ions, and superconducting qubits [102–110].

MBL phases are commonly probed using spectral statistics, which exhibit Poissonian level spacing distributions, reflecting the absence of level repulsion [41, 111]. By contrast, the thermal (ETH-obeying) phase shows Wigner-Dyson statistics characteristic of quantum chaos. The transition between these regimes is marked by a crossover in spectral properties [37, 41–44, 112, 113]. Dynamical observables, such as correlation functions, imbalance, magnetization, and return probabilities, are also extensively used [97, 102, 105, 114–121].

Rigorous mathematical work by Imbrie [122] establishes MBL persistence in strongly disordered, one-dimensional spin chains and proves the existence of a complete set of LIOMs, confirming emergent integrability in these phases. More recently, studies such as those by Roeck et al. [123] have demonstrated the absence of diffusion in strongly disordered spin chains, reinforcing this picture.

In reality, however, no quantum system is perfectly isolated. The environmental interaction, arising from optical cavities, engineered reservoirs, or measurements used in experimental setups, inevitably introduces dissipation and decoherence, resulting in non-unitary dynamics (see Fig. 1.1b). This motivates the use of non-Hermitian and open quantum system frameworks [124–127].

The standard approach for modeling these effects is the Markovian Lindblad master equation, which generalizes quantum evolution to include the environment's influence. This formalism rigorously captures both non-Hermitian dissipation and quantum jumps [125, 128–133]. Physically, open systems can often be described by a non-Hermitian effective Hamiltonian [134, 135], allowing access to novel regimes beyond Hermitian quantum mechanics. Recently, hybrid approaches combining Lindblad and non-Hermitian descriptions have emerged [136–138]. They rely on suitable deformations of the standard Lindblad equation and can be experimentally motivated [139–142].

Experimental progress in engineered controlled environments [143, 144] has revealed rich phenomena in open quantum systems. Depending on context, these are modeled either through Lindblad master equations or effective non-Hermitian Hamiltonians [133, 145]. Ultracold atomic setups, for example, enable systematic studies of many-body dynamics under dissipation, including entanglement generation [146, 147], dissipative quantum phase transitions [148], continuous time crystals [149], and measurement-induced transitions [150, 151]. Such developments have led to the idea of dissipation engineering, where environmental coupling is used to control and study quantum systems.

Non-Hermitian physics has since become a vibrant field. It plays a central role

in describing dissipative quantum systems [152–154], non-Hermitian optics [155–159], and the study of topological phases in open settings [160–171], highlighting the relevance of non-Hermitian and dissipative effects across diverse physical settings.

In this context, a central question concerns the fate of single-particle and many-body localization under environmental dissipation. Does localization survive, or does the system relax to a steady state? Addressing this question is crucial, as it probes the robustness of localization phenomena when coupled to external baths. The interplay between interactions, disorder, and environment has thus emerged as a rich research area at the intersection of quantum chaos and non-Hermitian physics [172–182]. Recently, MBL has been investigated in interacting non-Hermitian systems with disorder [183–186] and in quasiperiodic potentials [187–189], generating interest in localization within driven-dissipative settings. While localization and chaos in closed systems are comparatively well understood, their open-system counterparts remain less explored, with the identification of experimental platforms and diagnostics still an open challenge. The conjectures of quantum chaos were extended to dissipative systems by Grobe, Haake, and Sommers (GHS) [190, 191]. In the periodically kicked top with damping, they showed that if the underlying classical dynamics is integrable, the eigenvalues of the non-Hermitian evolution operator behave like uncorrelated complex levels, yielding two-dimensional Poisson statistics. Conversely, when the corresponding classical dynamics is chaotic, the eigenvalue statistics is described by non-Hermitian random matrix theory [192–194], showing universal cubic level repulsion.

Building on this framework, several spectral diagnostics have been generalized to non-Hermitian Hamiltonians [184, 195]. In particular, level-spacing statistics and complex spacing ratios [196] have been analyzed in open systems [189, 197–201], in non-Hermitian interacting disordered [184, 186, 202] and quasiperiodic models [187], as well as in non-Hermitian Dirac operators [203], dissipative quantum circuits [204], and higher-dimensional disordered systems [205, 206]. While these quantities capture nearest-neighbor correlations, another recently proposed diagnostic, the dissipative spectral form factor (which captures long-range correlations), extends traditional chaos indicators to non-Hermitian ensembles and has been studied for random matrices and various models [185, 207–212].

Recent research efforts have been made in the direction of generalizing ETH for open quantum systems to understand thermalization and ergodicity in driven-dissipative systems [213–217]. These works analyze the spectral properties of the Liouvillian superoperator, which governs the Markovian dynamics of open

systems, with eigenstates obeying statistical properties analogous to ETH in closed chaotic systems. Results indicate that local observables relax towards steady states that resemble thermal ensembles, with suppressed coherent oscillations. This emergent behavior provides a framework for identifying when the steady state of an open chaotic system appears thermal for local observables, thus connecting non-equilibrium steady states with traditional statistical mechanics.

There are also several unexplored avenues in non-interacting models coupled to environments, even though they appear to offer a more tractable framework. Most investigations rely on effective open-system approaches such as the Lindblad master equation. In this setting, the fate of localization under environmental coupling remains unsettled and actively debated, both in disordered and quasi-periodic lattices. Generally, coupling to a bath (damping/dephasing) or subjecting the system to continuous measurements introduces decoherence that tends to destroy localization [218–221].

Several works have studied dissipative extensions of the Anderson model. While these setups often yield trivial steady states (e.g., the vacuum), the transient dynamics remain highly nontrivial. Analyses of Liouvillian spectra, spectral gaps, and related measures have revealed disorder-induced transitions between localized and delocalized regimes [205, 218, 219, 222–230]. Yet, dynamical probes sometimes give contrasting results: several studies report the absence of dynamical localization, and instead find diffusion-like spreading [230–234]. This has led to the notion of regimes where spectral localization persists but dynamics exhibit delocalization [232–234], including experimental observations [235].

Interestingly, dissipation can also enhance localization when the setup is engineered carefully. Non-local or aperiodic dissipators [232, 236–238] have been shown to create exotic non-equilibrium steady states with controllable localization properties. Stronger coupling may even induce Zeno-like dynamics, freezing evolution and stabilizing localized phases [239, 240]. Thus, dissipation does not necessarily destroy localization; under carefully designed conditions, it can strengthen or reshape it.

Stochastic noise typically tends to destroy localization and induce slow dynamics [241, 242], while also producing logarithmic entanglement growth and anomalous transport. Such behavior is typically associated with many-body localized systems in closed settings, but arises here in non-interacting models subject to noise and dissipation. These results show that even in the absence of interactions, open disordered systems can host remarkably slow and unconventional dynamical regimes, producing signatures once thought to be exclusive to many-body localization.

Overall, the existing literature paints a non-universal picture in non-interacting regimes. In some cases, dephasing, noise, or continuous measurements restore delocalization; in others, localization survives or is even stabilized by tailored dissipation [243–245]. Experimental and numerical results further suggest that spectral localization may coexist with the absence of dynamical localization, or that transitions between localized and delocalized phases persist in open scenarios [232, 235, 246, 247] and in some cases, mobility edges appear due to environmental effects [228]. The outcome depends strongly on the bath coupling (local vs non-local), structure of dissipation (random, global, or quasi-periodic), and the diagnostic employed (spectral statistics, transport, or entanglement). The stability of single-particle localization in open non-interacting systems thus remains an open and central problem in non-equilibrium quantum physics.

1.2 Thesis Overview

This thesis addresses the impact of environmental coupling on one-dimensional quantum systems that exhibit localized and delocalized phases. A central focus is placed on understanding how driving and dissipation, introduced through interaction with an external environment, modify both the spectral and dynamical properties of these systems. Key open questions motivating this work include: Does environmental coupling destabilize, partially destroy, or entirely erase localization? Are signatures or reminiscences of the localized phase retained even in highly dissipative or driven regimes? By systematically probing these aspects, this thesis aims to outline the robustness and boundaries of localization phenomena under realistic open-system conditions, considering both non-interacting and interacting systems. It is worth noting that the term Anderson localization, as used in the following chapters, specifically refers to single-particle localization.

Chapter 2 explains the methodology and necessary background used to study the dynamics of open quantum systems. We discuss the exact methods used, like direct numerics for the correlation matrix and the quantum Langevin equation, which are non-perturbative methods. Then, we will discuss the quantum master equations, which rely on weak system-bath coupling, such as the Redfield and Lindblad Master equations.

The following chapters discuss the results of the thesis, which are divided into two main parts.

In the first part, we investigate open quantum systems with both disorder and nearest-neighbor interactions, using spectral and dynamical diagnostics. Both

the non-Hermitian Hamiltonian approach and the Lindblad master equation are employed to capture the signatures of quantum chaos and localization in the presence of dissipation or decoherence. In Chapter 3, we explore three non-Hermitian models using complex spacing ratios and dissipative spectral form factor to characterize their chaotic behaviour or lack of it. We find signatures of non-Hermitian many-body localization in these models and establish the correspondence with predictions from non-Hermitian random matrix theory (RMT). Building on this, we address the precise mechanisms by which quantum jumps may destabilize or destroy the many-body localized phase in chapter 4 by studying complex spacing ratios alongside with dynamics of imbalance and activity using a one-dimensional chain of hard-core bosons as a platform. We find that reducing the number of quantum jumps can stabilize the localized phase and promote its emergence. This part provides insight into both the spectral and dynamical aspects that environment-induced processes bring about in paradigms of many-body localization.

In the second part, we shift focus to the unitary dynamics of a composite system-environment (non-interacting) setup. Here, the system is an initially empty lattice, while the environment is modeled as a tight-binding chain at finite temperature and chemical potential. This setup enables a systematic investigation of particle injection and spreading within the lattice by analyzing observables such as spatial density profiles, total particle occupation, and the von-Neumann entropy. We consider a disorder-free tight-binding chain as my system in chapter 5, and find that the initial growth of particles (for both bosons and fermions) in the lattice is ballistic with time, and eventually the system relaxes to equilibrium. We also demonstrate the validity or invalidity of quantum master equations with exact dynamics in various regimes. In chapter 6, this approach is extended to quasi-periodic lattices that exhibit localization-delocalization transitions. The rich interplay between the system and environment, along with quasi-disorder, makes the dynamics very interesting and yields non-trivial dynamical growth of total occupation and Von Neumann entropy.

Together, in this thesis, these complementary approaches, dissipative system dynamics, and explicitly modeled system-environment unitary evolution, provide a broad and nuanced understanding of localization stability. This work bridges idealized isolated models and realistic experimental conditions where environments are unavoidable. The results have direct implications for controlling and detecting localized quantum phases in modern experimental platforms.

2

Theory of Open Quantum Systems

In this chapter, we present the methods used to study the dynamics of the systems considered in this thesis. Both non-perturbative and perturbative approaches are employed. The perturbative techniques fall under the broad category of quantum master equations [124–126], which are standard tools for describing the dynamics of open quantum systems. These approaches are quite general and can be applied in arbitrary geometries and dimensions, making them useful for a wide range of problems.

Specifically, we use four complementary approaches: (i) direct exact numerics for the correlation matrix, (ii) the exact quantum Langevin equation (QLE), (iii) the Redfield equation (perturbative and Markovian), and (iv) the local Lindblad equation (perturbative and Markovian). Each method has its own strengths and limitations, and together they provide a balanced and comprehensive framework for analyzing the dynamics of an open system.

2.1 Exact quantum dynamics for correlation matrix

We begin by describing the method of direct exact numerics, which is a non-perturbative way to study the dynamics of our setups. This method is particularly well-suited for systems governed by a quadratic Hamiltonian, i.e., non-interacting models. The key feature of such a Hamiltonian is that the equations of motion for the operators remain linear. As a direct consequence, the evolution of the two-point correlation functions forms a closed set, making the problem amenable. The Total Hamiltonian of the setup is given by,

$$H = \sum_{i,j} \mathcal{H}_{ij}\, \hat{d}_i^\dagger\, \hat{d}_j \equiv D^\dagger\, \mathcal{H}\, D \tag{2.1}$$

The dynamics are fully determined by the corresponding single-particle Hamiltonian matrix $\mathcal{H}$. In the setups considered here, we model a system that is connected to a bath. Both the system and the bath are described within the same quadratic Hamiltonian framework, such that the single-particle Hamiltonian $\mathcal{H}$ encodes not only the system and bath individually, but also their couplings. Within this approach, the goal is to evolve the joint dynamics of the system plus bath exactly.

The central object of interest is the two-point correlation function, defined over all degrees of freedom of both the system and the bath. Owing to the quadratic structure of the Hamiltonian, the equations of motion for this correlation matrix form a closed set and can be propagated directly in time using the single-particle Hamiltonian. Furthermore, Wick's theorem guarantees that the dynamics of the full density operator are completely determined by these two-point functions. Thus, by evolving the correlation matrix, the full unitary dynamics of the combined system-bath setup are captured exactly. Once the correlation matrix has been evolved, the observables of interest, such as the spatial density, can be extracted straightforwardly. Naturally, this procedure requires considering a large but finite bath. This ensures that the essential influence of the bath on the system is faithfully retained while keeping the numerical calculations tractable.

Let H_S and H_B denote the Hamiltonian of the system and the bath, respectively, with H_{SB} as the Hamiltonian describing their coupling. Let L and L_B be the number of sites in the system and bath respectively, such that $L_B \gg L$. We can rewrite the full Hamiltonian for the setup as

$$H = H_S + H_B + H_{SB} = \sum_{i,j=1}^{L+L_B} \mathcal{H}_{ij}\, \hat{d}_i^\dagger\, \hat{d}_j \equiv D^\dagger\, \mathcal{H}\, D \tag{2.2}$$

where $D = \{\hat{d}_i\}$ is a column vector containing all the annihilation operators of the system and the bath. Naturally, $D^\dagger = \{\hat{d}_i^\dagger\}$ is the row vector consisting of all the creation operators of the system and the bath. $\mathcal{H}$ is the single-particle Hamiltonian of the full setup and has dimension $(L + L_B) \times (L + L_B)$. The correlation matrix for the whole setup is given by $C(t)$

$$C(t) = \left\langle \left[D^\dagger(t)\right]^T \left[D^T(t)\right] \right\rangle \tag{2.3}$$

where the superscript T stands for the transpose of a matrix. The matrix element of the correlation matrix C is given as

$$C_{ij}(t) = \langle \hat{d}_i^\dagger(t) \hat{d}_j(t) \rangle \tag{2.4}$$

$\langle \ldots \rangle$ denotes an average over the initial state of the setup.

Following the Heisenberg equation of motion $\mathrm{i}\frac{\mathrm{d}}{\mathrm{d}t}O = \big[O, H\big]$, where we set $\hbar = 1$ throughout this thesis. For any operator $O(t)$, one can write

$$\frac{d}{dt}\left(\hat{d}_i^\dagger \hat{d}_j\right) = \mathrm{i}\Big[H, \hat{d}_i^\dagger \hat{d}_j\Big] = \mathrm{i}\sum_{r,s=1}^{L+L_B} \mathcal{H}_{rs}\Big[\hat{d}_r^\dagger \hat{d}_s, \hat{d}_i^\dagger \hat{d}_j\Big] \tag{2.5}$$

Using the commutation and anti-commutation relations for bosons and fermions, respectively, Eq. (2.5) can be simplified to

$$\frac{d}{dt}\left(\hat{d}_i^\dagger \hat{d}_j\right) = \mathrm{i}\sum_{r=1}^{L+L_B}\left(\mathcal{H}_{ri}\hat{d}_r^\dagger \hat{d}_j - \mathcal{H}_{jr}\hat{d}_i^\dagger \hat{d}_r\right) \tag{2.6}$$

Eq. (2.6) holds for both bosons and fermions. Using the fact that the single particle Hamiltonian $\mathcal{H}$ is symmetric (physical systems Hamiltonian is hermitian), we obtain the equation of motion for the correlation matrix $C(t)$, which is given by [248–250]

$$\dot{C}_{ij}(t) = \mathrm{i}\sum_{r=1}^{L+L_B}\Big(\mathcal{H}_{ir}\,C_{rj}(t) - C_{ir}(t)\,\mathcal{H}_{rj}\Big) = \mathrm{i}\Big[\mathcal{H}, C(t)\Big]_{ij} \tag{2.7}$$

The solution of which is given by,

$$C(t) = e^{\mathrm{i}\mathcal{H}t}C(0)e^{-\mathrm{i}\mathcal{H}t} \tag{2.8}$$

where $\mathcal{H}$ is the single particle Hamiltonian for the full setup and $C(0)$ is the correlation matrix at time $t = 0$.

2.2 Quantum Langevin Equation

In this section, we discuss the Quantum Langevin Equation (QLE) approach [251–259], which provides a non-perturbative method to evaluate the steady state properties of non-interacting setups. Owing to the bilinear form of the system-plus-bath Hamiltonian, this method enables exact calculations of transport and steady-state observables.

The central idea is to first solve the Heisenberg equations of motion for the bath degrees of freedom formally. Their solutions are then substituted back into the equations of motion for the system's degrees of freedom. As a result, the system dynamics takes the form of a generalized Langevin equation, where the effect of the bath appears as non-Markovian dissipation along with a stochastic noise term that has temporal correlations. This method gives exact results for the steady state whenever the system Hamiltonian is quadratic. The steady-state properties can be

obtained by solving the resulting generalized Langevin equations through Fourier transform techniques.

Let us begin by assuming a general non-interacting Hamiltonian for the entire setup, as well as the notation introduced in the previous section, remains unchanged.

$$\begin{aligned} H &= H_S + H_B + H_{SB} \\ H_S &= \sum_{i,j=1}^{L} \mathcal{H}^S_{ij} \hat{a}^\dagger_i \hat{a}_j, \quad H_B = \sum_{i,j=1}^{L_B} \mathcal{H}^B_{ij} \hat{b}^\dagger_i \hat{b}_j \\ H_{SB} &= \sum_{i=1}^{L} \sum_{j=1}^{L_B} \mathcal{H}^{SB}_{ij} \hat{a}^\dagger_i \hat{b}_j + h.c. \end{aligned} \tag{2.9}$$

Here, $\hat{a}_i$ and $\hat{a}^\dagger_i$ are the annihilation and creation operators for the lattice, while $\hat{b}_i$ and $\hat{b}^\dagger_i$ correspond to the bath. Note that $\hat{a}_i$ and $\hat{b}_i$ operators satisfy either commutation or anti-commutation algebra for bosons or fermions, respectively. The setup is initially assumed to be in a direct product state,

$$\hat{\rho}(0) = \hat{\rho}_S(0) \otimes \hat{\rho}^{th}_B(0) \tag{2.10}$$

with the bath in the thermal state characterized by temperature $T = (k_B\beta)^{-1}$ (where k_B is the Boltzmann constant henceforth set to 1 throughout this thesis) and chemical potential μ,

$$\rho_B(0) = \rho^{th}_B = \frac{e^{-\beta(H_B - \mu \hat{N}_B)}}{Z} \tag{2.11}$$

where $\hat{N}_B$ is the number operator for the bath and Z is the grand partition function for the bath. For the bath Hamiltonian, a unitary transformation U diagonalizes the matrix $\mathcal{H}^B$, yielding normal modes with eigenvalues λ^B_q,

$$H_B = \sum_{q=1}^{L_B} \lambda^B_q \, \hat{b}^\dagger_q \, \hat{b}_q, \qquad \hat{b}_i = \sum_{q=1}^{L_B} U_{iq} \, \hat{b}_q \tag{2.12}$$

with $\hat{b}_q$ being the annihilation operator of q-th normal mode of the bath with eigenvalues λ^B_q. The thermal correlations in this basis are

$$\langle \hat{b}^\dagger_i(0) \hat{b}_j(0) \rangle^{\text{th}} = \sum_{q=1}^{L_B} U^*_{iq} \, U_{jq} \, \bar{n}(\lambda^B_q) \tag{2.13}$$

where $\langle \hat{b}^\dagger_q \hat{b}_{q'} \rangle = \bar{n}(\lambda^B_q) \, \delta_{qq'}$. Here $\bar{n}(\omega)$ is Fermi-Bose function and is given by

$$\bar{n}(\omega) = \frac{1}{e^{\beta(w-\mu)} \pm 1} \tag{2.14}$$

Let us denote $\hat{A}(t) = \{\hat{a}_i(t)\}$ and $\hat{B}(t) = \{\hat{b}_i(t)\}$ as the column vectors consisting of system and bath annihilation operators, respectively. The Heisenberg equation of motion for operators is given as:

$$\dot{\hat{A}}(t) = -\mathrm{i}\mathcal{H}^S\hat{A}(t) - \mathrm{i}\mathcal{H}^{SB}\hat{B}(t) \tag{2.15}$$

$$\dot{\hat{B}}(t) = -\mathrm{i}\mathcal{H}^B\hat{B}(t) - \mathrm{i}\mathcal{H}^{SB\dagger}\hat{A}(t) \tag{2.16}$$

We first solve the bath equations in Eq. (2.16) and then substitute the solution to the system's equation of motion in Eq. (2.15). The formal solution of Eq. (2.16) is given by,

$$\hat{b}_i(t) = \mathrm{i}\sum_{r=1}^{L_B}\Big[g^+(t-t_0)\Big]_{ir}\hat{b}_r(t_0) + \int_{t_0}^{\infty}d\tau\sum_{r=1}^{L_B}\sum_{s=1}^{L}\Big[g^+(t-\tau)\Big]_{ir}\mathcal{H}^{SB\dagger}_{rs}\hat{a}_s(\tau) \tag{2.17}$$

where $i = 1, 2, \cdots L_B$ denotes the indices for bath operators. The Green's function

$$g^+(t) = -\mathrm{i}\,\theta(t)\,e^{-\mathrm{i}\mathcal{H}^B t} \tag{2.18}$$

is the solution of the homogeneous part of the Eq. (2.16) and $\theta(t)$ is the Heaviside step function. Substituting this solution in Eq. (2.15), we obtain the quantum Langevin equation (QLE) for the system operators as,

$$\dot{\hat{a}}_i(t) = -\mathrm{i}\sum_{s=1}^{L}\mathcal{H}^S_{is}\hat{a}_s(t) - \mathrm{i}\,\hat{\eta}_i(t) - \mathrm{i}\int_{t_0}^{\infty}d\tau\sum_{s=1}^{L}\Sigma^+_{is}(t-\tau)\,\hat{a}_s(\tau) \tag{2.19}$$

Note that, in Eq. (2.19), the effect of the bath appears as a self-energy and a noise term, which are given respectively as

$$\Sigma^+(t-\tau) = \mathcal{H}^{SB}\Big[g^+(t-\tau)\Big]\mathcal{H}^{SB\dagger} \tag{2.20}$$

$$\hat{\eta}(t) = \mathrm{i}\,\mathcal{H}^{SB}\Big[g^+(t-t_0)\Big]B(t_0) \tag{2.21}$$

The statistical property of the noise operator gets determined by the initial condition of the bath density operator, which is chosen to be thermal [Eq. (2.11)]. As a result, $\langle\hat{\eta}_i(t)\rangle = 0$. The noise correlation at different times can be expressed in terms of the normal modes of the bath as

$$\Big\langle\hat{\eta}^\dagger_i(t)\hat{\eta}_j(t')\Big\rangle = \sum_{r,r'=1}^{L_B}\mathcal{H}^{SB*}_{ir}\left(\sum_{q=1}^{L_B}U^*_{rq}U_{r'q}\bar{n}(\lambda^B_q)e^{\mathrm{i}\lambda^B_q(t-t')}\right)\mathcal{H}^{SB^T}_{r'j}\,\theta(t-t_0)\theta(t'-t_0) \tag{2.22}$$

Since we are interested in the steady-state limit, we first take $L_B \to \infty$ and then let $t_0 \to -\infty$. As a result, $\theta(t-t_0)$ and $\theta(t'-t_0)$ in Eq. (2.22) are always equal to unity. Let us now define Fourier transformation of $\hat{\eta}_i(t)$ as,

$$\tilde{\hat{\eta}}_i(\omega) = \int_{-\infty}^{\infty}dt\;e^{\mathrm{i}\omega t}\,\hat{\eta}_i(t) \tag{2.23}$$

and the corresponding inverse is given as

$$\hat{\eta}_i(t) = \int_{-\infty}^{\infty} \frac{d\omega}{2\pi}\, e^{-\mathrm{i}\omega t}\, \tilde{\hat{\eta}}_i(\omega) \tag{2.24}$$

Using Eq. (2.22) and Eq. (2.23), we get

$$\left\langle \tilde{\hat{\eta}}_i^{\dagger}(\omega)\tilde{\hat{\eta}}_j(\omega')\right\rangle = 4\pi^2\, \Gamma_{ji}(\omega)\, \bar{n}(\omega)\, \delta(\omega-\omega') \tag{2.25}$$

where,

$$\begin{aligned} \Gamma_{ji}(\omega) &= \sum_{r,r'=1}^{\infty} \mathcal{H}^{SB}_{jr'}\, \hat{\rho}_{r'r}(\omega) \mathcal{H}^{SB\dagger}_{ri} \\ \hat{\rho}_{r'r}(\omega) &= \sum_{q=1}^{\infty} U^{*}_{rq} U_{r'q}\, \delta(\omega-\lambda^{B}_{q}) \end{aligned} \tag{2.26}$$

We obtain the solution of Eq. (2.19) in the Fourier space as

$$\tilde{\hat{a}}_i(\omega) = \sum_{s=1}^{L} G^{+}_{is}(\omega)\, \tilde{\hat{\eta}}_s(\omega) \tag{2.27}$$

where $\tilde{\hat{a}}_i(\omega)$ is the Fourier transformation of $\hat{a}_i(t)$ with definition same as Eq. (2.23). The retarded Green's function $G^{+}(\omega)$ [260] that appears in Eq. (2.27) is given as

$$G^{+}(\omega) = \left[\omega I - \mathcal{H}^{S} - \Sigma^{+}(\omega)\right]^{-1} \tag{2.28}$$

where I is the $L-$dimensional Identity matrix and $\Sigma^{+}(\omega)$ is now the self-energy matrix in the Fourier space and is defined as,

$$\Sigma^{+}(\omega) = \mathcal{H}^{SB}\, \tilde{g}^{+}(\omega) \mathcal{H}^{SB\dagger} \tag{2.29}$$

Here, $\tilde{g}^{+}(\omega)$ is the Fourier transform of $g^{+}(t)$ [see Eq. (2.18)] and is given as

$$\left[\tilde{g}^{+}(\omega)\right]_{rr'} = \sum_{q=1}^{\infty} \frac{U_{rq} U^{*}_{r'q}}{\omega - \lambda^{B}_{q} + \mathrm{i}0^{+}} \tag{2.30}$$

where the small imaginary component appears to preserve the causality of $g^{+}(t)$. Finally, using Eq. (2.27) and the noise-noise correlation in Eq. (2.25), one can obtain the spatial local density $n_i(t) = \langle a_i^{\dagger}(t) a_i(t)\rangle$ in the steady state as

$$n_i(t\to\infty) = \int_{-\infty}^{\infty} d\omega \left[G^{+}(\omega)\Gamma(\omega)G^{-}(\omega)\right]_{ii} \bar{n}(\omega) \tag{2.31}$$

The integral in Eq. (2.31) can be performed numerically, and the steady state occupation at each site can be determined exactly. While the steady state can be

obtained exactly and straightforwardly using the QLE approach, computing the transient dynamics leading to the steady state is more challenging with QLE. This difficulty arises because QLE requires performing a Laplace transform for the time-dependent solution, whereas steady-state calculations rely on the simpler Fourier transform.

This formalism can be generally extended to a setup with multiple baths coupled to the system, given the quadratic Hamiltonian.

2.3 Redfield Quantum Master Equation

In this section, we will discuss the Redfield quantum master equation, a perturbative method used to obtain the state of the system. We provide the key steps that are involved in the derivation of this method. We start by writing the system-bath interaction Hamiltonian, given in Eq. (2.9), in the interaction picture as,

$$H^I_{SB}(t) = e^{\mathrm{i}\hat{H}_0 t} H_{SB} e^{-\mathrm{i}\hat{H}_0 t} = \sum_{i=1}^{L}\sum_{j=1}^{L_B} \mathcal{H}^{SB}_{ij} a^\dagger_i(t) b_j(t) + h.c. \tag{2.32}$$

where $\hat{H}_0 = \hat{H}_S + \hat{H}_B$ and

$$a_i(t) = e^{\mathrm{i}H_S t}\hat{a}_i e^{-\mathrm{i}H_S t}; \quad b_j(t) = e^{\mathrm{i}H_B t}\hat{b}_j e^{-\mathrm{i}H_B t} \tag{2.33}$$

where superscript "I" represents the interaction picture. Starting from the exact von-Neumann equation, one can write an exact equation governing the dynamics of the reduced density matrix for the system in the interaction picture as

$$\frac{d}{dt}\hat{\rho}^I_S(t) = -\int_0^t d\tau\, \mathrm{Tr_B}\left[H^I_{SB}(t), \left[H^I_{SB}(\tau), \hat{\rho}^I(\tau)\right]\right] \tag{2.34}$$

$\hat{\rho}(\tau)$ and $\hat{\rho}_S(\tau)$ are the density operator of the whole setup and reduced density matrix for the system, respectively. Now to arrive at the Redfield equation, one assumes (i) weak system-bath coupling limit (Born approximation) and (ii) Markovian limit [124, 125, 261]. The Born approximation involves expressing the total density matrix in the interaction picture $\hat{\rho}_I(\tau)$ as a direct product of the system and bath states, that is, $\hat{\rho}^I(\tau) = \hat{\rho}^I_S(\tau) \otimes \hat{\rho}^{\mathrm{th}}_B$ where $\hat{\rho}^{\mathrm{th}}_B$ denotes the thermal state of the bath. This approximation assumes that the system's influence on the bath is weak, so the bath density matrix remains essentially unchanged by the interaction and the overall system state.

The Markov approximation involves changing $\hat{\rho}^I_S(\tau)$ to $\hat{\rho}^I_S(t)$ and further extending the upper limit of the integral t to ∞, in Eq. (2.34). The Markovian

approximation used here can be justified under a separation of bath and systems time scales. In particular, the Markovian approximation is valid for system time scales much larger than the decay time scale of the bath. In other words, the system's evolution depends only on its present state. After some algebraic manipulations, we obtain the Redfield equation as [250, 262, 263]

$$\frac{d}{dt}\hat{\rho}_S^I(t) = -\int_0^\infty d\tau \, \mathrm{Tr_B}\left[H_{SB}^I(t), \left[H_{SB}^I(t-\tau), \hat{\rho}_S^I(\tau) \otimes \hat{\rho}_B^{\mathrm{th}}\right]\right] \tag{2.35}$$

The Redfield equation does not always guarantee complete positivity of the reduced density matrix [124], although it does preserve the trace. This lack of positivity can lead to unphysical results, such as negative probabilities, especially during transient dynamics or strong system-bath coupling. To address this issue, it is common to rewrite Eq. (2.35) in the eigen-basis of the system. In this basis, one can perform the secular approximation, which involves neglecting terms in the equation that oscillate rapidly with time compared to the typical timescales of the system's evolution. By discarding these oscillatory terms, whose contributions average out to zero over long periods, the resulting master equation, often called the Lindblad or Gorini Kossakowski Sudarshan Lindblad (GKSL) [264, 265] form, ensures both complete positivity and trace preservation. This makes the equation physically consistent for describing open system dynamics. Details of this derivation and the conditions for the secular approximation are discussed in Ref. [124].

2.4 Lindblad Quantum Master Equation

The Lindblad Quantum Master Equation is widely used to describe open quantum systems because it ensures completely positive and trace-preserving (CPTP) dynamics. Gorini, Kossakowski, Sudarshan [265], and Lindblad [264] proved that when a Markovian, CPTP non-unitary term is added to the unitary evolution of the density matrix, the resulting master equation must have a specific canonical form. In this form, the system Hamiltonian $\hat{H}$ generates the unitary part of the evolution, and a set of Lindblad operators $\{\hat{O}_m\}$ represent dissipative channels. The master equation, commonly called the Lindblad quantum master equation (QME), is written as

$$\frac{\partial \rho_S}{\partial t} = i[\rho_S, \hat{H}] + \sum_m \gamma_m \left(\hat{O}_m \rho \hat{O}_m^\dagger - \frac{1}{2}\{\hat{O}_m^\dagger \hat{O}_m, \rho\}\right) \tag{2.36}$$

where the rates $\gamma_m \geq 0$ guarantee complete positivity and preserve trace. The specific forms of $\hat{O}_m$ depend on the system and environment, often chosen phenomenologically. In particular, Local Lindblad [250, 266, 267] and global Lindblad equations [268–270] are accordingly employed, depending on the nature of dissipation and environmental interactions. This master equation framework is very versatile, effectively modeling a wide range of physical open quantum systems.

Note that although Redfield and Lindblad quantum master equations offer us the advantage of tracking both time dynamics and steady state, they involve perturbative and Markovian approximations.

2.5 Summary

In this chapter, we presented the theoretical framework and computational tools used to study open quantum systems, focusing on the dynamics that arise from their interaction with the environment. Capturing such non-unitary, dissipative behavior requires a balance between accuracy and analytical tractability. By combining exact numerical approaches with perturbative master equations, the chapter sets the foundation for understanding the evolution of quantum dynamics and aspects of thermalization under environmental influence. These tools collectively enable effective modeling of realistic quantum systems beyond isolated idealizations, framing the broader context for the thesis research on many-body open quantum dynamics.

3

Spectral Properties of Disordered Interacting Non-Hermitian Systems

3.1 Introduction

In this chapter, we study the spectral signatures of quantum chaos in disordered interacting non-Hermitian model Hamiltonians. Our main focus is on two quantities that have emerged as powerful tools in this context: the dissipative spectral form factor (DSFF) and the complex spacing ratio (CSR). Both measures allow us to characterize correlations in the complex spectrum of non-Hermitian operators and to distinguish between chaotic and integrable behavior. The models we study are motivated by platforms of direct experimental relevance, including ultracold atoms, trapped ions, and photonic systems [104, 145, 157, 158, 167]. These model Hamiltonians have an inhomogeneous (non-uniform density of states) spectrum in the complex plane with outliers at the edge of the spectrum, unlike the uniform homogeneous spectrum of non-hermitian random matrices. Understanding how these structural features impact spectral statistics and the manifestation of chaos is a central theme of this chapter.

We specifically consider three different model Hamiltonians (Fig. 3.1). Two of these are short-range models with different underlying symmetries, while the third incorporates long-range hopping. While many-body localization (MBL) was first proposed for closed systems having short-range hopping and interactions, the effect of long-range couplings has since drawn significant attention, owing to their relevance in experimental platforms such as ion traps and Rydberg arrays [103, 271–273]. In the Hermitian setting, it has been established that long-range interactions can preserve localization, whereas long-range hopping typically induces

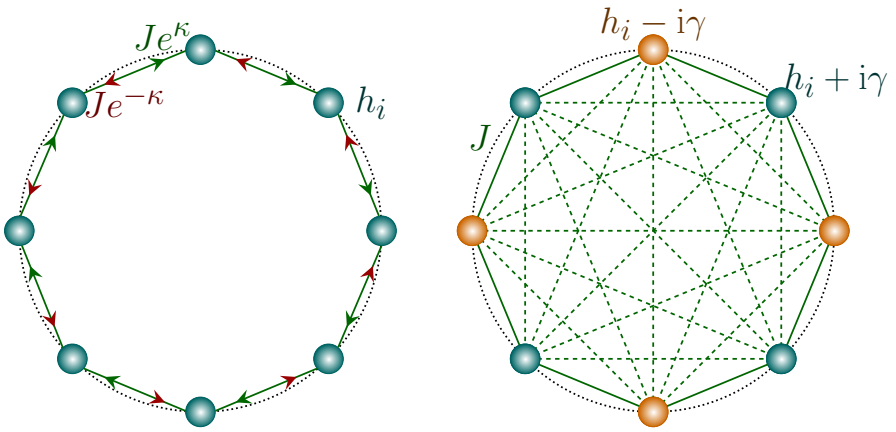

Figure 3.1: Schematic diagram showing the three models for representative system size. The diagram on the left illustrates model-I (Eq. (3.1)), where each lattice site, shown as a circle, is assigned a random onsite potential. The colored arrows indicate the non-reciprocal hopping amplitudes in opposite directions. The diagram on the right represents both model-II (Eq. (3.2)) and model-III (Eq. (3.3)). Here, the lattice sites alternate between teal-blue and orange circles, corresponding to onsite terms with imaginary contributions $+i\gamma$ and $-i\gamma$ respectively, in addition to random real onsite potentials. In model-II, only nearest-neighbor hoppings are present, so the dashed links are absent. In contrast, model-III includes both solid and dashed connections, with hopping amplitudes that decay with distance.

delocalization [274, 275]. Hence, it is natural to ask how long-range hopping influences spectral statistics and the stability of localization when dissipation is present. The third model serves as our platform to address this question.

The rest of this chapter is organized as follows. In Sec. 3.2, we introduce the non-Hermitian Hamiltonians under consideration. Sec. 3.3 presents the discussion on quantities of interest, namely the dissipative spectral form factor and the complex spacing ratio. In Sec. 3.4, we describe our findings across different parameter regimes, comparing them with the benchmarks of non-Hermitian random matrix theory in the weak disorder limit and Poisson statistics in the strong disorder regime. Finally, in Sec. 3.5, we summarize the results and provide an outlook. Certain details of the calculations and other relevant results are relegated to the appendix B.

3.2 Models

In this chapter, we consider three different non-hermitian models in one dimension (see Fig. 3.1). These are interacting systems of hard-core Bosons with a random disordered potential. The non-hermitian feature arises either through non-reciprocal hopping (model-I) or through complex onsite potentials (models II and III).

3.2.1 Model-I: Hatano-Nelson Hamiltonian

In this model, the particles hop through the one-dimensional disordered lattice with asymmetric nearest-neighbor hopping, where the degree of non-reciprocity is controlled by the real parameter $\kappa \in \mathbb{R}$. This is a generalization of the well-known non-interacting Hatano-Nelson model [276–279]. Initially proposed to investigate the depinning transition of flux lines in type-II superconductors with columnar defects, it captures how tilted flux lines traverse a disordered medium and transition from a pinned to a depinned state. A recent experiment mapped a one-dimensional nonreciprocal acoustic system onto the Hatano-Nelson model [280].

The Hamiltonian is given by [see Fig. 3.1(left)]

$$H = \sum_{i=1}^{L} \left[-J\left(e^{\kappa}\hat{b}_i^{\dagger}\,\hat{b}_{i+1} + e^{-\kappa}\hat{b}_{i+1}^{\dagger}\,\hat{b}_i\right) + U\,\hat{n}_i\,\hat{n}_{i+1} + h_i\,\hat{n}_i \right] \tag{3.1}$$

Here, $\hat{b}_i^{\dagger}$ is the creation operator corresponding to the creation of hard-core bosons at site i, and $\hat{n}_i = \hat{b}_i^{\dagger}\hat{b}_i$ counts the number of particles at site i. Hence, for our system of hard-core bosons, $\hat{n}_i$ can have any of the two possible values 1 and 0. The parameter $J \in \mathbb{R}$ sets the (reciprocal) hopping amplitude, while $U \in \mathbb{R}$ determines the strength of the nearest-neighbor interaction. The onsite potentials are real and randomly drawn from a uniform distribution $h_i \in [-h, h]$. This Hamiltonian preserves time-reversal symmetry, leading to eigenvalues that appear in complex conjugate pairs. As the disorder strength h is varied, the system exhibits both a transition between complex and real eigenvalue spectra and a many-body localization (MBL) transition [183, 184]. A representative sample plot of the spectrum at weak and strong disorder is plotted in Fig. 3.2.

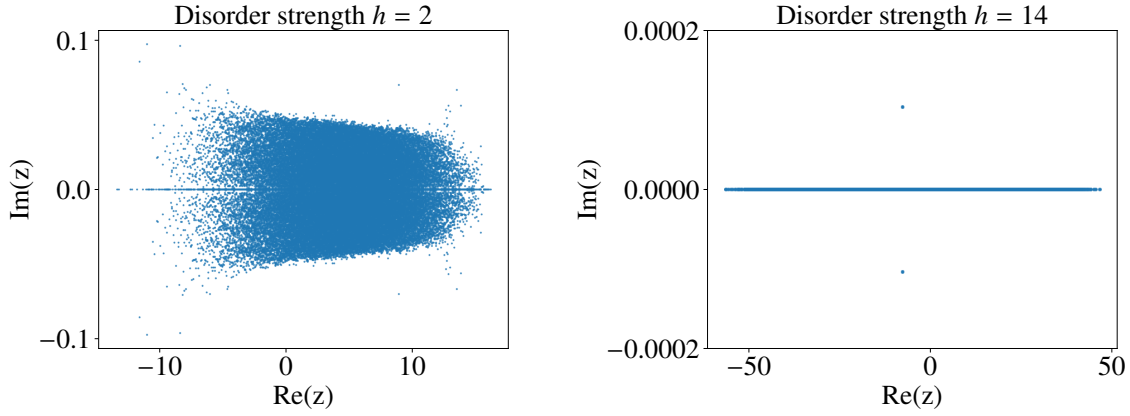

(a) $h = 2$ (b) $h = 14$

Figure 3.2: Model I - Energy Spectrum for $h = 2$ and 14 with $L = 18$

The symmetries and spectral properties of the Hamiltonian in Eq. (3.1) correspond to those of the Ginibre Orthogonal Ensemble (GinOE). Consequently, the eigenvalue statistics of this model at weak disorder are compared with GinOE predictions. In the strong disorder regime, the spectrum becomes real and uncorrelated, and hence, the level-spacing distribution will be compared with the 1D Poisson distribution.

3.2.2 Model-II: Gain-Loss Hamiltonian

This model is motivated by scenarios frequently encountered in the field of reservoir engineering, where engineered gain-loss processes give rise to effective non-Hermitian descriptions of quantum and classical systems. In such setups, local gain and loss are actively introduced or controlled, making the system an ideal platform to study non-Hermitian effects in a clean and tunable manner. These considerations have made the model a paradigmatic example in the study of non-Hermitian and parity-time (PT) symmetric physics [281, 282].

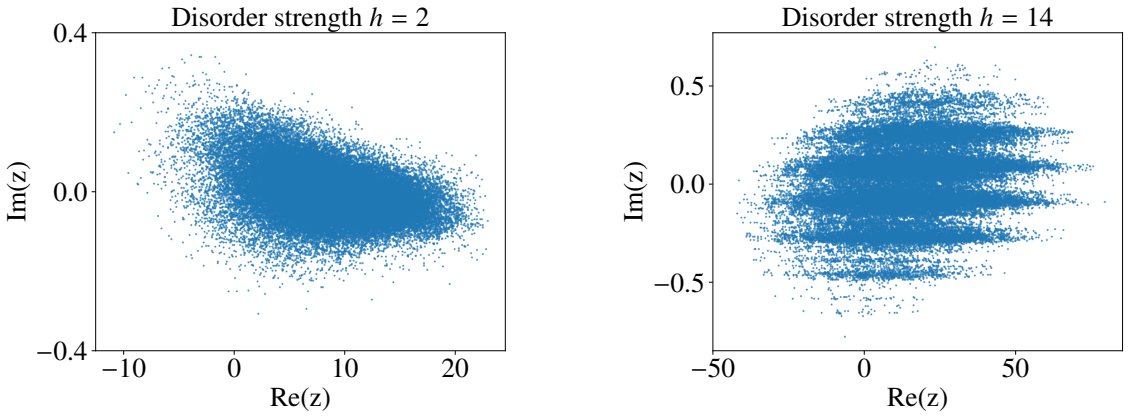

(a) $h = 2$ (b) $h = 14$

Figure 3.3: Model I - Energy Spectrum for $h = 2$ and 14 with $L = 18$

This model we work with is a disordered gain-loss system in which the real component of the onsite potential, h_i , is randomly drawn from a uniform distribution $h_i \in [-h, h]$. The imaginary component alternates in sign across the chain, given by $\pm i\gamma$, where γ denotes the gain-loss parameter. These alternating imaginary onsite terms tend to increase (gain) or decrease (loss) the local occupation, thereby introducing non-Hermiticity into the model. The Hamiltonian reads [see Fig. 3.1 (right)]

$$H = \sum_{i=1}^{L} \left[-J \left(\hat{b}_{i+1}^{\dagger} \hat{b}_i + \hat{b}_i^{\dagger} \hat{b}_{i+1} \right) + U \hat{n}_i \hat{n}_{i+1} + \left(h_i + i\gamma(-1)^i \right) \hat{n}_i \right] \tag{3.2}$$

This Hamiltonian breaks time-reversal symmetry and, notably, does not exhibit a complex-real eigenvalue transition. Nevertheless, it has been shown numerically to support a many-body localization (MBL) transition [184, 196]. The model is also characterized by a transposition symmetry ($H = H^T$). A representative sample plot of the spectrum at weak and strong disorder is plotted in Fig. 3.3.

The symmetries and spectral properties of this Hamiltonian correspond to the AI† ensemble. Therefore, for weak disorder, the eigenvalue statistics of this model are compared with those of the AI† ensemble, while in the strong disorder regime, the statistics are expected to be 2D Poisson for the strong disorder.

The significance of this model lies not only in its theoretical richness but also in its close connection with a wide array of experimental realizations. PT-symmetric balanced gain-loss configurations provide one of the most direct ways to access non-Hermitian phenomena and have been extensively realized across several physical platforms. Prominent examples include coupled optical waveguides with controlled gain and loss, and engineered optical meta-materials with engineered gain-loss gratings, which have enabled the controlled study of wave propagation and novel scattering properties. Lasers represent another quintessential application: gain is introduced through optical pumping while loss arises naturally from cavity leakage or unavoidable scattering. Such mechanisms not only provide fertile ground for exploring non-Hermitian effects but have also led to enhanced lasing functionalities, as seen in coupled laser oscillators and microcavity lasers [127, 157, 158, 281, 282]. Beyond optics, analogues of PT-symmetric and gain-loss systems have also been explored in electronic circuits, acoustic setups, and even mechanical systems.

3.2.3 Model-III: Long-Range Hamiltonian

While the first two models feature short-range nearest-neighbor hopping and interactions, this model is a long-range generalization of Model-II. Here, every lattice site is coupled to all other sites through hopping terms that decay with distance, whereas the nearest-neighbor interaction remains unchanged. The Hamiltonian is given by [see Fig. 3.1],

$$H = \sum_{i,j=1}^{L} \frac{-J}{|i-j|^{\alpha}} \left(\hat{b}_i^\dagger \hat{b}_j + \hat{b}_j^\dagger \hat{b}_i\right) + \sum_{i=1}^{L} \left[\left(h_i + \mathrm{i}\gamma(-1)^i\right)\hat{n}_i + U\hat{n}_i\hat{n}_{i+1}\right] \tag{3.3}$$

The range of hopping is controlled by the parameter α, where for positive α, the hopping strength decreases as the distance between the sites increases. The limiting cases include $\alpha = 0$, where each site couples to every other site with equal

strength t, and $\alpha \to \infty$, which recovers the nearest-neighbor hopping limit. This Hamiltonian preserves transposition symmetry and exhibits spectral statistics similar to Model-II in both chaotic and integrable regimes.

As discussed earlier, gain-loss models are experimentally relevant, but in realistic settings, particle hopping beyond nearest neighbors is expected, highlighting the importance of including long-range hopping as in Model-III. Experimental realizations of such long-range coupled systems have been reported [157].

All three Hamiltonians commute with the total particle number operator $\hat{N} = \sum_{i=1}^{L} \hat{n}_i$. Therefore, the Hamiltonians are block-diagonalizable in the particle number basis, where each block corresponds to a fixed particle number sector. We restrict our analysis to the half-filled sector for even L, for which the Hilbert space dimension is $\mathcal{N} = \binom{L}{L/2}$. We exactly diagonalize the Hamiltonian [283] and look for spectral properties for system sizes up to $L = 18$. For spectral statistics, disorder averages are computed over 4000, 200, and 100 samples for $L = 14$, 16, and 18, respectively. The eigenvalue spectrum from each disorder realization is recentered at the origin $(0, 0)$ in the complex plane, and all eigenvalues are normalized by the maximum absolute eigenvalue within that sample. This procedure ensures that the spectra from different disorder realizations occupy a common spatial scale in the complex plane.

Our computations use parameters $J = 1.0$, $U = 2.0$, $\kappa = 0.1$, and $\gamma = 0.1$, unless otherwise stated. The spectral statistics are compared with those of random matrices of dimension 10^4.

3.3 Spectral Observables

Spectral observables are quantities derived from the eigenvalue spectrum of the dynamical generator. They capture correlations among eigenvalues and thereby serve as key indicators of the spectral signatures associated with quantum chaos. In the following, we focus on spectral observables relevant for non-Hermitian dynamical generators, which play a central role in characterizing quantum chaos in driven-dissipative systems.

3.3.1 Complex spacing ratio (CSR)

For the hermitian systems, adjacent gap ratio is defined as $r_i = \min\{s_i, s_{i+1}\}/\max\{s_i, s_{i+1}\}$, where $s_i = E_{i+1} - E_i$ and E_i is the eigenvalue. This has been introduced [31, 32, 41, 42] and has been studied for a wide variety of physical systems [21, 40–

42, 45–52, 112, 284]. These diagnostics were soon generalized for non-Hermitian systems having complex eigenvalues by Prosen [196] and are referred to as complex spacing ratios. The complex spacing ratio for the n^{th} eigenvalue z_n is defined as

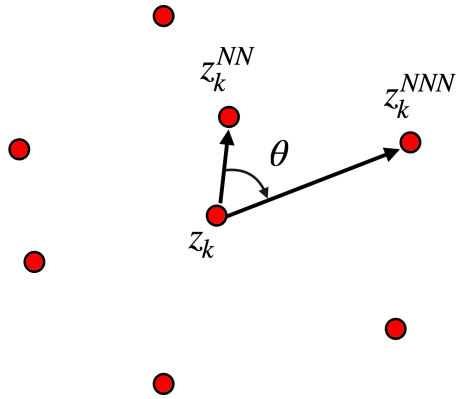

Figure 3.4: Sketch of Nearest and Next-to Nearest eigenvalue corresponding to z_k to define complex spacing ratios

the ratio of complex differences given by

$$\xi_n = \frac{z_n^{NN} - z_n}{z_n^{NNN} - z_n} = r_n e^{i\theta_n} \tag{3.4}$$

where z_n^{NN} and z_n^{NNN} are the nearest and next nearest neighbor of the eigenvalue z_n [see Fig. 3.4] respectively [196]. Here, the notion of distance is the absolute distance between eigenvalues in the complex plane. Note that r_n and θ_n are respectively the absolute value and the argument of the complex ratio ξ_n. The nearest-neighbor difference depends on the position of the eigenvalue in the complex spectrum, hence on the local density of states. However, in the ratio ξ_n, the effect of the local density of states is washed away, thereby making CSR a highly preferable diagnostic, and it is insensitive to the unfolding procedures. Note from the definition of CSR that $r_n \in [0, 1]$ and $\theta_n \in [-\pi, \pi] \quad \forall \quad n$. Here, the quantities of interest are the marginal distributions of r, denoted by $\rho(r)$, and marginal distributions of θ, denoted by $\rho(\theta)$, and the corresponding averages $\langle r \rangle$ and $\langle \cos\theta \rangle$, where the distributions are obtained considering all eigenvalues and disorder realizations.

We have briefly discussed the details of the relevant non-Hermitian random matrix ensembles in the appendix A.1. Both the distributions $\rho(r)$ and $\rho(\theta)$ have different behavior for different random matrix ensembles (see appendix A.2). The distributions $\rho(r)$ and $\rho(\theta)$ of these matrices show the manifestation of level repulsion for small r and θ. The average values $\langle r \rangle$ and $\langle \cos\theta \rangle$ are different for different matrix ensembles (tabulated in Table A.2). It is worth noting that, similar

to level spacing distributions, all three Ginibre ensembles (GinOE, GinUE, GinSE) have the same form for the marginal distributions of r and θ. On the other hand, for complex uncorrelated levels, the CSR is uniform inside a unit circle with the marginal distributions given by $\rho(r) = 2r$ and $\rho(\theta) = 1/(2\pi)$ [196]. The analytical expressions for the marginal distributions for the Ginibre random matrices are not known. Recently, attempts have been made to derive approximate analytical expressions for these distributions [285].

The statistics of ξ are indicative of the chaotic or regular nature of complex-valued spectra and can serve as diagnostics to locate the onset of chaos or localization [196]. For chaotic systems, the eigenvalues experience level repulsion resulting in a vanishing complex spacing ratio distribution at small r, and the ratio should spread all the neighbors of the reference level evenly around it, leading to a suppression of the ratio density for small angles, due to the level-repulsion, similar to Non-Hermitian Random Matrices with corresponding symmetry class. While for integrable systems, the complex spacing ratio is uniformly distributed inside a unit circle [196].

In principle, the CSR (ξ_n) can also be computed for a real spectrum. In fact, for real uncorrelated levels, the CSR turns out to be uniformly distributed between -1 and 1. Hence, the absolute values of the ratio given by r are uniformly distributed between 0 and 1. In other words, $\rho(r) = \Theta(1 - r)$ [196]. Similar computation for Gaussian Hermitian Ensembles is also done in Ref. [196].

3.3.2 Dissipative Spectral Form Factor

Spacing ratios only capture the repulsion between neighboring levels and thus allow us to only probe local spectral correlations. To measure long-range spectral correlations, one employs the spectral form factor [31, 32, 44]. It is another diagnostic to determine the dynamic nature of the system. More importantly, this is a non-trivial and analytically tractable diagnostic of quantum chaos.

For a generic Hermitian system (of dimension $\mathcal{N} \times \mathcal{N}$) having spectrum $\{E_i\}$, the density of states $\varrho(E)$, the Spectral Form Factor (SFF) for hermitian systems is defined as the Fourier transform of the two-point density correlation function $\langle \varrho(E)\varrho(E + \omega)\rangle$ and can be written in terms of eigenvalues conveniently as,

$$K(t) = \left\langle \sum_{n,m} e^{-\mathrm{i}(E_n - E_m)t} \right\rangle \tag{3.5}$$

where E_m is the m^{th} eigenvalue and t is the time.

For systems with Poisson statistics, SFF decays (with oscillations) and then saturates at long times, while for chaotic systems, it initially decays and then grows linearly, and saturates. Qualitatively, this is referred to as the 'dip-ramp-plateau' behavior. The initial decay is due to the density of states (non-universal feature), while the linear ramp reflects the phenomenon of spectral rigidity and is a universal feature of quantum chaos. SFF has been extensively studied for random ensembles [32] and for various physical systems [21, 43, 50–52, 112, 119].

Recently, SFF was generalized for non-hermitian systems having complex eigenvalues, known as the Dissipative Spectral Form Factor (DSFF) [207], and has been calculated for non-hermitian random matrices and several toy models [207, 208]. For a generic non-hermitian system (of dimension $\mathcal{N} \times \mathcal{N}$) having complex eigenvalues given by $z_n = x_n + \mathrm{i}y_n$, the density of states in the complex plane can be defined as

$$\varrho(z) = \sum_{n=1}^{\mathcal{N}} \delta^{(2)}(z - z_n) = \sum_{n=1}^{\mathcal{N}} \delta(x - x_n)\delta(y - y_n) \tag{3.6}$$

Similarly, the two-point density correlation function for a complex spectrum can be defined as $\langle \varrho(z_1)\varrho(z_2 + \omega)\rangle$ where ω is a complex variable $\omega = \omega_x + \mathrm{i}\omega_y$ and $\langle . \rangle$ denotes average over different ensembles. Hence, DSFF is defined as the 2D Fourier transform of the two-point density correlation function having a generalized time variable $\tau = t + \mathrm{i}s$, and it can be written in terms of eigenvalues as a function of (t, s) or (τ, τ^*) as follows [207],

$$K(\tau, \tau^*) = \frac{1}{\mathcal{N}} \left\langle \sum_{n,m=1}^{\mathcal{N}} e^{-\mathrm{i}\vec{z}_{mn}.\vec{\tau}} \right\rangle \tag{3.7}$$

Here $\vec{z}_{mn} = (x_m - x_n, y_m - y_n)$ is the difference between the two eigenvalues z_m and z_n, and $\vec{\tau} \equiv (t, s) = (|\tau| \cos\phi, |\tau| \sin\phi)$. The dot product in the parenthesis represents the product $\vec{z}_{mn}.\vec{\tau} = (x_m - x_n)t + (y_m - y_n)s$, which allows a natural interpretation in the complex plane: At a fixed angle and as a function of $|\tau|$, DSFF is the SFF of the projection of $\{z_n\}$ onto the radial axis specified by angle $\phi = \arg(\tau)$. It captures the long-range correlations among the real and the imaginary parts of the eigenvalues for all energy scales. Often it is useful to define the connected part of the DSFF, $K_c(\tau, \tau^*)$ as,

$$K_c(\tau, \tau^*) = \frac{1}{\mathcal{N}} \left[\left\langle \sum_{n,m=1}^{\mathcal{N}} e^{-\mathrm{i}\vec{z}_{mn}.\vec{\tau}} \right\rangle - \left| \left\langle \sum_{m=1}^{\mathcal{N}} e^{-\mathrm{i}\vec{z}_{m}.\vec{\tau}} \right\rangle \right|^2 \right] \tag{3.8}$$

For numerically efficient calculations, the expression of $K(\tau, \tau^*)$ in Eq. (3.7) can be rewritten as

$$K(\tau, \tau^*) = \left\langle \left| \sum_n e^{\mathrm{i}(z_n \tau^* + z_n^* \tau)/2} \right|^2 \right\rangle \tag{3.9}$$

which involves a single summation over complex eigenvalues z_n instead of a double summation in Eq. (3.7) over eigenvalue differences z_{mn}.

We re-center and rescale the complex spectrum within a unit disc $|z| < 1$. This ensures that the spectrum of each random sample spreads over the same region in the complex plane. The rationale behind doing that is to obtain a proper scaling of mean level-spacing with system size $\mathcal{N}$. As the mean area per eigenvalue is $\pi/\mathcal{N}$ (when averaged over disorder samples) and hence, the mean spacing would be $1/\sqrt{\mathcal{N}}$. This rescaling doesn't affect the CSR; however, this procedure is specifically important to the DSFF, and it helps us to map the universal features of the spectrum with those of random matrices, irrespective of the system sizes.

DSFF is discussed in detail in the Appendix A.3 for Non-Hermitian Random Ensembles. For GinUE, the DSFF has been calculated [207] and its analytical results are mentioned in Appendix A.3. The qualitative behavior of 'dip-ramp-plateau', analogous to SFFs [44], where the ramp is quadratic. It signifies the existence of level repulsion for Non-Hermitian random ensembles. The absence of a ramp signifies the absence of level repulsion for uncorrelated levels. The variation of DSFF for random ensembles is independent of $\phi = \arg(\tau)$ owing to the homogenous and isotropic distribution of the eigenvalues z_n, or more precisely, due to the rotational symmetry of the distribution of $z_{mn} = z_m - z_n$ [207] as discussed in appendix A.3.

The feature of the Ramp in DSFF is universal, but the time-scales at which this ramp appears depend on the system size. Furthermore, the slope of the ramp is determined by the Heisenberg time-scale τ_H, which in turn is a function of matrix size. Hence, first, we need to compute the Heisenberg time scale and then rescale the time to see the universal ramp for all system sizes. For RMT, the Heisenberg time-scale τ_H is proportional to the inverse of the mean level spacing (Δ), and this time-scale brings out the information about all the correlations among eigenvalues (when $|z_m - z_n| \approx \mathrm{O}(\Delta)$) and it scales as $\tau_H = O(\sqrt{\mathcal{N}})$ where $\mathcal{N}$ is the corresponding matrix size.

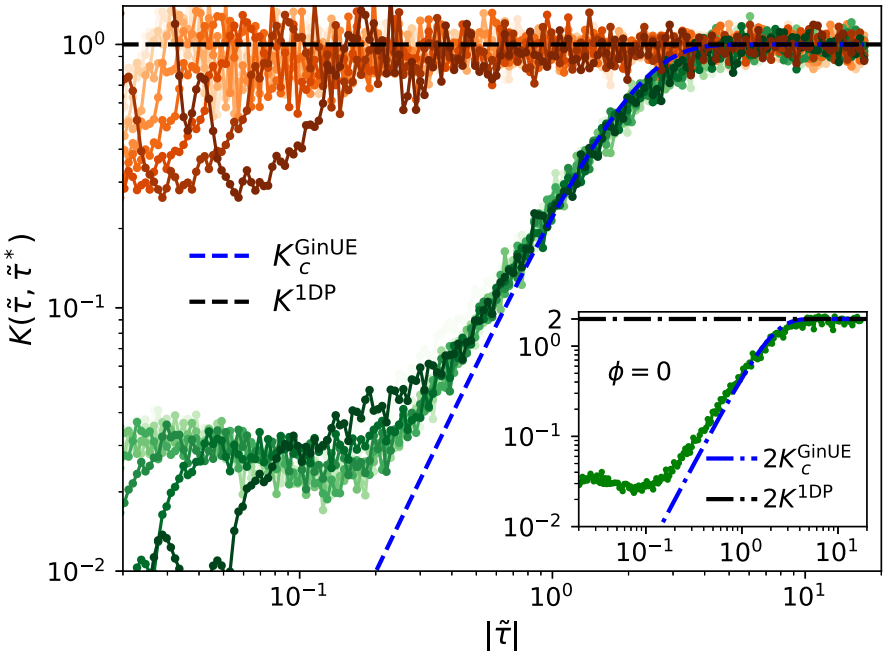

Figure 3.5: [Model-I, Eq. (3.1)] DSFF (Eq. (3.7)) for model-I as a function of rescaled time variable $|\tilde{\tau}|$ for different values of $\phi \in [\pi/20, 9\pi/20]$ shown for different values of $\phi \in [\pi/20, 9\pi/20]$ in increments of $\pi/20$. Results are presented for low disorder strength $h = 2$ (green) and high disorder strength $h = 14$ (orange), with lighter shades corresponding to smaller ϕ values and darker shades to larger ones. The blue dashed line represents the DSFF for the Ginibre Unitary Ensemble (K_c^{GinUE}), while the black line corresponds to uncorrelated random energy levels ($K_c^{\text{1D P}} = 1$). At weak disorder, the DSFF displays a non-linear ramp consistent with Ginibre random matrix theory predictions. In contrast, the absence of a ramp at strong disorder indicates uncorrelated energy levels and localization in the non-Hermitian system. The inset shows the DSFF at $\phi = 0$ for $h = 2$, which matches precisely with $2K_c^{\text{GinUE}}$.

3.4 Results

In this section, we will discuss our findings based on spectral quantities of interest, Dissipative Spectral Form Factor (DSFF), and Complex Spacing Ratios (CSR) on the three models (Eqns. (3.1),(3.2),(3.3)) discussed above.

3.4.1 Dissipative Spectral Form Factor

Fig. 3.5 shows the DSFF [Eq. (3.7)] for model-I as a function of the rescaled time variable $|\tilde{\tau}|$ for both weak ($h = 2$) and strong ($h = 14$) disorder strengths. The rescaled time variable is defined as $\tilde{\tau} = \tau/\tau_H$, chosen to shift the time axis to facilitate direct comparison with Random Matrix Theory predictions (see Appendix B.2 for details). For weak disoder ($h = 2$), at very small time scales $|\tilde{\tau}|$, the

DSFF starts from a value $\mathcal{N}$. After initial oscillatory behavior, the DSFF exhibits a non-linear ramp characteristic of the Ginibre random matrices, indicating chaotic behavior. At long times, the DSFF saturates to 1. For some intermediate time $\tilde{\tau}$ before the onset of ramp, DSFF $K(\tilde{\tau}, \tilde{\tau}^*)$ depends on both $|\tilde{\tau}|$ and ϕ, and this is an artifact of the absence of rotational symmetry in the distribution of z_{mn} for disordered system (see appendix B.1) unlike the rotationally symmetric distribution for random matrix (see Fig. A.5). Nonetheless, it turns out that there exists a deep connection between the models and random matrices, irrespective of the inhomogeneity and anisotropy of the underlying complex spectrum at intermediate and late time scales. The universal non-linear ramp obtained in model-I agrees with the analytical expression of DSFF for GinUE, given by [207],

$$K_c^{\text{GinUE}}(\tilde{\tau}, \tilde{\tau}^*) = 1 - \exp\left(-|\tilde{\tau}|^2/4\right) \tag{3.10}$$

The rescaled time variable is defined by $\tilde{\tau} = \tau/\tau_H$ where $\tau_H = \sqrt{\mathcal{N}}$ is the Heisenberg time for GinUE random matrices and is inversely proportional to the mean level spacing, which scales as $\sim 1/\sqrt{\mathcal{N}}$. The estimation of Heisenberg time for these model Hamiltonians is discussed in the appendix B.2.

Since the Hamiltonian of model-I is completely real and thus has complex conjugation symmetry ($H = H^*$), its behavior in the quantum chaotic regime should correspond to Ginibre orthogonal ensembles (GinOE) [164, 192, 286] instead of GinUE. However, just like level spacing distribution, DSFF also has the same form for all three Ginibre symmetry classes except for some special angles near $\phi = 0, \pi/2$ [207] for which the analytical expression is not known. A non-hermitian matrix belonging to GinOE has an eigenvalue spectrum comprises of complex conjugate pairs and a significant number of completely real eigenvalues. These give rise to accidental degeneracies when projected onto $\phi = 0, \pi/2$ directions. Because of these degeneracies at $\phi = 0$, the DSFF for GinOE is exactly twice the DSFF for GinUE ($K_c^{\text{GinOE}}|_{\phi=0} = 2K_c^{\text{GinUE}}$) in the limit of large matrix size. Thus, for generic values of ϕ away from 0 and $\pi/2$, it is justified to compare the DSFF of the GinOE class with that of the GinUE. On the other hand, for large disorder strength ($h = 14$), the DSFF saturates to $K = 1$ after an initial dip, and the absence of a ramp implies uncorrelated energy levels. We find that for intermediate values of h, especially in the proximity of the critical point for the localization transition [184], the data neither resembles RMT nor Poisson statistics. This is rooted in finite-size effects, and details are discussed in appendix B.3.

Fig. 3.6 shows the variation of DSFF as a function of the rescaled time variable $|\tilde{\tau}|$ for model-II [Eq. (3.2)]. This has the same qualitative feature as in Model-I. The ramp here does not match with the GinUE case, as the symmetry of the

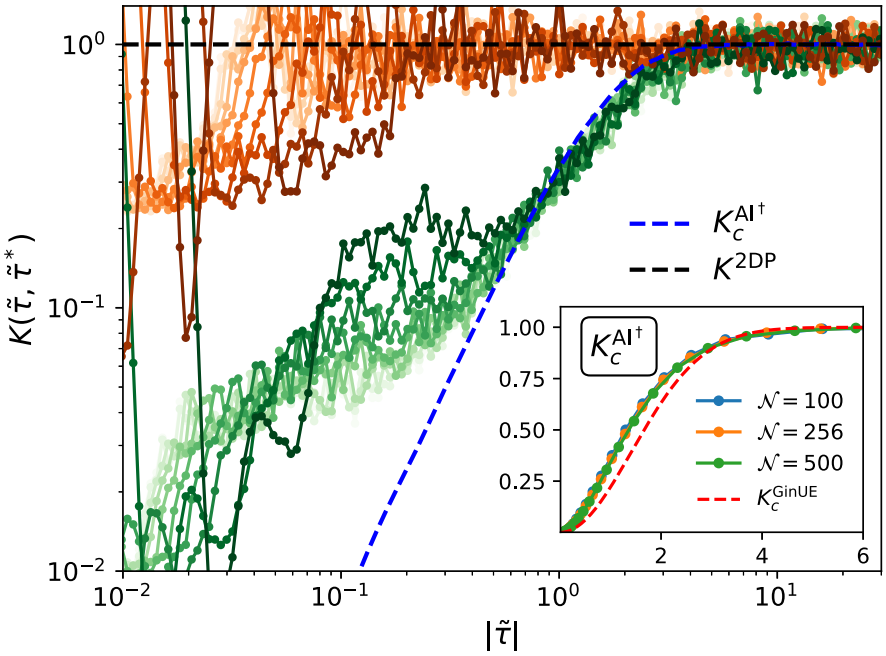

Figure 3.6: [Model-II, Eq. (3.2)] DSFF for model-*II*: Dissipative spectral form factor for model *II* as a function of rescaled time variable $|\tilde{\tau}|$ for different values of $\phi \in [0, 9\pi/20]$ in steps of $\pi/20$ for $h = 2$ (Green), 14 (Orange). The lowest value of ϕ in the given range corresponds to the lightest shade, while the highest value of ϕ corresponds to the darkest shade of the corresponding colors. The blue line shows DSFF for random matrices belonging to the AI† symmetry class, while the black line corresponds to the uncorrelated random complex energy levels. The inset shows the DSFF for random matrices of size $\mathcal{N} \times \mathcal{N}$ belonging to the AI† symmetry class, where the DSFF for GinUE is plotted as a red dashed line to highlight the difference between AI† and GinUE symmetry classes.

Hamiltonian does not conform with any of the Ginibre classes. The Hamiltonian of this model has a transposition symmetry ($H = H^T$) similar to the AI† symmetry class of non-hermitian matrices [164, 286]. We, therefore, calculate the DSFF for non-hermitian random matrices belonging to the AI† symmetry class (shown in the inset of Fig. 3.6) and compare it with the DSFF obtained for model-II at weak disorder. We find good agreement of the DSFF of model-II with that of AI† symmetry class at weak disorder, while at large disorder strength, it matches with that of uncorrelated complex energy levels.

Next, we discuss the effect of introducing long-range hopping in model-II (called model-III [Eq. (3.3)]). In Fig. 3.7, we show the DSFF for model-III. We tune the parameter α that controls the range of the hopping. While doing that, we fix the disorder strength at $h = 14$ such that in the presence of only short-range hopping (nearest-neighbor), the DSFF is similar to that obtained from uncorrelated random complex levels. From Eq. (3.3), it is evident that $\alpha \to \infty$ corresponds to a system

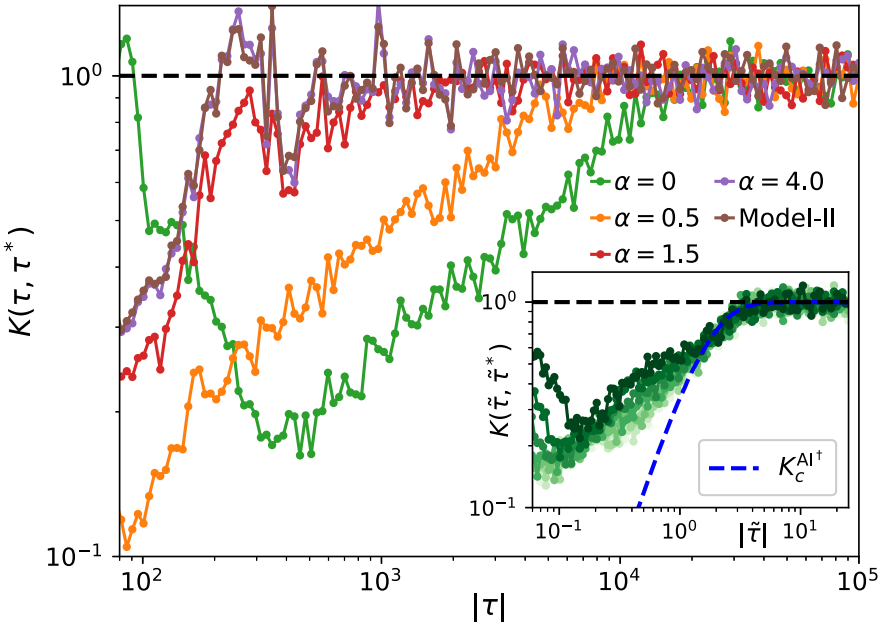

Figure 3.7: [Model-III, Eq. (3.3)] DSFF for model-III as a function of the time variable $|\tau|$ for different values of α at $\phi = 0.3\,\pi$ and system size $L = 16$. The disorder strength is fixed at $h = 14$. The DSFF for model-II, having only nearest-neighbor hopping ($\alpha \to \infty$), is also plotted in the same figure for comparison. The DSFF changes from that of uncorrelated complex levels (black dashed line) to that of AI† symmetry class (shown in inset) as the value of α is decreased. The inset shows agreement of $K_c^{\mathrm{AI}^\dagger}$ with the $\alpha = 0$ case, where different shades of green color represent different values of ϕ chosen from $[0, 9\pi/20]$ in steps of $\pi/20$.

comprising of only nearest-neighbor hopping. We see that as α is decreased, thereby increasing the range of hopping for the particles, the system becomes more chaotic. There is good agreement of the DSFF with that of AI† symmetry class when $\alpha = 0$ as shown in the inset of Fig. 3.7. This is because changing the range of the hopping does not change the symmetry of the Hamiltonian, therefore, implying that the Hamiltonian of model-III preserves the transposition symmetry ($H = H^T$). For intermediate values of α, the DSFF results neither fall into the RMT regime nor correspond to the Poisson statistics. This is again rooted in the finite-size effects. The enhancement of the chaotic signatures with the increasing range of hopping (decreasing α) in this non-hermitian Hamiltonian complements the understanding in the case of long-range Hermitian Hamiltonians, where the delocalization increases with an increase in the range of hopping [274, 275, 287].

All the DSFF results presented above for the three models were for the case when no unfolding procedure was involved. We find that one of the proposed unfolding procedures for such a complex eigen-spectrum, namely the conformal mapping [288], yields the same DSFF.

3.4.2 Complex spacing ratio (CSR)

Fig. 3.8 (a) represents the marginal distributions of r for model-I, as the disorder strength h is varied. Model-I has a complex-real spectral transition as a function of disorder strength h [184]. Despite this transition, we use the same definition of CSR (Eq. (3.4)) even for real eigenvalues in the strong disorder limit to facilitate the use of the same diagnostic for all disorder strengths. In the presence of strong disorder, where we expect uncorrelated energy levels from DSFF results (Fig. 3.5), the CSR (ξ_n) is real due to the real energy spectrum. In fact, for real uncorrelated energy levels, the CSR turns out to be uniformly distributed between -1 and 1.

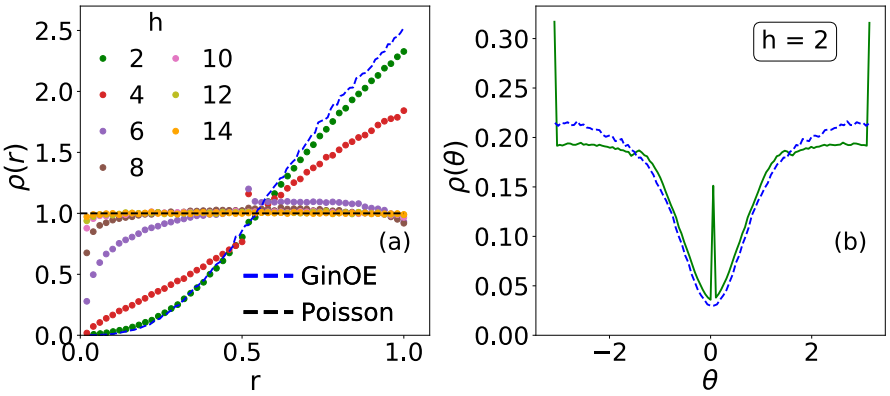

Figure 3.8: [Model-I,Eq. (3.1)] (a) Marginal distribution of r (left) for different values of h for $L = 18$. For weak disorder strength ($h = 2$), the distribution corresponds to that of GinOE (blue dashed line), while for large disorder $h = 14$, we see agreement with 1D Poisson statistics (black dashed). (b) The marginal distribution of θ (right) for $h = 2$ shows agreement with that of GinOE (blue dashed line) while the peaks at $0, \pi$ are due to the completely real eigenvalues. The variable θ becomes ill-defined at large disorder strength due to the completely real spectrum.

We find that in the presence of weak disorder($h = 2$), the marginal distribution of r corresponds to that of GinOE. As the disorder strength h is increased, the marginal distribution of r starts becoming more and more flat and eventually corresponds to 1D Poisson statistics, i.e., $\rho(r) = 1$, demonstrating the chaos to localization transition. Since we consider the entire spectrum for our results, we see some deviation from GinOE for larger values of r for $h = 2$ as shown in Fig. 3.8. Upon suitably going to the middle of the spectrum, as is usually done [184], the agreement between the distribution of r and that of GinOE becomes better as shown in appendix B.4 (Fig. B.3). Note that in Fig. B.3, there is still a discrepancy due to a small fraction of completely real eigenvalues of model-I, which are comparatively much less in GinOE random matrices. Since model-I undergoes a complex-real

transition as the disorder strength is increased, the marginal distribution of the angle θ is not particularly helpful. This is because θ can have only two values 0 and π. Nonetheless, for weak disorder strength ($h = 2$), the distribution of θ is well defined and agrees with that of GinOE [Fig. 3.8(b)].

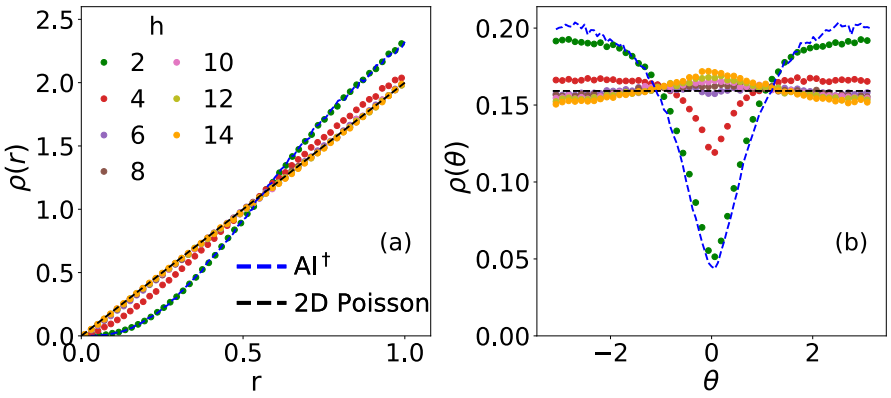

Figure 3.9: [Model-II, Eq. (3.2)] Marginal distributions of (left) r and (right) θ for different values of h for $L = 18$. For weak disorder strength ($h = 2$), both the marginal distributions correspond to that of AI† symmetry class (blue dashed), while for strong disorder strength $h = 14$, they correspond to that of 2D Poisson statistics (black dashed).

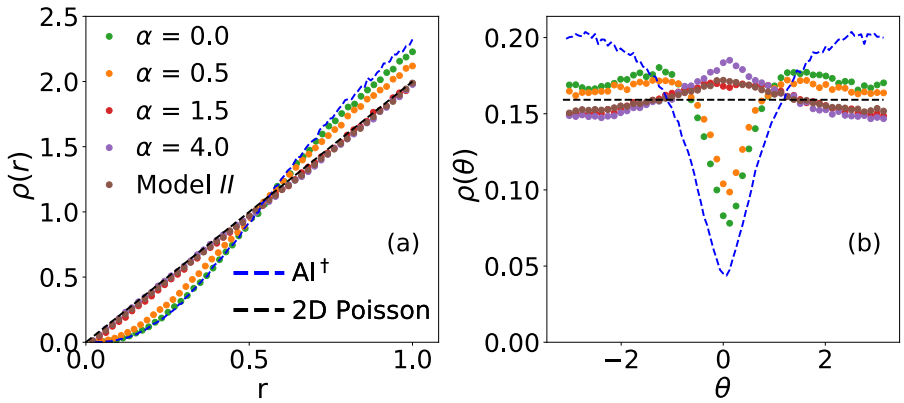

Figure 3.10: [Model III, Eq. (3.3)] Marginal distributions of (left) r and (right) θ for different values of α at $h = 14$ for system size $L = 16$. Both the marginal distributions change from that of 2D Poisson statistics (black dashed) to that of AI† symmetry class (blue dashed) as α decreases. In addition, we also plot the marginal distribution for model-II at $h = 14$ (which corresponds to $\alpha \to \infty$).

Fig. 3.9 shows the variation of the marginal distribution of r and θ as the disorder strength h is increased for model-II. For small disorder strength ($h = 2$), both the distributions correspond to that of the AI† symmetry class. As the disorder strength h is increased, both the marginal distributions tend to those corresponding to 2D Poisson statistics. In this case too, if one restricts the analysis

to the middle of the spectrum, the agreement with random matrix theory becomes better as shown in appendix B.4 (Fig. B.4).

Fig. 3.10 shows the marginal distribution of r and θ for model-III at disorder strength $h = 14$ as α is varied. Here too, the agreement with random matrix theory becomes better, taking just the middle of the spectrum (appendix B.4, Fig. B.5). Similar to DSFF, we notice that the behaviors of both the distributions $\rho(r)$ and $\rho(\theta)$ change from the case of 2D Poisson statistics to that of AI† symmetry class as the range of hopping is increased by decreasing α.

For intermediate values of h (or α for model-III), in all three models discussed above, both the DSFF and the CSR show neither perfect agreement with RMT nor Poisson statistics. This is owing to the finite-size effects in the vicinity of the critical point for the localization transition, as elaborated in appendix B.3. The marginal distributions $\rho(r)$ and $\rho(\theta)$ tend towards the expected RMT/ Poisson statistics as one increases the system size. It is worth mentioning that in addition to the marginal distributions, the average values of r and $\cos\theta$ can be computed and are summarized in tables (Table B.1,B.2,B.3) and figures (Fig. B.6,B.7) in the appendix B.4).

Another way to demonstrate the many-body localization transition when the disorder strength h or the α is tuned, by plotting the distribution of CSR in the complex plane for different parameters. Fig. 3.11 shows the ξ scatter distribution at fixed disorder strength $h = 14$ for model-III, demonstrating the transition as α is varied. We notice the behavior of these distributions changes from 2D Poisson statistics to that of AI† symmetry class as the range of hopping is increased.

3.5 Summary and Conclusions

In this chapter, we discuss spectral properties of three different non-hermitian Hamiltonians (Eqns. (3.1), (3.2), (3.3)), each of which is unique in its own way. We discuss two quantities, namely the dissipative spectral form factor (DSFF) and the complex spacing ratio (CSR), which serve as an excellent diagnostic to classify phases. For the two models with short-ranged hopping, we show that both the quantities DSFF (Figs. 3.5, 3.6) and CSR (Figs. 3.8, 3.9) capture the chaotic (localization) behavior at the weak (strong) disorder limit. In the chaotic regime, both quantities show agreement with that of the respective non-Hermitian random matrix ensembles despite the inhomogeneous and anisotropic distribution of the energy levels in the complex plane. In other words, both quantities show universal features in the chaotic regime despite local non-universal properties of the density

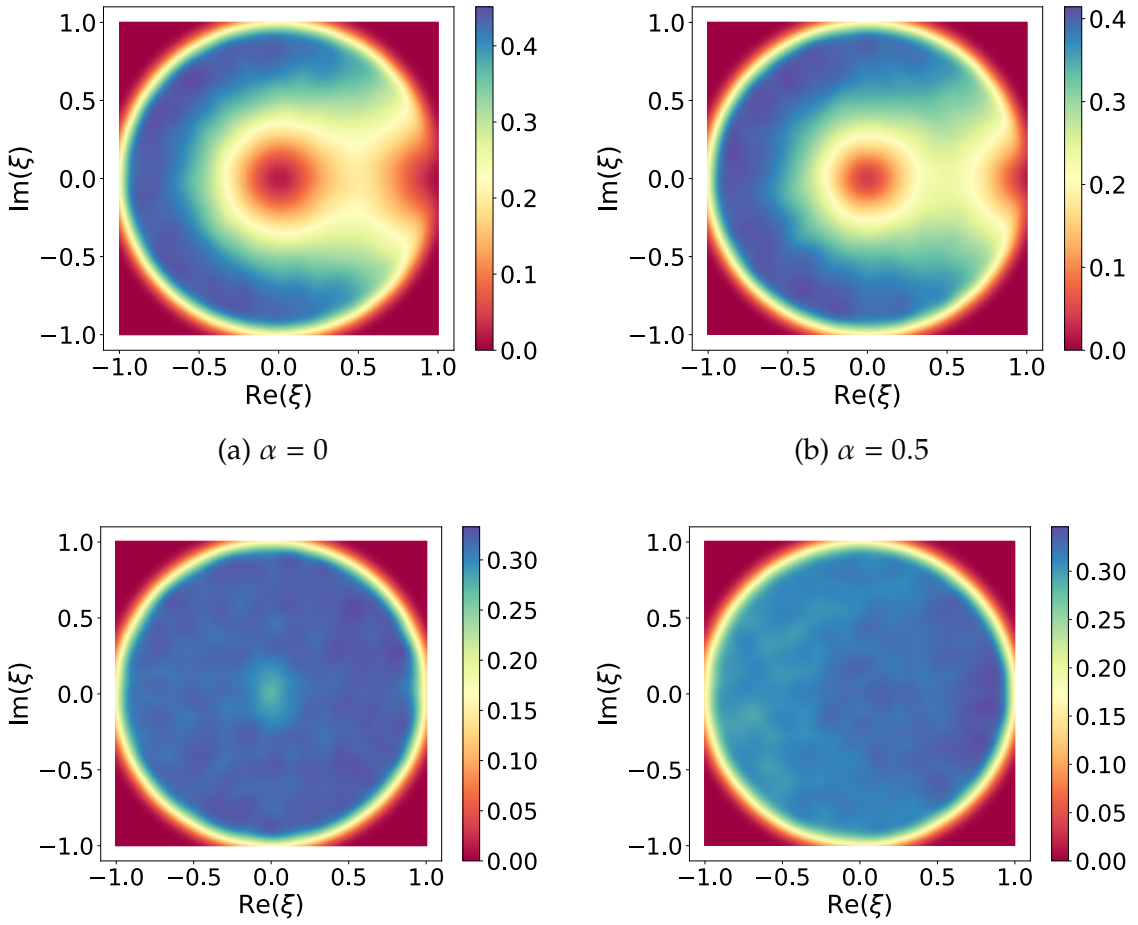

(a) $\alpha = 0$

(b) $\alpha = 0.5$

(c) $\alpha = 1.5$

(d) $\alpha = 4$

Figure 3.11: Distribution of complex spacing ratios in the complex plane for $L = 16$, evaluated at the middle of the spectrum, for different values of α [Model III, Eq. (3.3)] at $h = 14$. As α increases, the statistics transition from random matrix behavior to Poisson-like behavior.

of states. On the other hand, in the presence of strong disorder, we find that all the energy levels are uncorrelated and follow Poisson statistics.

We show that, despite the non-uniform density (clustering of eigenvalues) in the complex plane, the DSFF in these non-hermitian systems possesses the universal dip-ramp-plateau feature of the non-hermitian random matrices in the quantum chaotic regime. The ramp has a power-law variation with time, which is a characteristic of the Ginibre random matrices. Similarly, the CSR for these models shows agreement with RMT predictions in this regime. On the other hand, for large disorder strength, when the system possesses randomly distributed eigenvalues, the DSFF loses the characteristic dip-ramp-plateau structure. Instead, after an initial dip and fluctuation at small time scales $|\tau|$, it saturates to 1, indicating the lack of correlation among the eigenvalues in the large disorder regime. The CSR

for such a disorder strength shows Poisson statistics.

We also discuss long-range generalization for one of the models. We show that with the increasing range of hopping, the chaotic signatures enhance (Figs. 3.7, 3.10, 3.11). A disorder strength that is strong enough for generating uncorrelated energy levels in the case of short-range models becomes insufficient, and energy level correlations arise in the presence of long-range connectivity. In fact, in the limit of all-to-all coupling with the same hopping parameter strength, the DSFF and CSR correspond to that of RMT despite the disorder strength being quite large.

Authors contributions: This chapter is part of the work that was done in Collaboration with Dr. Soumi Ghosh and Prof. Manas Kulkarni.

4

Quantum jumps in driven-dissipative disordered many-body systems

4.1 Introduction

Building upon the chapter 3, where we explored spectral diagnostics of chaos in non-Hermitian Hamiltonians, we now turn to the broader framework of driven-dissipative quantum systems. Our central aim in this chapter is to connect the non-Hermitian description to the standard Lindblad equation and to study how quantum chaos can be characterized in the presence of Markovian reservoirs.

Non-Hermitian Hamiltonians have been widely employed, where the non-Hermiticity mimics hybridization with reservoirs and can be interpreted in terms of post-selection. In the Lindblad equation, part of the environmental effect is absorbed into an effective non-Hermitian Hamiltonian, while the remaining part manifests itself as quantum jumps. Recent work has introduced frameworks that bridge these two perspectives, showing how deformations of the Lindblad equation can interpolate between the non-Hermitian limit and full Lindblad dynamics [136–138]. These approaches are not only of theoretical interest but can also be experimentally realized in controlled settings [139–142].

In this chapter, we focus on the precise role of quantum jumps in shaping the fate of localized phases in open quantum systems. To investigate this, we consider a disordered one-dimensional chain of hard-core bosons subject to alternating gain and loss processes, illustrated schematically in Fig. 4.1. We introduce a ζ-deformation of the Lindblad master equation, where the quantum jump fugacity $\zeta \in [0, 1]$ continuously tunes between a non-Hermitian description ($\zeta = 0$) and standard Lindblad dynamics ($\zeta = 1$). This construction provides a controlled

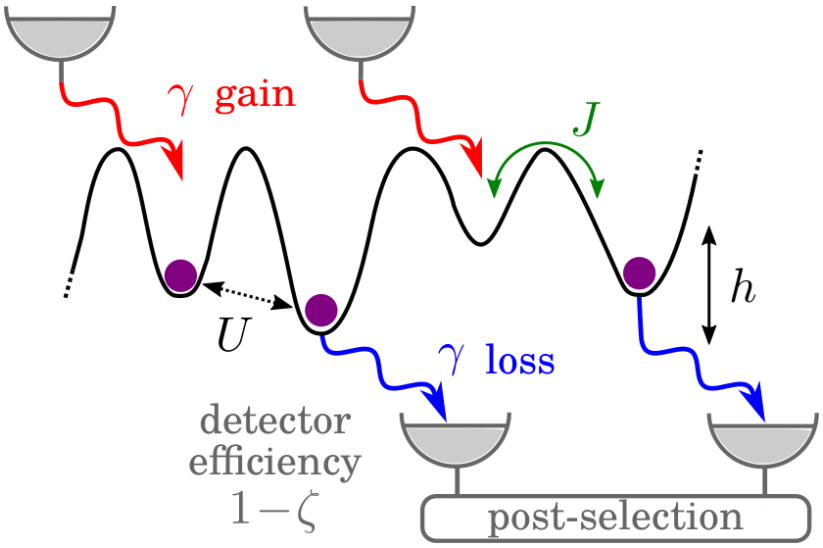

Figure 4.1: Sketch of the gain-loss model, see the Hamiltonian H in Eq. (4.8) and proposed protocol to implement the ζ-deformed Liouvillian $\mathcal{L}_\zeta$ in Eq. (4.6). Both gain and loss events are monitored by means of realistic detectors with efficiency $0 \leq 1-\zeta \leq 1$. Here, the post-selection interpretation consists of selecting those monitored trajectories with no jump. See the Appendix C.1 for details and an alternative protocol.

way to probe how localization signatures evolve as the contribution of quantum jumps is varied. By combining spectral and dynamical diagnostics across different values of ζ, this chapter aims to provide new insights into the stability of localized regimes in realistic open-system settings.

The rest of the chapter is organized as follows. In Sec. 4.2, we introduce the ζ-deformed Lindblad equation. The disordered gain-loss model is presented in Sec. 4.3. In Secs. 4.4.1 and 4.4.2, we analyze spectral and dynamical observables, respectively, and examine their dependence on both disorder strength and the jump fugacity ζ. Finally, in Sec. 4.5, we summarize the results, while additional technical details are given in the appendix C.

4.2 ζ-deformed theory

The dynamics of open quantum systems is generically described by the Lindblad equation,

$$\partial_t \rho(t) = \mathcal{L}\rho(t), \tag{4.1}$$

with the Liouvillian

$$\mathcal{L}\star := -\mathrm{i}\,[H,\star] + \sum_\alpha \left[\hat{O}_\alpha \star \hat{O}_\alpha^\dagger - \left\{\hat{O}_\alpha^\dagger \hat{O}_\alpha, \star\right\}/2\right] \tag{4.2}$$

where H is the system's Hamiltonian and the O_α's are the jump operators. This evolution can be unraveled into an ensemble of quantum-jump trajectories as,

$$\rho(t) = \sum_{n=0}^{\infty} \rho_n(t) \tag{4.3}$$

where $\rho_n(t)$ is the density matrix of the system subjected to precisely n quantum jumps until time t [128–133]. To interpolate between different dynamical regimes, we assign a weight $\zeta \in [0, 1]$ to each quantum jump. In analogy to the familiar terminology of the grand-canonical ensemble, it is referred to as the "quantum-jump fugacity". This defines a ζ-deformed ensemble of quantum trajectories where the density matrix $\rho_\zeta(t)$ is,

$$\rho_\zeta(t) = \frac{\sum_{n=0}^{\infty} \zeta^n \rho_n(t)}{\sum_{n=0}^{\infty} \zeta^n \mathrm{Tr}\left[\rho_n(t)\right]} \tag{4.4}$$

It evolves according to the following ζ-deformed Lindblad master equation,

$$\partial_t \rho_\zeta(t) = \Big(\mathcal{L}_\zeta - \mathrm{Tr}\left[\mathcal{L}_\zeta \rho_\zeta(t)\right]\Big)\rho_\zeta(t) \tag{4.5}$$

where the ζ-deformed Liouvillian is given by

$$\mathcal{L}_\zeta \star := -\mathrm{i}\,[H, \star] + \sum_{\alpha=1}^{M} \left[\zeta O_\alpha \star O_\alpha^\dagger - \frac{1}{2}\left\{O_\alpha^\dagger O_\alpha, \star\right\}\right] \tag{4.6}$$

The systematic and consistent construction of the theory is detailed in the appendix C.1. The standard Lindblad equation is recovered in the limit $\zeta = 1$, whereas the limit $\zeta = 0$ corresponds to an evolution generated by the non-Hermitian Hamiltonian is given by,

$$\tilde{H} = H - \frac{\mathrm{i}}{2} \sum_{\alpha=1}^{M} O_\alpha^\dagger O_\alpha \tag{4.7}$$

The subscript ζ in $\rho_\zeta(t)$ emphasizes that it arises from the deformed dynamics. The initial condition is $\rho_\zeta(0) = \rho(0)$, and Eq. (4.5) preserves positivity, Hermiticity, and trace. Trace preservation is ensured by the non-linear correction in the equation.

The observables predicted from Eq. (4.5) can be experimentally measured by post-selection protocols. In Fig. 4.1, we depict a possible protocol where both the quantum jumps due to gain and loss processes are monitored by means of detectors characterized by an efficiency $1 - \zeta$, *i.e.* the error rate of returning a no-click result when a jump occurred is ζ. Here, the post-selection protocol consists of discarding those trajectories where one or more jumps were monitored. Decreasing the efficiency of the detectors increases the average number of quantum jumps in the

post-selected dynamics, thereby tuning the effective dynamics. We discuss these post-selection protocols in detail in the Appendix C.2. We note that generalized Lindblad equations of the type of Eq. (4.5) appear in the studies of full-counting statistics, where they are referred to as tilted or twisted master equations [289–291].

4.3 Model

To understand the role of quantum jumps on the localized-delocalized transition in driven-dissipative many-body systems, we consider a disordered gain-loss model defined by the following Hamiltonian (see Fig. 4.1)

$$H = \sum_{i=1}^{L} h_i \hat{n}_i - J \sum_{i=1}^{L-1} \left(\hat{b}_i^\dagger \hat{b}_{i+1} + \text{H.c.} \right) + U \sum_{i=1}^{L-1} \hat{n}_i \hat{n}_{i+1} \tag{4.8}$$

with $\hat{n}_i = \hat{b}_i^\dagger \hat{b}_i$, and by the onsite jump operators

$$O_i = \begin{cases} \sqrt{2\gamma}\, \hat{b}_i^\dagger & \text{if } i \text{ is odd} \\ \sqrt{2\gamma}\, \hat{b}_i & \text{if } i \text{ is even} \end{cases} \tag{4.9}$$

Here, $\hat{b}_i^\dagger$ and $\hat{b}_i$ are the hard-core boson creation and annihilation operators on a one-dimensional lattice of length L, with open boundary conditions. The Hamiltonian in Eq. (4.8) is $U(1)$-symmetric, i.e. it conserves the total particle number $N = \sum_{i=1}^{L} \hat{n}_i$. h_i are independent random energy levels uniformly distributed in the interval $[-h, h]$. The parameters J and U denote the hopping and nearest-neighbor interaction strengths. γ sets the rates of the incoherent gain and loss occurring at alternating sites. Setting $U = 2J$ renders the model equivalent to the disordered Heisenberg spin chain, extensively studied in the context of Hermitian many-body localization (MBL) [41, 52, 99, 111]. Unless otherwise stated, we set $\gamma = 0.1J$ and $J = 1$.

The corresponding ζ-deformed Liouvillian $\mathcal{L}_\zeta$ [Eq. (4.6)] possesses a weak $U(1)$ symmetry, associated with the conservation of the particle-number difference between the bra and ket sides of the states upon acting with $\mathcal{L}_\zeta$, see details in the Appendix C.4. Throughout this work, we focus on the zero-charge sector of this symmetry for systems with $L = 8$ and $L = 10$ sites. In this sector, the Hilbert space dimension is given by $\mathcal{N} = \binom{2L}{L}$, and averages are taken over 160 ($L = 8$) and 100 ($L = 10$) disorder realizations.

From the perspective of random-matrix symmetries, the Liouvillian $\mathcal{L}_\zeta$ belongs to the Ginibre unitary ensemble (GinUE). Accordingly, spectral statistics follow GinUE behavior in chaotic regimes and cross over to two-dimensional Poisson

statistics in localized regimes. In the special case $\zeta = 0$, the deformed Liouvillian acquires an additional weak $U(1)$ symmetry corresponding to the independent conservation of particle numbers in the bra and ket sectors. In this limit, the dynamics is generated by the effective non-Hermitian Hamiltonian

$$\tilde{H} = H - \mathrm{i}\gamma \sum_{i=1}^{L} (-1)^i \hat{b}_i^\dagger \hat{b}_i, \qquad \zeta = 0 \tag{4.10}$$

which has recently been investigated in Refs. [184, 185, 196]. The model considered here, denoted as model-II [Eq. (3.2)] in chapter 3, but differs primarily in its boundary conditions: we impose open boundary conditions here, whereas in Chapter 3, we considered periodic boundaries. It is important to emphasize that this choice of boundaries does not change the key physical properties of the effective Hamiltonian $\tilde{H}$. It also conserves the total particle number and exhibits a non-Hermitian MBL transition [184, 185] as demonstrated in the chapter 3.

Now, in the next section, we explore this physics both from spectral and dynamical points of view in the general ζ-deformed theoretical framework that captures the effect of quantum jumps in a controllable fashion.

4.4 Results

4.4.1 Spectral Signatures

To gain insight into the role of quantum jumps on localization, we first analyze the spectral properties of the ζ-deformed Liouvillian $\mathcal{L}_\zeta$ introduced in Eq. (4.6) and obtain the spectrum by means of exact diagonalization [283]. Specifically, we characterize it using the complex spacing ratios [196] and compute the distribution of the complex spacing ratio ξ (Eq. (3.4)). Note that the non-linear trace term in $\mathcal{L}_\zeta$ acts only as an overall shift of the spectrum. Consequently, this term does not influence spacing-ratio statistics, and the level-statistics analysis remains well defined.

In a chaotic regime, the eigenvalues are correlated and experience strong level repulsion in the complex plane. Hence, the distributions of r and θ are generically dictated by the Ginibre Unitary Ensemble (GinUE), and their averages take the value $\langle r \rangle \approx 0.738$ and $-\langle \cos\theta \rangle \approx 0.244$. On the other hand, in a localized or integrable regime, the eigenvalues become uncorrelated, giving rise to a uniform distribution of spacing ratios within the unit circle [196]. This corresponds to two-dimensional Poisson statistics, for which $\langle r \rangle = 2/3$ and $-\langle \cos\theta \rangle = 0$.

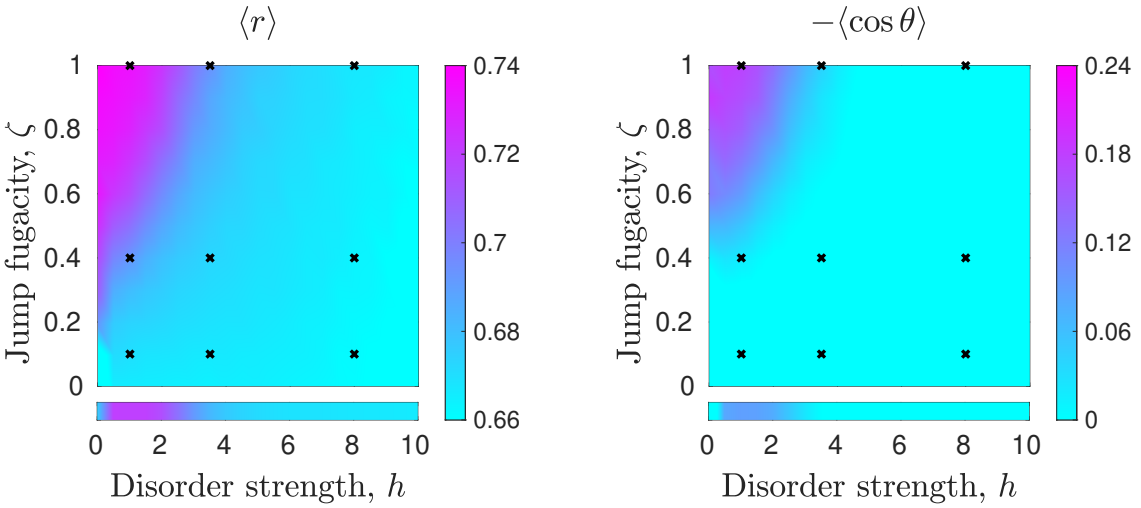

Figure 4.2: Complex spacing ratios of the spectrum of $\mathcal{L}_\zeta$ in Eq. (4.6): (left) $\langle r \rangle$ and (right) $-\langle \cos\theta \rangle$ computed by exact diagonalization of a system of $L = 8$ sites. The bottom strips correspond to results obtained from the spectrum of the non-Hermitian Hamiltonian $\tilde{H}$ (half-filling sector) in Eq. (4.10) for system size $L = 16$ averaged over 160 disorder samples. The nine black crosses in each panel correspond to the parameters at which the densities of complex spacing ratios are presented in Fig. 4.3.

In Fig. 4.2, we present the average spacing-ratio observables $\langle r \rangle$ and $-\langle \cos\theta \rangle$ as a function of both the disorder strength h and quantum-jump fugacity ζ. For the standard Lindblad evolution at $\zeta = 1$, we find a clear crossover between random matrix predictions at weak disorder, consistent with chaotic dynamics, and two-dimensional Poisson predictions at strong disorder, characteristic of localized behavior. Upon decreasing ζ, the location of this transition shifts to lower disorder strengths. In other words, reducing the number of quantum jumps facilitates the emergence of localization. In the $\zeta = 0$ case, the Liouvillian acquires an additional weak $U(1)$ symmetry, which implies that different particle-number sectors are conserved separately for bra and ket indices of the density matrix. This extra symmetry leads to spurious statistics, which are known to produce deceitful level attraction between eigenvalues of different symmetry sectors. We attribute the apparent loss of a delocalized phase in the vicinity of $\zeta = 0$ to a remnant of this extra symmetry. To circumvent this situation at $\zeta = 0$, one should resort to analyzing the spectrum of the non-Hermitian Hamiltonian [184, 185, 196] in Eq. (4.10). The corresponding results are presented in the lower strips of Fig. 4.2, where the non-Hermitian many-body localization transition is recovered.

In Fig. 4.3, we illustrate further these effects of disorder and quantum-jump fugacity by presenting representative plots of the distribution of complex spacing ratios ξ in Eq. (3.4) for different values of h and ζ. At strong disorder and weak

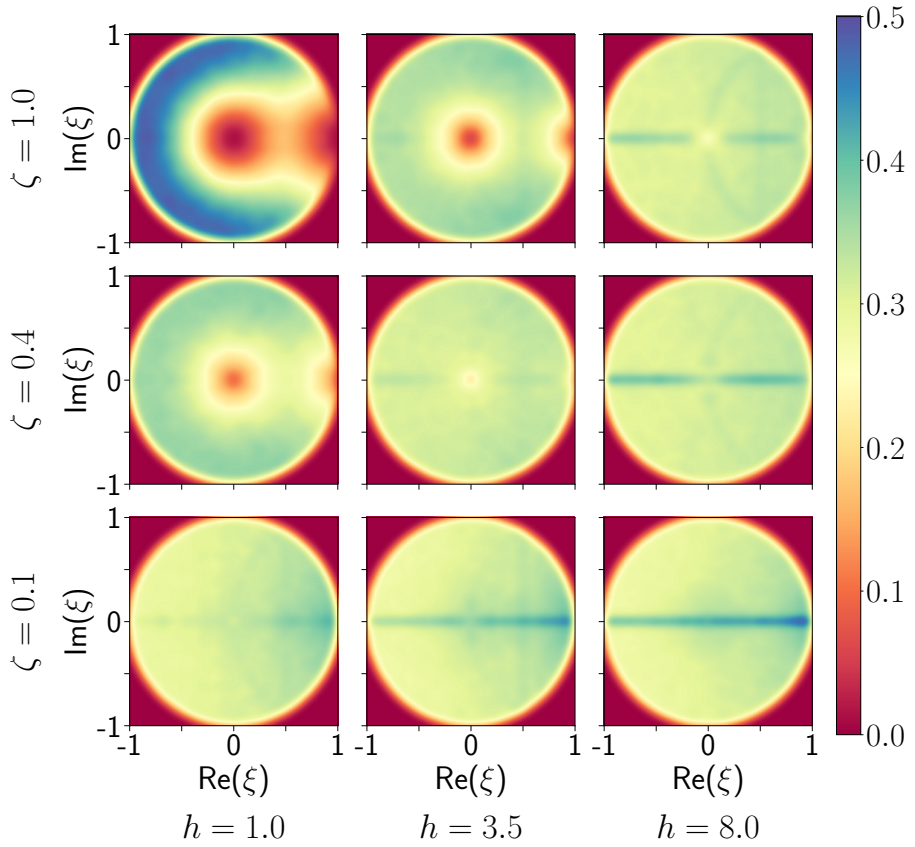

Figure 4.3: Distribution of complex spacing ratio [Eq. (3.4)] for representative values of disorder strength h and quantum-jump fugacity ζ for a system of $L = 8$ sites. For weak disorder and large ζ, the distribution is anisotropic and inhomogeneous, indicating chaotic statistics. For strong disorder or small ζ, the distribution becomes isotropic within the unit circle, signaling localization.

fugacity, we find that this distribution is isotropic and homogeneous within the unit circle, which is a hallmark of localized (integrable) systems. On the other hand, for weak disorder and large fugacity, the distribution is found to be anisotropic and inhomogeneous, which is expected for chaotic systems.

The intuitive physical picture behind these results can be phrased as follows. When $\zeta = 0$, the system dynamics reduce to those under a non-Hermitian Hamiltonian which conserves the total particle number. As a result, the dynamics remain confined within fixed-particle-number subspaces of the Hilbert space, and jumping to other subspaces is not possible. This conservation significantly restricts the accessible Hilbert space, thereby favoring localized behavior. However, when quantum jumps are introduced, they open pathways for the system to access different particle-number subspaces. As the parameter ζ increases, the likelihood of such jumps becomes higher, enhancing the connectivity between these subspaces and leading to stronger delocalization in the dynamics.

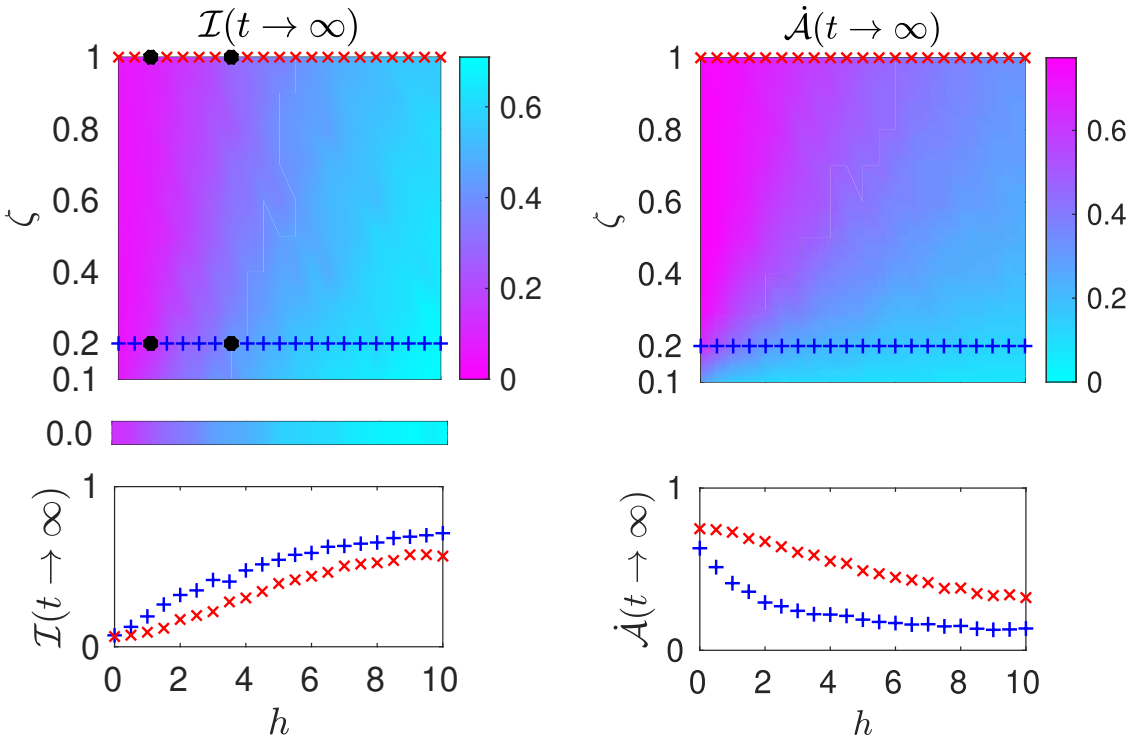

Figure 4.4: (Left panel) Steady-state imbalance, $\mathcal{I}(t\to\infty)$ [Eq. (4.12)], (Right panel) Steady-state rate of dynamical activity, $\dot{\mathcal{A}}(t\to\infty)$ [Eq. (4.13)] as a function of disorder strength h and quantum-jump-fugacity ζ. The lower strip corresponds to $\zeta = 0$. The lower panels correspond to the cuts at $\zeta = 0.2$ and $\zeta = 1$ indicated in the upper panels. The dynamics are generated by Eq. (4.5). For imbalance (resp. dynamical activity), we consider a system of $L = 10$ (resp. $L = 8$) sites averaged over 100 (resp. 160) disorder samples. The four black dots in the left panel correspond to the parameters at which the transient time-dynamics are produced in Fig. 4.5.

In summary, the spacing-ratio statistics across different (h, ζ) demonstrate a clear and consistent picture: the presence of quantum jumps acts to destabilize the localized phase by promoting ergodicity and chaotic behavior, while reducing or suppressing jumps stabilizes localization and pushes the transition to lower disorder strengths.

4.4.2 Dynamical signatures.

Having studied the spectral properties, we now turn to dynamical probes that directly capture the fate of memory in the presence of disorder and quantum jumps. Spectral statistics provide a global indicator of chaotic versus localized regimes, but dynamical observables are often more closely connected to experimental measurements. In this section, we investigate the time evolution of two key quantities:

1. Imbalance, defined in Eq. (4.12).

2. Rate of dynamical activity, defined in Eq. (4.13).

We choose to work with the charge density wave initial state,

$$\rho(0) = |1,0,1,0,\dots\rangle\langle 1,0,1,0,\dots| \tag{4.11}$$

which is a product state and a steady-state of the ζ-deformed gain-loss dynamics in the absence of particle hopping, $J = 0$. We numerically integrate the subsequent dynamics generated by Eq. (4.5) employing a standard fourth-order Runge-Kutta algorithm (RK45). We quantify the fate of the staggered order present in the initial state $\rho(0)$ by computing the dynamics of the Imbalance [102, 120],

$$\mathcal{I}(t) = \frac{\sum_{i=1}^{L}(-1)^{i+1}\mathrm{Tr}\left[\hat{b}_i^\dagger \hat{b}_i \rho_\zeta(t)\right]}{\sum_{i=1}^{L}\mathrm{Tr}\left[\hat{b}_i^\dagger \hat{b}_i \rho_\zeta(t)\right]} \tag{4.12}$$

Physically, the Imbalance emphasizes the inhomogeneity in the occupation along the lattice. This observable is directly measurable in cold-atom or superconducting qubit experiments. By construction, it lies in the interval $-1 \leq \mathcal{I}(t) \leq 1$, and takes the value $\mathcal{I}(0) = 1$ for the chosen initial state. A non-vanishing saturation value $\mathcal{I}(t \to \infty)$ is evidence for localization, whereas thermalization leads to $\mathcal{I}(t \to \infty) \to 0$.

Additionally, we also exploited the formal analogy between full-counting statistics (FCS) in grand-canonical ensembles [290] and the quantum trajectories ensemble interpretation of Lindblad dynamics [292, 293]. We computed the rate of dynamical activity [293, 294]

$$\dot{\mathcal{A}}(t) = \frac{1}{\zeta}\partial_t \langle \mathcal{R}(t)\rangle_\zeta \tag{4.13}$$

where $\langle \mathcal{R}(t)\rangle_\zeta$ is the number of quantum jumps occurring between time $t = 0$ to t averaged over the quantum trajectories generated by $\mathcal{L}_\zeta$. For the standard Lindblad evolution ($\zeta = 1$), the steady-state rate of dynamical activity is directly related to the imbalance as $\dot{\mathcal{A}}(t \to \infty) = \gamma\, L\,[1 - \mathcal{I}(t \to \infty)]$. This implies, when is dynamics are chaotic, the activity will be high, while the activity will be low for localized dynamics.

For $\zeta < 1$, $\dot{\mathcal{A}}(t \to \infty)$ involves additional contributions from two-time jump correlations. A detailed discussion of these properties of the activity, as well as their formal connection to full-counting statistics (FCS), is provided in Appendix C.3.

In Fig. 4.4, we present the steady-state imbalance $\mathcal{I}(t \to \infty)$ and rate of dynamical activity $\dot{\mathcal{A}}(t \to \infty)$ as a function of the disorder strength h and the

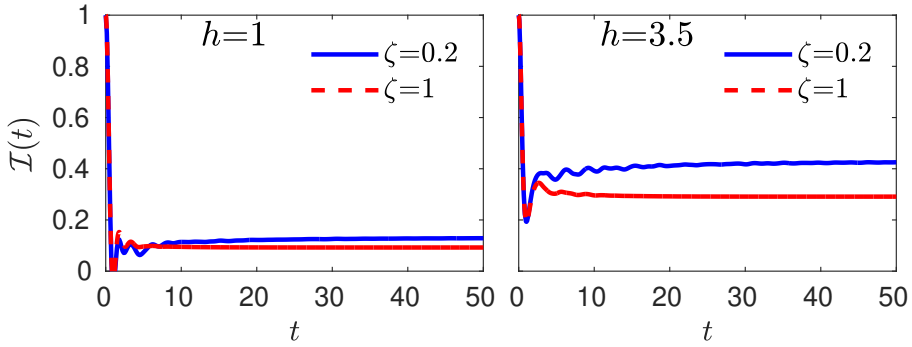

Figure 4.5: Dynamics of the imbalance $\mathcal{I}(t)$ [Eq. (4.12)] for representative values of the quantum-jump fugacity ζ and disorder strength h. The data is produced by numerical integration of Eq. (4.5) for a system of $L = 10$ sites and averaged over 100 disorder samples.

quantum-jump fugacity ζ. The results are consistent with those obtained from spectral statistics and obtained from numerical integration. For the standard Lindblad evolution $\zeta = 1$, we find a clear transition between a weak-disorder regime, characterized by a steady state with vanishing imbalance and finite rate of dynamical activity, and a strong-disorder regime, characterized by a steady state with imbalance close to unity and vanishing rate of activity. When ζ is reduced, the location of this transition shifts towards lower disorder strengths, indicating that quantum jumps tend to destabilize the localized regime. To better illustrate the influence of the disorder strength h and the quantum-jump fugacity ζ, the lower panels of Fig. 4.4 show the steady-state imbalance and rate of dynamical activity as a function of h for two representative values of ζ.

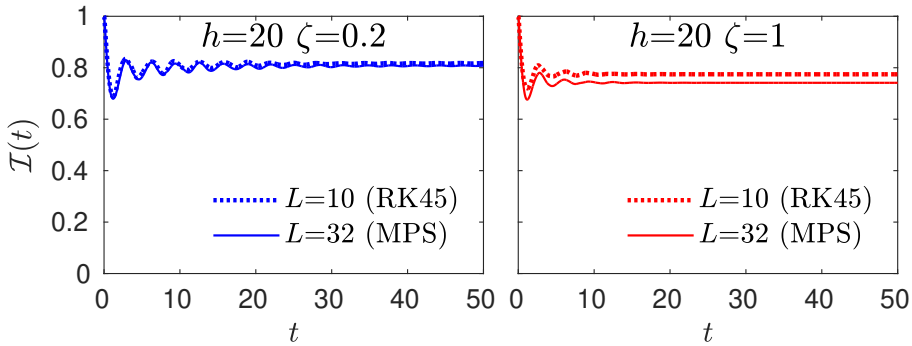

Figure 4.6: Dynamics of the imbalance $\mathcal{I}(t)$ for larger system, $L = 32$, at strong disorder $h = 20$, and for different values of quantum-jump fugacity ζ. These results are obtained using the time-dependent matrix product state (MPS) technique and averaged over 100 disorder samples. The dashed lines correspond to the results obtained by numerically exact integration of Eq. (4.5) for a system of $L = 10$ sites, shown for comparison.

Contrary to the results of the spectral statistics above, these dynamical indicators are not prone to subtleties involving symmetry sectors. However, at finite but very small ζ, the time it takes to reach the steady state diverges since the typical timescale between two jumps can be roughly estimated to be $\tau \sim 1/\gamma\zeta$. Indeed, the limits $t \to \infty$ and $\zeta \to 0$ are generically not expected to commute. This results in significant numerical challenges in capturing the steady state, and we do not provide data in the regime $\zeta \ll 1$.

In Fig. 4.5, we show the transient dynamics of imbalance from the initial state till the steady state for representative values of the disorder strength h and the quantum-jump fugacity ζ. The steady-state values increase with h and decrease with ζ. The timescale of the approach to the steady state is dictated by the inverse of the minimum Liouvillian gap [1]. We have used this spectral information to ensure the convergence of all steady-state results presented.

While the system sizes presented so far, up to $L = 10$, are state-of-the-art when it comes to exactly computing the dynamics of open quantum systems, they are still relatively small owing to the challenges posed by numerical time integration. To firmly assert the influence of quantum jumps on the localized regime, we resort to a time-dependent matrix product state (MPS) technique that allows us to reach much larger system sizes, up to $L = 32$. In practice, we implemented a time-evolving block decimation (TEBD) of a matrix product density operator (MPDO) representation of the ζ-deformed Lindblad evolution in Eq. (4.5). The results are averaged over 100 disorder samples. This technique produces reliable results deep in the localized regime, and we work at $h = 20$ where convergence is achieved with a maximal bond dimension $\chi = 2^7$. In Fig. 4.6, we show the transient dynamics of the imbalance from the initial state till the steady state for representative values of the quantum-jump fugacity ζ. The MPS results entirely validate the results obtained by numerically exact integration of systems of smaller sizes.

The analysis of imbalance and dynamical activity paints a consistent picture with spectral statistics. Reducing the quantum-jump fugacity ζ strengthens localization, as seen both in steady-state saturation and transient dynamics. Larger values of ζ inject stronger fluctuations, accelerating delocalization and erasing memory of initial states. The complementary use of exact diagonalization and tensor-network methods demonstrates that these features persist across system sizes, consolidating the conclusion that quantum jumps destabilize localized dynamics, while their suppression enhances localization even at weaker disorder.

[1] The Liouvillian gap is defined as minus the real part of the difference of eigenvalues with the largest and next largest real parts.

4.5 Summary and Conclusion

Our analysis of the influence of quantum jumps on the complex spectrum as well as on the dynamics of the ζ-deformed Liouvillian demonstrates that fewer quantum jumps can result in the emergence of localization at lower disorder strengths. In other words, post-selection can promote localization. We emphasize that this result is not merely a formal construction but is experimentally accessible using realistic detectors with finite efficiency.

Starting from a disordered many-body system that already hosts a localized regime, we have shown that post-selection can effectively lower the threshold disorder required for localization. This mechanism differs from measurement-induced phase transitions (MIPT) studied in systems such as random unitary circuits [295] or free fermions [296], where repeated measurements can localize otherwise featureless systems [297–299]. Importantly, MIPT experiments face significant challenges due to the need to generate and access a large number of measurement trajectories, whereas the ζ-deformed Lindblad framework offers both spectral and dynamical insights within a unified approach. This approach not only harnesses standard methods of full counting statistics to the study of Lindblad dynamics, but it is also physically realizable by means of realistic post-selection protocols in quantum optical setups.

Authors contributions: This chapter is part of the work that was done in Collaboration with Dr. Hari Kumar Yadalam, Prof. Camille Aron, and Prof. Manas Kulkarni. Dr. Hari Kumar Yadalam generated the TEBD and MPDO results.

5

Filling an empty lattice by local injection of quantum particles

5.1 Introduction

In the chapters 3 and 4, we investigated interacting disordered open quantum systems to determine whether many-body localization persists in open settings. Having explored these interacting systems, we now turn our focus to non-interacting setups and study the thermalization and quantum dynamics of open systems in Anderson-localized systems when they are coupled to a bath.

Unlike interacting models, whose Hilbert space grows exponentially with system size, non-interacting models can be represented in a single-particle basis, where the basis dimension increases only linearly. This makes it possible to analyze dynamics with greater control and to perform numerical studies on much larger lattices. Another key advantage is that the environment can be modeled explicitly as a large but finite bath with its own Hamiltonian. By coupling the system to such a bath and evolving the combined setup unitarily, one obtains an effectively open system while maintaining a globally closed Hamiltonian description. When the bath is thermodynamically large, it acts as a reservoir that exchanges particles or energy with the system, providing a natural framework to study the interplay between thermalization and localization in open settings.

Having these goals in mind, we first design a minimal setup to study the quantum dynamics between a system and its bath. We then extend this framework to systems that harbor localization physics in chapter 6. One natural starting point is to investigate the dynamics and equilibration of an initially empty lattice coupled to a reservoir. The resulting evolution involves a subtle interplay between

Hermitian and effective non-Hermitian dynamics (arising from finite system-bath coupling), together with thermalization processes governed by quantum statistics. This can give rise to non-trivial transient behavior as well as intricate steady states.

In this direction, several works have examined the quantum dynamics of open systems coupled to localized sinks [239, 240, 300–307]. Complementary studies have analyzed the problem of localized injection into initially empty lattices [308–311], providing insights into the spreading of particles and the approach to equilibrium.

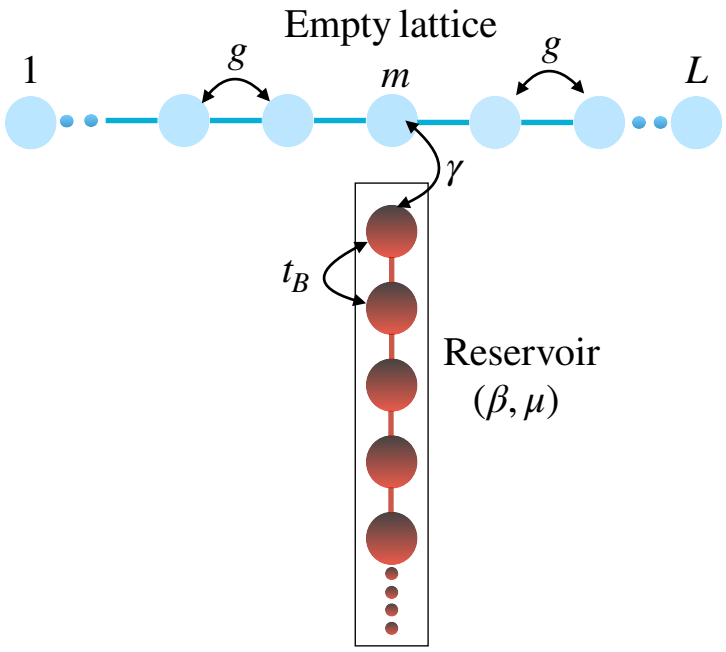

Figure 5.1: Schematic of our setup: an empty (blue) one-dimensional lattice [Eq. (5.1)] of size L is connected to a reservoir [Eq. (5.2)](red) at site m (the center of the lattice). The inter-site hopping parameter within the lattice (reservoir) is g (t_B). The coupling between the lattice and the reservoir is denoted by γ. The reservoir is maintained in equilibrium at inverse temperature β and chemical potential μ.

In this chapter, we consider a one-dimensional empty lattice (system) of size L coupled to a bosonic or fermionic reservoir at a particular site m (taken to be the center of the lattice), as illustrated in Fig. 5.1. Several natural questions arise: How many particles occupy the lattice at a given time? What does the space-resolved density profile look like at different time snapshots? How does this profile spread in time? To address these questions, we study the quantum dynamics of (i) the local density profile $n_i(t)$ on the lattice, and (ii) the total number of particles on the lattice, $N(t) = \sum_{i=1}^{L} n_i(t)$, and their subsequent approach to equilibration. To analyze this setup, we employ four complementary approaches, each with distinct advantages: (i) exact numerics for the correlation matrix [Sec. 2.1], (ii) the Redfield

equation (perturbative and Markovian) [Sec. 2.3], (iii) the local Lindblad equation (perturbative, Markovian, and valid in the weak hopping limit) [Sec. 2.4], and (iv) the exact quantum Langevin equation [Sec. 2.2] introduced earlier in Chapter 2.

The structure of this chapter is as follows. In Sec. 5.2, we present the system-bath setup and develop the relevant methods for this particular setup. Sec. 5.3 contains our results for bosons using all approaches, while Sec. 5.4 briefly discusses the corresponding fermionic case obtained from exact numerics. In Sec. 5.5, we place our results in the context of existing works and provide a detailed comparison. Finally, Sec. 5.6 summarizes our findings and outlines future directions. Some calculations are deferred to the appendix D.

5.2 Setup and Methodology

In this section, we will discuss our microscopic model for the injection of identical bosons/fermions in a one-dimensional lattice. The lattice initially is an empty tight-binding chain of L sites. The Hamiltonian of the lattice is given by,

$$H_S = g \sum_{i=1}^{L-1} \left(\hat{a}_i^\dagger \hat{a}_{i+1} + \hat{a}_{i+1}^\dagger \hat{a}_i \right) \tag{5.1}$$

where $\hat{a}_i$ ($\hat{a}_i^\dagger$) is the annihilation (creation) operator of the i-th site of the lattice. The hopping parameter is denoted by g. We inject the particles at a particular site (for example, near the middle) of the lattice by putting it in contact with a reservoir, which is represented by a semi-infinite tight-binding chain whose Hamiltonian is given by,

$$H_B = t_B \sum_{i=1}^{\infty} \left(\hat{b}_i^\dagger \hat{b}_{i+1} + \hat{b}_{i+1}^\dagger \hat{b}_i \right) \tag{5.2}$$

Here $\hat{b}_i$ ($\hat{b}_i^\dagger$) is the annihilation (creation) operator of the i-th site of the bath and t_B is the nearest neighbour hopping between the bath sites. Note that a_i and b_i operators satisfy either commutation or anti-commutation algebra for bosons or fermions, respectively. At $t = 0$, we switch on the coupling between the lattice and the bath, which can be described by the following Hamiltonian:

$$H_{SB} = \gamma \left(\hat{a}_m^\dagger \hat{b}_1 + \hat{b}_1^\dagger \hat{a}_m \right) \tag{5.3}$$

where γ is the coupling strength and the m-th site of the lattice is coupled to the first site of the bath (or point of contact). In this work, we couple the lattice at the middle site with the bath and hence, we choose $m = (N+1)/2$ for odd N and

$m = N/2+1$ for even N. The initial density operator $\hat{\rho}(t=0)$ for the setup is taken as a product state

$$\hat{\rho}(0) = \hat{\rho}_S(0) \otimes \hat{\rho}_B^{th}(0) \tag{5.4}$$

with the lattice initially being empty i.e., $\hat{\rho}_S(t=0) = |\mathbf{0}\rangle\langle\mathbf{0}|$ where $|\mathbf{0}\rangle$ denotes a state with all sites empty. In other words, the lattice is in vacuum. The bath density operator is in equilibrium at temperature $T = (k_B\beta)^{-1}$ and chemical potential μ,

$$\hat{\rho}_B^{th} = \frac{e^{-\beta(H_B - \mu\hat{N}_B)}}{Z} \tag{5.5}$$

where $\hat{N}_B$ is the number operator for the bath and Z is the grand partition function for the bath. The superscript "th" in Eq. (5.4) and Eq. (5.5) stands for thermal equilibrium.

With this generic setup in hand, our interest here is to study the quantum dynamics of the spatial density profile of bosons/fermions

$$n_i(t) = \left\langle \hat{a}_i^\dagger(t)\hat{a}_i(t) \right\rangle \tag{5.6}$$

where we use the Heisenberg representation for the operators and $\langle \ldots \rangle$ denotes an average over the initial density matrix $\hat{\rho}(0)$. We also look at the total number of particles in the lattice

$$N(t) = \sum_{i=1}^{L} n_i(t) \tag{5.7}$$

In order to have a detailed understanding of the quantities given in Eq. (5.6) and Eq. (5.7), we use four different approaches, which are elaborated in the next section.

5.2.1 Exact quantum dynamics

In this subsection, we describe how the method of exact numerics is employed to compute the observables of interest for the present setup. Using Eq. (2.8) along with the details provided in Sec. 2.1, the time evolution of the correlation matrix can be obtained. Initially, the initial correlation matrix $C(0)$ must be constructed from the initial density operator $\hat{\rho}(0)$. Since the lattice chain is initially in vacuum and is decoupled from the bath, all the two-point correlations of the form $\langle \hat{a}_i^\dagger(0)\hat{a}_j(0)\rangle$, $\langle \hat{a}_i^\dagger(0)\hat{b}_j(0)\rangle$ and $\langle \hat{b}_i^\dagger(0)\hat{a}_j(0)\rangle$ will be zero. The non-zero entries in $C(0)$ are the two-point correlations of the bath degrees of freedom and of the form $\langle \hat{b}_i^\dagger(0)\hat{b}_j(0)\rangle$. These entries can be obtained as follows. Recall that the bath Hamiltonian given

in Eq. (5.2) can be expressed as,

$$H_B = \sum_{i,j=1}^{L_B} \mathcal{H}^B_{ij} \hat{b}^\dagger_i \hat{b}_j \tag{5.8}$$

where $\mathcal{H}^B$ is the single particle Hamiltonian of the bath. This Hamiltonian can be easily diagonalized by a unitary transformation U, i.e., $\mathcal{H}^B = U\Lambda_B U^\dagger$ with Λ_B being a diagonal matrix with single particle eigenvalues as its entries. The Hamiltonian in the diagonal form can be written as

$$H_B = \sum_{q=1}^{L_B} \lambda^B_q \, \hat{b}^\dagger_q \, \hat{b}_q, \qquad \hat{b}_i = \sum_{q=1}^{L_B} U_{iq} \, \hat{b}_q \tag{5.9}$$

with $\hat{b}_q$ being the annihilation operator of q-th normal mode of the bath with eigenvalues λ^B_q. One can then easily find that

$$\langle \hat{b}^\dagger_i(0)\hat{b}_j(0)\rangle^{th} = \sum_{q=1}^{L_B} U^*_{iq} \, U_{jq} \, \bar{n}(\lambda^B_q) \tag{5.10}$$

where we have used the fact that $\langle \hat{b}^\dagger_q \hat{b}_{q'}\rangle = \bar{n}(\lambda^B_q)\, \delta_{qq'}$. Here $\bar{n}(\omega)$ can either be a Bose or a Fermi function and is given by

$$\bar{n}(\omega) = \frac{1}{e^{\beta(w-\mu)} \pm 1} \tag{5.11}$$

where $-$ and $+$ stand for bosons and fermions, respectively. With $C(0)$ constructed from all these initial correlations, we can now propagate the correlation matrix following Eq. (2.8) and suitably extract the required entries from $C(t)$ to compute $n_i(t)$ and thereby $N(t)$, as defined in Eq. (5.6) and Eq. (5.7), respectively. It should be noted that if $L_B \gg L$, then the system dynamics is almost equivalent to that when subjected to a true bath with infinite degrees of freedom.

Since this exact numerical recipe involves unitary evolution with respect to the Hamiltonian of the entire setup, it can become computationally difficult if the total size $L + L_B$ is large. Therefore, it is useful to study time dynamics for this setup following complementary approaches, such as the Redfield and Lindblad master equations, which are perturbative and Markovian in nature and can then be used to study lattices with a large number of sites.

5.2.2 Redfield Master Equation

In this subsection, we will obtain the Redfield master equation for the present setup and obtain the spatial density profile and total number of particles. We

start by writing the system-bath interaction Hamiltonian, given in Eq. (5.3), in the interaction picture as,

$$H_{SB}^{I}(t) = e^{\mathrm{i}\hat{H}_0 t} H_{SB} e^{-\mathrm{i}\hat{H}_0 t} = \gamma \left(\hat{a}_m^\dagger(t)\hat{b}_1(t) + \hat{b}_1^\dagger(t)\hat{a}_m(t) \right) \tag{5.12}$$

where $H_0 = H_S + H_B$ and

$$\hat{a}_m(t) = e^{\mathrm{i}\hat{H}_S t}\hat{a}_m e^{-\mathrm{i}\hat{H}_S t}; \quad \hat{b}_1(t) = e^{\mathrm{i}\hat{H}_B t}\hat{b}_1 e^{-\mathrm{i}\hat{H}_B t} \tag{5.13}$$

The Redfield master equation for this setup can be written from Eq. (2.35) as,

$$\begin{aligned}\frac{d}{dt}\hat{\rho}_S^I(t) = -\gamma^2 \int_0^\infty d\tau \Big[\Big\langle \hat{b}_1(t)\hat{b}_1^\dagger(\tau) \Big\rangle \Big[\hat{a}_m^\dagger(t), \hat{a}_m(\tau)\hat{\rho}_S^I(t) \Big] \\ + \Big\langle \hat{b}_1^\dagger(\tau)\hat{b}_1(t) \Big\rangle \Big[\hat{\rho}_S^I(t)\hat{a}_m(\tau), \hat{a}_m^\dagger(t) \Big] + h.c. \Big]\end{aligned} \tag{5.14}$$

In the Schrödinger picture, one gets,

$$\begin{aligned}\frac{d}{dt}\hat{\rho}_S(t) = \mathrm{i}\Big[\hat{\rho}_S(t), H_S\Big] - \gamma^2 \int_0^\infty d\tau \Big[\langle \hat{b}_1(t)\hat{b}_1^\dagger(\tau) \rangle \Big[\hat{a}_m^\dagger, \hat{a}_m(\tau - t)\hat{\rho}_S(t) \Big] \\ + \langle \hat{b}_1^\dagger(\tau)\hat{b}_1(t) \rangle \Big[\hat{\rho}_S(t)\hat{a}_m(\tau - t), \hat{a}_m^\dagger \Big] + h.c. \Big]\end{aligned} \tag{5.15}$$

Since the bath operators are defined in the interaction picture, the corresponding two-point correlation functions are known exactly, and using Eq. (5.10), one can write them in terms of the normal modes of the bath as,

$$\begin{aligned}\langle \hat{b}_1^\dagger(\tau)\hat{b}_1(t) \rangle &= \sum_q |U_{1q}|^2 \, e^{-\mathrm{i}\lambda_q^B(t-\tau)} \, \bar{n}(\lambda_q^B), \\ \langle \hat{b}_1(t)\hat{b}_1^\dagger(\tau) \rangle &= \sum_q |U_{1q}|^2 \, e^{-\mathrm{i}\lambda_q^B(t-\tau)} \left[1 \pm \bar{n}(\lambda_q^B) \right]\end{aligned} \tag{5.16}$$

where recall that, λ_q^B is the eigenvalue of the q-th mode of the bath and $\bar{n}(\omega)$ is defined in Eq. (5.11). In Eq. (5.16), the $\pm$ stands for bosons and fermions, respectively. We now express the above Redfield equation in Eq. (5.15) in terms of the eigenoperators of the system Hamiltonian. We first diagonalize the lattice Hamiltonian H_S and write,

$$H_S = \sum_{i,j=1}^{L} \mathcal{H}_{ij}^S \hat{a}_i^\dagger \hat{a}_j = \sum_{k=1}^{L} \lambda_k^S \hat{a}_k^\dagger \hat{a}_k \qquad \text{and} \quad \mathcal{H}^S = W \Lambda_S W^\dagger \tag{5.17}$$

and therefore the matrix W is responsible for diagonalizing the single-particle system Hamiltonian H_S, and Λ_S is the diagonal matrix containing the single particle eigenvalues of the system. Here

$$\hat{a}_i = \sum_{k=1}^{L} W_{ik} \hat{a}_k. \tag{5.18}$$

Following this diagonalization procedure and using Eq. (5.15) and Eq. (5.16), we can rewrite the Redfield equation as,

$$\dot{\hat{\rho}}_S(t) = \mathrm{i}\Big[\hat{\rho}_S(t), H_S\Big] - \sum_{k,k'=1}^{L} \int_{-\infty}^{\infty} \frac{d\omega}{2\pi}\Big[I(\omega)\mathcal{K}(\hat{\rho}_{SS}) + h.c.\Big] \tag{5.19}$$

where

$$I(\omega) = \int_0^{\infty} d\tau\, e^{-\mathrm{i}(\omega-\lambda^S_{k'})\tau} \tag{5.20}$$

and

$$\mathcal{K}(\hat{\rho}_S) = \Big[f_{kk'}(\omega) \pm F_{kk'}(\omega)\Big]\Big[\hat{a}^\dagger_k, \hat{a}_{k'}\hat{\rho}_S(t)\Big] + F_{kk'}(\omega)\Big[\hat{\rho}_S(t)\hat{a}_{k'}, \hat{a}^\dagger_k\Big] \tag{5.21}$$

The functions $f_{kk'}(\omega)$ and $F_{kk'}(\omega)$ in Eq. (5.21) are defined as,

$$\begin{aligned} f_{kk'}(\omega) &= W^*_{mk}\, W_{mk'}\, J(\omega) \\ F_{kk'}(\omega) &= W^*_{mk}\, W_{mk'}\, J(\omega)\, \bar{n}(\omega) \end{aligned} \tag{5.22}$$

where recall that the index m in W_{mk} refers to the m-th site of the lattice system that is connected with the bath. Note that the $\pm$ sign in Eq. (5.21) again refers to the boson/fermion case. Here, $J(\omega)$ is the spectral density of the bath, defined as,

$$J(\omega) \equiv 2\pi\,\gamma^2 \sum_q |U_{1q}|^2 \delta(\omega - \lambda^B_q) \tag{5.23}$$

Note that the two-point correlation functions of the system are given as

$$C_{k,k'}(t) = \langle \hat{a}^\dagger_k(t)\hat{a}_{k'}(t)\rangle = \mathrm{Tr}\big[\hat{a}^\dagger_k(0)\hat{a}_{k'}(0)\hat{\rho}_S(t)\big] \tag{5.24}$$

From Eq. (5.19), one can write down a differential equation for the two-point correlation function defined in Eq. (5.24) as [312, 313],

$$\frac{dC_{k,k'}(t)}{dt} = \mathrm{i}\lambda^S_k C_{k,k'}(t) + \frac{1}{2}\left[\tilde{F}_{k'k} - \sum_{\bar{k}=1}^{L} \tilde{f}_{k'\bar{k}}\, C_{k,\bar{k}}(t)\right] + (k \Longleftrightarrow k')^\dagger \tag{5.25}$$

where $(k \Longleftrightarrow k')^\dagger$ is a short form for the right-hand side of Eq. (5.25) when k and k' are interchanged and the terms are subjected to complex conjugation. The new functions (denoted by the symbol tilde) in Eq. (5.25) are defined as,

$$\begin{aligned} \tilde{f}_{k'\bar{k}} &= f_{k'\bar{k}}(\lambda^S_{\bar{k}}) - \mathrm{i}\,P\int_{-\infty}^{\infty} \frac{d\omega}{\pi}\frac{f_{k'\bar{k}}(\omega)}{\omega - \lambda^S_{\bar{k}}} \\ \tilde{F}_{k'k} &= F_{k'k}(\lambda^S_k) - \mathrm{i}\,P\int_{-\infty}^{\infty} \frac{d\omega}{\pi}\frac{F_{k'k}(\omega)}{\omega - \lambda^S_k} \end{aligned} \tag{5.26}$$

Here P refers to the Cauchy principal value. This particular form in Eq. (5.26) is obtained by writing $I(\omega)$ in Eq. (5.20) using the Sokhotski-Plemelj theorem. Eq. (5.25) forms a closed set of differential equations for the two-point correlation function, which can be solved numerically by grouping the equations in a matrix equation form. We therefore write the components of $C_{k,k'}(t)$ as a column vector with elements $\mathbf{C}_r$, $r = 1, 2, \ldots, L^2$ and denote it by $\vec{\mathbf{C}}(t)$, and rewrite Eq. (5.25) as

$$\frac{d\vec{\mathbf{C}}}{dt} = M\vec{\mathbf{C}} + \vec{\mathbf{Q}} \tag{5.27}$$

where M is the homogeneous part and is a $L^2 \times L^2$ matrix and $\vec{\mathbf{Q}}$ is a $L^2 \times 1$ column vector. This is often known as the Lyapunov Equation in the literature [314]. Note that the information about the quantum statistics is encoded only in the column vector $\vec{\mathbf{Q}}$, as a consequence of which the quantum dynamics of fermions and bosons differ. The formal solution to Eq. (5.27) with the initial condition $\vec{\mathbf{C}}(0) = 0$ (note that the lattice is initially empty) is given by,

$$\vec{\mathbf{C}}(t) = \int_0^t d\tau\, e^{M(t-\tau)}\vec{\mathbf{Q}} \tag{5.28}$$

We now rewrite the solution in Eq. (5.28) more explicitly. To do so, we first diagonalise M as $M = V\Lambda_M V^{-1}$, with Λ_M as diagonal matrix with entries λ_α^M and obtain

$$\mathbf{C}_r(t) = \int_0^t d\tau \sum_{\alpha,s=1}^{L^2} V_{r\alpha} e^{\lambda_\alpha^M (t-\tau)} V_{\alpha s}^{-1} \mathbf{Q}_s = \sum_{\alpha,s=1}^{L^2} \left(\frac{e^{\lambda_\alpha^M t} - 1}{\lambda_\alpha^M} \right) V_{r\alpha} V_{\alpha s}^{-1} \mathbf{Q}_s \tag{5.29}$$

The eigenvalues $\{\lambda_\alpha^M\}$ of the matrix M typically have negative real parts, ensuring a well-defined steady state as $t \to \infty$. However, this condition can be violated for certain parameter regimes, such as strong system-bath coupling, rendering the Redfield description unphysical. To analyze the dynamics, we consider the short and long-time behavior of the correlation matrix $\mathbf{C}_r(t)$. Let λ_L^M denote the eigenvalue with the largest real part magnitude and λ_S^M the one with the smallest of the matrix M. In the short-time limit, $t \ll 1/|\lambda_L^M|$, a Taylor expansion shows that all two-point correlations grow linearly with time, i.e.,

$$\mathbf{C}_r(t \ll 1) = \chi_r\, t + O(t^2) \tag{5.30}$$

with a slope

$$\chi_r = \left(\sum_{\alpha,s=1}^{L^2} V_{r\alpha} V_{\alpha s}^{-1} \mathbf{Q}_s \right) = \mathbf{Q}_r \tag{5.31}$$

We now discuss the long-time limit, i.e., $t \to \infty$. Note that Eq. (5.29) can be recasted as,

$$\mathbf{C}_r = \mathbf{C}_r^{SS} + \sum_{\alpha,s=1}^{L^2} V_{r\alpha} V_{\alpha s}^{-1} \mathbf{Q}_s \frac{e^{\lambda_\alpha^M t}}{\lambda_\alpha^M} \tag{5.32}$$

where the steady state correlation elements ($t \to \infty$) are given by,

$$\mathbf{C}_r^{SS} = -\sum_{\alpha,s=1}^{L^2} \frac{V_{r\alpha} V_{\alpha s}^{-1} \mathbf{Q}_s}{\lambda_\alpha^M} = -(M^{-1}\vec{\mathbf{Q}})_r \tag{5.33}$$

and the second term in Eq. (5.32) indicates a long-time exponential approach to the steady state. The eigenvalue, λ_S, with the smallest magnitude for the real part will determine the time scale, $1/|\mathrm{Re}[\lambda_S^M]|$, for convergence to the steady state. As the correlation functions are obtained in the diagonalized basis, to determine the spatial density profile, the final step is to come back to the local site basis, which gives,

$$n_i(t) = \langle \hat{a}_i^\dagger(t)\hat{a}_i(t)\rangle = \sum_{k,k'=1}^{L} W_{ik'} W_{ik}^* C_{k,k'}(t) \tag{5.34}$$

where recall that $C_{k,k'}$ is defined in Eq. (5.24). The total particle number [Eq. (5.7)] at early times ($t \ll 1$) is given by,

$$N(t) = \sum_{k=1}^{L} C_{k,k}(t) \approx t \sum_{k=1}^{L} \tilde{F}_{k,k} = t \sum_{k=1}^{L} |W_{mk}|^2 J(\lambda_k^S)\, \bar{n}(\lambda_k^S) \tag{5.35}$$

where recall that the λ_k^S are eigenvalues of the system's single-particle Hamiltonian $\mathcal{H}^S$. Eq. (5.35) clearly demonstrates an early time linear growth with different slopes for fermions and bosons. In the limiting case with very small inter-site hopping g, one can set $\lambda_k^S \approx 0$ (the eigenvalues of uncoupled lattice sites), as a result of which we get,

$$N(t) \approx t\, J(0)\, \bar{n}(0) \tag{5.36}$$

We will later see that this is exactly what one receives from the local Lindblad master equation. Note that in a suitable parameter regime, the Redfield approach can be simplified to a local Lindblad equation. As we will show in the next subsection, this allows for elegant analytical expressions for the local density $n_i(t)$ and the total occupation $N(t)$.

5.2.3 Local Lindblad Equation

In this subsection, we outline the Local Lindblad master equation approach applied to the present setup and present my results for the local density $n_i(t)$ as defined in Eq. (5.6) and the total particle number $N(t)$ from Eq. (5.7).

For our setup, if we derive a local Lindblad equation starting from the fully microscopic system-reservoir Hamiltonian [Eq.(5.1), Eq. (5.2), Eq. (5.3)], both incoherent pump and loss terms naturally arise in the Lindblad Equation, as given in Eq. (2.36). More explicitly, the systematically derived local Lindblad equation [250, 264–267] is given as

$$\dot{\hat{\rho}}_S = \mathrm{i}\Big[\hat{\rho}_S, H_S\Big] + \Gamma_G\Big[2\hat{a}_m^\dagger\hat{\rho}_S\hat{a}_m - \{\hat{a}_m\hat{a}_m^\dagger, \hat{\rho}_S\}\Big] + \Gamma_L\Big[2\hat{a}_m\hat{\rho}_S\hat{a}_m^\dagger - \{\hat{a}_m^\dagger\hat{a}_m, \hat{\rho}_S\}\Big] \tag{5.37}$$

where the gain Γ_G and the loss Γ_L coefficients are given by

$$\Gamma_G = \frac{J(0)}{2}\,\bar{n}(0), \qquad \Gamma_L = \frac{J(0)}{2}\,\big(1 \pm \bar{n}(0)\big) \tag{5.38}$$

Recall that $J(\omega)$ is the spectral density of the bath, defined in Eq. (5.23). Note that the zeros in the argument of $J(0)$ and $\bar{n}(0)$ in Eq. (5.38), because there is no onsite term in the system Hamiltonian given in Eq. (5.1). The $\pm$ sign in Eq. (5.38) stands for bosons and fermions, respectively. It is important to highlight that the validity of the local Lindblad equation in Eq. (5.37) relies on weak system-bath coupling γ as well as weak inter-site hopping parameter g within the lattice system.

Following Eq. (5.37), one can write down the equations of motion for the two-point correlation functions of the system $C_{i,j} = \langle\hat{a}_i^\dagger\hat{a}_j\rangle$,

$$\frac{dC_{i,j}}{dt} = \mathrm{i}\,g\,(C_{i-1,j} - C_{i,j+1} + C_{i+1,j} - C_{i,j-1}) - (\Gamma_L \mp \Gamma_G)(\delta_{im} + \delta_{jm})\,C_{i,j} + 2\,\Gamma_G\delta_{mi}\delta_{mj} \tag{5.39}$$

where $\mp$ stands for bosons and fermions, respectively. It is crucial to note that Γ_G and Γ_L [Eq. (5.38)] here are related by detailed balance, i.e., they are not independent of each other.

We now solve for the correlation functions given in Eq. (5.39) and use them to extract the local population $n_i(t)$ and total occupation $N(t)$. Without loss of generality, we consider the bath to be coupled to the lattice at site $m = 0$. Furthermore, we take the lattice size L to be infinite, extending from $-\infty$ to $+\infty$. Since the system is symmetric about the contact point, we restrict the analysis to the positive side of the lattice chain for simplicity. The spatial density profile $n_i(t)$ is given by [see Appendix D.1 for details],

$$n_i(t) = 2\,\Gamma_G \int_0^t d\tau\,|\tilde{S}_i(\tau)|^2 \tag{5.40}$$

where for large τ,

$$\tilde{S}_i(\tau) = \frac{i\,J_i(2\,g\,\tau)}{i + \tau\Gamma'} \tag{5.41}$$

Here J_i is the Bessel function of the first kind and,

$$\Gamma' = \Gamma_L \mp \Gamma_G = \frac{J(0)}{2} \tag{5.42}$$

where $\mp$ stands for bosons and fermions, respectively. Interestingly, the quantity Γ', introduced in Eq. (5.42), is independent of the particle statistics and remains strictly positive. As a result, the quantum statistics of particles enter the expression for the density profile as a multiplicative prefactor Γ_G [Eq. (5.38)].

In the limit where both the spatial site index $i \to \infty$ and time $t \to \infty$, while keeping the ratio i/t fixed, the analytical forms in Eqs. (5.40) and (5.41) exhibit an interesting scaling behavior. This scaling form captures how the density profile evolves asymptotically with space and time [see Appendix D.1 for detailed derivation].

$$n_i(t) = \Phi\left(\frac{i}{2gt}\right) \tag{5.43}$$

where the scaling function $\Phi(v)$ is exactly given by

$$\Phi(v) = \frac{4\,\Gamma_G\, g}{\pi} \int_1^{\frac{1}{v}} dz\, \frac{1}{\sqrt{z^2-1}}\, \frac{1}{(2\,g + z\,\Gamma')^2} \tag{5.44}$$

The integral representation in Eq. (5.44) is identical (after a suitable change of variables) to Eq. (31) in Ref. [306] in which the dual problem of particle loss was studied. The integral in Eq. (5.44) can be performed exactly to yield

$$\Phi(v) = \frac{\Gamma_G}{\Gamma'}\, \frac{\tilde{g}\,(1+v\,\tilde{g}) \log\left(\frac{1+v\,\tilde{g}}{\tilde{g}+v-\sqrt{(\tilde{g}^2-1)(1-v^2)}}\right) - \sqrt{(\tilde{g}^2-1)\,(1-v^2)}}{(\tilde{g}^2-1)^{3/2}\,(v\,\tilde{g}+1)}, \quad 0 < v < 1 \tag{5.45}$$

where the dimensionless parameters $\tilde{g}$ is given by

$$\tilde{g} = \frac{2g}{\Gamma'} = \frac{4g}{J(0)} \tag{5.46}$$

and recall that Γ' is given by Eq. (5.42) and $J(0)$ from Eq. (5.54) is given by

$$J(0) = \frac{2\gamma^2}{t_B} \tag{5.47}$$

Note that the scaling function $\Phi(v)$ in Eq. (5.45) admits the following limiting forms near $v \to 0$ and $v \to 1$:

$$\Phi(v) = \frac{1}{1-\tilde{g}^2} - \frac{\tilde{g}\log\left(\tilde{g}-\sqrt{\tilde{g}^2-1}\right)}{(\tilde{g}^2-1)^{3/2}} - \frac{v^2}{2} + O(v^3) \tag{5.48}$$

When $v \ll 1$, the decay of $\Phi(v)$ from its peak at $v = 0$ is parabolic. This limit, $v = 0$, corresponds to the behavior of the density profile in the bulk region of the lattice. The two constant terms in Eq. (5.48) represent the local density near the injection

site. On the other hand, the limit $\nu \to 1$ describes the density profile close to the edge of the lattice, yielding the expression

$$\Phi(\nu) = \frac{\sqrt{2(1-\nu)}}{1+\tilde{g}^2} + O\left[(1-\nu)^{3/2}\right] \quad \text{as } \nu \to 1 \tag{5.49}$$

From Eq. (5.49), it is noteworthy that the scaled density $\Phi(\nu)$ vanishes as a square root near the edge $\nu \to 1$. This square-root behavior reflects a characteristic decay of the density profile close to the boundary. Additionally, the analytical scaling form given in Eq. (5.44) is independent of quantum statistics, except for the prefactor (Γ_G). The total particle number $N(t)$ is given by [see Appendix. (D.1) for details]

$$\begin{aligned} N(t) &= \frac{4\,\Gamma_G\,\tilde{g}^2 t}{\pi} \int_1^\infty \frac{dz}{z} \frac{1}{\sqrt{z^2-1}} \frac{1}{(\tilde{g}+z)^2} \\ &= -\frac{2\,\Gamma_G\,t}{\pi(1-\tilde{g}^2)} \left[2\tilde{g} - \pi(1-\tilde{g}^2) + 2\big(1-2\tilde{g}^2\big) \frac{\cos^{-1}\left(\tilde{g}\right)}{\sqrt{1-\tilde{g}^2}} \right] \end{aligned} \tag{5.50}$$

Note that using the relation,

$$\frac{\cos^{-1}\left(\tilde{g}\right)}{\sqrt{1-\tilde{g}^2}} = -\frac{\log\left(\tilde{g}+\sqrt{\tilde{g}^2-1}\right)}{\sqrt{\tilde{g}^2-1}} \tag{5.51}$$

it is easy to see that Eq. (5.50) is always real for all values of $\tilde{g}$. From Eq. (5.50) it is clear that $N(t)$ always exhibits a linear growth in time. One can further simplify Eq. (5.50) in the limit of small and large $\tilde{g}$. We get,

$$N(t) = t\,\Gamma_G \left[\tilde{g}^2 - \frac{16}{3\pi}\tilde{g}^3 \right] + O(\tilde{g}^4) \qquad \text{when } \tilde{g} \ll 1 \tag{5.52}$$

and

$$N(t) = t\,\Gamma_G \left[2 + \frac{4}{\pi} \frac{1-\log(4)-2\log\left(\tilde{g}\right)}{\tilde{g}} \right] + O\left(\frac{1}{\tilde{g}^3}\right) \qquad \text{when } \tilde{g} \gg 1 \tag{5.53}$$

5.3 Numerical Results for Bosons

In this section, we present the numerical results for a one-dimensional nearest neighbour tight-binding lattice which is coupled to an equilibrium bath at a particular site [recall Fig. (5.1)]. The quantities of interest are (i) local occupation number $n_i(t)$ versus i at fixed time snapshots and (ii) the total occupation $N(t)$ versus t. We will mainly focus on presenting results for the bosonic case and will briefly discuss the fermionic case and highlight interesting similarities and differences between the two in Sec. (5.4).

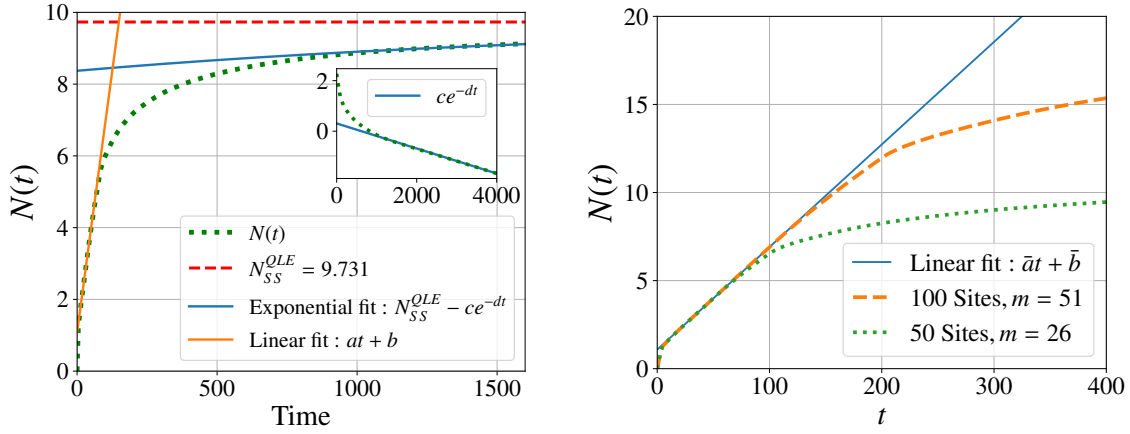

(a) $L = 40$ and $m = 21$ (b) Total occupation $N(t)$ for varying L.

Figure 5.2: Behaviour of total occupation $N(t)$ [Eq. (5.7)] versus time t for bosonic systems using exact numerics as described in Sec. (5.2.1). (a) The plot shows linear early-time growth and exponential late-time saturation. The red dashed line indicates the steady state value N_{SS}^{QLE} from the exact quantum Langevin equation approach (Sec. (2.2)). Early-time linear growth fitting parameters: $\bar{a} = 0.058$, $\bar{b} = 1.082$. Late-time exponential relaxation fit: $N_{SS}^{QLE} - \bar{c}\, e^{-dt}$ with $\bar{c} = 1.359$, $\bar{d} = 4.95 \times 10^{-4}$ and steady state $N_{SS}^{QLE} = 9.731$. The corresponding steady-state time scale is $t_{SS} \sim 2000$. The inset shows the plot of $\log\left(N_{SS}^{QLE} - N(t)\right)$ vs t (green dots), demonstrating the exponential relaxation at long times towards the steady state. (b) Comparison of initial growth of $N(t)$ across different system sizes with parameters consistent with (a), demonstrating that deviation from linear growth occurs at a characteristic time scaling with L. The parameters are $g = 0.5$, $\gamma = 1$, $t_B = 1$, $\beta = 1$, and $\mu = -2.01$.

Unless otherwise stated, we choose the following parameters for the simulations. For the bath, we fix the parameters as inter-site hopping $t_B = 1$, chemical potential $\mu = -2.01$, and inverse temperature $\beta = 1$. For the direct numerics, discussed in Sec. (5.2.1), we always choose $L_B = 4096$. We connect the bath at a particular site m of the lattice, and the bath is considered to be a semi-infinite one-dimensional tight-binding chain, and the corresponding form of the spectral density $J(\omega)$ can be obtained exactly as discussed in Ref. [250]. For our case, it is given as $J(\omega) \equiv 2\pi\gamma^2 \sum_q |U_{1q}|^2 \delta(\omega - \lambda_q^B)$, where U is the unitary matrix which diagonalizes Bath's Hamiltonian.

Because of infinite degrees of freedom, the energy spectrum of the bath can be considered continuous. For our case of the Hamiltonian in Eq. (5.2), bath eigenenergies are $E\left(q\right) = -2t_B \cos q$ and $U_{1q} = \sqrt{\frac{2}{\pi}} \sin q$, with $0 \leqslant q \leqslant \pi$. We get

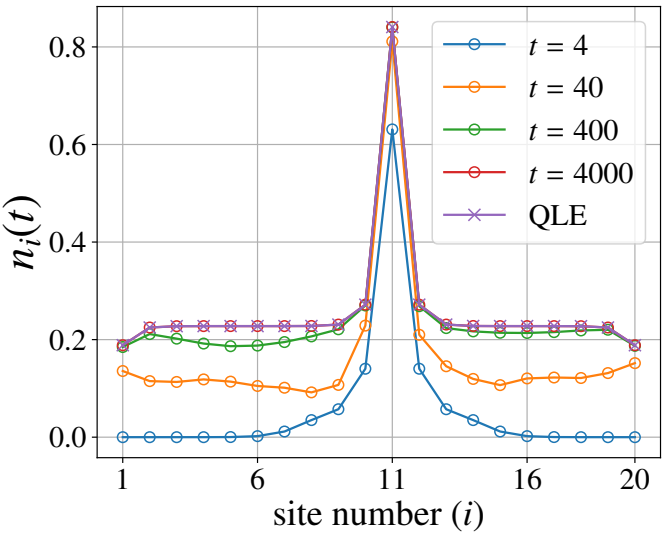

Figure 5.3: Local density profile $n_i(t)$ [Eq. (5.6)] for bosons with $L = 20$ lattice sites with $m = 11$ for various time snapshots, using direct numerics (empty circles), as discussed in Sec. (5.2.1). The long-time limit of this density profile agrees perfectly with that obtained from QLE (cross), as discussed in Sec. (2.2). The parameters are $t_B = 1$, $g = 0.5$, $\beta = 1$, $\mu = -2.01$ and $\gamma = 1$.

the spectral density $J(\omega)$ as,

$$J(\omega) = 4\gamma^2 \int_0^\pi dq \sin^2 q \ \delta\left(\omega + 2t_B \cos q\right) = \frac{2\gamma^2}{t_B}\sqrt{1 - \frac{\omega^2}{4\,t_B^2}} \tag{5.54}$$

Before proceeding further, note that depending on the method employed and specific quantities of interest, the system size L, hopping parameter g, and the system-bath coupling γ are chosen by taking into account computational feasibility and better clarity of presentation.

5.3.1 Non-perturbative regime in system-bath coupling

In Fig.(5.2a), we show the total occupation $N(t)$ [Eq. (5.7)] as a function of time t, obtained using the exact numerics described in Sec.(5.2.1). At early times, the growth of $N(t)$ exhibits linear behavior, while at longer times, we observe an exponential relaxation towards a steady state. To benchmark this steady state, we also present the steady state value obtained from the quantum Langevin equation approach in Sec. (2.2). The long-time limit of $N(t)$ from exact numerics approaches this steady state value. The inset of Fig.(5.2a) makes the exponential relaxation more apparent and is consistent with the relaxation dynamics of finite-size systems coupled to a generic bath. This exponential relaxation can, in fact, be rigorously established following the Redfield approach [Sec. 5.2.2]. Importantly,

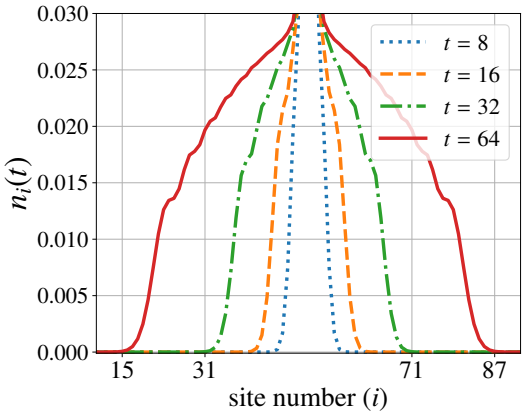

(a) Spatial density profile $n_i(t)$ at short times

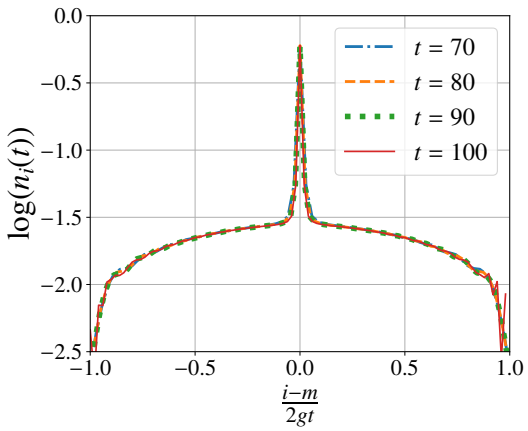

(b) Scaled plot of $\log\left(n_i(t)\right)$

Figure 5.4: Behaviour and propogation of local density profile $n_i(t)$ [Eq. (5.6)] for bosons with $L = 100$ sites and bath attached at site $m = 51$, demonstrated using exact numerics. Fig. (a) shows the density profile at relatively short times, spreading at velocity $c = 2g$, representing ballistic propagation of the density front. Fig (b) presents a scaled plot of $\log\left(n_i(t)\right)$ further illustrating the ballistic scaling form of the spatial density profile. These results indicate the presence of scaling (see also Fig. 5.4b). The parameters are $t_B = 1$, $g = 0.25$, $\beta = 1$, $\mu = -2.01$, and $\gamma = 1$.

$N(t)$ saturates eventually to a finite value is a direct consequence of the finite system size. To ensure that the steady state is reached within a reasonable timescale, we have chosen $\gamma = 1$, corresponding to the non-perturbative regime of the system-bath interaction. It is natural, however, to expect that the relaxation time to reach steady state, t_{SS}, increases with system size L.

For an infinite lattice, one would expect the total occupation $N(t)$ to keep on growing linearly. To demonstrate this, we use direct numerics Sec. (5.2.1) and present in Fig.(5.2b) the behavior of $N(t)$ as a function of t for different system sizes. The influence of finite-size effects becomes apparent beyond a characteristic timescale that scales with the system size L, leading to deviation from the initial linear growth.

In Fig. (5.3), we present the spatial density profile $n_i(t)$ [Eq.(5.6)] as a function of the site index i at different time snapshots, obtained using direct numerics. In the long-time limit, this spatial profile shows excellent agreement with the result obtained from the quantum Langevin equation approach [Sec.(2.2)]. Note that here we choose the lattice size $L = 20$ and the bath attached at site $m = 11$. Therefore, this particular site shows maximum average local occupation and eventually thermalizes with the bath, saturating to a finite steady value. The nearby sites gradually develop local occupation and finally settle down to a finite

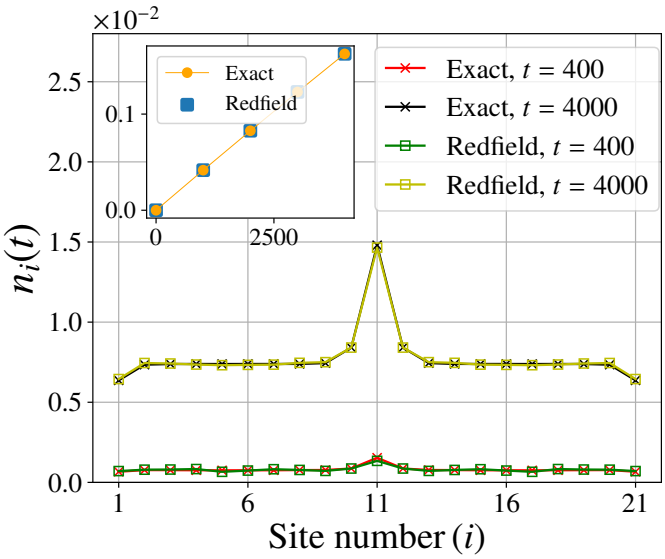

Figure 5.5: Local density profile $n_i(t)$ [Eq. (5.6)] for bosons with $m = 11$ for various time snapshots ($t = 400$, $t = 4000$) using exact numerics (cross). There is good agreement of these results with those obtained using the Redfield equation approach (squares), discussed in Sec. (5.2.2). The inset shows total occupation $N(t)$ [Eq. (5.7)] for $t = 1000, 2000, 3000, 4000$ obtained from these two approaches. The parameters are $t_B = 1$, $g = 0.5$, $\gamma = 0.01$, $\beta = 1$, and $\mu = -2.01$.As a consequence of weak system-bath coupling $\gamma = 0.01$, the time to reach steady state is very long and much higher than the times presented here, and the steady value of local density is far from the values presented here.

value, owing to indirect thermalization with the bath. In Fig. (5.4a), we present a zoomed-in view of the spread of spatial density profiles $n_i(t)$ for a system size $L = 100$, with the bath attached at site $m = 51$, shown at different time snapshots. The ballistic spread of the density profile is clearly visible, with a characteristic velocity of $2g$, where g denotes the inter-site hopping strength in the lattice. This indicates an underlying scaling form of the profile, which is demonstrated in Fig. (5.4b).

It should be emphasized that the parameters used in Fig. (5.2a), Fig. (5.2b), Fig. (5.3), Fig. (5.4a), and Fig. (5.4b) are identical, except for the hopping parameter g and the system size L, which are varied as required.

5.3.2 Perturbative regime in system-bath coupling

Now, we will discuss the regime of weak system-bath coupling, which further allows us to employ the Redfield [Sec. 5.2.2] and Local Lindblad [Sec. 5.2.3] approaches. In contrast to Fig. (5.2) and Fig. (5.3), where strong system-bath coupling was used, we set $\gamma = 0.01$ to ensure the system remains in the weak

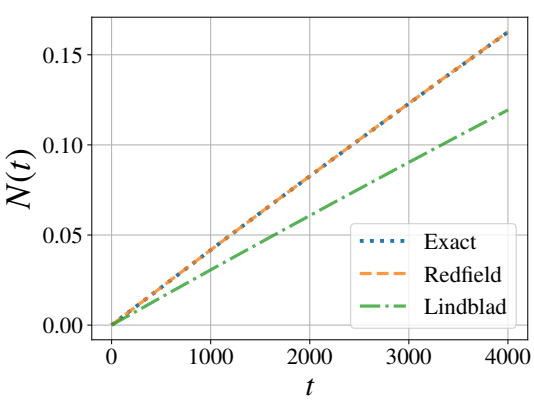

(a) $L = 21$, $g = 0.5$, $\gamma = 0.01$, $m = 11$

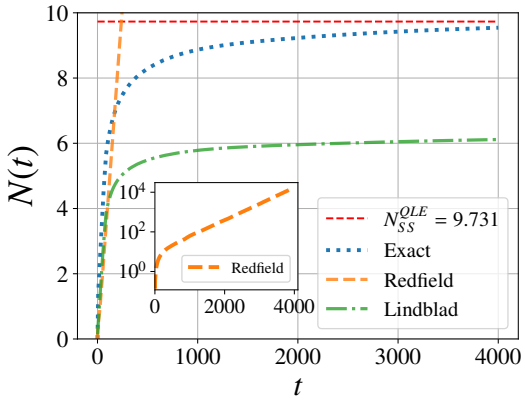

(b) $L = 40$, $g = 0.5$, $\gamma = 1$, $m = 21$

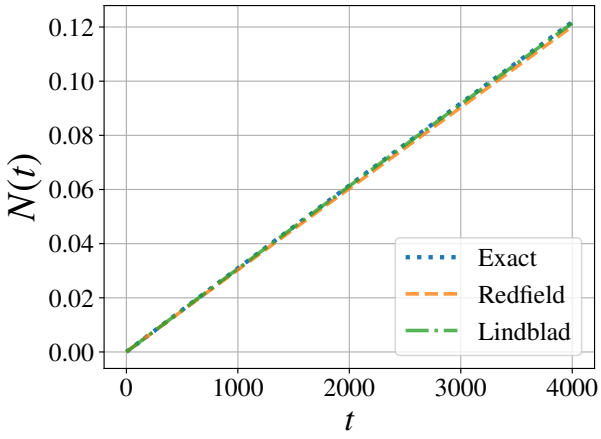

(c) $L = 41$, $g = 0.05$, $\gamma = 0.01$, $m = 21$

Figure 5.6: Behaviour of total occupation $N(t)$ [Eq. (5.7)] versus t for bosonic systems of different sizes and parameters with $t_B = 1$, $\beta = 1$, and $\mu = -2.01$. Each panel compares exact numerics, Redfield, and local Lindblad approaches. For (a), the Redfield approach agrees well with exact numerics, whereas the Lindblad method deviates. For (b), neither perturbative approach matches the exact numerics, indicating their invalidity for this regime. For (c), both perturbative methods agree well with exact numerics, demonstrating their validity under these parameters. See text for detailed discussion.

(perturbative) system–bath coupling regime in Fig. (5.5). We retain the value of $g = 0.5$ as before, which therefore does not fall in the validity of the local Lindblad equation approach, as was also mentioned in Sec. (5.2.3).

In Fig. 5.5, we first compare the spatial density profile $n_i(t)$ obtained from exact numerics with that obtained using the Redfield approach, discussed in Sec. (5.2.2). We observe perfect agreement at various time snapshots. Moreover, the inset in Fig. 5.5 also shows excellent agreement between the two approaches for the

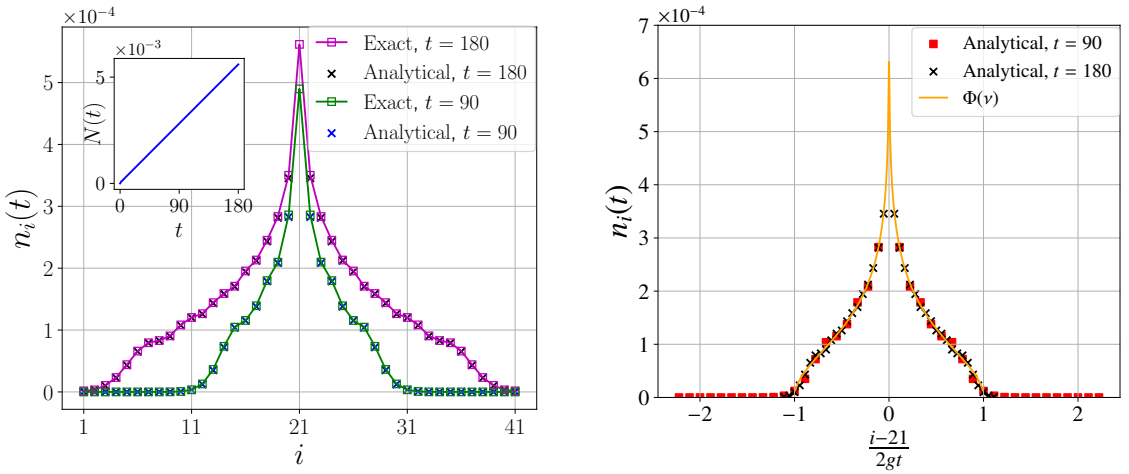

(a) Spatial density profile $n_i(t)$ (b) Spatial scaled density profile $n_i(t)$

Figure 5.7: Spatial density profiles $n_i(t)$ [Eq. (5.6)] for bosons with system size $L = 41$ with$m = 21$, for two different time snapshots $t = 90$ and $t = 180$. Fig (a) compares results from exact numerics and the analytical results from the Local Lindblad approach [Eqs. (5.40) and (5.41) in Sec. (5.2.3)], showing excellent agreement except at the bath site where the analytical expression is not valid. The inset displays the total occupation $N(t)$ versus t, with a slope matching $2\Gamma_G$ as predicted by Eq. (5.53). Fig. (b) shows the corresponding scaled density profiles based on the analytical solution and the scaling form [Eq. (5.44)]. The weak inter-site hopping ($g = 0.05$) supports the validity of the Lindblad approximation. The Parameters are $t_B = 1$, $g = 0.05$, $\beta = 1$, $\mu = -2.01$, and $\gamma = 0.01$.

total occupation $N(t)$ [Eq. (5.7)]. The slope obtained from this inset plot perfectly matches the slope extracted following the short-time (relative to the time to reach the steady state) dynamics described by Eq. (5.35). It is important to emphasize that, as a consequence of a lower value of the system-bath coupling γ, the time required to reach the steady state is very long and much larger than the time snapshots presented in Fig. 5.5. This further implies that the steady value of the local density is far from the values shown in Fig. 5.5.

For the same parameter values as in Fig 5.5, we show the results for total occupation $N(t)$ in Fig. 5.6a following the exact numerics, Redfield, and Lindblad approach. We find an excellent agreement between the exact numerics and the Redfield approach, whereas the result obtained from the Lindblad approach differs significantly due to the chosen relatively large g value. It is also worth noting that, for sufficiently large g and γ, the Redfield shows an exponential growth in the total occupation number, as shown in Fig. 5.6b, further indicating a complete breakdown of the perturbative approach as discussed earlier in section 5.2.2. In Fig. 5.6c, we show the results for $N(t)$ by reducing both the g value and the γ value, and see an almost perfect agreement between all three complementary methods.

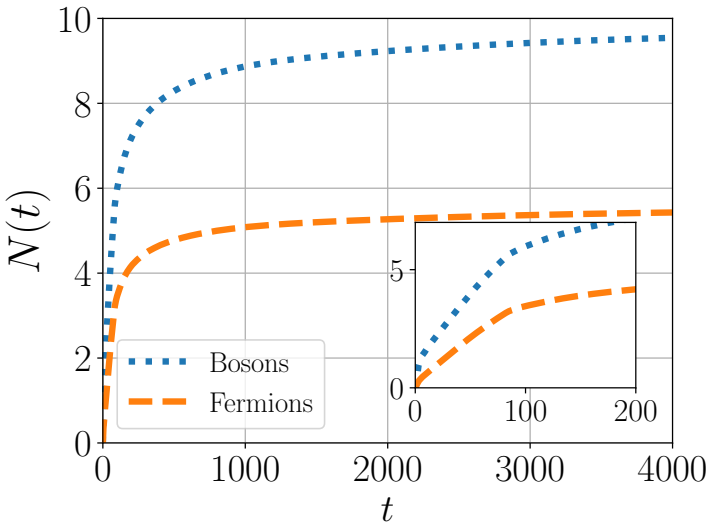

Figure 5.8: Comparison between fermions and bosons for total occupation $N(t)$ for $L = 40$ sites with bath attached at $m = 21$, following exact numerics. It is clear from the plot that the eventual saturation value for fermions is smaller than that of bosons. The inset denotes the zoomed version of the dynamics at relatively short times and clearly shows that the rate of growth for the fermionic case is smaller than that of the bosonic case. The parameters chosen are $t_B = 1$, $g = 0.5$, $\beta = 1$, $\mu = -2.01$ and $\gamma = 1$. Note that although we have presented the results only from exact numerics, similar trends can be obtained following other methods.

This detailed comparison thus provides clear guiding principles for identifying the appropriate parameter regimes in which exact numerics, the Redfield, and the Lindblad methods remain valid and reliable.

In Fig. 5.7a, we plot the spatial density $n_i(t)$ for two different time snapshots and demonstrate excellent agreement between the analytical results given by Eqs. (5.40) and (5.41) with exact numerics [Sec. (5.2.1)]. The inset in Fig. 5.7a shows a plot for $N(t)$ vs t from exact numerics in the same parameter regime, which shows a perfect linear growth with slope $2\Gamma_G$ and therefore matches with the prediction in Eq. (5.53) from the Lindblad equation [Sec. 5.2.3]. In Fig. 5.7b, we demonstrate excellent agreement between the scaled version of data in Fig. 5.7a, analytical scaling form [Sec. (5.2.3)] given in Eq. (5.44). The parameters used in Fig. 5.7 are the same as the parameters used for Fig. 5.6c.

5.4 Numerical Results for Fermions

So far, we have presented results for bosonic systems. We now briefly turn to the case of fermions, highlighting the similarities and differences. We find that owing

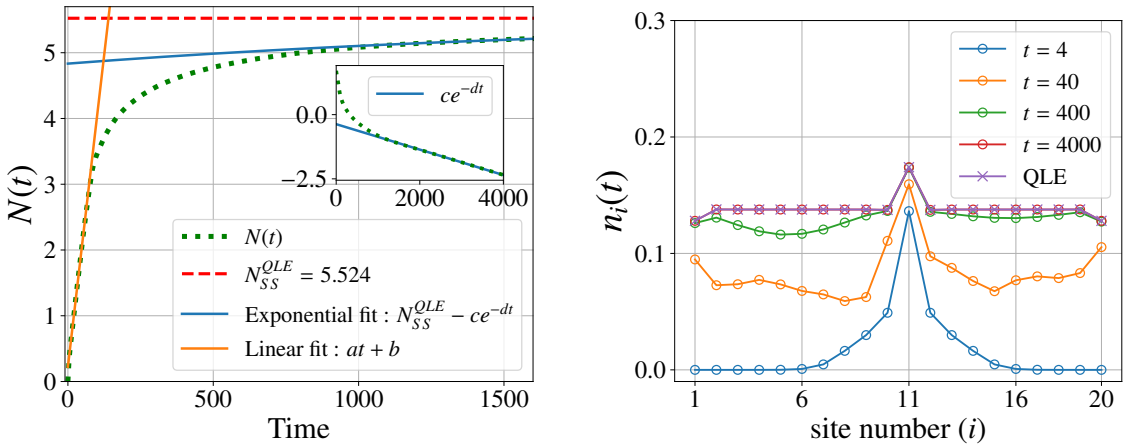

(a) $L = 40$ and $m = 21$ (b) $L = 20$ and $m = 11$

Figure 5.9: (a) Behaviour of $N(t)$ versus time t for fermionic systems using exact numerics. The plot shows linear early-time growth and exponential late-time saturation. The red dashed line indicates the steady state value N_{SS}^{QLE} from the exact quantum Langevin equation approach. Early-time linear growth fitting parameters: $\bar{a} = 0.038, \bar{b} = 0.223$. Late-time exponential relaxation fit: $N_{SS}^{QLE} - \bar{c}\, e^{-\bar{d}t}$ with $\bar{c} = 0.69$, $\bar{d} = 4.95 \times 10^{-4}$ and steady state $N_{SS}^{QLE} = 5.524$. The inset shows the plot of $\log\left(N_{SS}^{QLE} - N(t)\right)$ vs t (green dots). (b) Local density profile $n_i(t)$ [Eq. (5.6)] for fermions for various time snapshots, using exact numerics (empty circles). The long-time limit of this density profile agrees perfectly with that obtained from QLE (cross). The parameters are $t_B = 1$, $g = 0.5$, $\beta = 1$, $\mu = -2.01$ and $\gamma = 1$. Note that the parameters chosen here are the same as in Fig. 5.3.

to the Pauli exclusion principle, fermions experience occupation blockade, which makes their quantum dynamics different from that of bosons.

The rate of growth of $N(t)$ at small times is higher for bosons as they are not limited by the Pauli exclusion principle obeyed by fermions. As a result, fermions exhibit slower growth of $N(t)$ and, in the long-time limit overall total occupation within the lattice is significantly lower in comparison with bosons. Nevertheless, similar to bosons, the fermions also exhibit overall early-time linear growth and exponential relaxation at long times. In Fig. 5.8 and Fig. 5.9a, we demonstrate these trends following the exact numerics for fermions. In Fig. 5.9b, we plot the spatial density profile for fermions at different time snapshots following exact numerics, and a relatively lower value in population compared to bosons is clearly observed, owing to the Pauli exclusion principle. In Fig. 5.10a, we show the ballistic growth of the density profile for fermions, similar to the bosonic case, and the corresponding scaling behavior is illustrated in Fig. 5.10b using exact numerics. In suitable parameter regimes, one can employ the other methods [Sec. (5.2.2), Sec. (5.2.3), Sec. (2.2)] for fermions and notice similar trends.

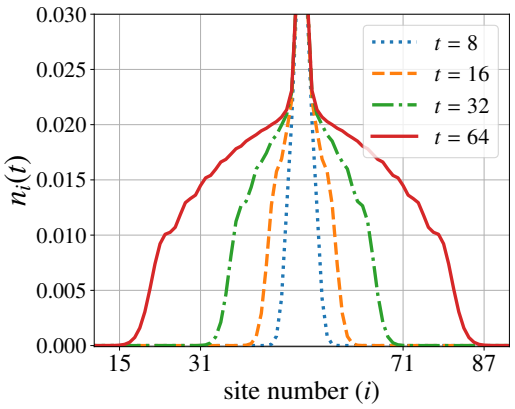

(a) Spatial density profile $n_i(t)$ at short times.

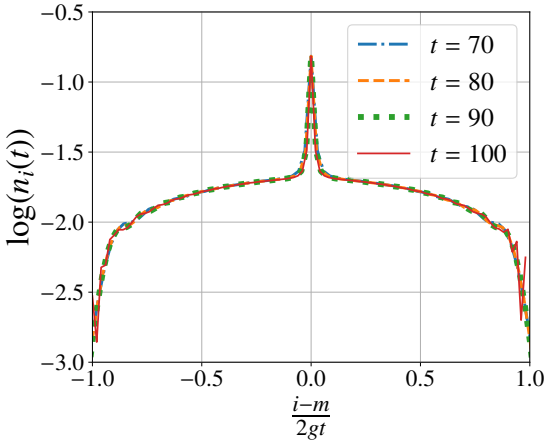

(b) Scaled plot of $\log(n_i(t))$

Figure 5.10: Behaviour and propagation of the local density profile $n_i(t)$ [Eq. (5.6)] for fermions in a lattice ($L = 100$) with bath attached at $m = 51$, showing ballistic spread. Fig.(a) presents the density profile growth at short times, with the density front propagating at velocity $c = 2g$ representing ballistic growth. Fig.(b) shows a scaled plot of $\log(n_i(t))$, further illustrating the ballistic scaling form. The parameters are $t_B = 1$, $g = 0.25$, $\beta = 1$, $\mu = -2.01$, and $\gamma = 1$.

5.5 Discussions and Comparisons with Previous Works

As mentioned earlier, local gain or loss experienced by a system due to its connection to a reservoir is an actively investigated area of research. We therefore place our work in the context of certain recent contributions. In our setup, the bath is responsible for the simultaneous injection and removal of bosons or fermions, with rates that obey a detailed balance condition. In other words, injection and removal are not independent processes but are related by equilibrium constraints. All the methods employed in this work [Sec. 5.2] respect this condition.

If one instead considers a pure injection process, thus violating detailed balance, the resulting short- and long-time dynamics can change drastically [308, 309]. For bosons, it has been shown that an incoherent pump without loss channels can lead to dynamical transitions [309]. The total particle number $N(t)$ [Eq. (5.7)] can then display either exponential or power-law growth depending on the pump strength. In contrast, the corresponding fermionic setup [308] does not exhibit such transitions, and $N(t)$ grows linearly in time. This striking difference illustrates how the presence or absence of Pauli exclusion can dramatically alter many-body dynamics.

Formally, incorporating only incoherent pumping at a local site corresponds to

artificially setting the loss coefficient $\Gamma_L = 0$ in the Lindblad equation [Eq. (5.37)], thereby breaking detailed balance. In that case, one obtains the equation of motion for the correlation function directly from Eq. (5.39). Indeed, this limit reproduces the known results: linear growth of $N(t)$ for fermions [308], and exponential or power-law growth for bosons [309].

It is important to stress, however, that when detailed balance is respected, setting $\Gamma_L = 0$ is not physically allowed. From Eq. (5.38), one finds that for bosons, $\Gamma_L > \Gamma_G$ always holds. As a result, the term $-(\Gamma_L \mp \Gamma_G)(\delta_{im} + \delta_{jm})$ in Eq. (5.39) is always negative for bosons. An analogous statement holds for fermions. Thus, in both cases, Eq. (5.39) has a strong structural resemblance to the fermionic lattice model with only incoherent pumping ($\Gamma_L = 0$), discussed in Ref. [308]. This structural similarity explains why, across all methods employed here, we consistently observe linear growth of $N(t)$ for both bosons and fermions.

5.6 Summary and Conclusions

In this chapter, we have demonstrated how a complex interplay between unitary and non-unitary dynamics, together with quantum statistics, gives rise to rich quantum dynamics and non-trivial steady states. Specifically, we considered the setup where an empty lattice is locally connected to a reservoir [Fig. 5.1]. The main observables of interest were the local spatial density profile, $n_i(t)$ [Eq. (5.6)], and the total occupation, $N(t)$ [Eq. (5.7)], both of which were analyzed using four complementary methods.

Our results show that for both bosons and fermions, the initial growth of the total occupation $N(t)$ is linear in time, followed by exponential saturation to a constant value when the lattice is finite [Fig. 5.2a]. In the limit of an infinite lattice, $N(t)$ continues to grow linearly without saturation [Fig. 5.2b]. The local spatial density profile $n_i(t)$ exhibits ballistic spreading for both bosonic [Fig. 5.4a and Fig. 5.4b] and fermionic [Fig. (5.10a) and (5.10b)] cases. At any fixed lattice coordinate, $n_i(t)$ initially grows in time and eventually saturates owing to equilibration with the bath [Fig. 5.3 and 5.9b]. Our analysis reveals both universal features and key differences between bosons and fermions, the cause of which is rooted in quantum statistics [Fig. 5.8].

Unlike previous phenomenological approaches [308, 309], our framework is based on a microscopic description and, crucially, enforces the detailed balance condition. We show that this condition fundamentally shapes the quantum dynamics. Furthermore, we find that, in suitable regimes, the spatial density

profiles admit simple analytical forms [Fig. 5.7a and 5.7b].

A challenging and interesting direction for future work is to extend this analysis to situations where the lattice hosts interacting bosons or fermions, thereby exploring how interactions alter quantum dynamics and thermalization in locally coupled open systems.

Authors contributions: This chapter is part of the work that was done in Collaboration with Akash Trivedi, Prof. Bijay Kumar Agarwalla, Prof. Abhishek Dhar, Prof. Manas Kulkarni, Prof. Anupam Kundu, and Prof. Sanjib Sabhapandit.

6

Local Injection of quantum particles in quasiperiodic lattice

6.1 Introduction

Building on the chapter 5, here we address the problem of a tight-binding bath coupled to an incommensurate non-interacting lattice that undergoes a localization-delocalization transition. The goal is to investigate the dynamical behavior of the system across different regimes and analyze the scaling of the initial growth of observables of interest.

The model of interest is the Aubry-André-Harper (AAH) lattice, a paradigmatic one-dimensional quasi-periodic system that exhibits a localization-delocalization transition as the strength of the quasi-periodic potential is tuned [315]. The AAH model has been widely studied theoretically and experimentally, most notably in cold atoms using bi-chromatic optical lattices [79, 316–318], where this transition can be directly observed.

The interplay between localization and environmental coupling in non-interacting settings has been extensively explored in the framework of open quantum systems. Many approaches rely on effective descriptions using the Lindblad master equation in disordered and quasi-periodic lattices, focusing on both spectral properties [205, 218, 219, 222–229, 236] and dynamical features [231–235]. These studies have revealed a variety of phenomena: dissipation can, in some cases, enhance localization through carefully engineered jump operators [243–245], while in other cases, such as global dephasing or continuous monitoring, it can destroy localization altogether [247]. Despite this progress, most works remain restricted to effective dissipation models. By contrast, there are very few works where both

the bath and system are treated as a composite setup, with their exact dynamics studied microscopically [230, 243].

In this chapter, we address this gap by investigating the exact time evolution of an initially empty AAH lattice coupled to a bath that injects particles into the system. This setup offers a direct approach to studying how quasiperiodicity and environmental coupling together affect the system's dynamics, beyond effective Lindblad treatments. For reference, we also comment on comparisons with local Lindblad dynamics. The focus is to understand how the system responds in the delocalized, localized, and critical regimes, and in particular, whether reminiscence of localization remains once the system exchanges particles and correlations with the bath.

To explore these questions, we analyze the time evolution of two key observables: the total occupation number and the von Neumann entropy between the system and bath. These observables allow us to probe several fundamental issues: How does the lattice fill over time in different phases? How does the Von-neumann entropy growth reflect the filling dynamics, and what distinct features appear across the three regimes? What are the long-time equilibration properties in this non-unitary evolution?.

The chapter is organized as follows. Section 6.2 introduces the system-bath setup, followed by Section 6.3, which outlines the methods relevant to this framework. In Section 6.4, we describe the calculation of entanglement entropy. The results of the dynamics across different regimes of the quasi-periodic lattice are presented in Section 6.5. In Section 6.6, we discuss certain physical aspects of this chapter. Finally, in Sec. 6.7, we summarize the main findings along with an outlook.

6.2 Setup

In this section, we will describe the setup for the injection of spinless quantum particles into a one-dimensional Aubry-André-Harper (AAH) lattice [315] of size L. The AAH lattice is a tight-binding chain with on-site quasiperiodic modulation, governed by the Hamiltonian

$$H_S = \sum_{i=1}^{L-1} g\left(\hat{a}_{i+1}^\dagger \hat{a}_i + \hat{a}_i^\dagger \hat{a}_{i+1}\right) + \sum_{i=1}^{L} h_i \hat{a}_i^\dagger \hat{a}_i \tag{6.1}$$

with the on-site potential given by

$$h_i = 2\lambda \cos\left(2\pi\alpha i + \varphi\right) \tag{6.2}$$

Here, $\hat{a}_i^\dagger(\hat{a}_i)$ denotes the creation (annihilation) operator corresponding to the i^{th} lattice site, and obeys the canonical anti-commutation (commutation) algebra for fermions (bosons), respectively. The parameters g and λ denote the nearest-neighbor hopping and on-site potential strengths, respectively. The parameter $\alpha = (\sqrt{5}-1)/2$ is an irrational number chosen to introduce quasi-periodic (incommensurate) modulation into the lattice, making the onsite terms h_i act like quasi-disorder or correlated disorder. Here, ϕ is an arbitrary phase, and the results are obtained by averaging over $\varphi \in [0, 2\pi]$ with 100 evenly distributed realizations. More details on the model can be found in Refs. [319, 320]

When $\lambda = 0$, the lattice reduces to the clean tight-binding case with no disorder. The isolated AAH model is well known for its self-duality under Fourier transform, which leads to a sharp phase transition at $\lambda = g$. Specifically,

- For $\lambda < g$, all single-particle eigenstates are extended (delocalized regime) in real space.
- For $\lambda = g$, the eigenstates are multifractal (critical regime).
- For $\lambda > g$, all eigenstates are exponentially localized in real space.

In the localized phase, the eigenstate localized at site i has the form

$$\psi_i(x) = \mathcal{N}\, e^{-|i-x|/\sigma} \tag{6.3}$$

where σ is the localization length and is given by,

$$\sigma = \frac{1}{\log\left(\frac{\lambda}{g}\right)} \tag{6.4}$$

The transport properties in the three regimes are distinct: ballistic in the delocalized phase, sub-diffusive in the critical regime, and completely suppressed in the localized regime [321–325].

We model the reservoir (bath) as a semi-infinite tight-binding chain with hopping amplitude t_B, as done in the chapter 5.

$$H_B = t_B \sum_{i=1}^{\infty} \left(\hat{b}_i^\dagger \hat{b}_{i+1} + \hat{b}_{i+1}^\dagger \hat{b}_i\right) \tag{6.5}$$

where $\hat{b}_i$ ($\hat{b}_i^\dagger$) represent annihilation (creation) operators for bath sites and satisfy the anti-commutation (commutation) algebra for fermions (bosons), respectively.

The AAH lattice is coupled with a bath at one edge of the lattice. The coupling between the bath and lattice is given by the following Hamiltonian,

$$H_{SB} = \gamma\left(\hat{b}_0^\dagger \hat{a}_1 + \hat{a}_1^\dagger \hat{b}_0\right) \tag{6.6}$$

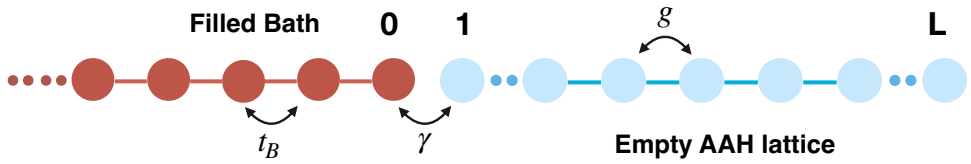

Figure 6.1: Schematic representation of the setup: The Aubry-Andre-Harper (AAH) lattice [Eq. (6.1)] of length L is coupled at one edge to a semi-infinite reservoir modeled as a tight-binding bath [Eq. (6.5)].

where γ is the system-bath coupling strength. The full Hamiltonian for the setup is therefore

$$H = H_S + H_B + H_{SB} \tag{6.7}$$

We now discuss the initial state considered in this chapter. At $t = 0$, the composite setup is prepared in the product state,

$$\hat{\rho}(t = 0) = \hat{\rho}_S(0) \otimes \hat{\rho}_B(0) \tag{6.8}$$

with the AAH lattice initially empty, $\hat{\rho}_S(t = 0) = |\mathbf{0}\rangle\langle\mathbf{0}|$. Henceforth, we will consider the fermionic problem and the bath is initially in a filled configuration, i.e., $\hat{\rho}_B(t = 0) = |\mathbf{1}\rangle\langle\mathbf{1}|$. As will be discussed later, this configuration is particularly well-suited for studying entanglement dynamics between the AAH lattice and the bath.

Albeit we discuss the fermionic case, it is worth noting that, owing to the quadratic form of the total Hamiltonian, the above framework is equally applicable to the bosonic case as well. However, for bosonic baths, the analog of the fully filled initial configuration is not physical. Nonetheless, one can consider the thermal initial state as defined in Eq. (5.5) and work with bosons for this setup.

Finally, the main observables throughout our study include the total number of particles in the AAH lattice,

$$N(t) = \sum_{i=1}^{L} n_i(t) \tag{6.9}$$

and the von Neumann entropy of the reduced system state (6.20), which will be discussed in detail in Sec. (6.4)

A schematic illustration of the setup is shown in Fig. 6.1, where the AAH lattice is coupled at one end to a semi-infinite reservoir. Throughout this chapter, unless otherwise stated, we use the parameters listed in Table 6.1.

Parameter	Value
System's hopping g	1
Bath's hopping t_B	2
System-Bath coupling γ	1

Table 6.1: Table of Parameters

6.3 Methods

6.3.1 Exact Numerics for Correlation Matrix

We employ exact numerical methods to evolve the correlation matrix, as outlined in Sec. 2.1, to compute the observables of interest for the present setup. Using Eq. (2.8), the correlation matrix can be evolved in time. For the case of a filled bath, the initial correlation matrix $C(0)$ is diagonal and takes the form

$$C(0) = \text{diag}(\underbrace{0, 0, \ldots, 0}_{L}, \underbrace{1, 1, \ldots, 1}_{L_B}) \tag{6.10}$$

where the zeros correspond to the initially empty AAH lattice sites, and the ones correspond to the fully occupied bath sites.

6.3.2 Local Lindblad Equation

For this setup, the Lindblad Equation, having both incoherent pump and loss terms at the first site of the lattice, is given as,

$$\dot{\hat{\rho}}_S(t) = \mathrm{i}\left[\hat{\rho}_S(t), H_S\right] + \Gamma_G\left[2\hat{a}_1^\dagger \hat{\rho}_S(t)\hat{a}_1 - \{\hat{a}_1\hat{a}_1^\dagger, \hat{\rho}_S(t)\}\right] + \Gamma_L\left[2\hat{a}_1\hat{\rho}_S(t)\hat{a}_1^\dagger - \{\hat{a}_1^\dagger\hat{a}_1, \hat{\rho}_S(t)\}\right] \tag{6.11}$$

where the gain Γ_G and the loss Γ_L coefficients are given by,

$$\Gamma_G = \frac{J(h_1)}{2}\,\bar{n}(h_1), \qquad \Gamma_L = \frac{J(h_1)}{2}\left(1 - \bar{n}(h_1)\right) \tag{6.12}$$

h_1 [see Eq. (6.2)] is the onsite potential at the first site of the lattice, and $\bar{n}(\omega)$ is the Fermi function and is equal to 1, since the bath is fully-filled. $J(\omega)$ is the spectral density of the bath. For the bath we considered, the corresponding form of the spectral density $J(\omega)$ can be obtained exactly, given as [250]

$$J(\omega) = \frac{2\gamma^2}{t_B}\sqrt{1 - \frac{\omega^2}{4\,t_B^2}} \tag{6.13}$$

The correlation matrix is given by,

$$C_{ij}(t) = \mathrm{Tr}\left[\hat{a}_i^\dagger \hat{a}_j \hat{\rho_S}(t)\right] \tag{6.14}$$

Using Eqn. (6.11), one can write the evolution equation of the correlation matrix,

$$\begin{aligned}\frac{dC_{i,j}}{dt} &= \mathrm{i}g\left(C_{i-1,j} - C_{i,j+1} + C_{i+1,j} - C_{i,j-1}\right) + i(h_i - h_j)C_{i,j} \\ &\quad -(\Gamma_L + \Gamma_G)\left(\delta_{i1} + \delta_{j1}\right)C_{i,j} + 2\Gamma_G\delta_{i1}\delta_{j1}\end{aligned} \tag{6.15}$$

Eq. (6.15) can be further recast as,

$$\frac{dC(t)}{dt} = XC(t) + C(t)X^\dagger + 2M_G \tag{6.16}$$

where X is referred to as the damping matrix in the literature.

$$X = \mathrm{i}\mathcal{H}^S - (M_L + M_G) \tag{6.17}$$

where $\mathcal{H}^S$ is the single-particle Hamiltonian of the lattice. M_L and M_G are Hermitian matrices, coming from the gain and loss term of the Lindblad equation, and are given by,

$$(M_L)_{ij} = \Gamma_L\delta_{i1}\delta_{j1}, \qquad (M_G)_{ij} = \Gamma_G\delta_{i1}\delta_{j1} \tag{6.18}$$

The form of the Eq. (6.16) is commonly referred to as the Lyapunov equation and is well-suited to perform numerical computations.

6.4 Entanglement Entropy

For the filled bath with fermions, it is natural to investigate the entanglement dynamics between the system and the bath. To characterize the dynamics across different regimes, we analyze the scaling behavior of the entanglement entropy growth.

When the initial state of the entire setup is pure, the bipartite entanglement entropy between subsystems A and B reduces to the von Neumann entropy of the reduced density matrix. Formally,

$$\rho = |\Psi\rangle\langle\Psi|, \qquad \rho_A = \mathrm{Tr}_B\left[\rho\right], \qquad S = -\mathrm{Tr}\left[\rho_A \ln \rho_A\right] \tag{6.19}$$

For my setup, this corresponds to

$$S = -\mathrm{Tr}\left[\hat{\rho}_S \ln \hat{\rho}_S\right] \tag{6.20}$$

Where $\hat{\rho}_S$ is the reduced density matrix of the system obtained by tracing out the bath degrees of freedom. Next, we provide the derivation of the computation of the entanglement entropy [Eq. (6.20)] in terms of the eigenvalues of the system's correlation matrix.

Since the full Hamiltonian is quadratic and we start from a Gaussian initial state, the total state remains Gaussian at all times, fully characterized by its two-point correlation functions due to Wick's theorem. Consequently, the reduced density matrix $\hat{\rho}_S(t)$ is also Gaussian and can be expressed as

$$\hat{\rho}_S(t) = \frac{\exp\left[-\sum_{i,j} \hat{a}_i^\dagger A_{ij}(t) \hat{a}_j\right]}{Z(t)} \tag{6.21}$$

where $A(t)$ is a Covariance matrix, and $Z(t)$ is the partition function. Let's denote the system's correlation matrix C as,

$$C_{mn}(t) = \mathrm{Tr}\left[\hat{a}_m^\dagger \hat{a}_n \hat{\rho}_S(t)\right] \tag{6.22}$$

This correlation matrix is diagonalized by a unitary transformation U, such that

$$U^\dagger C U = \tilde{C} = \mathrm{diag}\left(c_1, c_2, \ldots, c_{N-1}, c_N\right) \tag{6.23}$$

where the matrix $\tilde{C}$ is the diagonal matrix with eigenvalues c_m. Defining new fermionic operators as,

$$\hat{a}'_m = \sum_l U_{l,m} \hat{a}_l, \quad m = 1, \ldots, N \tag{6.24}$$

which preserve the canonical anti-commutation relations, $\left\{\hat{a}'_m, \hat{a}'^\dagger_n\right\} = \delta_{m,n}$ and the reduced density matrix is diagonal in this new basis. The two-point correlations of these new modes satisfy

$$\left\langle \hat{a}'^\dagger_m \hat{a}'_n \right\rangle = \delta_{m,n} c_m(t) \tag{6.25}$$

Hence, the system decomposes effectively into independent fermionic modes with occupations $c_m(t)$. From this, the corresponding Fermi-Dirac distribution for each fermion can be found. Consequently, the density matrix $\rho_S(t)$ is formally given by,

$$\hat{\rho}_S(t) = \prod_{m=1}^{N} \frac{\exp\left[-f_m(t) \hat{a}'^\dagger_m \hat{a}'_m\right]}{1 + \exp\left[-f_m(t)\right]}, \qquad f_m(t) = \ln\left(\frac{1}{c_m(t)} - 1\right) \tag{6.26}$$

The partition function factorizes as

$$Z(t) = \prod_{m=1}^{N} \left[1 + \exp\left(-f_m(t)\right)\right] \tag{6.27}$$

From this form, the von Neumann entropy becomes

$$\begin{aligned} S(t) &= -\,\mathrm{Tr}\left[\rho_S(t) \ln \rho_S(t)\right] \\ &= -\,\mathrm{Tr}\left[\rho_S(t)\left(\ln\left(\frac{1}{Z(t)}\right) - \sum_{m=1}^{L} f_m(t) \hat{a}'^\dagger_m \hat{a}'_m\right)\right] \\ &= \mathrm{Tr}\left[\rho_S(t) \sum_{m=1}^{L} \ln\left[1 + \exp\left(-f_m(t)\right)\right]\right] + \sum_{m=1}^{L} \mathrm{Tr}\left[\rho_S f_m(t) \hat{a}'^\dagger_m \hat{a}'_m\right] \end{aligned} \tag{6.28}$$

Using $\langle \hat{a}_m'^{\dagger} \hat{a}_m' \rangle$ to write second term to get,

$$S(t) = \sum_{m=1}^{L} \left[\ln \left[1 + \exp\left(-f_m(t)\right) \right] + \frac{f_m(t)}{1 + \exp\left(f_m(t)\right)} \right] \tag{6.29}$$

Re-expressing in terms of the eigenvalues $c_m(t)$, the entanglement entropy simplifies to the well-known fermionic form:

$$S(t) = -\sum_{m=1}^{N} \left[(1 - c_m(t)) \ln(1 - c_m(t)) + c_m(t) \ln c_m(t) \right] \tag{6.30}$$

This formula in Eq. (6.30) provides an efficient way to compute the entanglement entropy from the eigenvalues of the correlation matrix at any time t.

6.5 Results

In this section, we present numerical results for a quasi-periodic lattice coupled at one end to a tight-binding bath (See Fig. 6.1). The analysis focuses on two quantities using exact numerics [Sec. 6.3.1]:

1. The total occupation $N(t)$, as defined in Eq. (6.9)
2. The Von Neumann entropy $S(t)$, as defined by Eq. (6.20).

The time evolution of $N(t)$ reveals the filling process of the lattice in various phases, while $S(t)$ is calculated using Eq. (6.30), based on the eigenvalues of the correlation matrix. We will also corroborate the results obtained from exact numerics with the Local Lindblad Equation discussed in Sec. 6.3.2. This combined approach provides a comprehensive understanding of the dynamics and statistical properties of the system. It is important to point out that the three regimes, delocalized ($\lambda < 1$), critical ($\lambda = 1.0$), and localized ($\lambda > 1$), indicate the value of λ but do not represent the phase of the full setup, as this is no longer an isolated AAH lattice.

In Fig. 6.2, we present the time evolution of the total occupation $N(t)$ [Eq. (6.9)] obtained from exact numerics for the delocalized ($\lambda = 0.2$), critical ($\lambda = 1.0$), and localized ($\lambda = 1.2$) regimes, for various system sizes.

In the delocalized phase ($\lambda = 0.2$), shown in Fig. 6.2a, $N(t)$ grows linearly at short times, followed by an exponential relaxation towards a steady state at long times. For increasing system sizes, the $N(t)$ curves collapse onto each other up to a characteristic timescale (which depends on system size L), demonstrating ballistic growth. Beyond this timescale, finite-size effects become apparent, leading to

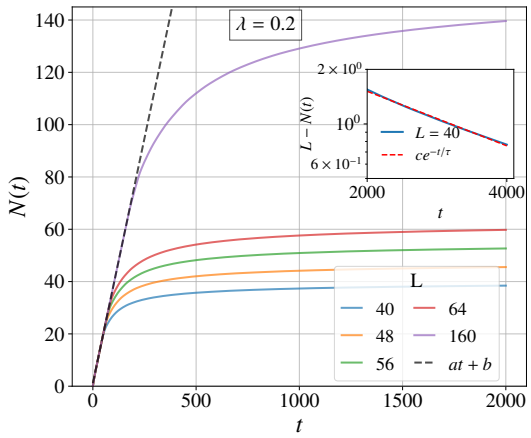

(a) $\lambda = 0.2$

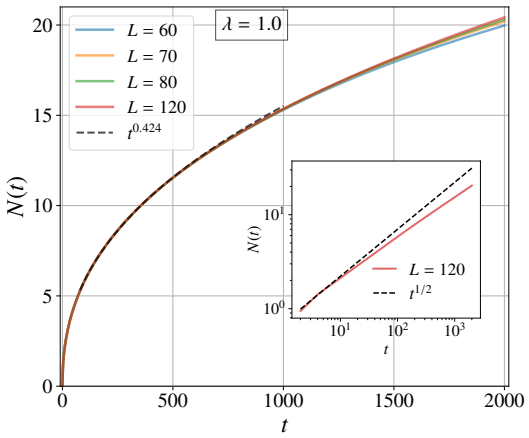

(b) $\lambda = 1.0$

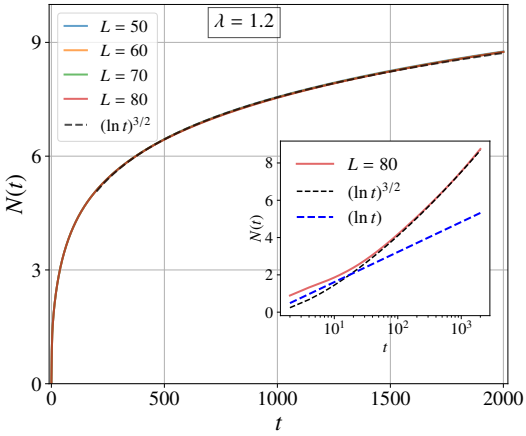

(c) $\lambda = 1.2$

Figure 6.2: Behaviour of total occupation $N(t)$ [Eq. (6.9)] versus time obtained from exact numerics for three distinct regimes, for various system sizes. (a) Delocalized regime ($\lambda = 0.2$): The plot displays initial linear growth followed by exponential relaxation to the steady state. The black dashed line corresponds to a linear fit of the initial growth. The inset shows $L-N(t)$ versus t on a semi-log scale, illustrating the exponential relaxation at long times towards saturation. (b) Critical regime ($\lambda = 1.0$): The plot illustrates nearly diffusive growth at early times, with the black dashed line providing the fit. The inset compares the initial growth of $N(t)$ with the $t^{1/2}$ scaling on a log-log scale, highlighting the subtle difference with conventional diffusive behavior in this regime. (c) Localized regime ($\lambda = 1.2$): The plot reveals polylogarithmic growth initially, with a corresponding fit shown as a black dashed line. The inset presents the same data on a semi-log scale to clearly display the polylogarithmic dynamics. A key observation in all plots is that the initial growth overlaps for all system sizes for each of the phases, which suggests that the dynamical scaling persists in the thermodynamic limit.

deviations from linear behaviour and the eventual onset of equilibration. The steady state corresponds to the lattice being fully-filled, i.e. $N(t \to \infty) \to L$. The

inset of Fig. 6.2a illustrates the exponential approach to equilibrium by plotting $L-N(t)$ versus time for system size $L = 40$, consistent with the relaxation dynamics of finite-size systems coupled to a generic bath. The ballistic growth and the subsequent exponential relaxation of $N(t)$ observed in the delocalized phase ($\lambda < 1$) are similar to those reported for the clean lattice case (Fig. 5.2), discussed in chapter 5.

In the critical regime ($\lambda = 1.0$), shown in Fig. 6.2b, $N(t)$ exhibits close to diffusive growth (t^p, with $p \sim 0.5$). For increasing system sizes, the curves overlap up to characteristic timescales (which depend on system size L), after which finite-size effects lead to deviations as the system approaches equilibration. The steady state again corresponds to a fully-filled lattice, but the relaxation process is considerably slower compared to the delocalized case ($\lambda < 1$), with characteristic timescales increasing as the quasi-disorder strength λ is tuned towards 1 from below. The inset of Fig. 6.2b shows a comparison of $N(t)$ for system size $L = 120$ with the conventional diffusive scaling, eluciating the slight departure from $t^{1/2}$ in the critical regime. It is worth noting that these results are consistent with both isolated and open system properties of the AAH lattice, where close to diffusive behavior has been reported [321, 322, 324].

In the localized regime ($\lambda = 1.2$), shown in Fig. 6.2c, $N(t)$ exhibits a polylogarithmic growth with time. Although the system is ultimately expected to saturate to a fully-filled state, the growth is extremely slow. The inset of Fig. 6.2c presents $N(t)$ in comparison with standard logarithmic scaling on a semi-log scale, making the polylogarithmic behavior evident.

Overall, the fact that our numerical observation of the initial growth of $N(t)$ for different system sizes coincides for each regime in Fig. 6.2 indicates that the dynamical scaling in every regime should persist in the thermodynamic limit.

In Fig. 6.3, we present the time evolution of the Von Neumann entropy $S(t)$ [Eq. (6.30)] obtained from exact numerics for the delocalized ($\lambda = 0.2$), critical ($\lambda = 1.0$), and localized ($\lambda = 1.2$) regimes, for various system sizes.

In the delocalized phase ($\lambda = 0.2$), depicted in Fig. 6.3a, $S(t)$ exhibits a characteristic Page curve [326, 327]: an initial linear growth followed by an exponential decay towards zero after reaching its maximum at the Page time. For increasing system sizes, these curves coincide up to this Page time (which depends on system size L). Beyond this point, finite-size effects become significant; the lattice eventually fills and becomes spatially homogeneous (and equilibrates), leading to the entanglement entropy decay to zero. The inset of Fig. 6.3a illustrates this exponential decay towards zero for system size $L = 40$.

In the critical regime ($\lambda = 1.0$), shown in Fig. 6.3b, $S(t)$ also follows a Page

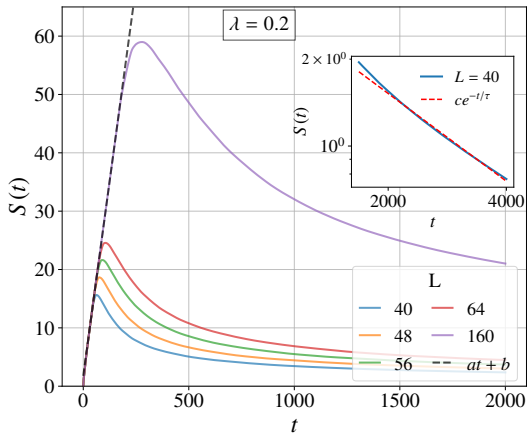

(a) $\lambda = 0.2$

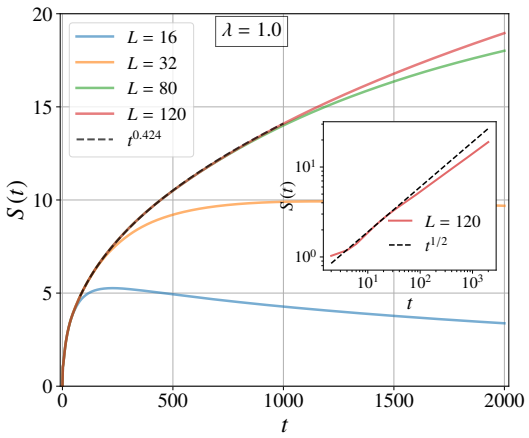

(b) $\lambda = 1.0$

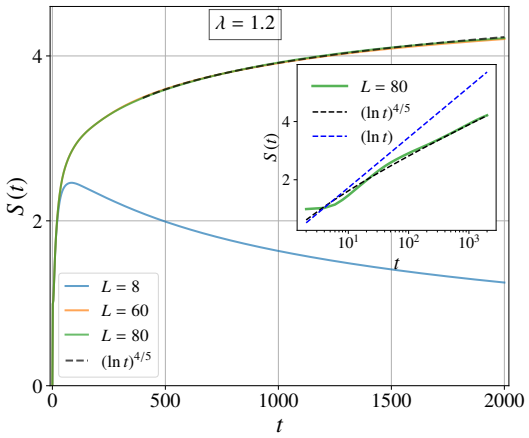

(c) $\lambda = 1.2$

Figure 6.3: Behaviour of the Von Neumann entropy $S(t)$ [Eq. (6.30)] versus time, obtained from exact numerics for three regimes for various system sizes. (a) Delocalized regime ($\lambda = 0.2$): $S(t)$ exhibits initial linear growth followed by exponential decay towards zero after the Page time. The black dashed line is a linear fit to the initial growth. The inset presents $S(t)$ on a semi-log scale, illustrating the exponential decay at long times. (b) Critical regime ($\lambda = 1.0$): $S(t)$ shows nearly diffusive growth, with the black dashed line being the fit, followed by decay towards zero after the Page time, as visible for system size $L = 16$ dynamics. The inset compares the growth with the $t^{1/2}$ scaling on a log-log scale, highlighting the subtle difference with standard diffusive scaling. (c) Localized regime ($\lambda = 1.2$): $S(t)$ demonstrates initial polylogarithmic growth, with a corresponding fit indicated by the black dashed line, followed by decay towards zero after the Page time, which can be seen from system size $L = 8$ dynamics. The inset displays the growth of $S(t)$ in comparison with standard logarithmic scaling on a semi-log scale to clearly reveal the polylogarithmic behavior. An important observation is that for each of the regimes, the initial growth of entropy overlaps across system sizes, indicating that dynamical scaling persists in the thermodynamic limit.

curve profile, characterized by slower, nearly diffusive growth (t^p, with $p \sim 0.5$) at early times. For increasing system sizes, these curves overlap up to the Page time, beyond which finite-size effects dominate and the entropy gradually decreases from its peak value towards zero. Due to the slow dynamics of this regime, the subsequent decay of entropy is likewise slow. The inset compares $S(t)$ for system size $L = 120$ with $t^{1/2}$ scaling on a log-log scale, emphasizing the departure from the standard diffusive behavior during the initial growth.

In the localized regime ($\lambda = 1.2$), illustrated in Fig. 6.3c, the Page curve dynamics feature an even slower, polylogarithmic increase of $S(t)$ at early times. Curves for different system sizes again overlap up to the Page time, after which finite-size effects induce the entropy decay from its maximum towards zero. Even for small system sizes, the extremely slow dynamical nature results in a very gradual entropy decay. The inset of Fig. 6.3c displays $S(t)$ in comparison with standard logarithmic scaling on a semi-log scale, highlighting the polylogarithmic growth behavior.

Overall, these results illustrate how the Page curve dynamics evolve distinctively for each phase, with the initial growth overlapping across system sizes, thereby confirming the persistence of dynamical scaling in the thermodynamic limit.

So far, the results discussed were obtained from the exact numerics [Sec. 6.3.1]. Next, we discuss the numerical findings obtained via the Local Lindblad Equation [Sec. 6.3.2]. We recall that the Lindblad equation was employed in chapter 4 as a phenomenological approach to model arbitrary system-bath couplings, while in chapter 5, the focus shifted to the weak system-bath coupling regime. In this weak coupling regime, the dynamics can become extremely slow due to strong quasi-disorder and a low rate of particle injection. To overcome this limitation, we explore parameter regimes corresponding to strong coupling. Because the Lindblad equation is completely positive and trace-preserving (CPTP), the qualitative features of the dynamics remain physically meaningful, and the dynamical scaling is expected to be consistent with that obtained from exact numerics. However, a thorough quantitative agreement between the Lindblad approach and exact dynamics is not expected, especially beyond weak coupling limits [250, 328]. In the localized regime ($\lambda > 1$), characterized by logarithmically slow dynamics, direct exact numerics is impractical for long-time studies. Here, especially the Lindblad formalism provides a practical alternative that captures similar dynamical scaling for key observables.

Figure 6.4 shows the time evolution of the total occupation $N(t)$ [Eq. (6.9)]

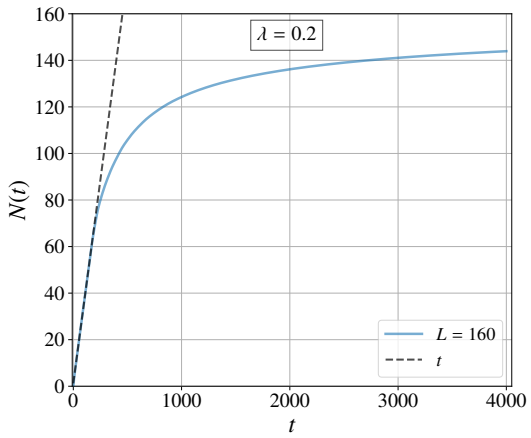

(a) $\lambda = 0.2$

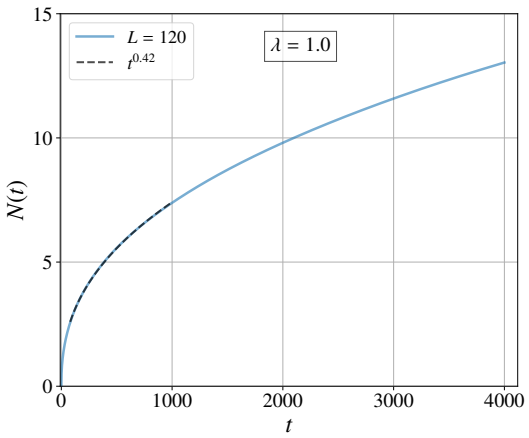

(b) $\lambda = 1.0$

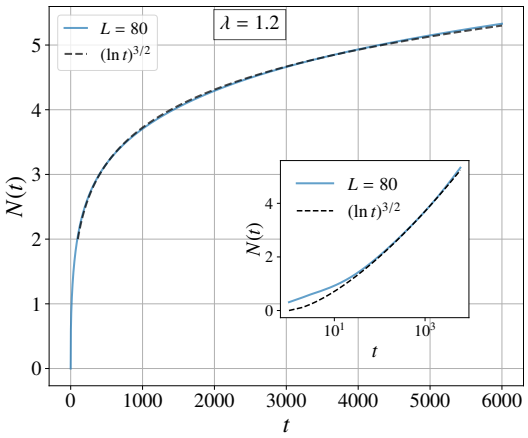

(c) $\lambda = 1.2$

Figure 6.4: Behaviour of total occupation $N(t)$ versus time obtained from Local Lindblad Equation [Sec. 6.3.2] for (a) delocalized, (b) critical, and (c) localized regimes for a representative system size. In these plots, the same characteristic scaling exponent of occupation growth is observed as in Fig. 6.2, obtained using exact numerics across each of the three regimes. The black dashed lines are the curves whose functional form is given in the legends.

obtained from the local Lindblad equation [Sec. 6.3.2] in the delocalized ($\lambda = 0.2$), critical ($\lambda = 1.0$), and localized ($\lambda = 1.2$) regimes. The characteristic scaling of occupation growth observed here matches that obtained from exact numerics (Fig. 6.2). The chosen parameters correspond to strong system-bath coupling (See Table 6.1). The qualitative agreement-particularly the preservation of characteristic dynamical scaling for each of the three regimes, holds. This reinforces and strengthens the claims we made based on exact numerics.

In this section on numerical results, to illustrate the dynamics across different regimes, system sizes were chosen to best highlight characteristic behaviors. It should be noted that identical system sizes are not always required to demonstrate

the key growth patterns and main observations. Instead, selecting appropriate sizes for each regime enables a clearer representation of the underlying dynamics.

6.6 Discussions

In the isolated Aubry-André-Harper (AAH) model, particle spreading occurs ballistically in the delocalized regime and is nearly diffusive at the critical point. When a single bath is attached to one end of the one-dimensional lattice, the extensive properties of the system's eigenstates are expected to remain largely unchanged, as the number of baths is non-extensive. Consequently, the scaling behavior of transport and particle spreading is anticipated to resemble that in the isolated lattice for the delocalized and critical regimes. However, in the localized regime, where transport is absent in the isolated system, the presence of the bath facilitates particle injection and subsequent spreading (albeit extremely slow in nature) within the lattice.

This injection mechanism leads to non-trivial dynamical scaling in the time evolution of the total occupation. In the Localized regime, the overlap between the system's eigenstates and the bath contact point decays exponentially with the distance of the localization center from the contact site [226]. As a result, eigenstates localized far from the contact remain essentially unaffected and contribute only weak, logarithmic transport from the bath to the system. In contrast, dissipation broadens eigenstates localized near the contact point, which likely accounts for the enhanced transport and the observed scaling behavior beyond logarithmic growth.

We expect that particle transport from the bath into the system will continue until the lattice becomes fully occupied. Because the bath is chosen to be infinite, particle spreading will continue logarithmically at long times in the localized phase, occurring over extremely long timescales. The coupling strength between the system and the bath governs the extent to which eigenstates broaden.

6.7 Summary and Outlook

In this chapter, we have explored the rich quantum dynamics emerging from the interplay of unitary and non-unitary processes in a quasiperiodic system. Specifically, we considered an initially empty Aubry-André-Harper (AAH) lattice locally coupled to a reservoir, as depicted in Fig. 6.1. The primary observables were the total occupation, $N(t)$ [Eq. (6.9)], and the Von Neumann entropy, $S(t)$

[Eq. (6.20)], both analyzed using exact numerics [Sec. 6.3.1]. To further support the findings, we also studied the evolution of total occupation using the local Lindblad equation [Sec. 6.3.2].

The results demonstrate that the initial growth of the total occupation $N(t)$ exhibits distinct dynamical behaviors depending on the regime: linear growth in the delocalized phase, nearly diffusive growth at the critical point, and polylogarithmic growth in the localized phase. This initial growth is followed by relaxation towards a fully-filled steady state, as shown in Fig. 6.2. However, the timescales for reaching this steady state increase with both the strength of quasi-disorder λ and system size L. Similarly, the Von Neumann entropy shows corresponding initial growth patterns - linear, nearly diffusive, and polylogarithmic - followed by decay towards zero at long times, as illustrated in Fig. 6.3. Moreover, employing the local Lindblad equation to model the system's evolution under arbitrary system-bath coupling confirms the same value (as obtained from exact numerics) of the characteristic dynamical exponent of total occupation $N(t)$ in each of the three regimes.

One promising future direction is motivated by recent work by Mallick and Krapivsky [308, 309], studying particle injection in open quantum systems. In particular, exploring particle injection using the local Lindblad equation with arbitrary gain and loss coefficients in the Aubry-André-Harper lattice for bosons and fermions presents an exciting opportunity. While fermionic systems are expected to show similar dynamical scaling, bosonic systems may exhibit richer behavior. Previous work [309] has demonstrated that an incoherent pump without loss channels can induce dynamical phase transitions in bosons, where the total particle number $N(t)$ grows either exponentially or as a power law depending on the pump strength.

The interplay between incoherent gain and loss processes and quasiperiodicity in the lattice could give rise to a diverse range of dynamical scaling behaviors for $N(t)$, alongside non-trivial scaling of particle spreading within the lattice. These effects are expected to be strongly influenced by the strength of the quasi-disorder. Investigating this problem is an ongoing research project I'm pursuing that promises deeper insight into open quantum systems with quasiperiodic structure.

An important open question concerns the characteristics of long-time dynamics, particularly the scaling of relaxation times toward steady states as a function of system size in the various phases of the AAH lattice. While the total occupation, being linear in the density matrix, is expected to exhibit one type of scaling, the von Neumann entropy, as a non-linear function, may show different behavior.

Additionally, applying hydrodynamic approaches to the setup introduced in Chapter 5 could provide analytical expressions for spatial density profiles and entropy evolution over time, offering a pathway to compute relaxation timescales analytically.

Authors contributions: This chapter is part of the ongoing work in Collaboration with Prof. Bijay Kumar Agarwalla, Prof. Abhishek Dhar, Prof. Manas Kulkarni, Prof. Anupam Kundu, and Prof. Sanjib Sabhapandit.

7

Conclusion

A major challenge in modern physics is to understand whether quantum systems thermalize when subject to disorder and environmental interactions. This thesis examines the impact of dissipation and external driving influence localization-delocalization transitions, focusing on the spectral and dynamical properties of both interacting systems that exhibit many-body localization and non-interacting systems that exhibit Anderson localization. The central objective is to examine whether coupling to the environment destroys localization entirely or whether signatures of the localized phase can still endure in open quantum systems/non-Hermitian systems.

In Chapter 2, we outline the theoretical framework and methods used to study the dynamics of open quantum systems. The discussion combines exact numerical techniques with perturbative approaches to capture both non-perturbative and weak-coupling regimes. Exact methods provide accurate descriptions in specific settings, while quantum master equations offer versatile tools for exploring dissipative dynamics in broader contexts. Together, these approaches establish a comprehensive foundation for analyzing the quantum dynamics in the presence of the environment and are quite useful for a wide range of problems in many-body systems.

In Chapter 3, we study three non-Hermitian disordered interacting quantum systems, focusing on spectral signatures to identify the presence/absence of quantum chaos. Spectral diagnostics such as the dissipative spectral form factor and complex spacing ratios are discussed, which reveal clear signatures of chaotic behavior at weak disorder, consistent with predictions from non-Hermitian random matrix theory. On the other hand, strong disorder leads to uncorrelated spectra, which is characteristic of localization. These tools capture universal features that are signatures of chaos and random matrix theory. DSFF possesses the

universal dip-ramp-plateau in the chaotic regime; it loses the characteristic dip-ramp-plateau structure in the absence of chaos. Similarly, CSR has an anisotropic distribution (RMT) in the presence of chaos, while a homogeneous distribution (Poisson) in its absence. Extending one of the models to include long-range hopping further demonstrates how increasing connectivity enhances chaotic features, with correlations persisting even at strong disorder.

In chapter 4, we study a one-dimensional chain of disordered interacting systems using deformed Lindblad dynamics to probe how quantum jumps influence the ergodic to many-body localization transition. By analyzing spectral observables such as complex spacing ratios together with dynamical measures like imbalance and activity, we find that controlling the quantum jumps can stabilize the localized phase and promote its emergence. In other words, post-selection can promote localization. We emphasize that this result is not merely a formal construction but is experimentally accessible using realistic detectors with finite efficiency. This result highlights a mechanism distinct from measurement-induced phase transitions and demonstrates that post-selection can be used to preserve localization in open many-body systems, offering both theoretical insight and experimental feasibility.

In the second part of this thesis, we investigate the unitary dynamics of a non-interacting lattice coupled to a reservoir modeled as a tight-binding chain at finite temperature and chemical potential. In Chapter 5, we focus on a disorder-free lattice, which is initially empty, and show how the interplay between unitary evolution and non-unitary effects gives rise to rich quantum dynamics in simple setups. By analyzing observables such as spatial density profiles and total occupation, we show that particle spreading is ballistic at early times, with finite systems eventually relaxing to equilibrium while infinite lattices exhibit unbounded growth. The results reveal both universal features and distinct differences between bosons and fermions arising from quantum statistics. Furthermore, by comparing exact results with quantum master equations, we also demonstrate their validity or invalidity in various regimes. Unlike phenomenological descriptions, the framework employed here enforces detailed balance, providing a consistent foundation for understanding spreading, equilibration, and steady states in open non-interacting quantum systems.

Continuing from chapter 5, we extend the analysis to non-interacting quasiperiodic systems in chapter 6. We study the dynamics of an empty Aubry-André-Harper (AAH) lattice, which exhibits a localization-delocalization transition coupled to a reservoir. This setup allows a direct investigation of how quasi-periodicity and environmental coupling influence the system's dynamics. By examining the

time evolution of key observables such as the total occupation and the von Neumann entropy, we show that the system exhibits very rich quantum dynamics and distinct dynamical scaling across different regimes: linear growth in the delocalized phase, nearly diffusive behavior at the critical point, and polylogarithmic growth in the localized phase. While finite systems eventually relax to steady states, the timescales strongly depend on both quasi-disorder and system size. Comparisons with Lindblad dynamics confirm the robustness of these results. Overall, the study highlights how the interplay between quasiperiodicity and bath coupling leads to rich transport phenomena, revealing that localization signatures (e.g., polylogarithmic growth) can persist even under continuous particle exchange with an environment.

In this thesis, we have investigated the stability and robustness of localization phenomena - both single-particle and many-body localization - in the presence of environmental interactions. The motivation is rooted in a broader effort to understand how dissipation and decoherence influence localization in quantum systems. The primary focus has been on damping-type dissipators, though the role of dephasing, with its rich and distinctive physical implications, is a compelling direction for future exploration. Using several paradigmatic models, including both non-interacting and interacting systems with disorder in non-Hermitian and open-system frameworks, we have examined how environmental coupling modifies spectral and dynamical properties.

The results presented in this thesis demonstrate the existence of a delocalization-localization transition in dissipative dynamics. We also show that controlled environmental setups (e.g., tuning the quantum jumps) can both stabilize and enhance the localized phase under suitable conditions. Through detailed analysis of dynamical observables, this work further characterizes the signatures of these phases, drawing connections between theoretical models and realistic experimental implementations. Thus, the findings contribute to a deeper understanding of how localized quantum phases may be controlled and detected in current and future experiments.

Bibliography

[1] J. M. Lourenço. *The NOVAthesis LaTeX Template User's Manual*. NOVA University Lisbon. 2021. URL: https://github.com/joaomlourenco/novathesis/raw/main/template.pdf (cit. on p. iv).

[2] M. Kardar. *Statistical physics of particles*. Cambridge University Press, 2007. URL: https://www.cambridge.org/9780521873420 (cit. on p. 1).

[3] F. Reif. *Fundamentals of statistical and thermal physics*. Waveland Press, 2009 (cit. on p. 1).

[4] L. D. Landau and E. M. Lifshitz. *Statistical Physics: Volume 5*. Vol. 5. Elsevier, 2013 (cit. on p. 1).

[5] R. K. Pathria and P. D. Beale. *Statistical Mechanics*. 3rd ed. Amsterdam ; Boston: Elsevier/Academic Press, 2011. ISBN: 978-0-12-382188-1 (cit. on p. 1).

[6] M. Kardar. *Statistical physics of fields*. Cambridge University Press, 2007. ISBN: 978-0521873413. URL: https://www.cambridge.org/9780521873413 (cit. on p. 1).

[7] E. Ott. *Chaos in dynamical systems*. Cambridge university press, 2002 (cit. on p. 1).

[8] S. H. Strogatz. *Nonlinear dynamics and chaos with student solutions manual: With applications to physics, biology, chemistry, and engineering*. CRC press, 2018 (cit. on p. 1).

[9] J.-P. Eckmann and D. Ruelle. "Ergodic theory of chaos and strange attractors". In: *Reviews of modern physics* 57.3 (1985), p. 617 (cit. on p. 1).

[10] L. Boltzmann. "Weitere Studien über das Wärmegleichgewicht unter Gasmolekülen". In: *Sitzungsberichte der Kaiserlichen Akademie der Wissenschaften in Wien. Mathematisch-naturwissenschaftliche Klasse* 66 (1872), pp. 275–370 (cit. on p. 1).

[11] J. C. Maxwell. "On Boltzmann's theorem on the average distribution of energy in a system of material points". In: *Transactions of the Cambridge Philosophical Society* 12 (1879), p. 547 (cit. on p. 1).

[12] P. Reichert. "The Ergodic Hypothesis: A Typicality Statement". In: *Physics and the Nature of Reality: Essays in Memory of Detlef Dürr*. Ed. by A. Bassi et al. Cham: Springer International Publishing, 2024, pp. 285–299. ISBN: 978-3-031-45434-9. DOI: 10.1007/978-3-031-45434-9_20. URL: https://doi.org/10.1007/978-3-031-45434-9_20 (cit. on p. 1).

[13] M. Cattaneo et al. "Thermalization is typical in large classical and quantum harmonic systems". In: *Phys. Rev. Res.* 7 (3 2025-07), p. L032002. DOI: 10.1103/h9fj-ylgm. URL: https://link.aps.org/doi/10.1103/h9fj-ylgm (cit. on p. 1).

[14] Y. G. Sinai. "On the Foundations of the Ergodic Hypothesis for a Dynamical System of Statistical Mechanics". In: *Soviet Mathematics - Doklady* 4 (1963), pp. 1818–1822 (cit. on p. 1).

[15] Y. G. Sinai. "Dynamical systems with elastic reflections". In: *Russian Mathematical Surveys* 25.2 (1970), p. 137 (cit. on p. 1).

[16] L. A. Bunimovich. "On the ergodic properties of nowhere dispersing billiards". In: *Communications in Mathematical Physics* 65.3 (1979), pp. 295–312. URL: https://doi.org/10.1007/BF01197884 (cit. on p. 1).

[17] N. Simányi. "Proof of the ergodic hypothesis for typical hard ball systems". In: *Annales Henri Poincaré*. Vol. 5. 2. Springer. 2004, pp. 203–233. DOI: 10.1007/s00023-004-0166-8. URL: https://doi.org/10.1007/s00023-004-0166-8 (cit. on p. 1).

[18] E. A. Yuzbashyan. "Generalized microcanonical and Gibbs ensembles in classical and quantum integrable dynamics". In: *Annals of Physics* 367 (2016), pp. 288–296. ISSN: 0003-4916. DOI: https://doi.org/10.1016/j.aop.2016.02.002. URL: https://www.sciencedirect.com/science/article/pii/S0003491616000403 (cit. on p. 2).

[19] M. Rigol et al. "Relaxation in a Completely Integrable Many-Body Quantum System: An Ab Initio Study of the Dynamics of the Highly Excited States of 1D Lattice Hard-Core Bosons". In: *Phys. Rev. Lett.* 98 (5 2007-02), p. 050405. DOI: 10.1103/PhysRevLett.98.050405. URL: https://link.aps.org/doi/10.1103/PhysRevLett.98.050405 (cit. on p. 2).

[20] L. Vidmar and M. Rigol. "Generalized Gibbs ensemble in integrable lattice models". In: *Journal of Statistical Mechanics: Theory and Experiment* 2016.6 (2016-06), p. 064007. DOI: 10.1088/1742-5468/2016/06/064007. URL: https://dx.doi.org/10.1088/1742-5468/2016/06/064007 (cit. on p. 2).

[21] L. D'Alessio et al. "From quantum chaos and eigenstate thermalization to statistical mechanics and thermodynamics". In: *Adv. Phys.* 65.3 (2016), pp. 239–362. DOI: 10.1080/00018732.2016.1198134. URL: https://doi.org/10.1080/00018732.2016.1198134 (cit. on pp. 2, 3, 25, 28).

[22] T. Mori et al. "Thermalization and prethermalization in isolated quantum systems: a theoretical overview". In: *Journal of Physics B: Atomic, Molecular and Optical Physics* 51.11 (2018-05), p. 112001. DOI: 10.1088/1361-6455/aabcdf. URL: https://dx.doi.org/10.1088/1361-6455/aabcdf (cit. on pp. 2, 3).

[23] J. BRICMONT. "SCIENCE OF CHAOS OR CHAOS IN SCIENCE?" In: *Annals of the New York Academy of Sciences* 775.1 (1995), pp. 131–175. DOI: https://doi.org/10.1111/j.1749-6632.1996.tb23135.x. eprint: https://nyaspubs.onlinelibrary.wiley.com/doi/pdf/10.1111/j.1749-6632.1996.tb23135.x. URL: https://nyaspubs.onlinelibrary.wiley.com/doi/abs/10.1111/j.1749-6632.1996.tb23135.x (cit. on p. 2).

[24] E. Fermi et al. *Studies of the nonlinear problems*. Tech. rep. Los Alamos National Lab.(LANL), Los Alamos, NM (United States), 1955 (cit. on p. 2).

[25] Y. Liu and D. He. "Chaotic route to classical thermalization: A real-space analysis". In: *Phys. Rev. E* 109 (6 2024-06), p. 064115. DOI: 10.1103/PhysRevE.109.064115. URL: https://link.aps.org/doi/10.1103/PhysRevE.109.064115 (cit. on p. 2).

[26] S. Ganapa, A. Apte, and A. Dhar. "Thermalization of local observables in the α-FPUT chain". In: *Journal of Statistical Physics* 180.1 (2020), pp. 1010–1030 (cit. on p. 2).

[27] G. P. Berman and F. M. Izrailev. "The Fermi–Pasta–Ulam problem: Fifty years of progress". In: *Chaos: An Interdisciplinary Journal of Nonlinear Science* 15.1 (2005-03). ISSN: 1089-7682. DOI: 10.1063/1.1855036. URL: http://dx.doi.org/10.1063/1.1855036 (cit. on p. 2).

[28] J. v. Neumann. "Beweis des Ergodensatzes und desH-Theorems in der neuen Mechanik". In: *Zeitschrift für Physik* 57.1 (1929), pp. 30–70. DOI: 10.1007/BF01339852. URL: https://doi.org/10.1007/BF01339852 (cit. on p. 2).

[29] S. Goldstein et al. "Long-time behavior of macroscopic quantum systems". In: *The European Physical Journal H* 35.2 (2010), pp. 173–200. DOI: 10.1140/epjh/e2010-00007-7. URL: https://doi.org/10.1140/epjh/e2010-00007-7 (cit. on p. 2).

[30] E. P. Wigner. "Random Matrices in Physics". In: *SIAM Review* 9.1 (1967), pp. 1–23. DOI: 10.1137/1009001. eprint: https://doi.org/10.1137/1009001. URL: https://doi.org/10.1137/1009001 (cit. on p. 2).

[31] M. L. Mehta. *Random matrices*. Vol. 142. Elsevier, 2004 (cit. on pp. 2, 3, 25, 27).

[32] F. Haake. "Quantum signatures of chaos". In: *Quantum Coherence in Mesoscopic Systems*. Springer, 1991, pp. 583–595 (cit. on pp. 2, 3, 25, 27, 28).

[33] P. J. Forrester. *Log-gases and random matrices (LMS-34)*. Princeton University Press, 2010 (cit. on pp. 2, 132).

[34] M. V. Berry, M. Tabor, and J. M. Ziman. "Level clustering in the regular spectrum". In: *Proc. R. Soc. London, Ser. A* 356.1686 (1977), pp. 375–394. DOI: 10.1098/rspa.1977.0140. URL: https://royalsocietypublishing.org/doi/abs/10.1098/rspa.1977.0140 (cit. on p. 2).

[35] M. V. Berry. "Regular and irregular semiclassical wavefunctions". In: *Journal of Physics A: Mathematical and General* 10.12 (1977-12), p. 2083. DOI: 10.1088/0305-4470/10/12/016. URL: https://dx.doi.org/10.1088/0305-4470/10/12/016 (cit. on p. 2).

[36] O. Bohigas, M. J. Giannoni, and C. Schmit. "Characterization of Chaotic Quantum Spectra and Universality of Level Fluctuation Laws". In: *Phys. Rev. Lett.* 52 (1 1984-01), pp. 1–4. DOI: 10.1103/PhysRevLett.52.1. URL: https://link.aps.org/doi/10.1103/PhysRevLett.52.1 (cit. on p. 3).

[37] P. Kos, M. Ljubotina, and T. ž. Prosen. "Many-Body Quantum Chaos: Analytic Connection to Random Matrix Theory". In: *Phys. Rev. X* 8 (2 2018-06), p. 021062. DOI: 10.1103/PhysRevX.8.021062. URL: https://link.aps.org/doi/10.1103/PhysRevX.8.021062 (cit. on pp. 3, 6).

[38] T. Guhr, A. Müller–Groeling, and H. A. Weidenmüller. "Random-matrix theories in quantum physics: common concepts". In: *Physics Reports* 299.4 (1998), pp. 189–425. ISSN: 0370-1573. DOI: https://doi.org/10.1016/S0370-1573(97)00088-4. URL: https://www.sciencedirect.com/science/article/pii/S0370157397000884 (cit. on p. 3).

[39] U. Smilansky. "Quantum chaos and random matrix theory — Some new results". In: *Physica D: Nonlinear Phenomena* 109.1 (1997). Proceedings of the Workshop on Physics and Dynamics between Chaos, Order, and Noise, pp. 153–162. ISSN: 0167-2789. DOI: https://doi.org/10.1016/S0167-2789(97)00166-8. URL: https://www.sciencedirect.com/science/article/pii/S0167278997001668 (cit. on p. 3).

[40] R. Modak and S. Mukerjee. "Finite size scaling in crossover among different random matrix ensembles in microscopic lattice models". In: *New Journal of Physics* 16.9 (2014-09), p. 093016. DOI: 10.1088/1367-2630/16/9/093016. URL: https://dx.doi.org/10.1088/1367-2630/16/9/093016 (cit. on pp. 3, 25).

[41] V. Oganesyan and D. A. Huse. "Localization of interacting fermions at high temperature". In: *Phys. Rev. B* 75 (15 2007-04), p. 155111. DOI: 10.1103/PhysRevB.75.155111. URL: https://link.aps.org/doi/10.1103/PhysRevB.75.155111 (cit. on pp. 3, 6, 25, 42).

[42] Y. Y. Atas et al. "Distribution of the Ratio of Consecutive Level Spacings in Random Matrix Ensembles". In: *Phys. Rev. Lett.* 110 (8 2013-02), p. 084101. DOI: 10.1103/PhysRevLett.110.084101. URL: https://link.aps.org/doi/10.1103/PhysRevLett.110.084101 (cit. on pp. 3, 6, 25).

[43] A. Prakash, J. H. Pixley, and M. Kulkarni. "Universal spectral form factor for many-body localization". In: *Phys. Rev. Res.* 3 (1 2021-02), p. L012019. DOI: 10.1103/PhysRevResearch.3.L012019. URL: https://link.aps.org/doi/10.1103/PhysRevResearch.3.L012019 (cit. on pp. 3, 6, 28).

[44] J. Liu. "Spectral form factors and late time quantum chaos". In: *Phys. Rev. D* 98 (8 2018-10), p. 086026. DOI: 10.1103/PhysRevD.98.086026. URL: https://link.aps.org/doi/10.1103/PhysRevD.98.086026 (cit. on pp. 3, 6, 27, 29, 139).

[45] T. A. Brody et al. "Random-matrix physics: spectrum and strength fluctuations". In: *Rev. Mod. Phys.* 53 (3 1981-07), pp. 385–479. DOI: 10.1103/RevModPhys.53.385. URL: https://link.aps.org/doi/10.1103/RevModPhys.53.385 (cit. on pp. 3, 25).

[46] V. Kota. "Embedded random matrix ensembles for complexity and chaos in finite interacting particle systems". In: *Physics Reports* 347.3 (2001), pp. 223–288. ISSN: 0370-1573. DOI: https://doi.org/10.1016/S0370-1573(00)00113-7. URL: https://www.sciencedirect.com/science/article/pii/S0370157300001137 (cit. on pp. 3, 26).

[47] L. F. Santos. "Integrability of a disordered Heisenberg spin-1/2 chain". In: *Journal of Physics A: Mathematical and General* 37.17 (2004-04), p. 4723. DOI: 10.1088/0305-4470/37/17/004. URL: https://dx.doi.org/10.1088/0305-4470/37/17/004 (cit. on pp. 3, 26).

[48] A. Gubin and L. F. Santos. "Quantum chaos: An introduction via chains of interacting spins 1/2". In: *American Journal of Physics* 80.3 (2012-03), pp. 246–251. ISSN: 0002-9505. DOI: 10.1119/1.3671068. eprint: https://pubs.aip.org/aapt/ajp/article-pdf/80/3/246/13068848/246_1_online.pdf. URL: https://doi.org/10.1119/1.3671068 (cit. on pp. 3, 26).

[49] R. Modak, S. Mukerjee, and S. Ramaswamy. "Universal power law in crossover from integrability to quantum chaos". In: *Phys. Rev. B* 90 (7 2014-08), p. 075152. DOI: 10.1103/PhysRevB.90.075152. URL: https://link.aps.org/doi/10.1103/PhysRevB.90.075152 (cit. on pp. 3, 26).

[50] H. Kim and D. A. Huse. "Ballistic Spreading of Entanglement in a Diffusive Nonintegrable System". In: *Phys. Rev. Lett.* 111 (12 2013-09), p. 127205. DOI: 10.1103/PhysRevLett.111.127205. URL: https://link.aps.org/doi/10.1103/PhysRevLett.111.127205 (cit. on pp. 3, 26, 28).

[51] V. K. B. Kota. *Embedded random matrix ensembles in quantum physics*. Vol. 884. Springer, 2014 (cit. on pp. 3, 26, 28).

[52] D. A. Abanin et al. "Colloquium: Many-body localization, thermalization, and entanglement". In: *Rev. Mod. Phys.* 91 (2 2019-05), p. 021001. DOI: 10.1103/RevModPhys.91.021001. URL: https://link.aps.org/doi/10.1103/RevModPhys.91.021001 (cit. on pp. 3, 5, 26, 28, 42).

[53] J. M. Deutsch. "Quantum statistical mechanics in a closed system". In: *Phys. Rev. A* 43 (4 1991-02), pp. 2046–2049. DOI: 10.1103/PhysRevA.43.2046. URL: https://link.aps.org/doi/10.1103/PhysRevA.43.2046 (cit. on p. 3).

[54] M. Srednicki. "Chaos and quantum thermalization". In: *Phys. Rev. E* 50 (2 1994-08), pp. 888–901. DOI: 10.1103/PhysRevE.50.888. URL: https://link.aps.org/doi/10.1103/PhysRevE.50.888 (cit. on p. 3).

[55] M. Rigol, V. Dunjko, and M. Olshanii. "Thermalization and its mechanism for generic isolated quantum systems". In: *Nature* 452.7189 (2008-04), pp. 854–858. ISSN: 1476-4687. DOI: 10.1038/nature06838. URL: https://doi.org/10.1038/nature06838 (cit. on pp. 3, 4).

[56] C. Gogolin and J. Eisert. "Equilibration, thermalisation, and the emergence of statistical mechanics in closed quantum systems". In: *Reports on Progress in Physics* 79.5 (2016-04), p. 056001. DOI: 10.1088/0034-4885/79/5/056001. URL: https://dx.doi.org/10.1088/0034-4885/79/5/056001 (cit. on p. 3).

[57] F. Borgonovi et al. "Quantum chaos and thermalization in isolated systems of interacting particles". In: *Physics Reports* 626 (2016). Quantum chaos and thermalization in isolated systems of interacting particles, pp. 1–58. ISSN: 0370-1573. DOI: https://doi.org/10.1016/j.physrep.2016.02.005. URL: https://www.sciencedirect.com/science/article/pii/S0370157316000831 (cit. on p. 3).

[58] J. M. Deutsch. "Eigenstate thermalization hypothesis". In: *Rep. Prog. Phys.* 81.8 (2018-07), p. 082001. DOI: 10.1088/1361-6633/aac9f1. URL: https://dx.doi.org/10.1088/1361-6633/aac9f1 (cit. on p. 3).

[59] T. Saha et al. "Thermalization of isolated quantum many-body system and the role of entanglement". In: *Physics Letters A* 509 (2024), p. 129501. ISSN: 0375-9601. DOI: https://doi.org/10.1016/j.physleta.2024.129501. URL: https://www.sciencedirect.com/science/article/pii/S0375960124001968 (cit. on p. 3).

[60] C. Murthy and M. Srednicki. "Bounds on Chaos from the Eigenstate Thermalization Hypothesis". In: *Phys. Rev. Lett.* 123 (23 2019-12), p. 230606. DOI: 10.1103/PhysRevLett.123.230606. URL: https://link.aps.org/doi/10.1103/PhysRevLett.123.230606 (cit. on p. 3).

[61] M. Ueda. "Quantum equilibration, thermalization and prethermalization in ultracold atoms". In: *Nature Reviews Physics* 2.12 (2020), pp. 669–681. DOI: 10.1038/s42254-020-0237-x. URL: https://doi.org/10.1038/s42254-020-0237-x (cit. on p. 3).

[62] M. Alishahiha and M. J. Vasli. *Eigenstate Thermalization Hypothesis: A Short Review*. 2025. arXiv: 2501.07243 [hep-th]. URL: https://arxiv.org/abs/2501.07243 (cit. on p. 3).

[63] A. M. Kaufman et al. "Quantum thermalization through entanglement in an isolated many-body system". In: *Science* 353.6301 (2016), pp. 794–800. DOI: 10.1126/science.aaf6725. eprint: https://www.science.org/doi/pdf/10.1126/science.aaf6725. URL: https://www.science.org/doi/abs/10.1126/science.aaf6725 (cit. on p. 4).

[64] C. Neill et al. "Ergodic dynamics and thermalization in an isolated quantum system". In: *Nature Physics* 12.11 (2016), pp. 1037–1041. DOI: 10.1038/nphys3830. URL: https://doi.org/10.1038/nphys3830 (cit. on p. 4).

[65] Q.-Q. Wang et al. "Experimental verification of generalized eigenstate thermalization hypothesis in an integrable system". In: *Light: Science Applications* 11.1 (2022), p. 194. DOI: 10.1038/s41377-022-00887-5. URL: https://doi.org/10.1038/s41377-022-00887-5 (cit. on p. 4).

[66] F. Kranzl et al. "Experimental Observation of Thermalization with Noncommuting Charges". In: *PRX Quantum* 4 (2 2023-04), p. 020318. DOI: 10.1103/PRXQuantum.4.020318. URL: https://link.aps.org/doi/10.1103/PRXQuantum.4.020318 (cit. on p. 4).

[67] J. P. Pekola and B. Karimi. "Quantum thermalization via multiwave mixing". In: *Phys. Rev. Res.* 6 (4 2024-10), p. L042023. DOI: 10.1103/PhysRevResearch.6.L042023. URL: https://link.aps.org/doi/10.1103/PhysRevResearch.6.L042023 (cit. on p. 4).

[68] C. Bertoni et al. "Typical thermalization of low-entanglement states". In: *Communications Physics* 8.1 (2025), p. 301. DOI: 10.1038/s42005-025-02161-7. URL: https://doi.org/10.1038/s42005-025-02161-7 (cit. on p. 4).

[69] S. Goldstein et al. "Canonical Typicality". In: *Phys. Rev. Lett.* 96 (5 2006-02), p. 050403. DOI: 10.1103/PhysRevLett.96.050403. URL: https://link.aps.org/doi/10.1103/PhysRevLett.96.050403 (cit. on p. 4).

[70] S. Popescu, A. J. Short, and A. Winter. "Entanglement and the foundations of statistical mechanics". In: *Nature Physics* 2.11 (2006), pp. 754–758. DOI: 10.1038/nphys444. URL: https://doi.org/10.1038/nphys444 (cit. on p. 4).

[71] R. Nandkishore and D. A. Huse. "Many-Body Localization and Thermalization in Quantum Statistical Mechanics". In: *Annual Review of Condensed Matter Physics* 6.1 (2015), pp. 15–38. DOI: 10.1146/annurev-conmatphys-031214-014726. URL: https://doi.org/10.1146/annurev-conmatphys-031214-014726 (cit. on pp. 4, 5).

[72] M. Gring et al. "Relaxation and Prethermalization in an Isolated Quantum System". In: *Science* 337.6100 (2012), pp. 1318–1322. DOI: 10.1126/science.1224953. eprint: https://www.science.org/doi/pdf/10.1126/science.1224953. URL: https://www.science.org/doi/abs/10.1126/science.1224953 (cit. on p. 4).

[73] T. Kinoshita, T. Wenger, and D. S. Weiss. "A quantum Newton's cradle". In: *Nature* 440.7086 (2006), pp. 900–903. DOI: 10.1038/nature04693. URL: https://doi.org/10.1038/nature04693 (cit. on p. 4).

[74] P. W. Anderson. "Absence of Diffusion in Certain Random Lattices". In: *Phys. Rev.* 109 (5 1958-03), pp. 1492–1505. DOI: 10.1103/PhysRev.109.1492. URL: https://link.aps.org/doi/10.1103/PhysRev.109.1492 (cit. on pp. 4, 5).

[75] C. Guan and X. Guan. "A brief introduction to Anderson Localization". In: 2019. URL: https://api.semanticscholar.org/CorpusID:211195988 (cit. on p. 5).

[76] A. Scardicchio and T. Thiery. *Perturbation theory approaches to Anderson and Many-Body Localization: some lecture notes*. 2017. arXiv: 1710.01234 [cond-mat.dis-nn]. URL: https://arxiv.org/abs/1710.01234 (cit. on p. 5).

[77] G. Modugno. "Anderson localization in Bose–Einstein condensates". In: *Reports on Progress in Physics* 73.10 (2010-09), p. 102401. DOI: 10.1088/0034-4885/73/10/102401. URL: https://dx.doi.org/10.1088/0034-4885/73/10/102401 (cit. on p. 5).

[78] J. Billy et al. "Direct observation of Anderson localization of matter waves in a controlled disorder". In: *Nature* 453.7197 (2008), pp. 891–894. DOI: 10.1038/nature07000. URL: https://doi.org/10.1038/nature07000 (cit. on p. 5).

[79] G. Roati et al. "Anderson localization of a non-interacting Bose–Einstein condensate". In: *Nature* 453.7197 (2008), pp. 895–898 (cit. on pp. 5, 74).

[80] S. S. Kondov et al. "Three-Dimensional Anderson Localization of Ultracold Matter". In: *Science* 334.6052 (2011), pp. 66–68. DOI: 10.1126/science.1209019. eprint: https://www.science.org/doi/pdf/10.1126/science.1209019. URL: https://www.science.org/doi/abs/10.1126/science.1209019 (cit. on p. 5).

[81] F. Jendrzejewski et al. "Three-dimensional localization of ultracold atoms in an optical disordered potential". In: *Nature Physics* 8.5 (2012), pp. 398–403. DOI: 10.1038/nphys2256. URL: https://doi.org/10.1038/nphys2256 (cit. on p. 5).

[82] G. Semeghini et al. "Measurement of the mobility edge for 3D Anderson localization". In: *Nature Physics* 11.7 (2015), pp. 554–559. DOI: 10.1038/nphys3339. URL: https://doi.org/10.1038/nphys3339 (cit. on p. 5).

[83] C. Hainaut et al. "Experimental realization of an ideal Floquet disordered system". In: *New Journal of Physics* 21.3 (2019-03), p. 035008. DOI: 10.1088/1367-2630/ab0a79. URL: https://dx.doi.org/10.1088/1367-2630/ab0a79 (cit. on p. 5).

[84] D. S. Wiersma et al. "Localization of light in a disordered medium". In: *Nature* 390.6661 (1997), pp. 671–673. DOI: 10.1038/37757. URL: https://doi.org/10.1038/37757 (cit. on p. 5).

[85] M. Störzer et al. "Observation of the Critical Regime Near Anderson Localization of Light". In: *Phys. Rev. Lett.* 96 (6 2006-02), p. 063904. DOI: 10.1103/PhysRevLett.96.063904. URL: https://link.aps.org/doi/10.1103/PhysRevLett.96.063904 (cit. on p. 5).

[86] T. Schwartz et al. "Transport and Anderson localization in disordered two-dimensional photonic lattices". In: *Nature* 446.7131 (2007), pp. 52–55 (cit. on p. 5).

[87] Y. Lahini et al. "Anderson Localization and Nonlinearity in One-Dimensional Disordered Photonic Lattices". In: *Phys. Rev. Lett.* 100 (1 2008-01), p. 013906. DOI: 10.1103/PhysRevLett.100.013906. URL: https://link.aps.org/doi/10.1103/PhysRevLett.100.013906 (cit. on p. 5).

[88] M. Segev, Y. Silberberg, and D. N. Christodoulides. "Anderson localization of light". In: *Nature Photonics* 7.3 (2013), pp. 197–204. DOI: 10.1038/nphoton.2013.30. URL: https://doi.org/10.1038/nphoton.2013.30 (cit. on p. 5).

[89] T. Sperling et al. "Direct determination of the transition to localization of light in three dimensions". In: *Nature Photonics* 7.1 (2013), pp. 48–52. DOI: 10.1038/nphoton.2012.313. URL: https://doi.org/10.1038/nphoton.2012.313 (cit. on p. 5).

[90] L. Fleishman and P. W. Anderson. "Interactions and the Anderson transition". In: *Phys. Rev. B* 21 (6 1980-03), pp. 2366–2377. DOI: 10.1103/PhysRevB.21.2366. URL: https://link.aps.org/doi/10.1103/PhysRevB.21.2366 (cit. on p. 5).

[91] B. L. Altshuler et al. "Quasiparticle Lifetime in a Finite System: A Nonperturbative Approach". In: *Phys. Rev. Lett.* 78 (14 1997-04), pp. 2803–2806. DOI: 10.1103/PhysRevLett.78.2803. URL: https://link.aps.org/doi/10.1103/PhysRevLett.78.2803 (cit. on p. 5).

[92] D. Basko, I. Aleiner, and B. Altshuler. "Metal–insulator transition in a weakly interacting many-electron system with localized single-particle states". In: *Ann. Phys.* 321.5 (2006), pp. 1126–1205. ISSN: 0003-4916. DOI: https://doi.org/10.1016/j.aop.2005.11.014. URL: https://www.sciencedirect.com/science/article/pii/S0003491605002630 (cit. on p. 5).

[93] F. Alet and N. Laflorencie. "Many-body localization: An introduction and selected topics". In: *Comptes Rendus Physique* 19.6 (2018), pp. 498–525. ISSN: 1631-0705. DOI: https://doi.org/10.1016/j.crhy.2018.03.003. URL: https://www.sciencedirect.com/science/article/pii/S163107051830032X (cit. on p. 5).

[94] J. H. Bardarson, F. Pollmann, and J. E. Moore. "Unbounded Growth of Entanglement in Models of Many-Body Localization". In: *Phys. Rev. Lett.* 109 (1 2012-07), p. 017202. DOI: 10.1103/PhysRevLett.109.017202. URL: https://link.aps.org/doi/10.1103/PhysRevLett.109.017202 (cit. on p. 5).

[95] M. Serbyn, Z. Papi ć, and D. A. Abanin. "Universal Slow Growth of Entanglement in Interacting Strongly Disordered Systems". In: *Phys. Rev. Lett.* 110 (26 2013-06), p. 260601. DOI: 10.1103/PhysRevLett.110.260601. URL: https://link.aps.org/doi/10.1103/PhysRevLett.110.260601 (cit. on p. 5).

[96] B. Bauer and C. Nayak. "Area laws in a many-body localized state and its implications for topological order". In: *Journal of Statistical Mechanics: Theory and Experiment* 2013.09 (2013-09), P09005. DOI: 10.1088/1742-5468

/2013/09/p09005. URL: https://doi.org/10.1088/1742-5468/2013/09/p09005 (cit. on p. 5).

[97] M. Žnidari č, T. ž. Prosen, and P. Prelov šek. "Many-body localization in the Heisenberg XXZ magnet in a random field". In: *Phys. Rev. B* 77 (6 2008-02), p. 064426. DOI: 10.1103/PhysRevB.77.064426. URL: https://link.aps.org/doi/10.1103/PhysRevB.77.064426 (cit. on pp. 5, 6).

[98] M. Serbyn, Z. Papi ć, and D. A. Abanin. "Local Conservation Laws and the Structure of the Many-Body Localized States". In: *Phys. Rev. Lett.* 111 (12 2013-09), p. 127201. DOI: 10.1103/PhysRevLett.111.127201. URL: https://link.aps.org/doi/10.1103/PhysRevLett.111.127201 (cit. on p. 5).

[99] D. A. Abanin and Z. Papić. "Recent progress in many-body localization". In: *Ann. Phys. (Berlin, Ger.)* 529.7 (2017), p. 1700169. DOI: https://doi.org/10.1002/andp.201700169. URL: https://onlinelibrary.wiley.com/doi/abs/10.1002/andp.201700169 (cit. on pp. 5, 42).

[100] D. A. Huse, R. Nandkishore, and V. Oganesyan. "Phenomenology of fully many-body-localized systems". In: *Phys. Rev. B* 90 (17 2014-11), p. 174202. DOI: 10.1103/PhysRevB.90.174202. URL: https://link.aps.org/doi/10.1103/PhysRevB.90.174202 (cit. on p. 5).

[101] A. Chandran et al. "Constructing local integrals of motion in the many-body localized phase". In: *Phys. Rev. B* 91 (8 2015-02), p. 085425. DOI: 10.1103/PhysRevB.91.085425. URL: https://link.aps.org/doi/10.1103/PhysRevB.91.085425 (cit. on p. 5).

[102] M. Schreiber et al. "Observation of many-body localization of interacting fermions in a quasirandom optical lattice". In: *Science* 349.6250 (2015), pp. 842–845. DOI: 10.1126/science.aaa7432. URL: https://www.science.org/doi/abs/10.1126/science.aaa7432 (cit. on pp. 6, 47).

[103] J. Smith et al. "Many-body localization in a quantum simulator with programmable random disorder". In: *Nat. Phys.* 12.10 (2016), pp. 907–911. DOI: 10.1038/nphys3783. URL: https://doi.org/10.1038/nphys3783 (cit. on pp. 6, 20).

[104] J.-y. Choi et al. "Exploring the many-body localization transition in two dimensions". In: *Science* 352.6293 (2016), pp. 1547–1552. DOI: 10.1126/science.aaf8834. eprint: https://www.science.org/doi/pdf/10.112

6/science.aaf8834. URL: https://www.science.org/doi/abs/10.1126/science.aaf8834 (cit. on pp. 6, 20).

[105] P. Bordia et al. "Coupling Identical one-dimensional Many-Body Localized Systems". In: *Phys. Rev. Lett.* 116 (14 2016-04), p. 140401. DOI: 10.1103/PhysRevLett.116.140401. URL: https://link.aps.org/doi/10.1103/PhysRevLett.116.140401 (cit. on p. 6).

[106] P. Roushan et al. "Spectroscopic signatures of localization with interacting photons in superconducting qubits". In: *Science* 358.6367 (2017), pp. 1175–1179. DOI: 10.1126/science.aao1401 (cit. on p. 6).

[107] K. Xu et al. "Emulating Many-Body Localization with a Superconducting Quantum Processor". In: *Phys. Rev. Lett.* 120 (5 2018-02), p. 050507. DOI: 10.1103/PhysRevLett.120.050507. URL: https://link.aps.org/doi/10.1103/PhysRevLett.120.050507 (cit. on p. 6).

[108] K. X. Wei, C. Ramanathan, and P. Cappellaro. "Exploring Localization in Nuclear Spin Chains". In: *Phys. Rev. Lett.* 120 (7 2018-02), p. 070501. DOI: 10.1103/PhysRevLett.120.070501. URL: https://link.aps.org/doi/10.1103/PhysRevLett.120.070501 (cit. on p. 6).

[109] A. Lukin et al. "Probing entanglement in a many-body–localized system". In: *Science* 364.6437 (2019), pp. 256–260. DOI: 10.1126/science.aau0818 (cit. on p. 6).

[110] M. Gong et al. "Experimental characterization of the quantum many-body localization transition". In: *Phys. Rev. Res.* 3 (3 2021-07), p. 033043. DOI: 10.1103/PhysRevResearch.3.033043. URL: https://link.aps.org/doi/10.1103/PhysRevResearch.3.033043 (cit. on p. 6).

[111] A. Pal and D. A. Huse. "Many-body localization phase transition". In: *Phys. Rev. B* 82 (17 2010-11), p. 174411. DOI: 10.1103/PhysRevB.82.174411. URL: https://link.aps.org/doi/10.1103/PhysRevB.82.174411 (cit. on pp. 6, 42).

[112] M. Prasad et al. "Transition to chaos in extended systems and their quantum impurity models". In: *Journal of Physics A: Mathematical and Theoretical* 57.1 (2023-12), p. 015308. DOI: 10.1088/1751-8121/ad119c. URL: https://dx.doi.org/10.1088/1751-8121/ad119c (cit. on pp. 6, 26, 28).

[113] M. Prasad et al. "Long-ranged spectral correlations in eigenstate phases". In: *Journal of Physics A: Mathematical and Theoretical* 57.1 (2023-12), p. 015003. DOI: 10.1088/1751-8121/ad1342. URL: https://dx.doi.org/10.1088/1751-8121/ad1342 (cit. on p. 6).

[114] M. Serbyn, Z. Papi ć, and D. A. Abanin. "Quantum quenches in the many-body localized phase". In: *Phys. Rev. B* 90 (17 2014-11), p. 174302. DOI: 10.1103/PhysRevB.90.174302. URL: https://link.aps.org/doi/10.1103/PhysRevB.90.174302 (cit. on p. 6).

[115] H. P. Lüschen et al. "Observation of Slow Dynamics near the Many-Body Localization Transition in One-Dimensional Quasiperiodic Systems". In: *Phys. Rev. Lett.* 119 (26 2017-12), p. 260401. DOI: 10.1103/PhysRevLett.119.260401. URL: https://link.aps.org/doi/10.1103/PhysRevLett.119.260401 (cit. on p. 6).

[116] V. Ros and M. Müller. "Remanent Magnetization: Signature of Many-Body Localization in Quantum Antiferromagnets". In: *Phys. Rev. Lett.* 118 (23 2017-06), p. 237202. DOI: 10.1103/PhysRevLett.118.237202. URL: https://link.aps.org/doi/10.1103/PhysRevLett.118.237202 (cit. on p. 6).

[117] P. Prelovšek et al. "Density correlations and transport in models of many-body localization". In: *Annalen der Physik* 529.7 (2017), p. 1600362. DOI: https://doi.org/10.1002/andp.201600362. eprint: https://onlinelibrary.wiley.com/doi/pdf/10.1002/andp.201600362. URL: https://onlinelibrary.wiley.com/doi/abs/10.1002/andp.201600362 (cit. on p. 6).

[118] A. Chakraborty, P. Gorantla, and R. Sensarma. "Memories of initial states and density imbalance in the dynamics of noninteracting and interacting disordered systems". In: *Phys. Rev. B* 102 (22 2020-12), p. 224306. DOI: 10.1103/PhysRevB.102.224306. URL: https://link.aps.org/doi/10.1103/PhysRevB.102.224306 (cit. on p. 6).

[119] P. Sierant et al. "Many-body localization in the age of classical computing*". In: *Reports on Progress in Physics* 88.2 (2025-01), p. 026502. DOI: 10.1088/1361-6633/ad9756. URL: https://dx.doi.org/10.1088/1361-6633/ad9756 (cit. on pp. 6, 28).

[120] P. Sierant and J. Zakrzewski. "Challenges to observation of many-body localization". In: *Phys. Rev. B* 105 (22 2022-06), p. 224203. DOI: 10.1103/PhysRevB.105.224203. URL: https://link.aps.org/doi/10.1103/PhysRevB.105.224203 (cit. on pp. 6, 47).

[121] D. Guo, T. Hu, and J. Hong. "Localization and dynamics in one-dimensional and two-dimensional Gaussian disordered quantum spin systems". In: *Results in Physics* 76 (2025), p. 108407. ISSN: 2211-3797. DOI: https://doi.

org/10.1016/j.rinp.2025.108407. URL: https://www.sciencedirect.com/science/article/pii/S2211379725003018 (cit. on p. 6).

[122] J. Z. Imbrie. "On Many-Body Localization for Quantum Spin Chains". In: *Journal of Statistical Physics* 163.5 (2016), pp. 998–1048. DOI: 10.1007/s10955-016-1508-x. URL: https://doi.org/10.1007/s10955-016-1508-x (cit. on p. 6).

[123] W. D. Roeck et al. *Absence of Normal Heat Conduction in Strongly Disordered Interacting Quantum Chains*. 2025. arXiv: 2408.04338 [math-ph]. URL: https://arxiv.org/abs/2408.04338 (cit. on p. 6).

[124] H.-P. Breuer and F. Petruccione. *The theory of open quantum systems*. Oxford University Press, 2002 (cit. on pp. 6, 11, 17, 18, 147).

[125] H. J. Carmichael. *Statistical methods in quantum optics 1: master equations and Fokker-Planck equations*. Vol. 1. Springer Science & Business Media, 1999 (cit. on pp. 6, 11, 17, 147).

[126] A. Rivas and S. F. Huelga. *Open quantum systems*. Vol. 10. Springer, 2012 (cit. on pp. 6, 11).

[127] Y. Ashida, Z. Gong, and M. Ueda. "Non-Hermitian physics". In: *Adv. Phys.* 69.3 (2020), pp. 249–435. DOI: 10.1080/00018732.2021.1876991. URL: https://doi.org/10.1080/00018732.2021.1876991 (cit. on pp. 6, 24).

[128] J. Dalibard, Y. Castin, and K. Mølmer. "Wave-function approach to dissipative processes in quantum optics". In: *Phys. Rev. Lett.* 68 (5 1992-02), pp. 580–583. DOI: 10.1103/PhysRevLett.68.580. URL: https://link.aps.org/doi/10.1103/PhysRevLett.68.580 (cit. on pp. 6, 41, 148).

[129] K. Mølmer, Y. Castin, and J. Dalibard. "Monte Carlo wave-function method in quantum optics". In: *J. Opt. Soc. Am. B* 10.3 (1993-03), pp. 524–538. DOI: 10.1364/JOSAB.10.000524. URL: http://opg.optica.org/josab/abstract.cfm?URI=josab-10-3-524 (cit. on pp. 6, 41, 148).

[130] R. Dum, P. Zoller, and H. Ritsch. "Monte Carlo simulation of the atomic master equation for spontaneous emission". In: *Phys. Rev. A* 45 (7 1992-04), p. 4879. DOI: 10.1103/PhysRevA.45.4879. URL: https://link.aps.org/doi/10.1103/PhysRevA.45.4879 (cit. on pp. 6, 41, 148).

[131] K. Mølmer and Y. Castin. "Monte Carlo wavefunctions in quantum optics". In: *Quantum Semiclass. Opt.* 8.1 (1996-02), p. 49. DOI: 10.1088/1355-5111/8/1/007. URL: https://doi.org/10.1088/1355-5111/8/1/007 (cit. on pp. 6, 41, 148).

[132] M. B. Plenio and P. L. Knight. "The quantum-jump approach to dissipative dynamics in quantum optics". In: *Rev. Mod. Phys.* 70 (1 1998-01), pp. 101–144. DOI: 10.1103/RevModPhys.70.101. URL: https://link.aps.org/doi/10.1103/RevModPhys.70.101 (cit. on pp. 6, 41, 148).

[133] A. J. Daley. "Quantum trajectories and open many-body quantum systems". In: *Adv. Phys.* 63.2 (2014), pp. 77–149. DOI: 10.1080/00018732.2014.933502. URL: https://doi.org/10.1080/00018732.2014.933502 (cit. on pp. 6, 41, 147, 148).

[134] C. M. Bender. "Making sense of non-Hermitian Hamiltonians". In: *Reports on Progress in Physics* 70.6 (2007-05), p. 947. DOI: 10.1088/0034-4885/70/6/R03. URL: https://dx.doi.org/10.1088/0034-4885/70/6/R03 (cit. on p. 6).

[135] N. Moiseyev. *Non-Hermitian Quantum Mechanics*. Cambridge University Press, 2011 (cit. on p. 6).

[136] K. G. Zloshchastiev and A. Sergi. "Comparison and unification of non-Hermitian and Lindblad approaches with applications to open quantum optical systems". In: *J. Mod. Opt.* 61.16 (2014), pp. 1298–1308. DOI: 10.1080/09500340.2014.930528. URL: https://doi.org/10.1080/09500340.2014.930528 (cit. on pp. 6, 39, 149).

[137] F. Minganti et al. "Quantum exceptional points of non-Hermitian Hamiltonians and Liouvillians: The effects of quantum jumps". In: *Phys. Rev. A* 100 (6 2019-12), p. 062131. DOI: 10.1103/PhysRevA.100.062131. URL: https://link.aps.org/doi/10.1103/PhysRevA.100.062131 (cit. on pp. 6, 39).

[138] F. Minganti et al. "Hybrid-Liouvillian formalism connecting exceptional points of non-Hermitian Hamiltonians and Liouvillians via postselection of quantum trajectories". In: *Phys. Rev. A* 101 (6 2020-06), p. 062112. DOI: 10.1103/PhysRevA.101.062112. URL: https://link.aps.org/doi/10.1103/PhysRevA.101.062112 (cit. on pp. 6, 39, 151, 152).

[139] J. C. Bergquist et al. "Observation of Quantum Jumps in a Single Atom". In: *Phys. Rev. Lett.* 57 (14 1986-10), pp. 1699–1702. DOI: 10.1103/PhysRevLett.57.1699. URL: https://link.aps.org/doi/10.1103/PhysRevLett.57.1699 (cit. on pp. 6, 39).

[140] T. Sauter et al. "Observation of Quantum Jumps". In: *Phys. Rev. Lett.* 57 (14 1986-10), pp. 1696–1698. DOI: 10.1103/PhysRevLett.57.1696. URL: https://link.aps.org/doi/10.1103/PhysRevLett.57.1696 (cit. on pp. 6, 39).

[141] Z. K. Minev et al. "To catch and reverse a quantum jump mid-flight". In: *Nature* 570.7760 (2019), pp. 200–204. DOI: 10.1038/s41586-019-1287-z. URL: https://doi.org/10.1038/s41586-019-1287-z (cit. on pp. 6, 39).

[142] W. Chen et al. "Quantum Jumps in the Non-Hermitian Dynamics of a Superconducting Qubit". In: *Phys. Rev. Lett.* 127 (14 2021-09), p. 140504. DOI: 10.1103/PhysRevLett.127.140504. URL: https://link.aps.org/doi/10.1103/PhysRevLett.127.140504 (cit. on pp. 6, 39).

[143] K. W. Murch et al. "Cavity-Assisted Quantum Bath Engineering". In: *Phys. Rev. Lett.* 109 (18 2012-10), p. 183602. DOI: 10.1103/PhysRevLett.109.183602. URL: https://link.aps.org/doi/10.1103/PhysRevLett.109.183602 (cit. on p. 6).

[144] M. E. Kimchi-Schwartz et al. "Stabilizing Entanglement via Symmetry-Selective Bath Engineering in Superconducting Qubits". In: *Phys. Rev. Lett.* 116 (24 2016-06), p. 240503. DOI: 10.1103/PhysRevLett.116.240503. URL: https://link.aps.org/doi/10.1103/PhysRevLett.116.240503 (cit. on p. 6).

[145] T. E. Lee and C.-K. Chan. "Heralded Magnetism in Non-Hermitian Atomic Systems". In: *Phys. Rev. X* 4 (4 2014-10), p. 041001. DOI: 10.1103/PhysRevX.4.041001. URL: https://link.aps.org/doi/10.1103/PhysRevX.4.041001 (cit. on pp. 6, 20).

[146] J. T. Barreiro et al. "Experimental multiparticle entanglement dynamics induced by decoherence". In: *Nature Physics* 6.12 (2010), pp. 943–946. DOI: 10.1038/nphys1781 (cit. on p. 6).

[147] H. Krauter et al. "Entanglement Generated by Dissipation and Steady State Entanglement of Two Macroscopic Objects". In: *Phys. Rev. Lett.* 107 (8 2011-08), p. 080503. DOI: 10.1103/PhysRevLett.107.080503. URL: https://link.aps.org/doi/10.1103/PhysRevLett.107.080503 (cit. on p. 6).

[148] T. Tomita et al. "Observation of the Mott insulator to superfluid crossover of a driven-dissipative Bose-Hubbard system". In: *Science Advances* 3.12 (2017), e1701513. DOI: 10.1126/sciadv.1701513. eprint: https://www.science.org/doi/pdf/10.1126/sciadv.1701513. URL: https://www.science.org/doi/abs/10.1126/sciadv.1701513 (cit. on p. 6).

[149] P. Kongkhambut et al. "Observation of a continuous time crystal". In: *Science* 377.6606 (2022), pp. 670–673. DOI: 10.1126/science.abo3382. eprint: https://www.science.org/doi/pdf/10.1126/science.abo3382. URL: https://www.science.org/doi/abs/10.1126/science.abo3382 (cit. on p. 6).

[150] C. Noel et al. "Measurement-induced quantum phases realized in a trapped-ion quantum computer". In: *Nature Physics* 18.7 (2022), pp. 760–764. DOI: 10.1038/s41567-022-01619-7. URL: https://doi.org/10.1038/s41567-022-01619-7 (cit. on p. 6).

[151] J. M. Koh et al. "Measurement-induced entanglement phase transition on a superconducting quantum processor with mid-circuit readout". In: *Nature Physics* 19.9 (2023), pp. 1314–1319. DOI: 10.1038/s41567-023-02076-6. URL: https://doi.org/10.1038/s41567-023-02076-6 (cit. on p. 6).

[152] M. Müller et al. *Engineered Open Systems and Quantum Simulations with Atoms and Ions*. 2012. DOI: 10.48550/ARXIV.1203.6595. URL: https://arxiv.org/abs/1203.6595 (cit. on p. 7).

[153] S. Denisov et al. "Universal Spectra of Random Lindblad Operators". In: *Phys. Rev. Lett.* 123 (14 2019-10), p. 140403. DOI: 10.1103/PhysRevLett.123.140403. URL: https://link.aps.org/doi/10.1103/PhysRevLett.123.140403 (cit. on p. 7).

[154] L. Sá, P. Ribeiro, and T. Prosen. "Spectral and steady-state properties of random Liouvillians". In: *Journal of Physics A: Mathematical and Theoretical* 53.30 (2020-07), p. 305303. DOI: 10.1088/1751-8121/ab9337. URL: https://doi.org/10.1088/1751-8121/ab9337 (cit. on p. 7).

[155] K. G. Makris et al. "Beam Dynamics in $\mathcal{PT}$ Symmetric Optical Lattices". In: *Phys. Rev. Lett.* 100 (10 2008-03), p. 103904. DOI: 10.1103/PhysRevLett.100.103904. URL: https://link.aps.org/doi/10.1103/PhysRevLett.100.103904 (cit. on p. 7).

[156] V. V. Konotop, J. Yang, and D. A. Zezyulin. "Nonlinear waves in $\mathcal{PT}$-symmetric systems". In: *Rev. Mod. Phys.* 88 (3 2016-07), p. 035002. DOI: 10.1103/RevModPhys.88.035002. URL: https://link.aps.org/doi/10.1103/RevModPhys.88.035002 (cit. on p. 7).

[157] R. El-Ganainy et al. "Non-Hermitian physics and PT symmetry". In: *Nature Physics* 14.1 (2018-01), pp. 11–19. ISSN: 1745-2481. DOI: 10.1038/nphys4323. URL: https://doi.org/10.1038/nphys4323 (cit. on pp. 7, 20, 24, 25).

[158] S. K. Gupta et al. "Parity-Time Symmetry in Non-Hermitian Complex Optical Media". In: *Advanced Materials* 32.27 (2020), p. 1903639. DOI: https://doi.org/10.1002/adma.201903639. URL: https://onlinelibrary.wiley.com/doi/abs/10.1002/adma.201903639 (cit. on pp. 7, 20, 24).

[159] A. F. Tzortzakakis, K. G. Makris, and E. N. Economou. "Non-Hermitian disorder in two-dimensional optical lattices". In: *Phys. Rev. B* 101 (1 2020-01), p. 014202. DOI: 10.1103/PhysRevB.101.014202. URL: https://link.aps.org/doi/10.1103/PhysRevB.101.014202 (cit. on p. 7).

[160] J. M. Zeuner et al. "Observation of a Topological Transition in the Bulk of a Non-Hermitian System". In: *Phys. Rev. Lett.* 115 (4 2015-07), p. 040402. DOI: 10.1103/PhysRevLett.115.040402. URL: https://link.aps.org/doi/10.1103/PhysRevLett.115.040402 (cit. on p. 7).

[161] Z. Gong et al. "Topological Phases of Non-Hermitian Systems". In: *Phys. Rev. X* 8 (3 2018-09), p. 031079. DOI: 10.1103/PhysRevX.8.031079. URL: https://link.aps.org/doi/10.1103/PhysRevX.8.031079 (cit. on p. 7).

[162] H. Shen, B. Zhen, and L. Fu. "Topological Band Theory for Non-Hermitian Hamiltonians". In: *Phys. Rev. Lett.* 120 (14 2018-04), p. 146402. DOI: 10.1103/PhysRevLett.120.146402. URL: https://link.aps.org/doi/10.1103/PhysRevLett.120.146402 (cit. on p. 7).

[163] M. A. Bandres et al. "Topological insulator laser: Experiments". In: *Science* 359.6381 (2018), eaar4005. DOI: 10.1126/science.aar4005. URL: https://www.science.org/doi/abs/10.1126/science.aar4005 (cit. on p. 7).

[164] K. Kawabata et al. "Symmetry and Topology in Non-Hermitian Physics". In: *Phys. Rev. X* 9 (4 2019-10), p. 041015. DOI: 10.1103/PhysRevX.9.041015. URL: https://link.aps.org/doi/10.1103/PhysRevX.9.041015 (cit. on pp. 7, 31, 32).

[165] A. Ghatak et al. "Observation of non-Hermitian topology and its bulk-edge correspondence in an active mechanical metamaterial". In: *Proceedings of the National Academy of Sciences* 117.47 (2020), pp. 29561–29568. DOI: 10.1073/pnas.2010580117. URL: https://www.pnas.org/doi/abs/10.1073/pnas.2010580117 (cit. on p. 7).

[166] R. Su et al. "Direct measurement of a non-Hermitian topological invariant in a hybrid light-matter system". In: *Science Advances* 7.45 (2021), eabj8905. DOI: 10.1126/sciadv.abj8905. URL: https://www.science.org/doi/abs/10.1126/sciadv.abj8905 (cit. on p. 7).

[167] X. Zhang et al. "Observation of higher-order non-Hermitian skin effect". In: *Nature Communications* 12.1 (2021-09), p. 5377. ISSN: 2041-1723. DOI: 10.1038/s41467-021-25716-y. URL: https://doi.org/10.1038/s41467-021-25716-y (cit. on pp. 7, 20).

[168] L.-Z. Tang et al. "Topological Anderson insulators in two-dimensional non-Hermitian disordered systems". In: *Phys. Rev. A* 101 (6 2020-06), p. 063612. DOI: 10.1103/PhysRevA.101.063612. URL: https://link.aps.org/doi/10.1103/PhysRevA.101.063612 (cit. on p. 7).

[169] K. Kawabata, K. Shiozaki, and S. Ryu. "Many-body topology of non-Hermitian systems". In: *Phys. Rev. B* 105 (16 2022-04), p. 165137. DOI: 10.1103/PhysRevB.105.165137. URL: https://link.aps.org/doi/10.1103/PhysRevB.105.165137 (cit. on p. 7).

[170] L.-Z. Tang et al. "Localization and topological transitions in non-Hermitian quasiperiodic lattices". In: *Phys. Rev. A* 103 (3 2021-03), p. 033325. DOI: 10.1103/PhysRevA.103.033325. URL: https://link.aps.org/doi/10.1103/PhysRevA.103.033325 (cit. on p. 7).

[171] S.-B. Zhang et al. "Symmetry breaking and spectral structure of the interacting Hatano-Nelson model". In: *Phys. Rev. B* 106 (12 2022-09), p. L121102. DOI: 10.1103/PhysRevB.106.L121102. URL: https://link.aps.org/doi/10.1103/PhysRevB.106.L121102 (cit. on p. 7).

[172] H. P. Lüschen et al. "Signatures of Many-Body Localization in a Controlled Open Quantum System". In: *Phys. Rev. X* 7 (1 2017-03), p. 011034. DOI: 10.1103/PhysRevX.7.011034. URL: https://link.aps.org/doi/10.1103/PhysRevX.7.011034 (cit. on p. 7).

[173] I. Vakulchyk et al. "Signatures of many-body localization in steady states of open quantum systems". In: *Phys. Rev. B* 98 (2 2018-07), p. 020202. DOI: 10.1103/PhysRevB.98.020202. URL: https://link.aps.org/doi/10.1103/PhysRevB.98.020202 (cit. on p. 7).

[174] X. Xu, C. Guo, and D. Poletti. "Interplay of interaction and disorder in the steady state of an open quantum system". In: *Phys. Rev. B* 97 (14 2018-04), p. 140201. DOI: 10.1103/PhysRevB.97.140201. URL: https://link.aps.org/doi/10.1103/PhysRevB.97.140201 (cit. on p. 7).

[175] M. H. Fischer, M. Maksymenko, and E. Altman. "Dynamics of a Many-Body-Localized System Coupled to a Bath". In: *Phys. Rev. Lett.* 116 (16 2016-04), p. 160401. DOI: 10.1103/PhysRevLett.116.160401. URL: https://link.aps.org/doi/10.1103/PhysRevLett.116.160401 (cit. on p. 7).

[176] M. V. Medvedyeva, T. Prosen, and M. Žnidarič. "Influence of dephasing on many-body localization". In: *Phys. Rev. B* 93 (9 2016-03), p. 094205. DOI: 10.1103/PhysRevB.93.094205. URL: https://link.aps.org/doi/10.1103/PhysRevB.93.094205 (cit. on p. 7).

[177] B. Everest et al. "Role of interactions in a dissipative many-body localized system". In: *Phys. Rev. B* 95 (2 2017-01), p. 024310. DOI: 10.1103/PhysRevB.95.024310. URL: https://link.aps.org/doi/10.1103/PhysRevB.95.024310 (cit. on p. 7).

[178] E. van Nieuwenburg et al. "Dynamics of many-body localization in the presence of particle loss". In: *Quantum Sci. Technol* 3.1 (2017-12), 01LT02. DOI: 10.1088/2058-9565/aa9a02. URL: https://dx.doi.org/10.1088/2058-9565/aa9a02 (cit. on p. 7).

[179] Z. Lenar či č et al. "Critical Behavior near the Many-Body Localization Transition in Driven Open Systems". In: *Phys. Rev. Lett.* 125 (11 2020-09), p. 116601. DOI: 10.1103/PhysRevLett.125.116601. URL: https://link.aps.org/doi/10.1103/PhysRevLett.125.116601 (cit. on p. 7).

[180] P. Kos, T. Prosen, and B. Bertini. "Thermalization dynamics and spectral statistics of extended systems with thermalizing boundaries". In: *Phys. Rev. B* 104 (21 2021-12), p. 214303. DOI: 10.1103/PhysRevB.104.214303. URL: https://link.aps.org/doi/10.1103/PhysRevB.104.214303 (cit. on p. 7).

[181] A. Rubio-Abadal et al. "Many-Body Delocalization in the Presence of a Quantum Bath". In: *Phys. Rev. X* 9 (4 2019-10), p. 041014. DOI: 10.1103/PhysRevX.9.041014. URL: https://link.aps.org/doi/10.1103/PhysRevX.9.041014 (cit. on p. 7).

[182] J. Mák, M. J. Bhaseen, and A. Pal. "Statics and dynamics of non-Hermitian many-body localization". In: *Communications Physics* 7.1 (2024), p. 92. DOI: 10.1038/s42005-024-01576-y. URL: https://doi.org/10.1038/s42005-024-01576-y (cit. on p. 7).

[183] A. Panda and S. Banerjee. "Entanglement in nonequilibrium steady states and many-body localization breakdown in a current-driven system". In: *Phys. Rev. B* 101 (18 2020-05), p. 184201. DOI: 10.1103/PhysRevB.101.184201. URL: https://link.aps.org/doi/10.1103/PhysRevB.101.184201 (cit. on pp. 7, 22).

[184] R. Hamazaki, K. Kawabata, and M. Ueda. "Non-Hermitian Many-Body Localization". In: *Phys. Rev. Lett.* 123 (9 2019-08), p. 090603. DOI: 10.1103/PhysRevLett.123.090603. URL: https://link.aps.org/doi/10.1103/PhysRevLett.123.090603 (cit. on pp. 7, 22, 24, 31, 34, 43, 44, 149).

[185] S. Ghosh, S. Gupta, and M. Kulkarni. "Spectral properties of disordered interacting non-Hermitian systems". In: *Phys. Rev. B* 106 (13 2022-10), p. 134202. DOI: 10.1103/PhysRevB.106.134202. URL: https://link.aps.org/doi/10.1103/PhysRevB.106.134202 (cit. on pp. 7, 43, 44).

[186] K. Suthar et al. "Non-Hermitian many-body localization with open boundaries". In: *Phys. Rev. B* 106 (6 2022-08), p. 064208. DOI: 10.1103/PhysRevB.106.064208. URL: https://link.aps.org/doi/10.1103/PhysRevB.106.064208 (cit. on p. 7).

[187] L.-J. Zhai, S. Yin, and G.-Y. Huang. "Many-body localization in a non-Hermitian quasiperiodic system". In: *Phys. Rev. B* 102 (6 2020-08), p. 064206. DOI: 10.1103/PhysRevB.102.064206. URL: https://link.aps.org/doi/10.1103/PhysRevB.102.064206 (cit. on p. 7).

[188] C. M. Dai, Y. Zhang, and X. X. Yi. "Dynamical localization in non-Hermitian quasicrystals". In: *Phys. Rev. A* 105 (2 2022-02), p. 022215. DOI: 10.1103/PhysRevA.105.022215. URL: https://link.aps.org/doi/10.1103/PhysRevA.105.022215 (cit. on p. 7).

[189] M. Prasad et al. "Dissipative quantum dynamics, phase transitions, and non-Hermitian random matrices". In: *Phys. Rev. A* 105 (5 2022-05), p. L050201. DOI: 10.1103/PhysRevA.105.L050201. URL: https://link.aps.org/doi/10.1103/PhysRevA.105.L050201 (cit. on p. 7).

[190] R. Grobe, F. Haake, and H.-J. Sommers. "Quantum Distinction of Regular and Chaotic Dissipative Motion". In: *Phys. Rev. Lett.* 61 (17 1988-10), pp. 1899–1902. DOI: 10.1103/PhysRevLett.61.1899. URL: https://link.aps.org/doi/10.1103/PhysRevLett.61.1899 (cit. on p. 7).

[191] R. Grobe and F. Haake. "Universality of cubic-level repulsion for dissipative quantum chaos". In: *Phys. Rev. Lett.* 62 (25 1989-06), pp. 2893–2896. DOI: 10.1103/PhysRevLett.62.2893. URL: https://link.aps.org/doi/10.1103/PhysRevLett.62.2893 (cit. on p. 7).

[192] J. Ginibre. "Statistical Ensembles of Complex, Quaternion, and Real Matrices". In: *Journal of Mathematical Physics* 6.3 (1965), pp. 440–449. DOI: 10.1063/1.1704292. URL: https://doi.org/10.1063/1.1704292 (cit. on pp. 7, 31).

[193] H. J. Sommers et al. "Spectrum of Large Random Asymmetric Matrices". In: *Phys. Rev. Lett.* 60 (19 1988-05), pp. 1895–1898. DOI: 10.1103/PhysRevLett.60.1895. URL: https://link.aps.org/doi/10.1103/PhysRevLett.60.1895 (cit. on p. 7).

[194] N. Lehmann and H.-J. Sommers. "Eigenvalue statistics of random real matrices". In: *Phys. Rev. Lett.* 67 (8 1991-08), pp. 941–944. DOI: 10.1103/PhysRevLett.67.941. URL: https://link.aps.org/doi/10.1103/PhysRevLett.67.941 (cit. on p. 7).

[195] G. Akemann et al. "Universal Signature from Integrability to Chaos in Dissipative Open Quantum Systems". In: *Phys. Rev. Lett.* 123 (25 2019-12), p. 254101. DOI: 10.1103/PhysRevLett.123.254101. URL: https://link.aps.org/doi/10.1103/PhysRevLett.123.254101 (cit. on p. 7).

[196] L. Sá, P. Ribeiro, and T. Prosen. "Complex Spacing Ratios: A Signature of Dissipative Quantum Chaos". In: *Phys. Rev. X* 10 (2 2020-04), p. 021019. DOI: 10.1103/PhysRevX.10.021019. URL: https://link.aps.org/doi/10.1103/PhysRevX.10.021019 (cit. on pp. 7, 24, 26, 27, 43, 44).

[197] K. Wang, F. Piazza, and D. J. Luitz. "Hierarchy of Relaxation Timescales in Local Random Liouvillians". In: *Phys. Rev. Lett.* 124 (10 2020-03), p. 100604. DOI: 10.1103/PhysRevLett.124.100604. URL: https://link.aps.org/doi/10.1103/PhysRevLett.124.100604 (cit. on p. 7).

[198] I. Yusipov and M. Ivanchenko. "Quantum Lyapunov exponents and complex spacing ratios: Two measures of dissipative quantum chaos". In: *Chaos* 32.4 (2022), p. 043106. DOI: https://doi.org/10.1063/5.0082046. URL: https://aip.scitation.org/doi/10.1063/5.0082046 (cit. on p. 7).

[199] A. Rubio-García, R. A. Molina, and J. Dukelsky. "From integrability to chaos in quantum Liouvillians". In: *SciPost Phys. Core* 5 (2 2022), p. 26. DOI: 10.21468/SciPostPhysCore.5.2.026. URL: https://scipost.org/10.21468/SciPostPhysCore.5.2.026 (cit. on p. 7).

[200] R. Hamazaki et al. "Lindbladian Many-Body Localization". In: (2022). DOI: 10.48550/ARXIV.2206.02984. URL: https://arxiv.org/abs/2206.02984 (cit. on p. 7).

[201] S. Gupta et al. "Quantum jumps in driven-dissipative disordered many-body systems". In: *Phys. Rev. A* 109 (5 2024-05), p. L050201. DOI: 10.1103/PhysRevA.109.L050201. URL: https://link.aps.org/doi/10.1103/PhysRevA.109.L050201 (cit. on p. 7).

[202] A. M. García-García, L. Sá, and J. J. M. Verbaarschot. "Symmetry Classification and Universality in Non-Hermitian Many-Body Quantum Chaos by the Sachdev-Ye-Kitaev Model". In: *Phys. Rev. X* 12 (2 2022-05), p. 021040. DOI: 10.1103/PhysRevX.12.021040. URL: https://link.aps.org/doi/10.1103/PhysRevX.12.021040 (cit. on p. 7).

[203] T. Kanazawa and T. Wettig. "New universality classes of the non-Hermitian Dirac operator in QCD-like theories". In: *Phys. Rev. D* 104 (1 2021-07), p. 014509. DOI: 10.1103/PhysRevD.104.014509. URL: https://link.aps.org/doi/10.1103/PhysRevD.104.014509 (cit. on p. 7).

[204] L. Sá, P. Ribeiro, and T. ž. Prosen. "Integrable nonunitary open quantum circuits". In: *Phys. Rev. B* 103 (11 2021-03), p. 115132. DOI: 10.1103/PhysRevB.103.115132. URL: https://link.aps.org/doi/10.1103/PhysRevB.103.115132 (cit. on p. 7).

[205] X. Luo, T. Ohtsuki, and R. Shindou. "Universality Classes of the Anderson Transitions Driven by Non-Hermitian Disorder". In: *Phys. Rev. Lett.* 126 (9 2021-03), p. 090402. DOI: 10.1103/PhysRevLett.126.090402. URL: https://link.aps.org/doi/10.1103/PhysRevLett.126.090402 (cit. on pp. 7, 8, 74).

[206] K. Yan et al. "Anderson localization and multifractal spectrum at the transition point in a two-dimensional non-Hermitian AII† system". In: *Journal of Physics: Condensed Matter* 34.16 (2022-02), p. 165002. DOI: 10.1088/1361-648x/ac50dc. URL: https://doi.org/10.1088/1361-648x/ac50dc (cit. on p. 7).

[207] J. Li, T. ž. Prosen, and A. Chan. "Spectral Statistics of Non-Hermitian Matrices and Dissipative Quantum Chaos". In: *Phys. Rev. Lett.* 127 (17 2021-10), p. 170602. DOI: 10.1103/PhysRevLett.127.170602. URL: https://link.aps.org/doi/10.1103/PhysRevLett.127.170602 (cit. on pp. 7, 28, 29, 31, 136, 138, 140).

[208] S. Shivam et al. "Many-Body Quantum Chaos and Emergence of Ginibre Ensemble". In: *Phys. Rev. Lett.* 130 (14 2023-04), p. 140403. DOI: 10.1103/PhysRevLett.130.140403. URL: https://link.aps.org/doi/10.1103/PhysRevLett.130.140403 (cit. on pp. 7, 28).

[209] M. Prasad et al. "Assessment of spectral phases of non-Hermitian quantum systems through complex and singular values". In: *Phys. Rev. B* 111 (16 2025-04), p. L161408. DOI: 10.1103/PhysRevB.111.L161408. URL: https://link.aps.org/doi/10.1103/PhysRevB.111.L161408 (cit. on p. 7).

[210] G. Cipolloni and N. Grometto. "The Dissipative Spectral Form Factor for I.I.D. Matrices". In: *Journal of Statistical Physics* 191.2 (2024), p. 21. DOI: 10.1007/s10955-024-03237-4. URL: https://doi.org/10.1007/s10955-024-03237-4 (cit. on p. 7).

[211] S. Sen and S. Kumar. *Exact and asymptotic dissipative spectral form factor for elliptic Ginibre unitary ensemble*. 2024. arXiv: 2407.17148 [cond-mat.stat-mech]. URL: https://arxiv.org/abs/2407.17148 (cit. on p. 7).

[212] J. Li et al. *Spectral form factor in chaotic, localized, and integrable open quantum many-body systems*. 2024. arXiv: 2405.01641 [cond-mat.stat-mech]. URL: https://arxiv.org/abs/2405.01641 (cit. on p. 7).

[213] S. Moudgalya et al. "Extension of the eigenstate thermalization hypothesis to nonequilibrium steady states". In: *Phys. Rev. B* 100 (4 2019-07), p. 045112. DOI: 10.1103/PhysRevB.100.045112. URL: https://link.aps.org/doi/10.1103/PhysRevB.100.045112 (cit. on p. 7).

[214] T. Shirai and T. Mori. "Thermalization in open many-body systems based on eigenstate thermalization hypothesis". In: *Phys. Rev. E* 101 (4 2020-04), p. 042116. DOI: 10.1103/PhysRevE.101.042116. URL: https://link.aps.org/doi/10.1103/PhysRevE.101.042116 (cit. on p. 7).

[215] G. Cipolloni and J. Kudler-Flam. "Non-Hermitian Hamiltonians violate the eigenstate thermalization hypothesis". In: *Phys. Rev. B* 109 (2 2024-01), p. L020201. DOI: 10.1103/PhysRevB.109.L020201. URL: https://link.aps.org/doi/10.1103/PhysRevB.109.L020201 (cit. on p. 7).

[216] G. Almeida et al. *Universality, Robustness, and Limits of the Eigenstate Thermalization Hypothesis in Open Quantum Systems*. 2025. arXiv: 2504.10261 [cond-mat.stat-mech]. URL: https://arxiv.org/abs/2504.10261 (cit. on p. 7).

[217] F. Ferrari, V. Savona, and F. Minganti. *Chaos and thermalization in open quantum systems*. 2025. arXiv: 2505.18260 [quant-ph]. URL: https://arxiv.org/abs/2505.18260 (cit. on p. 7).

[218] M. Hunter-Gordon et al. "Quantum simulation of the dephasing Anderson model". In: *Phys. Rev. A* 102 (2 2020-08), p. 022407. DOI: 10.1103/PhysRevA.102.022407. URL: https://link.aps.org/doi/10.1103/PhysRevA.102.022407 (cit. on pp. 8, 74).

[219] Y. Rath and F. Mintert. "Prominent interference peaks in the dephasing Anderson model". In: *Phys. Rev. Res.* 2 (2 2020-05), p. 023161. DOI: 10.1103/PhysRevResearch.2.023161. URL: https://link.aps.org/doi/10.1103/PhysRevResearch.2.023161 (cit. on pp. 8, 74).

[220] S. R. Taylor and A. Scardicchio. "Subdiffusion in a one-dimensional Anderson insulator with random dephasing: Finite-size scaling, Griffiths effects, and possible implications for many-body localization". In: *Phys. Rev. B* 103 (18 2021-05), p. 184202. DOI: 10.1103/PhysRevB.103.184202. URL: https://link.aps.org/doi/10.1103/PhysRevB.103.184202 (cit. on p. 8).

[221] X. Turkeshi et al. "Destruction of localization by thermal inclusions: Anomalous transport and Griffiths effects in the Anderson and André-Aubry-Harper models". In: *SciPost Phys.* 12 (2022), p. 189. DOI: 10.21468/SciPostPhys.12.6.189. URL: https://scipost.org/10.21468/SciPostPhys.12.6.189 (cit. on p. 8).

[222] T. Prosen. "Third quantization: a general method to solve master equations for quadratic open Fermi systems". In: *New Journal of Physics* 10.4 (2008), p. 043026 (cit. on pp. 8, 74).

[223] B. Zhou, X. Wang, and S. Chen. "Exponential size scaling of the Liouvillian gap in boundary-dissipated systems with Anderson localization". In: *Phys. Rev. B* 106 (6 2022-08), p. 064203. DOI: 10.1103/PhysRevB.106.064203. URL: https://link.aps.org/doi/10.1103/PhysRevB.106.064203 (cit. on pp. 8, 74).

[224] F. Song, S. Yao, and Z. Wang. "Non-Hermitian Skin Effect and Chiral Damping in Open Quantum Systems". In: *Phys. Rev. Lett.* 123 (17 2019-10), p. 170401. DOI: 10.1103/PhysRevLett.123.170401. URL: https://link.aps.org/doi/10.1103/PhysRevLett.123.170401 (cit. on pp. 8, 74).

[225] Z.-Y. Zheng, X. Wang, and S. Chen. "Exact solution of the boundary-dissipated transverse field Ising model: Structure of the Liouvillian spectrum and dynamical duality". In: *Phys. Rev. B* 108 (2 2023-07), p. 024404. DOI: 10.1103/PhysRevB.108.024404. URL: https://link.aps.org/doi/10.1103/PhysRevB.108.024404 (cit. on pp. 8, 74).

[226] V. Berger et al. *Numerical Study of Disordered Noninteracting Chains Coupled to a Local Lindblad Bath*. 2024. arXiv: 2412.03233 [cond-mat.dis-nn]. URL: https://arxiv.org/abs/2412.03233 (cit. on pp. 8, 74, 87).

[227] T. Mori. *Liouvillian-gap analysis of open quantum many-body systems in the weak dissipation limit*. 2024. arXiv: 2311.10304 [cond-mat.stat-mech]. URL: https://arxiv.org/abs/2311.10304 (cit. on pp. 8, 74).

[228] S. Longhi. "Dephasing-Induced Mobility Edges in Quasicrystals". In: *Phys. Rev. Lett.* 132 (23 2024-06), p. 236301. DOI: 10.1103/PhysRevLett.132.236301. URL: https://link.aps.org/doi/10.1103/PhysRevLett.132.236301 (cit. on pp. 8, 9, 74).

[229] A. Ghatak et al. "Diffraction and pseudospectra in non-Hermitian quasiperiodic lattices". In: *Phys. Rev. E* 110 (6 2024-12), p. 064228. DOI: 10.1103/PhysRevE.110.064228. URL: https://link.aps.org/doi/10.1103/PhysRevE.110.064228 (cit. on pp. 8, 74).

[230] H. Cui et al. "Open dynamics in the Aubry-André-Harper model coupled to a finite bath: The influence of localization in the system and dimensionality of bath". In: *Physics Letters A* 421 (2022), p. 127778. ISSN: 0375-9601. DOI: https://doi.org/10.1016/j.physleta.2021.127778. URL: https://www.sciencedirect.com/science/article/pii/S0375960121006423 (cit. on pp. 8, 75).

[231] Z. Xu and S. Chen. "Dynamical evolution in a one-dimensional incommensurate lattice with $\mathcal{PT}$ symmetry". In: *Phys. Rev. A* 103 (4 2021-04), p. 043325. DOI: 10.1103/PhysRevA.103.043325. URL: https://link.aps.org/doi/10.1103/PhysRevA.103.043325 (cit. on pp. 8, 74).

[232] S. Longhi. "Anderson Localization in Dissipative Lattices". In: *Annalen der Physik* 535.5 (2023), p. 2200658. DOI: https://doi.org/10.1002/andp.202200658. eprint: https://onlinelibrary.wiley.com/doi/pdf/10.1002/andp.202200658. URL: https://onlinelibrary.wiley.com/doi/abs/10.1002/andp.202200658 (cit. on pp. 8, 9, 74).

[233] A. F. Tzortzakakis et al. "Transport and spectral features in non-Hermitian open systems". In: *Phys. Rev. Res.* 3 (1 2021-03), p. 013208. DOI: 10.1103/PhysRevResearch.3.013208. URL: https://link.aps.org/doi/10.1103/PhysRevResearch.3.013208 (cit. on pp. 8, 74).

[234] A. Leventis, K. G. Makris, and E. N. Economou. "Non-Hermitian jumps in disordered lattices". In: *Phys. Rev. B* 106 (6 2022-08), p. 064205. DOI: 10.1103/PhysRevB.106.064205. URL: https://link.aps.org/doi/10.1103/PhysRevB.106.064205 (cit. on pp. 8, 74).

[235] S. Weidemann et al. "Coexistence of dynamical delocalization and spectral localization through stochastic dissipation". In: *Nature Photonics* 15.8 (2021), pp. 576–581. DOI: 10.1038/s41566-021-00823-w. URL: https://doi.org/10.1038/s41566-021-00823-w (cit. on pp. 8, 9, 74).

[236] I. Yusipov et al. "Localization in Open Quantum Systems". In: *Phys. Rev. Lett.* 118 (7 2017-02), p. 070402. DOI: 10.1103/PhysRevLett.118.070402. URL: https://link.aps.org/doi/10.1103/PhysRevLett.118.070402 (cit. on pp. 8, 74).

[237] S. Roy and J. Gong. *Aperiodic Dissipation as a Mechanism for Steady-State Localization*. 2025. arXiv: 2506.15108 [quant-ph]. URL: https://arxiv.org/abs/2506.15108 (cit. on p. 8).

[238] T. Li, Y.-S. Zhang, and W. Yi. "Engineering dissipative quasicrystals". In: *Phys. Rev. B* 105 (12 2022-03), p. 125111. DOI: 10.1103/PhysRevB.105.125111. URL: https://link.aps.org/doi/10.1103/PhysRevB.105.125111 (cit. on p. 8).

[239] D. A. Zezyulin et al. "Macroscopic Zeno Effect and Stationary Flows in Nonlinear Waveguides with Localized Dissipation". In: *Phys. Rev. Lett.* 109 (2 2012-07), p. 020405. DOI: 10.1103/PhysRevLett.109.020405. URL:

https://link.aps.org/doi/10.1103/PhysRevLett.109.020405 (cit. on pp. 8, 52).

[240] H. Fröml et al. "Ultracold quantum wires with localized losses: Many-body quantum Zeno effect". In: *Phys. Rev. B* 101 (14 2020-04), p. 144301. DOI: 10.1103/PhysRevB.101.144301. URL: https://link.aps.org/doi/10.1103/PhysRevB.101.144301 (cit. on pp. 8, 52).

[241] T. L. M. Lezama and Y. B. Lev. "Logarithmic, noise-induced dynamics in the Anderson insulator". In: *SciPost Phys.* 12 (2022), p. 174. DOI: 10.21468/SciPostPhys.12.5.174. URL: https://scipost.org/10.21468/SciPostPhys.12.5.174 (cit. on p. 8).

[242] D. S. Bhakuni, T. L. M. Lezama, and Y. B. Lev. "Noise-induced transport in the Aubry-André-Harper model". In: *SciPost Phys. Core* 7 (2024), p. 023. DOI: 10.21468/SciPostPhysCore.7.2.023. URL: https://scipost.org/10.21468/SciPostPhysCore.7.2.023 (cit. on p. 8).

[243] H. Cui et al. "Localization-enhanced dissipation in a generalized Aubry-André-Harper model coupled with Ohmic baths". In: *Physics Letters A* 448 (2022), p. 128314. ISSN: 0375-9601. DOI: https://doi.org/10.1016/j.physleta.2022.128314. URL: https://www.sciencedirect.com/science/article/pii/S0375960122003966 (cit. on pp. 9, 74, 75).

[244] X. Yang, X.-P. Jiang, and L. Pan. *Dissipation-Enhanced Localization in a Disorder-Free $\mathbb{Z}_2$ Lattice Gauge System*. 2025. arXiv: 2509.06642 [quant-ph]. URL: https://arxiv.org/abs/2509.06642 (cit. on pp. 9, 74).

[245] S. Longhi. "Phase transitions in a non-Hermitian Aubry-André-Harper model". In: *Phys. Rev. B* 103 (5 2021-02), p. 054203. DOI: 10.1103/PhysRevB.103.054203. URL: https://link.aps.org/doi/10.1103/PhysRevB.103.054203 (cit. on pp. 9, 74).

[246] F. Thompson, Y. Huang, and A. Kamenev. "Localization of Lindbladian fermions". In: *Phys. Rev. B* 109 (17 2024-05), p. 174201. DOI: 10.1103/PhysRevB.109.174201. URL: https://link.aps.org/doi/10.1103/PhysRevB.109.174201 (cit. on p. 9).

[247] X. Yang et al. "Dissipation-induced transition between delocalization and localization in the three-dimensional Anderson model". In: *Phys. Rev. B* 111 (13 2025-04), p. 134203. DOI: 10.1103/PhysRevB.111.134203. URL: https://link.aps.org/doi/10.1103/PhysRevB.111.134203 (cit. on pp. 9, 74).

[248] A. Sharma and E. Rabani. "Landauer current and mutual information". In: *Phys. Rev. B* 91 (8 2015-02), p. 085121. DOI: 10.1103/PhysRevB.91.085121. URL: https://link.aps.org/doi/10.1103/PhysRevB.91.085121 (cit. on p. 13).

[249] J. M. Bhat and A. Dhar. "Transport in spinless superconducting wires". In: *Phys. Rev. B* 102 (22 2020-12), p. 224512. DOI: 10.1103/PhysRevB.102.224512. URL: https://link.aps.org/doi/10.1103/PhysRevB.102.224512 (cit. on p. 13).

[250] A. Purkayastha, A. Dhar, and M. Kulkarni. "Out-of-equilibrium open quantum systems: A comparison of approximate quantum master equation approaches with exact results". In: *Phys. Rev. A* 93 (6 2016-06), p. 062114. DOI: 10.1103/PhysRevA.93.062114. URL: https://link.aps.org/doi/10.1103/PhysRevA.93.062114 (cit. on pp. 13, 18, 19, 60, 63, 78, 85).

[251] A. Dhar and D. Sen. "Nonequilibrium Green's function formalism and the problem of bound states". In: *Phys. Rev. B* 73 (8 2006-02), p. 085119. DOI: 10.1103/PhysRevB.73.085119. URL: https://link.aps.org/doi/10.1103/PhysRevB.73.085119 (cit. on p. 13).

[252] A. Dhar, K. Saito, and P. Hänggi. "Nonequilibrium density-matrix description of steady-state quantum transport". In: *Phys. Rev. E* 85 (1 2012-01), p. 011126. DOI: 10.1103/PhysRevE.85.011126. URL: https://link.aps.org/doi/10.1103/PhysRevE.85.011126 (cit. on p. 13).

[253] A. Dhar and D. Roy. "Heat transport in harmonic lattices". In: *Journal of Statistical Physics* 125.4 (2006), pp. 801–820. URL: https://doi.org/10.1007/s10955-006-9235-3 (cit. on p. 13).

[254] J.-S. Wang, X. Ni, and J.-W. Jiang. "Molecular dynamics with quantum heat baths: Application to nanoribbons and nanotubes". In: *Phys. Rev. B* 80 (22 2009-12), p. 224302. DOI: 10.1103/PhysRevB.80.224302. URL: https://link.aps.org/doi/10.1103/PhysRevB.80.224302 (cit. on p. 13).

[255] G. W. Ford, J. T. Lewis, and R. F. O'Connell. "Quantum Langevin equation". In: *Phys. Rev. A* 37 (11 1988-06), pp. 4419–4428. DOI: 10.1103/PhysRevA.37.4419. URL: https://link.aps.org/doi/10.1103/PhysRevA.37.4419 (cit. on p. 13).

[256] D. Segal, A. Nitzan, and P. Hänggi. "Thermal conductance through molecular wires". In: *The Journal of chemical physics* 119.13 (2003), pp. 6840–6855. URL: https://doi.org/10.1063/1.1603211 (cit. on p. 13).

[257] U. Zürcher and P. Talkner. "Quantum-mechanical harmonic chain attached to heat baths. II. Nonequilibrium properties". In: *Phys. Rev. A* 42 (6 1990-09), pp. 3278–3290. DOI: 10.1103/PhysRevA.42.3278. URL: https://link.aps.org/doi/10.1103/PhysRevA.42.3278 (cit. on p. 13).

[258] Y.-C. Chen, J. L. Lebowitz, and C. Liverani. "Dissipative quantum dynamics in a boson bath". In: *Phys. Rev. B* 40 (7 1989-09), pp. 4664–4682. DOI: 10.1103/PhysRevB.40.4664. URL: https://link.aps.org/doi/10.1103/PhysRevB.40.4664 (cit. on p. 13).

[259] N. Bondyopadhaya and D. Roy. "Nonequilibrium electrical, thermal and spin transport in open quantum systems of topological superconductors, semiconductors and metals". In: *Journal of Statistical Physics* 187.2 (2022), pp. 1–49. DOI: https://doi.org/10.1007/s10955-022-02902-w (cit. on p. 13).

[260] S. Datta. "Nanoscale device modeling: the Green's function method". In: *Superlattices and Microstructures* 28.4 (2000), pp. 253–278. ISSN: 0749-6036. DOI: https://doi.org/10.1006/spmi.2000.0920. URL: https://www.sciencedirect.com/science/article/pii/S0749603600909200 (cit. on p. 16).

[261] G. S. Agarwal. *Quantum optics*. Cambridge University Press, 2012 (cit. on p. 17).

[262] A. G. Redfield. "On the theory of relaxation processes". In: *IBM Journal of Research and Development* 1.1 (1957), pp. 19–31. DOI: 10.1147/rd.11.0019 (cit. on p. 18).

[263] K. Blum. *Density Matrix Theory and Applications*. New York, London: Plenum Press, 1981. DOI: https://doi.org/10.1007/978-1-4615-6808-7 (cit. on p. 18).

[264] G. Lindblad. "On the generators of quantum dynamical semigroups". In: *Communications in Mathematical Physics* 48.2 (1976), pp. 119–130. DOI: https://doi.org/10.1007/BF01608499 (cit. on pp. 18, 60).

[265] V. Gorini, A. Kossakowski, and E. C. G. Sudarshan. "Completely positive dynamical semigroups of N-level systems". In: *Journal of Mathematical Physics* 17.5 (1976), pp. 821–825. URL: https://doi.org/10.1063/1.522979 (cit. on pp. 18, 60).

[266] D. Tupkary et al. "Fundamental limitations in Lindblad descriptions of systems weakly coupled to baths". In: *Physical Review A* 105.3 (2022), p. 032208 (cit. on pp. 19, 60).

[267] D. Manzano. "A short introduction to the Lindblad master equation". In: *Aip Advances* 10.2 (2020), p. 025106. DOI: https://doi.org/10.1063/1.5115323 (cit. on pp. 19, 60).

[268] F. Nathan and M. S. Rudner. "Universal Lindblad equation for open quantum systems". In: *Physical Review B* 102.11 (2020), p. 115109 (cit. on p. 19).

[269] A. Schnell. "Global Becomes Local: Efficient Many-Body Dynamics for Global Master Equations". In: *Phys. Rev. Lett.* 134 (25 2025-06), p. 250401. DOI: 10.1103/1q5b-p2bf. URL: https://link.aps.org/doi/10.1103/1q5b-p2bf (cit. on p. 19).

[270] F. Campaioli, J. H. Cole, and H. Hapuarachchi. "Quantum Master Equations: Tips and Tricks for Quantum Optics, Quantum Computing, and Beyond". In: *PRX Quantum* 5 (2 2024-06), p. 020202. DOI: 10.1103/PRXQuantum.5.020202. URL: https://link.aps.org/doi/10.1103/PRXQuantum.5.020202 (cit. on p. 19).

[271] S. Choi et al. "Observation of discrete time-crystalline order in a disordered dipolar many-body system". In: *Nature* 543.7644 (2017-03), pp. 221–225. ISSN: 1476-4687. DOI: 10.1038/nature21426. URL: https://doi.org/10.1038/nature21426 (cit. on p. 20).

[272] J. Zhang et al. "Observation of a discrete time crystal". In: *Nature* 543.7644 (2017-03), pp. 217–220. ISSN: 1476-4687. DOI: 10.1038/nature21413. URL: https://doi.org/10.1038/nature21413 (cit. on p. 20).

[273] J. Rovny, R. L. Blum, and S. E. Barrett. "Observation of Discrete-Time-Crystal Signatures in an Ordered Dipolar Many-Body System". In: *Phys. Rev. Lett.* 120 (18 2018-05), p. 180603. DOI: 10.1103/PhysRevLett.120.180603. URL: https://link.aps.org/doi/10.1103/PhysRevLett.120.180603 (cit. on p. 20).

[274] S. Nag and A. Garg. "Many-body localization in the presence of long-range interactions and long-range hopping". In: *Phys. Rev. B* 99 (22 2019-06), p. 224203. DOI: 10.1103/PhysRevB.99.224203. URL: https://link.aps.org/doi/10.1103/PhysRevB.99.224203 (cit. on pp. 21, 33).

[275] S. Roy and D. E. Logan. "Self-consistent theory of many-body localisation in a quantum spin chain with long-range interactions". In: *SciPost Phys.* 7 (4 2019), p. 42. DOI: 10.21468/SciPostPhys.7.4.042. URL: https://scipost.org/10.21468/SciPostPhys.7.4.042 (cit. on pp. 21, 33).

[276] N. Hatano and D. R. Nelson. "Localization Transitions in Non-Hermitian Quantum Mechanics". In: *Phys. Rev. Lett.* 77 (3 1996-07), pp. 570–573. DOI: 10.1103/PhysRevLett.77.570. URL: https://link.aps.org/doi/10.1103/PhysRevLett.77.570 (cit. on p. 22).

[277] N. Hatano and D. R. Nelson. "Vortex pinning and non-Hermitian quantum mechanics". In: *Phys. Rev. B* 56 (14 1997-10), pp. 8651–8673. DOI: 10.1103/PhysRevB.56.8651. URL: https://link.aps.org/doi/10.1103/PhysRevB.56.8651 (cit. on p. 22).

[278] N. Hatano and D. R. Nelson. "Non-Hermitian delocalization and eigenfunctions". In: *Phys. Rev. B* 58 (13 1998-10), pp. 8384–8390. DOI: 10.1103/PhysRevB.58.8384. URL: https://link.aps.org/doi/10.1103/PhysRevB.58.8384 (cit. on p. 22).

[279] D. R. Nelson and N. M. Shnerb. "Non-Hermitian localization and population biology". In: *Phys. Rev. E* 58 (2 1998-08), pp. 1383–1403. DOI: 10.1103/PhysRevE.58.1383. URL: https://link.aps.org/doi/10.1103/PhysRevE.58.1383 (cit. on p. 22).

[280] A. Maddi et al. "Exact analog of the Hatano-Nelson model in one-dimensional continuous nonreciprocal systems". In: *Phys. Rev. Res.* 6 (1 2024-03), p. L012061. DOI: 10.1103/PhysRevResearch.6.L012061. URL: https://link.aps.org/doi/10.1103/PhysRevResearch.6.L012061 (cit. on p. 22).

[281] C. M. Bender et al. *PT Symmetry*. WORLD SCIENTIFIC (EUROPE), 2019. DOI: 10.1142/q0178. eprint: https://www.worldscientific.com/doi/pdf/10.1142/q0178. URL: https://www.worldscientific.com/doi/abs/10.1142/q0178 (cit. on pp. 23, 24).

[282] C. M. Bender and D. W. Hook. "$\mathcal{PT}$-symmetric quantum mechanics". In: *Rev. Mod. Phys.* 96 (4 2024-10), p. 045002. DOI: 10.1103/RevModPhys.96.045002. URL: https://link.aps.org/doi/10.1103/RevModPhys.96.045002 (cit. on pp. 23, 24).

[283] G. Lami, M. Collura, and N. Ranabhat. *Beginner's Lecture Notes on Quantum Spin Chains, Exact Diagonalization and Tensor Networks*. 2025. arXiv: 2503.03564 [cond-mat.str-el]. URL: https://arxiv.org/abs/2503.03564 (cit. on pp. 25, 43).

[284] L. F. Santos and M. Rigol. "Onset of quantum chaos in one-dimensional bosonic and fermionic systems and its relation to thermalization". In: *Phys. Rev. E* 81 (3 2010-03), p. 036206. DOI: 10.1103/PhysRevE.81.036206. URL: https://link.aps.org/doi/10.1103/PhysRevE.81.036206 (cit. on p. 26).

[285] I. G. Dusa and T. Wettig. "Approximation formula for complex spacing ratios in the Ginibre ensemble". In: *Phys. Rev. E* 105 (4 2022-04), p. 044144. DOI: 10.1103/PhysRevE.105.044144. URL: https://link.aps.org/doi/10.1103/PhysRevE.105.044144 (cit. on p. 27).

[286] R. Hamazaki et al. "Universality classes of non-Hermitian random matrices". In: *Phys. Rev. Research* 2 (2 2020-06), p. 023286. DOI: 10.1103/PhysRevResearch.2.023286. URL: https://link.aps.org/doi/10.1103/PhysRevResearch.2.023286 (cit. on pp. 31, 32, 132).

[287] E. Khatami et al. "Quantum quenches in disordered systems: Approach to thermal equilibrium without a typical relaxation time". In: *Phys. Rev. E* 85 (5 2012-05), p. 050102. DOI: 10.1103/PhysRevE.85.050102. URL: https://link.aps.org/doi/10.1103/PhysRevE.85.050102 (cit. on p. 33).

[288] H. Markum, R. Pullirsch, and T. Wettig. "Non-Hermitian Random Matrix Theory and Lattice QCD with Chemical Potential". In: *Phys. Rev. Lett.* 83 (3 1999-07), pp. 484–487. DOI: 10.1103/PhysRevLett.83.484. URL: https://link.aps.org/doi/10.1103/PhysRevLett.83.484 (cit. on p. 33).

[289] M. Esposito, U. Harbola, and S. Mukamel. "Nonequilibrium fluctuations, fluctuation theorems, and counting statistics in quantum systems". In: *Rev. Mod. Phys.* 81 (4 2009-12), p. 1665. DOI: 10.1103/RevModPhys.81.1665. URL: https://link.aps.org/doi/10.1103/RevModPhys.81.1665 (cit. on p. 42).

[290] J. P. Garrahan and I. Lesanovsky. "Thermodynamics of Quantum Jump Trajectories". In: *Phys. Rev. Lett.* 104 (16 2010-04), p. 160601. DOI: 10.1103/PhysRevLett.104.160601. URL: https://link.aps.org/doi/10.1103/PhysRevLett.104.160601 (cit. on pp. 42, 47).

[291] H. K. Yadalam, B. K. Agarwalla, and U. Harbola. "Counting statistics of energy transport across squeezed thermal reservoirs". In: *Phys. Rev. A* 105 (6 2022-06), p. 062219. DOI: 10.1103/PhysRevA.105.062219. URL:

https://link.aps.org/doi/10.1103/PhysRevA.105.062219 (cit. on p. 42).

[292] G. Manzano and R. Zambrini. "Quantum thermodynamics under continuous monitoring: A general framework". In: *AVS Quantum Sci.* 4.2 (2022), p. 025302. DOI: 10.1116/5.0079886. URL: https://doi.org/10.1116/5.0079886 (cit. on p. 47).

[293] G. T. Landi et al. "Current Fluctuations in Open Quantum Systems: Bridging the Gap Between Quantum Continuous Measurements and Full Counting Statistics". In: *PRX Quantum* 5 (2 2024-04), p. 020201. DOI: 10.1103/PRXQuantum.5.020201. URL: https://link.aps.org/doi/10.1103/PRXQuantum.5.020201 (cit. on p. 47).

[294] J. P. Garrahan, A. D. Armour, and I. Lesanovsky. "Quantum trajectory phase transitions in the micromaser". In: *Phys. Rev. E* 84 (2 2011-08), p. 021115. DOI: 10.1103/PhysRevE.84.021115. URL: https://link.aps.org/doi/10.1103/PhysRevE.84.021115 (cit. on p. 47).

[295] B. Skinner, J. Ruhman, and A. Nahum. "Measurement-Induced Phase Transitions in the Dynamics of Entanglement". In: *Phys. Rev. X* 9 (3 2019-07), p. 031009. DOI: 10.1103/PhysRevX.9.031009. URL: https://link.aps.org/doi/10.1103/PhysRevX.9.031009 (cit. on p. 50).

[296] M. Buchhold et al. "Effective Theory for the Measurement-Induced Phase Transition of Dirac Fermions". In: *Phys. Rev. X* 11 (4 2021-10), p. 041004. DOI: 10.1103/PhysRevX.11.041004. URL: https://link.aps.org/doi/10.1103/PhysRevX.11.041004 (cit. on p. 50).

[297] Y. Li, X. Chen, and M. P. A. Fisher. "Measurement-driven entanglement transition in hybrid quantum circuits". In: *Phys. Rev. B* 100 (13 2019-10), p. 134306. DOI: 10.1103/PhysRevB.100.134306. URL: https://link.aps.org/doi/10.1103/PhysRevB.100.134306 (cit. on p. 50).

[298] M. J. Gullans and D. A. Huse. "Dynamical Purification Phase Transition Induced by Quantum Measurements". In: *Phys. Rev. X* 10 (4 2020-10), p. 041020. DOI: 10.1103/PhysRevX.10.041020. URL: https://link.aps.org/doi/10.1103/PhysRevX.10.041020 (cit. on p. 50).

[299] A. Zabalo et al. "Critical properties of the measurement-induced transition in random quantum circuits". In: *Phys. Rev. B* 101 (6 2020-02), p. 060301. DOI: 10.1103/PhysRevB.101.060301. URL: https://link.aps.org/doi/10.1103/PhysRevB.101.060301 (cit. on p. 50).

[300] P. Barmettler and C. Kollath. "Controllable manipulation and detection of local densities and bipartite entanglement in a quantum gas by a dissipative defect". In: *Phys. Rev. A* 84 (4 2011-10), p. 041606. DOI: 10.1103/PhysRevA.84.041606. URL: https://link.aps.org/doi/10.1103/PhysRevA.84.041606 (cit. on p. 52).

[301] G. Kordas, S. Wimberger, and D. Witthaut. "Decay and fragmentation in an open Bose-Hubbard chain". In: *Phys. Rev. A* 87 (4 2013-04), p. 043618. DOI: 10.1103/PhysRevA.87.043618. URL: https://link.aps.org/doi/10.1103/PhysRevA.87.043618 (cit. on p. 52).

[302] M. Kiefer-Emmanouilidis and J. Sirker. "Current reversals and metastable states in the infinite Bose-Hubbard chain with local particle loss". In: *Phys. Rev. A* 96 (6 2017-12), p. 063625. DOI: 10.1103/PhysRevA.96.063625. URL: https://link.aps.org/doi/10.1103/PhysRevA.96.063625 (cit. on p. 52).

[303] D. Sels and E. Demler. "Thermal radiation and dissipative phase transition in a BEC with local loss". In: *Annals of Physics* 412 (2020), p. 168021. DOI: https://doi.org/10.1016/j.aop.2019.168021. URL: https://www.sciencedirect.com/science/article/pii/S0003491619302763 (cit. on p. 52).

[304] R. Labouvie et al. "Bistability in a Driven-Dissipative Superfluid". In: *Phys. Rev. Lett.* 116 (23 2016-06), p. 235302. DOI: 10.1103/PhysRevLett.116.235302. URL: https://link.aps.org/doi/10.1103/PhysRevLett.116.235302 (cit. on p. 52).

[305] P. E. Dolgirev et al. "Non-Gaussian correlations imprinted by local dephasing in fermionic wires". In: *Physical Review B* 102.10 (2020), p. 100301 (cit. on p. 52).

[306] V. Alba and F. Carollo. "Noninteracting fermionic systems with localized losses: Exact results in the hydrodynamic limit". In: *Phys. Rev. B* 105 (5 2022-02), p. 054303. DOI: 10.1103/PhysRevB.105.054303. URL: https://link.aps.org/doi/10.1103/PhysRevB.105.054303 (cit. on pp. 52, 61).

[307] F. Tarantelli and E. Vicari. "Out-of-equilibrium quantum dynamics of fermionic gases in the presence of localized particle loss". In: *Phys. Rev. A* 105 (4 2022-04), p. 042214. DOI: 10.1103/PhysRevA.105.042214. URL: https://link.aps.org/doi/10.1103/PhysRevA.105.042214 (cit. on p. 52).

[308] P. Krapivsky, K. Mallick, and D. Sels. "Free fermions with a localized source". In: *Journal of Statistical Mechanics: Theory and Experiment* 2019.11 (2019), p. 113108. URL: https://doi.org/10.1088/1742-5468/ab4e8e (cit. on pp. 52, 71, 72, 88, 159, 160, 163).

[309] P. Krapivsky, K. Mallick, and D. Sels. "Free bosons with a localized source". In: *Journal of Statistical Mechanics: Theory and Experiment* 2020.6 (2020), p. 063101. URL: https://doi.org/10.1088/1742-5468/ab8118 (cit. on pp. 52, 71, 72, 88, 159, 160).

[310] M. Butz and H. Spohn. "Dynamical phase transition for a quantum particle source". In: *Annales Henri Poincaré*. Vol. 10. 7. Springer. 2010, pp. 1223–1249. DOI: 10.1007/s00023-010-0021-z (cit. on p. 52).

[311] P. Krapivsky, J. Luck, and K. Mallick. "Survival of classical and quantum particles in the presence of traps". In: *Journal of Statistical Physics* 154.6 (2014), pp. 1430–1460. DOI: https://doi.org/10.1007/s10955-014-0936-8 (cit. on p. 52).

[312] Z. Zhuang, J. Merino, and J. B. Marston. "Transport in conductors and rectifiers: Mean-field Redfield equations and nonequilibrium Green's functions". In: *Phys. Rev. B* 102 (12 2020-09), p. 125147. DOI: 10.1103/PhysRevB.102.125147. URL: https://link.aps.org/doi/10.1103/PhysRevB.102.125147 (cit. on p. 57).

[313] J. Wu. "Non-equilibrium stationary states from the equation of motion of open systems". In: *New Journal of Physics* 12.8 (2010), p. 083042. DOI: https://doi.org/10.1088/1367-2630/12/8/083042 (cit. on p. 57).

[314] A. Purkayastha. "Lyapunov equation in open quantum systems and non-Hermitian physics". In: *Phys. Rev. A* 105 (6 2022-06), p. 062204. DOI: 10.1103/PhysRevA.105.062204. URL: https://link.aps.org/doi/10.1103/PhysRevA.105.062204 (cit. on p. 58).

[315] S. Aubry and G. André. "Analyticity breaking and Anderson localization in incommensurate lattices". In: *Ann. Israel Phys. Soc* 3.133 (1980), p. 18 (cit. on pp. 74, 75).

[316] B. Deissler et al. "Delocalization of a disordered bosonic system by repulsive interactions". In: *Nature physics* 6.5 (2010), pp. 354–358 (cit. on p. 74).

[317] Y. Lahini et al. "Observation of a Localization Transition in Quasiperiodic Photonic Lattices". In: *Phys. Rev. Lett.* 103 (1 2009-06), p. 013901. DOI: 10.1103/PhysRevLett.103.013901. URL: https://link.aps.org/doi/10.1103/PhysRevLett.103.013901 (cit. on p. 74).

[318] Y. E. Kraus et al. "Topological States and Adiabatic Pumping in Quasicrystals". In: *Phys. Rev. Lett.* 109 (10 2012-09), p. 106402. DOI: 10.1103/PhysRevLett.109.106402. URL: https://link.aps.org/doi/10.1103/PhysRevLett.109.106402 (cit. on p. 74).

[319] M. Gonçalves et al. "Hidden dualities in 1D quasiperiodic lattice models". In: *SciPost Phys.* 13 (2022), p. 046. DOI: 10.21468/SciPostPhys.13.3.046. URL: https://scipost.org/10.21468/SciPostPhys.13.3.046 (cit. on p. 76).

[320] G. Domínguez-Castro and R. Paredes. "The Aubry–André model as a hobbyhorse for understanding the localization phenomenon". In: *European Journal of Physics* 40.4 (2019), p. 045403 (cit. on p. 76).

[321] V. K. Varma, C. de Mulatier, and M. Žnidari č. "Fractality in nonequilibrium steady states of quasiperiodic systems". In: *Phys. Rev. E* 96 (3 2017-09), p. 032130. DOI: 10.1103/PhysRevE.96.032130. URL: https://link.aps.org/doi/10.1103/PhysRevE.96.032130 (cit. on pp. 76, 83).

[322] A. Purkayastha et al. "Anomalous transport in the Aubry-André-Harper model in isolated and open systems". In: *Phys. Rev. B* 97 (17 2018-05), p. 174206. DOI: 10.1103/PhysRevB.97.174206. URL: https://link.aps.org/doi/10.1103/PhysRevB.97.174206 (cit. on pp. 76, 83).

[323] H. Hiramoto and S. Abe. "Dynamics of an Electron in Quasiperiodic Systems. I. Fibonacci Model". In: *Journal of the Physical Society of Japan* 57.1 (1988), pp. 230–240. DOI: 10.1143/JPSJ.57.230. eprint: https://doi.org/10.1143/JPSJ.57.230. URL: https://doi.org/10.1143/JPSJ.57.230 (cit. on p. 76).

[324] A. Szabó and U. Schneider. "Non-power-law universality in one-dimensional quasicrystals". In: *Phys. Rev. B* 98 (13 2018-10), p. 134201. DOI: 10.1103/PhysRevB.98.134201. URL: https://link.aps.org/doi/10.1103/PhysRevB.98.134201 (cit. on pp. 76, 83).

[325] J. Zhong et al. "Shape of the Quantum Diffusion Front". In: *Phys. Rev. Lett.* 86 (12 2001-03), pp. 2485–2489. DOI: 10.1103/PhysRevLett.86.2485. URL: https://link.aps.org/doi/10.1103/PhysRevLett.86.2485 (cit. on p. 76).

[326] P. Calabrese and J. Cardy. "Evolution of entanglement entropy in one-dimensional systems". In: *Journal of Statistical Mechanics: Theory and Experiment* 2005 (2005), P04010 (cit. on p. 83).

[327] M. Saha, M. Kulkarni, and A. Dhar. "Generalized Hydrodynamic Description of the Page Curve–like Dynamics of a Freely Expanding Fermionic Gas". In: *Phys. Rev. Lett.* 133 (23 2024-12), p. 230402. DOI: 10.1103/PhysRevLett.133.230402. URL: https://link.aps.org/doi/10.1103/PhysRevLett.133.230402 (cit. on p. 83).

[328] A. Trivedi et al. "Filling an empty lattice by local injection of quantum particles". In: *Phys. Rev. A* 108 (5 2023-11), p. 052204. DOI: 10.1103/PhysRevA.108.052204. URL: https://link.aps.org/doi/10.1103/PhysRevA.108.052204 (cit. on p. 85).

[329] M. Abramowitz and I. A. Stegun. "Handbook of Mathematical Functions". In: *US Department of Commerce* 10 (1972) (cit. on p. 162).

[330] *NIST Digital Library of Mathematical Functions*. F. W. J. Olver, A. B. Olde Daalhuis, D. W. Lozier, B. I. Schneider, R. F. Boisvert, C. W. Clark, B. R. Miller, B. V. Saunders, H. S. Cohl, and M. A. McClain, eds. URL: http://dlmf.nist.gov/ (cit. on p. 162).

A

Random Matrix Theory

In this appendix, we briefly discuss the relevant non-Hermitian random matrix ensembles and present the results for complex spacing ratios and the dissipative spectral form factor.

A.1 Random Matrix Ensembles

Random Matrix Theory (RMT) provides a natural framework to describe universal spectral statistics in both Hermitian and non-Hermitian systems. For Hermitian ensembles, the Gaussian ensembles are the Gaussian Orthogonal Ensemble (GOE), Gaussian Unitary Ensemble (GUE), and Gaussian Symplectic Ensemble (GSE), characterized by Dyson index $\beta = 1, 2, 4$ respectively. Their level-spacing distributions reveal short-range correlations between eigenvalues.

The non-Hermitian counterparts are the Ginibre ensembles: Ginibre Orthogonal Ensemble (GinOE), Ginibre Unitary Ensemble (GinUE), and Ginibre Symplectic Ensemble (GinSE). A remarkable feature of these ensembles is that they exhibit cubic level repulsion, a form of universality unique to non-Hermitian RMT [286]. In addition to the Gaussian and Ginibre classes, the AI† ensemble plays a central role for models with transposition symmetry, defined by the constraint $H = H^T$ for non-Hermitian matrices.

The construction of such ensembles follows simple prescriptions: depending on whether the ensemble is real or complex, the entries of a random matrix X are chosen as real or complex independent and identically distributed (i.i.d.) Gaussian variables. Symmetries of the Ensembles put additional constraints on this construction (see Table A.1).

The eigenvalue spectrum of a non-Hermitian random matrix of dimension $\mathcal{N} \times \mathcal{N}$ typically fills a uniform disk of radius $R = \sqrt{\mathcal{N}}$. Upon normalization, $H' = H/\sqrt{\mathcal{N}}$, this spectrum reduces to a disk of unit radius [33] (see Fig. A.1).

Hermiticity	Class	Reality	Symmetry	Constraint	Construction
Hermitian	GOE	Real	Time-reversal	$H = H^T$	$H = (X + X^T)/2$
	GUE	Complex	None	$H = H^\dagger$	$H = (X + X^\dagger)/2$
Non-Hermitian	GinOE	Real	Time-reversal	$H = H^\star$	$H = X$
	GinUE	Complex	None	None	$H = X$
	AI†	Complex	Transposition	$H = H^T$	$H = (X + X^T)/2$

Table A.1: Summary of Hermitian and Non-Hermitian RMT Ensembles.

For reference, the main symmetries of the commonly used ensembles are summarized in Table A.1. Alongside these ensembles, the case of uncorrelated spectra is also considered, where eigenvalues are drawn as i.i.d. random numbers from uniform distributions (real for Hermitian, complex for non-Hermitian). These uncorrelated levels will have corresponding Poisson distributions.

To numerically examine these universality classes, we generated ensembles of size 10^4, averaged over 100 realizations, for GinUE, GinOE, AI†, and uncorrelated complex spectra. The Ginibre ensembles display a nearly uniform eigenvalue density across the disk, while deviations appear only at the edges (see Fig. A.1). Importantly, these edge fluctuations are statistically insignificant compared to the bulk eigenvalues, and thus the bulk captures the universal features of the spectrum. From here on, we focus exclusively on the non-Hermitian ensembles most relevant to the models discussed in this thesis.

Note: The eigenvalues of a Ginibre Orthogonal Ensemble (GinOE) matrix can be either real or occur in complex-conjugate pairs. This originates from the fact that GinOE matrices have real entries but are non-Hermitian.

A.2 Spacing-Ratios Distributions

In this section, we present the results of complex spacing ratios (CSR) for the non-Hermitian random matrix ensembles. The CSR is defined in the equation (3.3.1). This definition is applied to the non-Hermitian RMT ensembles, and the spacing ratios distributions are studied. Figure A.2 shows the marginal distributions of the radial part r and the angular component θ for GinOE, GinUE, AI†, and 2D Poisson ensembles. GinOE and GinUE exhibit identical distributions, while the AI† ensemble demonstrates distinct statistical behavior.

The distributions of the complex spacing ratios ξ are illustrated in Fig. A.3. For

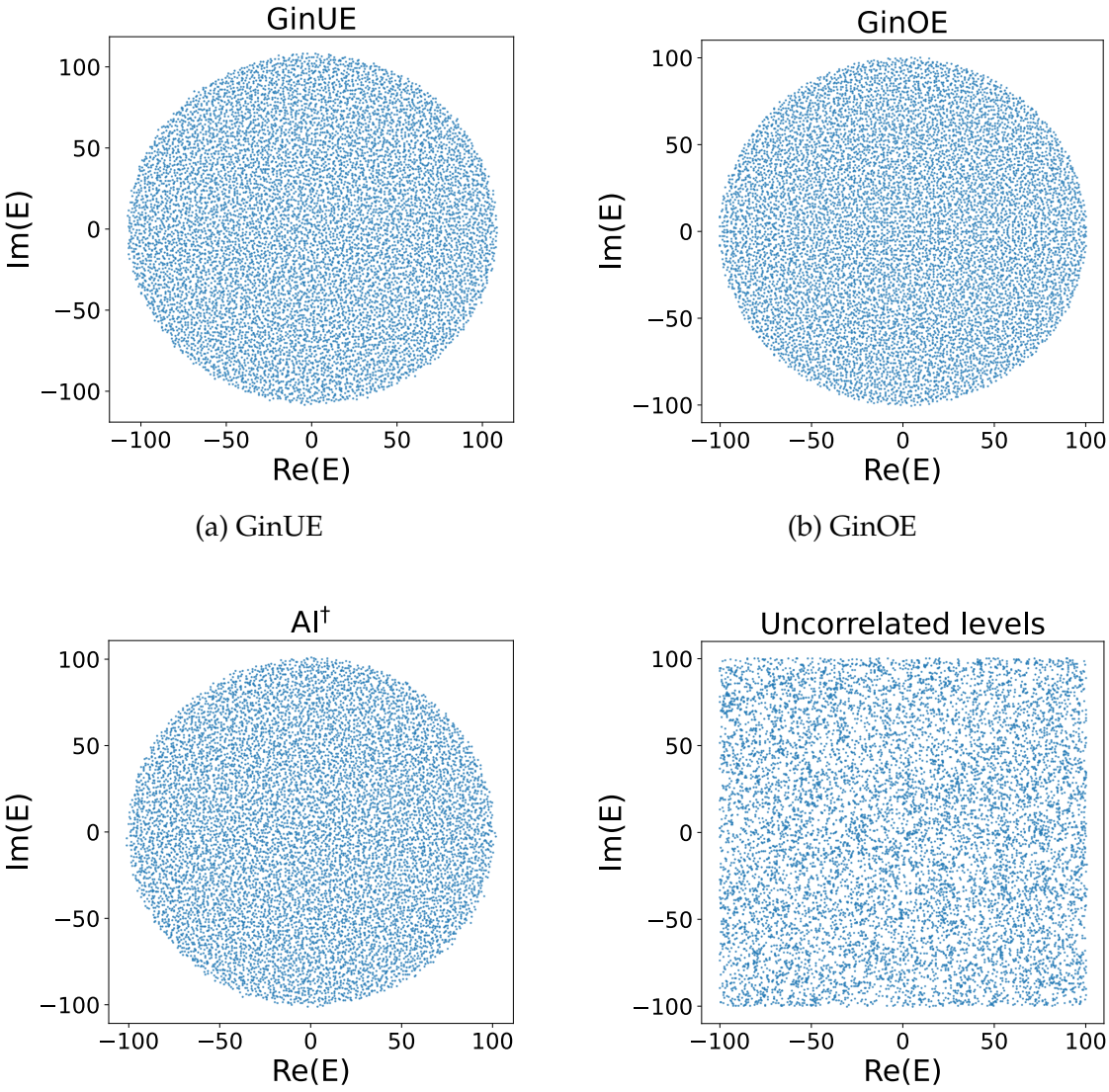

(a) GinUE

(b) GinOE

(c) AI†

(d) Complex Uncorrelated

Figure A.1: Representative eigenvalue spectra for GinUE, GinOE, AI†, and complex uncorrelated ensembles for a single realization.

the random matrix ensembles, the scatter plot reveals an anisotropic distribution, while the uncorrelated levels yield a uniform distribution over the unit disk. These plots clearly demonstrate the manifestation of level repulsion: for random matrix spectra, the ratio density is suppressed near $r = 0$, and eigenvalues tend to distribute evenly around the reference level, leading to suppression at small angular separations. In contrast, the uncorrelated spectrum shows no such suppression, producing a homogeneous distribution across the unit circle.

To quantitatively compare these ensembles, Table A.2 reports the averaged observables obtained from spacing-ratio distributions. The values of $\langle r \rangle$ and

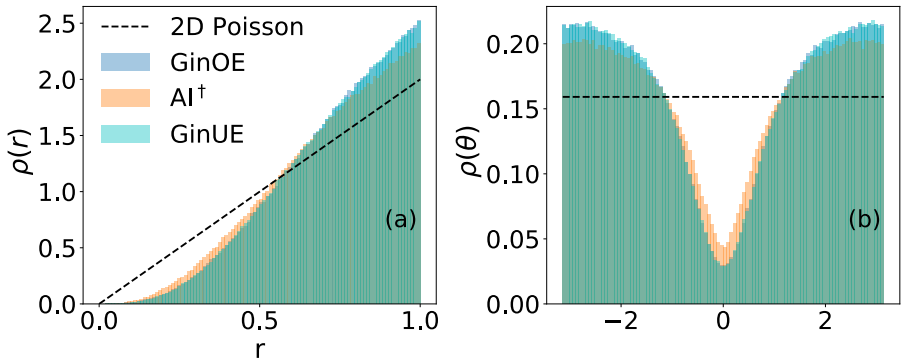

Figure A.2: Complex spacing ratios: Marginal distributions of (left) r and (right) θ for GinOE (blue), AI† (orange), GinUE (cyan) and 2D Poisson (black dashed) RMT Classes. It is clear from these plots that GinOE and GinUE have identical distributions, while GinOE and AI† have different distributions.

$-\langle\cos\theta\rangle$ clearly distinguish between Ginibre, AI†, and Poisson ensembles, confirming that the ratio statistics serve as good indicators of spectral correlations in non-Hermitian random matrices.

Class	$-\langle\cos\theta\rangle$	$\langle r\rangle$
Complex Levels	-0.00472	0.66628
GinUE	0.24696	0.73857
GinOE	0.24440	0.73849
AI†	0.19290	0.72187

Table A.2: Average quantities from spacing-ratio distributions for non-Hermitian ensembles.

A.3 Dissipative Spectral Form Factor

In this section, we present the results of the Dissipative Spectral Form Factor (DSFF) for non-Hermitian random matrices. The DSFF was introduced in Sec. 3.3.2 [Eq. (3.7)] and is now applied to the non-Hermitian RMT ensembles. This diagnostic provides a way to probe long-range spectral correlations in the complex plane.

Before discussing results, it is useful to recall that the spectra of non-Hermitian random matrices are rescaled to lie within the unit disk $|z| < 1$, ensuring that the mean level spacing scales appropriately with system size. The eigenvalue density of these ensembles is rotationally invariant, as shown earlier in Fig. A.1. For the

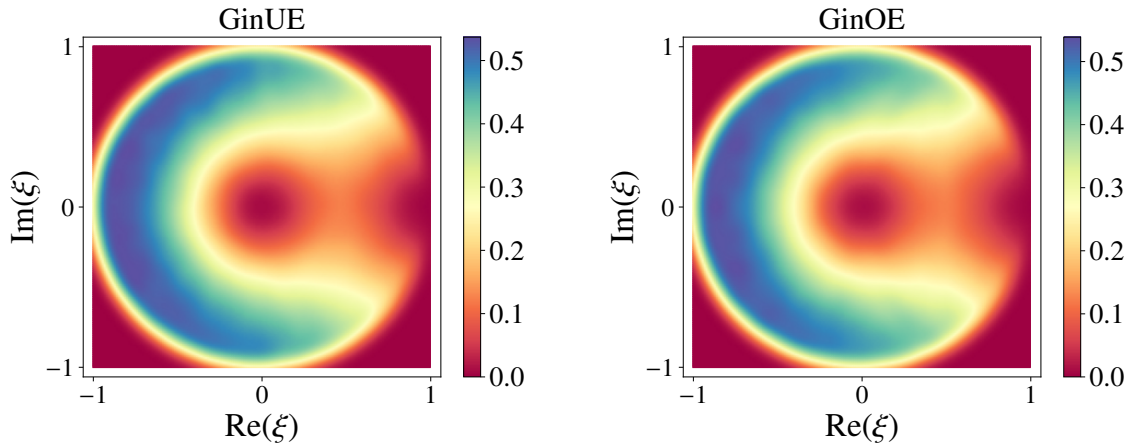

(a) GinUE (b) GinOE

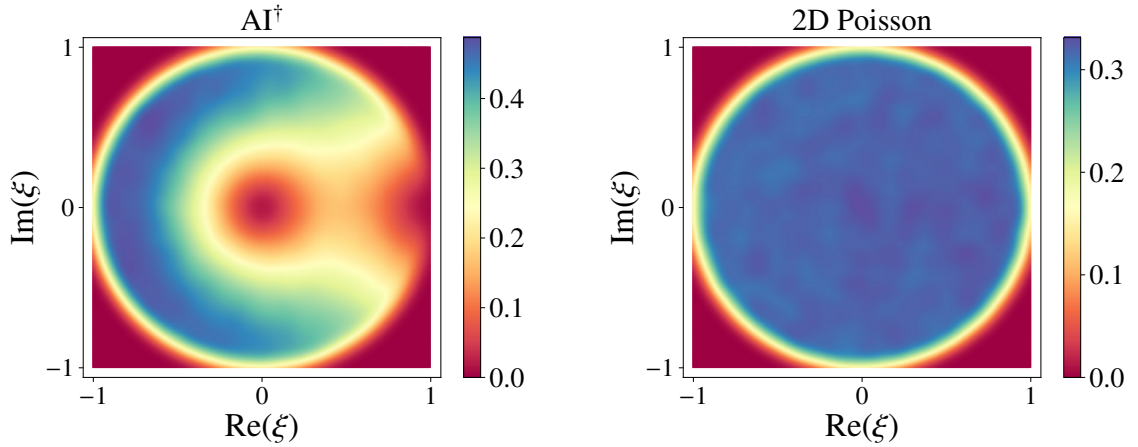

(c) AI† (d) Uncorrelated levels

Figure A.3: Distribution of complex spacing ratios in the complex plane for non-Hermitian random ensembles. Ginibre ensemble scatter plot has some quantitative contrasting features than the AI† plot, and the uncorrelated levels spacing ratios are distributed uniformly in the unit circle.

GinUE, the DSFF has an analytic form [207],

$$K_{\text{GinUE}}(\tau,\tau^*) = 1 + \mathcal{N}\,{}_1F_1\left(\mathcal{N}+1;2;-\frac{|\tau|^2}{4\mathcal{N}}\right)^2 - \sum_{n,m=0}^{\mathcal{N}-1}\frac{(\max(m,n)!)^2}{\mathcal{N}n!m!(|m-n|!)^2}\,{}_1F_1\left(\max(m,n)+1;|m-n|+1;-\frac{|\tau|^2}{4\mathcal{N}}\right)^2 \quad \text{(A.1)}$$

where ${}_1F_1(a,b;z) = \sum_{n=0}^{\infty} a^{(n)}z^n/b^{(n)}n!$ is the confluent Kummer hypergeometric function. In the large-$\mathcal{N}$ limit, retaining the leading terms gives [207],

$$K_{\text{GinUE}}(\tau,\tau^*) = 1 + \mathcal{N}\frac{4J_1(|\tau|)^2}{|\tau|^2} - \exp\left(-\frac{|\tau|^2}{4\mathcal{N}}\right) \quad \text{(A.2)}$$

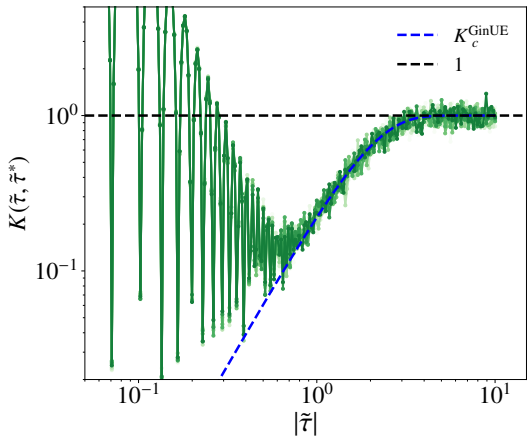

(a) GinUE

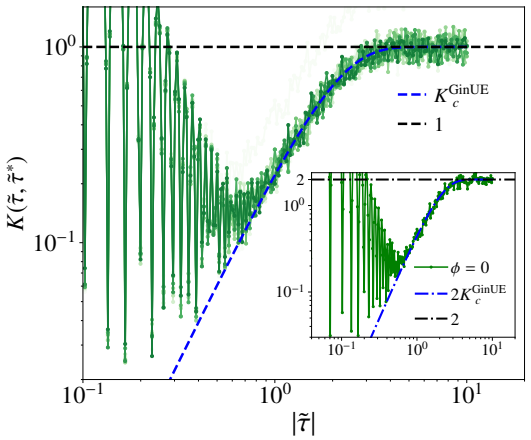

(b) GinOE

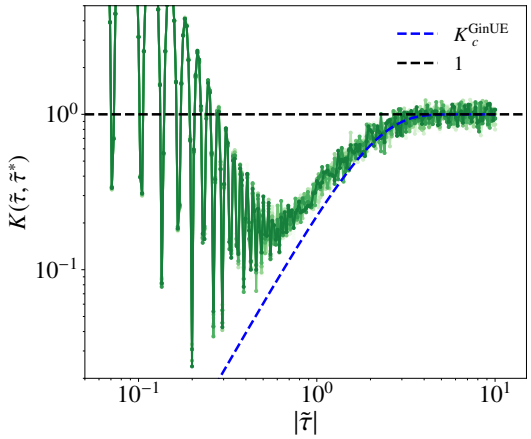

(c) AI†

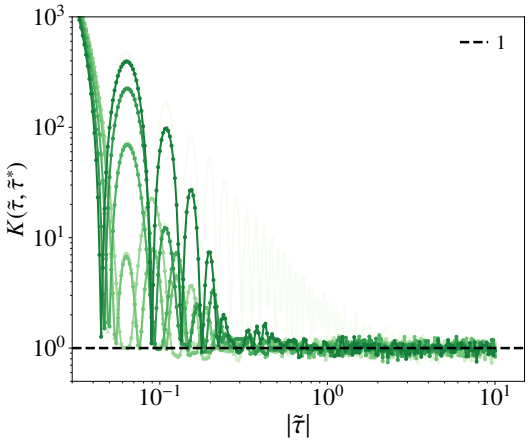

(d) Complex Uncorrelated levels

Figure A.4: DSFF vs. $|\tau|$ for non-Hermitian ensembles as a function of rescaled time variable $|\tilde{\tau}|$ for different values of $\phi \in [\pi/20, 9\pi/20]$ shown for different values of $\phi \in [\pi/20, 9\pi/20]$ in increments of $\pi/20$, with lighter shades corresponding to smaller ϕ values and darker shades to larger ones. All results are for $N = 10^4$. The DSFF has been normalized such that GinUE and Poisson classes saturate to one at long times. The blue dashed line represents the analytical form of DSFF for GinUE (K_c^{GinUE}), while the black line corresponds to a horizontal line representing unity. The inset in plot (b) shows the DSFF for GinOE at $\phi = 0$, whose ramp matches precisely with $2K_c^{\mathrm{GinUE}}$.

where $J_\mu(x)$ is the Bessel function of the first kind.

For the complex uncorrelated levels, the DSFF is given by,

$$K_{\mathrm{Poi}}\ (\tau, \tau^*) = 1 + (\mathcal{N} - 1)e^{-|\tau|^2} \tag{A.3}$$

Here, K_{Poi} starts from $\mathcal{N}$ at small times but decays rapidly since eigenvalues are completely uncorrelated. Asymptotically, it reaches 1, coming from the diagonal

contributions ($m = n$ terms in Eq. (3.7)).

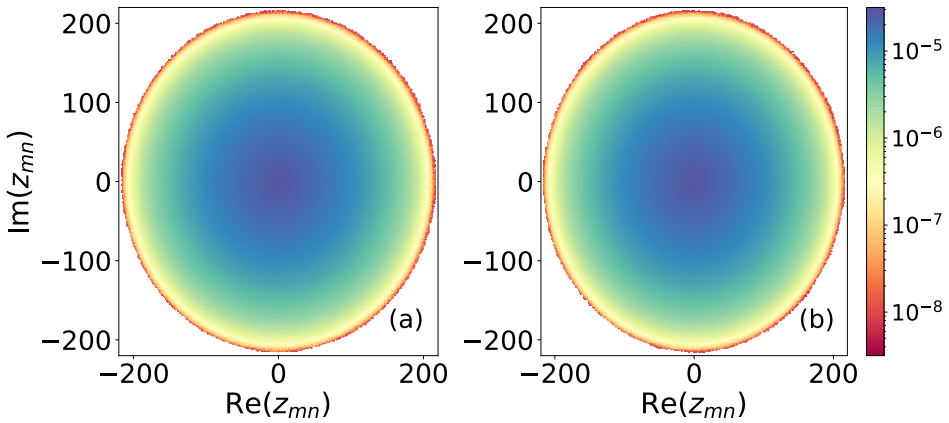

(a) GinUE

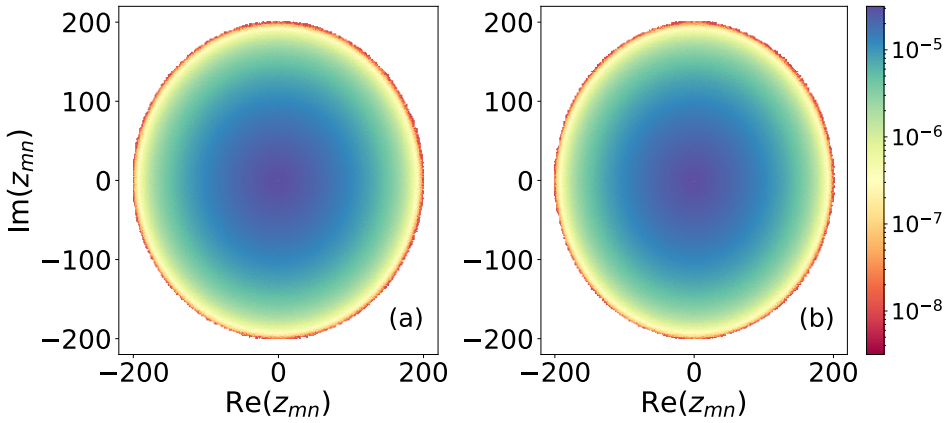

(b) GinOE

Figure A.5: Distributions of pairwise eigenvalue differences $z_{mn} = z_m - z_n$ for (a) GinUE and (b) GinOE ensembles. Both ensembles exhibit approximate rotational symmetry in the complex plane, consistent with the isotropic nature of their eigenvalue distributions.

Now, we discuss some exceptional cases within RMT. For GinOE, the spectrum consists of both real eigenvalues and complex-conjugate pairs. The fraction of real eigenvalues decreases with increasing matrix size, but their presence has a significant effect on spectral diagnostics. In particular, the complex-conjugate pairs give rise to effective two-fold accidental degeneracies when the differences $\{z_{mn}\}$ are projected onto the $\phi = 0$ direction, while the real eigenvalues produce accidental degeneracies along the radial axis when projected at $\phi = \pi/2$ for which the analytical expression is not known. Consequently, DSFF for $\phi = 0$ exactly twice the DSFF for GinUE ($K_c^{\mathrm{GinOE}}|_{\phi=0} = 2K_c^{\mathrm{GinUE}}$) in the limit of large matrix size. For generic projection angles ϕ away from 0 and $\pi/2$, the GinOE ensemble reproduces the results of the GinUE. Similar degeneracies appear in the GinSE class, although for different reasons [207], which is beyond the scope of this work.

In Fig. A.4, the DSFF obtained from Eq. (3.7) is shown as a function of rescaled time variable $|\tilde{\tau}|$ for different non-Hermitian ensembles. The rescaled time variable is defined as $\tilde{\tau} = \tau/\tau_H$, where τ_H is equal to $\sqrt{\mathcal{N}}$ for non-Hermitian ensembles. The DSFF captures universal spectral correlations and exhibits the characteristic "dip-ramp-plateau" structure, analogous to the spectral form factor (SFF) in Hermitian ensembles [44]. For GinUE, the numerical DSFF agrees well with the analytical ramp from Eq. (A.2). GinOE shows angle-dependent behavior due to the presence of real and conjugate-pair eigenvalues, but for general projection angles, its DSFF follows that of GinUE up to an overall multiplicative factor. For the $\mathrm{AI}^\dagger$ ensemble, the DSFF shows systematic deviations from Ginibre statistics, consistent with its different symmetry class, while the Poisson ensemble displays exponential decay in the absence of correlations.

Figure A.5 illustrates the distribution of pairwise eigenvalue differences $z_{mn} = z_m - z_n$ for GinUE and GinOE ensembles. Both ensembles display the expected rotational symmetry in the complex plane, reflecting the isotropy of their spectra.

Overall, for large $\mathcal{N}$, the DSFF for Ginibre ensembles grows quadratically at intermediate times, $K_{\mathrm{GinUE}} \simeq |\tau|^2/4$, before saturating to a constant value in the long-time limit. This "quadratic ramp" is the hallmark of chaotic spectral correlations in non-Hermitian matrices.

B

Spectral Properties of Disordered Interacting Non-Hermitian Systems

B.1 Distribution of complex energy differences

In this appendix, we discuss the distribution of the difference in complex energies $z_{mn} = z_m - z_n$. This analysis is of pivotal importance since it is the main ingredient in dissipative spectral form factor (DSFF), which captures all long-range correlations of complex eigenvalues [Eq. (3.7)]. In Fig. B.1, the distribution of z_{mn} for two distinct representative samples in the complex plane for all three models in the chaotic regime is shown. The color map shows the density of these energy differences.

The energy spectra for the disordered systems in the complex plane are inhomogeneous and anisotropic. This is also reflected in the complex energy differences as seen in Fig. B.1. As a consequence, the DSFF as a function of $|\tau|$ depends on the choice of the angle $\phi = \arg(\tau)$. This is reflected in the early time behavior of the DSFF after the initial dip. At intermediate times, the DSFF is robust to this ϕ variation, thereby leading to a universal ramp feature. The late time behavior is manifested as a plateau, which is ϕ independent as expected. Such ϕ dependency in DSFF, which stems from the lack of rotational symmetry in the energy spectrum and energy differences, is absent in non-hermitian random matrix ensembles and certain non-hermitian models [207].

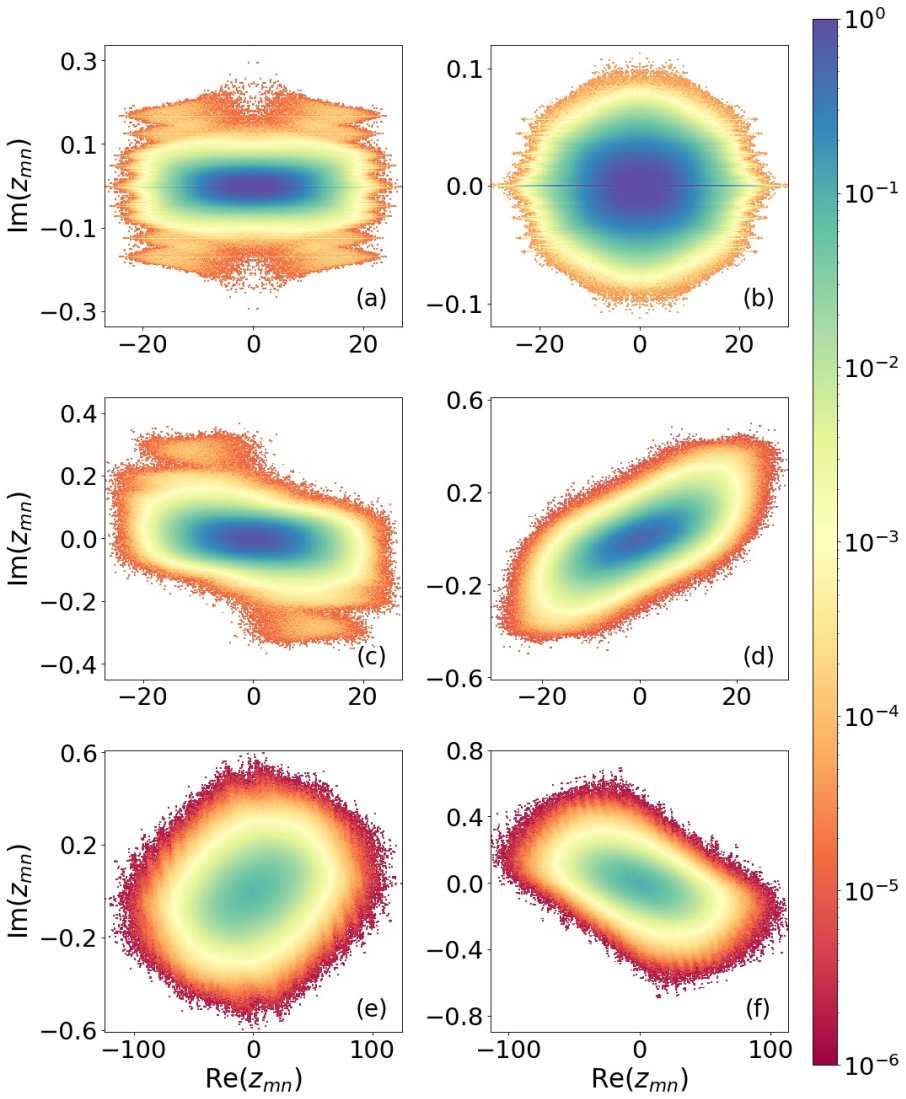

Figure B.1: Distribution of complex energy difference considering two separate disorder samples each for Model-I [(a),(b)] ($h = 2$), Model-II [(c),(d)] ($h = 2$) and Model-III ($h = 14, \alpha = 0$) [(e),(f)] at system size $L = 16$. The color map shows the density of the energy differences z_{mn} in the complex plane. This clearly shows the lack of rotational symmetry, unlike non-hermitian random matrix ensembles.

B.2 Estimation of Heisenberg time

Here, we discuss the calculation of the Heisenberg time for the models. For the DSFF of model-I to agree with the analytical form of the DSFF for GinOE random matrices given by Eq. (3.10), we define the Heisenberg time scale τ_H which scales the bare time τ as $\tilde{\tau} = \tau/\tau_H$. To estimate τ_H, one first locates the time scale τ^* after which the DSFF shows universal behavior (non-linear ramp) and fits the curve

$$f_K(\tau, m) = 1 - \exp\left[-m|\tau|^2\right] \tag{B.1}$$

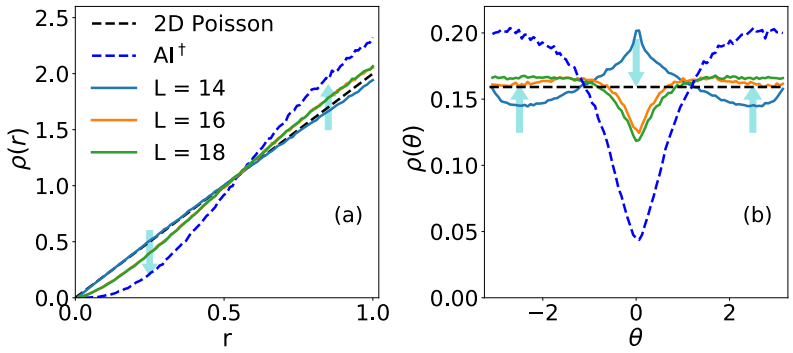

Figure B.2: [Model-II, Eq. (3.2)] Marginal distributions for (left) r and (right) θ for $h = 4$ for different system sizes L for entire spectrum statistics. We find evidence of deviations from the expected RMT behavior due to the finite-size effect. In other words, upon increasing system size, we notice that our results approach those of marginal distributions for AI† symmetry class.

with the numerical data of the DSFF where m is the fitting parameter and τ_H is extracted as $\tau_H = \frac{1}{2\sqrt{m}}$. For better accuracy, we calculate τ_H for different choices of ϕ and take the average over ϕ to calculate the Heisenberg time used for rescaling the time axis in Fig. 3.5. In the case of model-II and model-III, we compare the numerical data with the DSFF of AI† symmetry class for which the analytical expression is not known yet. However, we use the same fitting function Eq. (B.1) to get an estimate of τ_H (just like model-I) and use that to shift the numerical result for AI† symmetry class to show agreement between model-II/model-III with that of AI† symmetry class. This procedure of estimating τ_H works well because the DSFF for GinOE and AI† symmetry class have common basic features despite having different functional variations as depicted in the inset of Fig. 3.6.

B.3 Finite-size effects in complex spacing ratio

Now we discuss the deviation of the complex spacing ratios (CSR) from the RMT predictions for the models at the intermediate disorder strengths between the chaotic and the localized regimes. In the main text, the DSFF and the CSR for different models are shown deep in the chaotic and the localized regime, where there is good agreement with the corresponding RMT/ Poisson statistics at the system size $L = 18$. However, this does not hold for intermediate disorder strengths near the critical point for the localization transition, where both the DSFF and CSR are prone to finite-size effects.

Fig. B.2 shows the variation of both the marginal distributions of r and θ for different system sizes at $h = 4$ for model-II, which corresponds to the intermediate

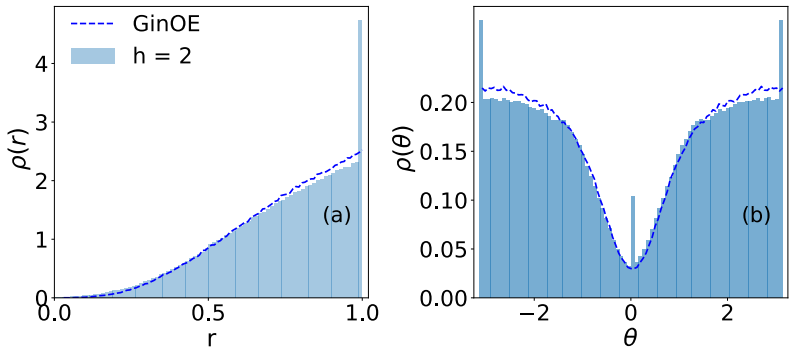

Figure B.3: [Model-I, Eq. (3.1)] Marginal distributions of (left) r and (right) θ at $h = 2$ for system size $L = 18$ considering only middle of spectrum. Both the distributions agree with that of GinOE (blue Dashed).

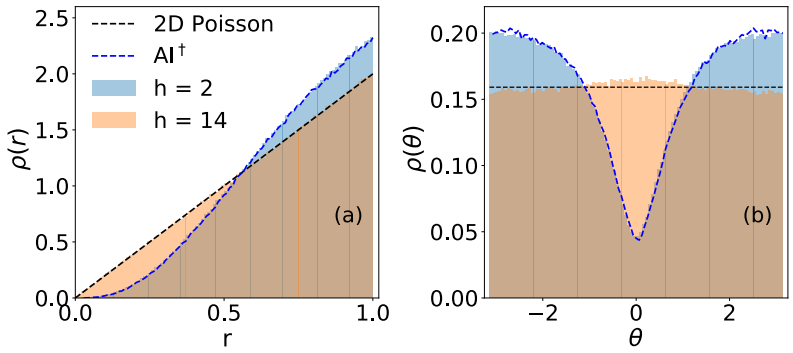

Figure B.4: [Model-II, Eq. (3.2)] Marginal distributions of (left) r and (right) θ at $h = 2$ (blue) and $h = 14$ (orange) for system size $L = 18$ considering only middle of the spectrum. The distributions agree perfectly with that of AI† symmetry class (blue dashed) and 2D Poisson statistics (black dashed) at $h = 2$ and $h = 14$ respectively.

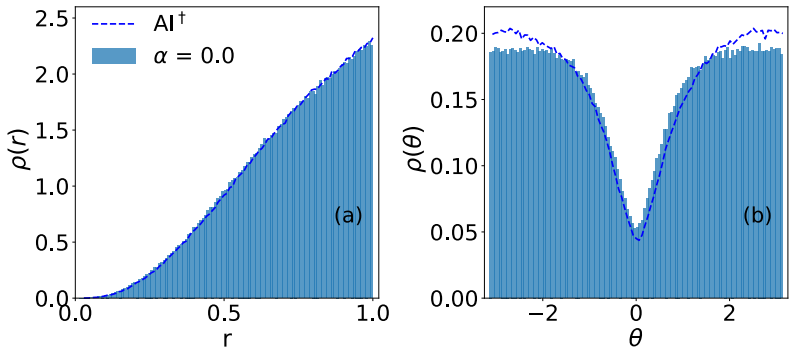

Figure B.5: [Model-III, Eq. (3.3)] Marginal distributions of (left) r and (right) θ at $h = 14$, $\alpha = 0$ for system size $L = 16$ considering only middle of the spectrum. The distributions agree well with that of the AI† class.

disorder strength for this model. For system size, $L = 14$, both the marginal distributions show similarity with the 2D Poisson statistics, implying uncorrelated

	GinOE	h							1D P
		2	4	6	8	10	12	14	
$-\langle\cos\theta\rangle$	0.244	0.196	0.018	0.023	×	×	×	×	×
$\langle r\rangle$	0.738	0.736	0.703	0.553	0.508	0.502	0.501	0.5	1/2
$-\langle\cos\theta\rangle_M$	0.244	0.228	0.039	0.019	×	×	×	×	×
$\langle r\rangle_M$	0.738	0.737	0.723	0.564	0.509	0.502	0.501	0.5	1/2

Table B.1: [Model-I] Average of r and $\cos\theta$ for different disorder strength h using entire spectrum and the middle of the spectrum. The subscript M in the first column represents the average extracted for the middle of the spectrum. Since model-I goes through a complex-real transition as the disorder is increased, the θ variable is ill-suited for $h \geq 6$. These parameter regimes are therefore represented by $\times$ in the row of $-\langle\cos\theta\rangle_M$.

	AI†	h							2D P
		2	4	6	8	10	12	14	
$-\langle\cos\theta\rangle$	0.193	0.16	0.039	−0.005	−0.011	−0.015	−0.021	−0.028	0
$\langle r\rangle$	0.722	0.722	0.686	0.669	0.668	0.667	0.667	0.666	2/3
$-\langle\cos\theta\rangle_M$	0.193	0.186	0.071	0.007	−0.001	−0.003	−0.007	−0.014	0
$\langle r\rangle_M$	0.722	0.722	0.692	0.669	0.667	0.667	0.667	0.667	2/3

Table B.2: [Model-II] Average of r and $\cos\theta$ for different disorder strength using entire spectrum and middle of the spectrum (denoted by subscript M) at system size $L = 18$.

random complex energy levels. This, in fact, turns out to be a finite-size effect, and as the system size increases, both the quantities deviate from the Poisson statistics and tend to approach the statistics of the AI† symmetry class. However, it never reaches the statistics of this symmetry class for the choice of system sizes, making the analysis inconclusive for intermediate disorder strengths. Similarly, for other intermediate values of disorder strength h for all the models, finite-size effects can be visible both in the marginal distribution and DSFF, which makes the identification of the critical parameter for the chaotic-localization transition difficult.

B.4 Complex level spacing ratio for middle of the spectrum

In section 3.4.2, the marginal distributions of r and θ for the complex spacing ratio (CSR) were computed using the entire spectrum. These distributions in Figs. 3.8, 3.9, 3.10 show good agreement with the marginal distributions for the random matrices and Poisson statistics in both the chaotic and the localized

	AI†	α				2D P
		0.0	0.5	1.5	4.0	
$-\langle\cos\theta\rangle$	0.193	0.069	−0.041	−0.032	−0.047	0
$\langle r\rangle$	0.722	0.715	0.7	0.667	0.664	2/3
$-\langle\cos\theta\rangle_M$	0.193	0.147	0.104	−0.004	−0.021	0
$\langle r\rangle_M$	0.722	0.72	0.705	0.67	0.666	2/3

Table B.3: [Model-III] Average of r and $\cos\theta$ for different α at disorder strength $h = 14$ using the entire spectrum and the middle of the spectrum (denoted by subscript M) at system size $L = 16$.

regimes, respectively. However, there are minor discrepancies that are rooted in contributions coming from complex eigenvalues close to the edges. A common practice is to consider the middle of the spectrum. The prescription we employ when we refer to the middle of the spectrum is as follows. We consider ±10% span of the complex spectrum from its centre/middle.

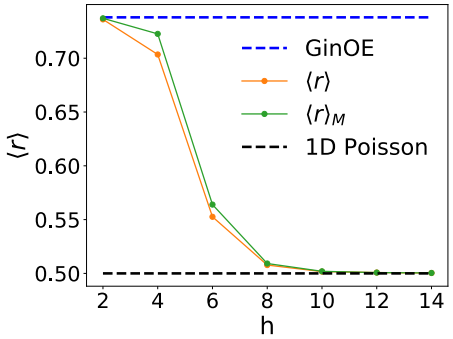

Figure B.6: [Model-I, Eq. (3.1)] Average of $\langle r\rangle$ and $\langle r\rangle_M$ as a function of disorder strength h for system size $L = 18$. Here $\langle r\rangle_M$ is defined by taking only the middle of the spectrum.

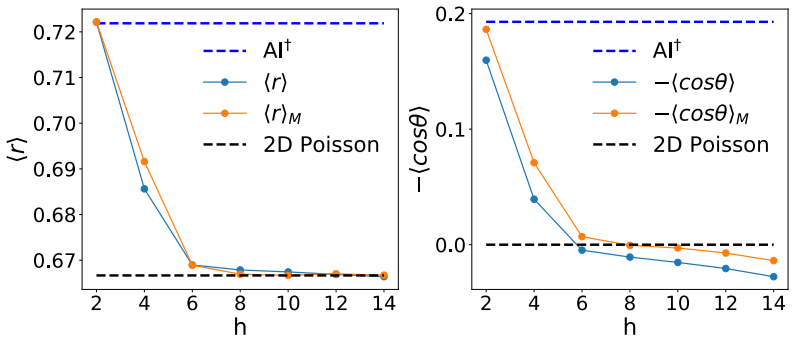

Figure B.7: [Model-II, Eq. (3.2)] (left) Average of $\langle r\rangle$ and $\langle r\rangle_M$, and (right) average of $-\langle\cos\theta\rangle$ and $-\langle\cos\theta\rangle_M$ as a function of disorder strength h for system size $L = 18$. Here again, $\langle.\rangle_M$ is defined by taking only the middle of the spectrum.

In Fig. B.3, we show the marginal distributions of r and θ in the chaotic regime

($h = 2$) for model-I (Eq. (3.1)). Both these distributions agree very well with GinOE, and the comparison is much better than Fig. 3.8, where the entire spectrum was considered. Fig. B.4 shows the spacing ratio distributions for $h = 2$ and $h = 14$ with $L = 18$ for model-II (Eq. (3.2)). One can see that the marginal distributions are in perfect agreement with those of $\text{AI}^{\dagger}$ and 2D Poisson statistics at $h = 2$ and $h = 14$, respectively. The agreement is better than the one shown in Fig. 3.9, which was made considering the entire spectrum. In Fig. B.5, we show similar agreement for the middle of the spectrum for model-III (Eq. (3.3)).

In addition to the marginal distributions, we also compute the average value of r and $\cos\theta$ for all three models. These are tabulated in Tables B.1, B.2 and B.3. The quantitative differences between the full spectrum and the middle of the spectrum are also highlighted in the three tables. In Fig. B.6, we show $\langle r \rangle$ versus disorder strength for model-I using both the entire spectrum and the middle of the spectrum. Similarly, Fig. B.7 shows $\langle r \rangle$ and $-\langle \cos\theta \rangle$ as a function of the disorder strength for model-II.

C

Quantum jumps in driven-dissipative disordered many-body systems

C.1 Construction of the ζ-deformed theory

In this Section, we first briefly review the quantum jump trajectory interpretation of standard Lindblad master equations. Later, we discuss the deformation of the Lindblad equation introduced in the main manuscript in the language of quantum jump trajectories. Finally, we connect this deformation to physical post-selection protocols and non-Hermitian Hamiltonians.

C.1.1 Quantum jump trajectory interpretation of standard Lindblad dynamics

Let us consider a generic open quantum many-body system described by the following standard Lindblad master equation [124, 125, 133]

$$\partial_t \rho(t) = \mathcal{L}\rho(t) \tag{C.1}$$

with the Liouvillian

$$\mathcal{L}\star = -\mathrm{i}\,[H, \star] + \sum_{\alpha=1}^{M} \mathcal{D}[O_\alpha]\star \tag{C.2}$$

where H is the (Hermitian) Hamiltonian, $\mathcal{D}[O]\star := O \star O^\dagger - \frac{1}{2}\left\{O^\dagger O, \star\right\}$ is the standard Lindblad dissipator, and the O_α's are the jump operators where $\alpha = 1, 2, \ldots M$ labels the dissipation channels. Let us start from a generic initial

state, described by a statistical mixture of pure states,

$$\rho(0) = \sum_m p_m |\psi_m(0)\rangle\langle\psi_m(0)| \,, \text{ with } \langle\psi_m(0)|\psi_m(0)\rangle = 1 \,, \; p_m > 0 \,, \text{ and } \sum_m p_m = 1 \tag{C.3}$$

At time t, the state of the system is given by

$$\rho(t) = \mathrm{e}^{\mathcal{L}t}\rho(0) \tag{C.4}$$

The standard quantum-trajectory interpretation of the Lindblad dynamics [128–133] involves separating the term responsible for the quantum jumps as

$$\mathcal{L} = \mathcal{L}_0 + \mathcal{L}_\mathrm{J} \tag{C.5}$$

with the quantum-jump contribution reading

$$\mathcal{L}_\mathrm{J} \star := \sum_{\alpha=1}^{M} O_\alpha \star O_\alpha^\dagger \tag{C.6}$$

and $\mathcal{L}_0$ containing both the unitary dynamics generated by H and the non-Hermitian contribution from the dissipators,

$$\mathcal{L}_0 \star := -\mathrm{i}\tilde{H} \star + \star \, \mathrm{i}\tilde{H}^\dagger \tag{C.7}$$

Here, the effective non-Hermitian Hamiltonian $\tilde{H}$ is defined as

$$\tilde{H} := H - \frac{\mathrm{i}}{2}\sum_{\alpha=1}^{M} O_\alpha^\dagger O_\alpha \tag{C.8}$$

The time evolution of the density matrix given in Eq. (C.4) can now be formally re-expressed as a

$$\rho(t) = \sum_{n=0}^{\infty} \int_0^t \mathrm{d}\tau_n \cdots \int_0^{\tau_2} \mathrm{d}\tau_1 \mathrm{e}^{\mathcal{L}_0(t-\tau_n)} \mathcal{L}_\mathrm{J} \mathrm{e}^{\mathcal{L}_0(\tau_n-\tau_{n-1})} \cdots \mathrm{e}^{\mathcal{L}_0(\tau_2-\tau_1)} \mathcal{L}_\mathrm{J} \mathrm{e}^{\mathcal{L}_0\tau_1} \rho(0) \tag{C.9}$$

where

$$\mathrm{e}^{\mathcal{L}_0\lambda} \star = \mathrm{e}^{-\mathrm{i}\tilde{H}\lambda} \star \mathrm{e}^{\mathrm{i}\tilde{H}^\dagger\lambda} \tag{C.10}$$

for any parameter λ. The expression in Eq. (C.9) can be interpreted as a Dyson series that sums over all the possible quantum jumps interrupting the dynamics generated by $\mathcal{L}_0$. The $n = 0$ term corresponds to the non-Hermitian (no-jump) evolution. Equation (C.9), along with Eq. (C.3), can be further rewritten as,

$$\rho(t) = \sum_{n=0}^{\infty} \rho_n(t) \tag{C.11}$$

where the operator $\rho_n(t)$ is the contribution to the density matrix corresponding to evolution with a fixed number n of quantum jumps occurring between time $t = 0$ and t, and that reads

$$\rho_0(t) = \mathrm{e}^{\mathcal{L}_0 t}\rho(0) \tag{C.12}$$

$$\rho_n(t) = \sum_m p_m \underbrace{\sum_{\alpha_1=1}^{M} \cdots \sum_{\alpha_n=1}^{M} \int_0^t \mathrm{d}\tau_n \cdots \int_0^{\tau_2} \mathrm{d}\tau_1}_{\text{sum over all trajectories with } n \text{ jumps}} P_m^{\boldsymbol{\alpha}_n,\boldsymbol{\tau}_n}(t) \left|\psi_m^{\boldsymbol{\alpha}_n,\boldsymbol{\tau}_n}(t)\right\rangle \left\langle\psi_m^{\boldsymbol{\alpha}_n,\boldsymbol{\tau}_n}(t)\right| \ , \ n \geq 1 \tag{C.13}$$

The symbols $\boldsymbol{\alpha}_n$ and $\boldsymbol{\tau}_n$ stand for the sequence of jump channels $(\alpha_1, \alpha_2, \ldots, \alpha_n)$ and jump times $(\tau_1, \tau_2, \ldots, \tau_n)$, respectively, and used Eq. (C.10) in writing Eq. (C.13). Along with the initial state index m, these two sequences define a single quantum trajectory between time $t = 0$ and t with a total of n quantum jumps. $\left|\psi_m^{\boldsymbol{\alpha}_n,\boldsymbol{\tau}_n}(t)\right\rangle$ is the normalized conditional wave function of the system at time t which started in state $|\psi_m(0)\rangle$ and underwent an evolution with the precise sequence of jump channels $\boldsymbol{\alpha}_n$ and jump times $\boldsymbol{\tau}_n$. It reads

$$\left|\psi_m^{\boldsymbol{\alpha}_n,\boldsymbol{\tau}_n}(t)\right\rangle = \frac{\left|\tilde{\psi}_m^{\boldsymbol{\alpha}_n,\boldsymbol{\tau}_n}(t)\right\rangle}{\sqrt{P_m^{\boldsymbol{\alpha}_n,\boldsymbol{\tau}_n}(t)}} \tag{C.14}$$

where

$$\left|\tilde{\psi}_m^{\boldsymbol{\alpha}_n,\boldsymbol{\tau}_n}(t)\right\rangle := \mathrm{e}^{-\mathrm{i}\tilde{H}(t-\tau_n)} O_{\alpha_n} \mathrm{e}^{-\mathrm{i}\tilde{H}(\tau_n-\tau_{n-1})} O_{\alpha_{n-1}} \cdots \mathrm{e}^{-\mathrm{i}\tilde{H}(\tau_2-\tau_1)} O_{\alpha_1} \mathrm{e}^{-\mathrm{i}\tilde{H}\tau_1} |\psi_m(0)\rangle \tag{C.15}$$

and $P_m^{\boldsymbol{\alpha}_n,\boldsymbol{\tau}_n}(t)$ is the probability of a quantum trajectory introduced above, given by

$$P_m^{\boldsymbol{\alpha}_n,\boldsymbol{\tau}_n}(t) = \left\langle\tilde{\psi}_m^{\boldsymbol{\alpha}_n,\boldsymbol{\tau}_n}(t)\middle|\tilde{\psi}_m^{\boldsymbol{\alpha}_n,\boldsymbol{\tau}_n}(t)\right\rangle. \tag{C.16}$$

Importantly, the fact that $\rho_n(t)$ can be written in the form of $\sum_\mu P_\mu |\psi_\mu\rangle\langle\psi_\mu|$ with $P_\mu \geq 0$ ensures its positive semi-definiteness. $\mathrm{Tr}\,\rho_n(t)$ is precisely the probability of having experienced n quantum jumps from time $t = 0$ to t. This gives a probabilistic meaning to the quantum trajectories. The special case of trajectories with no jump ($n = 0$) corresponds to the evolution generated by the non-hermitian Hamiltonian $\tilde{H}$ in Eq. (C.8) [136, 184]:

$$|\psi(t)\rangle = \frac{\mathrm{e}^{-\mathrm{i}\tilde{H}t}|\psi(0)\rangle}{\sqrt{\langle\psi(t)|\psi(t)\rangle}} \tag{C.17}$$

Notably, taking the time-derivative of Eq. (C.13), one may check that the dynamics of the operators $\rho_n(t)$ follow

$$\partial_t \rho_n(t) = \mathcal{L}_0 \rho_n(t) + \mathcal{L}_\mathrm{J} \rho_{n-1}(t) \text{ for } n \geq 1 \tag{C.18}$$

$$\partial_t \rho_0(t) = \mathcal{L}_0 \rho_0(t) \tag{C.19}$$

This expresses the fact that a quantum state at time t that is the result of $n-1$ jumps may either evolve linearly to time $t + \mathrm{d}t$ under the action of $\tilde{H}$ or be subject to an n^{th} jump.

C.1.2 ζ-deformed Lindblad dynamics

Starting from Eq. (C.11), and its quantum trajectory interpretation, we now generalize the trajectory ensemble to a grand canonical ensemble by introducing a quantum jump fugacity ζ, with $0 \leq \zeta \leq 1$, which weights the trajectories with different numbers of jumps n. From this perspective, the number of quantum jumps n is analogous to the number of particles in the standard construction of statistical mechanics. The corresponding grand-canonical density matrix is constructed as

$$\rho_\zeta(t) := \frac{1}{Z_\zeta(t)} \sum_{n=0}^{\infty} \zeta^n \rho_n(t)\,, \text{ where } Z_\zeta(t) := \sum_{n=0}^{\infty} \zeta^n \mathrm{Tr}[\rho_n(t)] \tag{C.20}$$

is the grand-canonical partition function, ensuring $\mathrm{Tr}[\rho_\zeta(t)] = 1$ at all times and where $\rho_n(t)$ is given in Eq. (C.13). The original density matrix $\rho(t)$ in Eq. (C.11) is recovered by setting $\zeta = 1$ in Eq. (C.20). The no-jump case is recovered by setting $\zeta = 0$.

The time evolution of the grand-canonical density matrix $\rho_\zeta(t)$ introduced in Eq. (C.20) can be computed by using the conditional evolution Eq. (C.18). One obtains the following ζ-deformed Lindblad master equation

$$\partial_t \rho_\zeta(t) = \Big(\mathcal{L}_\zeta - \mathrm{Tr}\left[\mathcal{L}_\zeta \rho_\zeta(t) \right] \Big) \rho_\zeta(t), \tag{C.21}$$

where the ζ-deformed Liouvillian

$$\mathcal{L}_\zeta := \mathcal{L}_0 + \zeta \mathcal{L}_\mathrm{J} = -\mathrm{i}\,[H, \star] + \sum_\alpha \left[\zeta O_\alpha \star O_\alpha^\dagger - \frac{1}{2} \left\{ O_\alpha^\dagger O_\alpha, \star \right\} \right]. \tag{C.22}$$

The evolution in Eq. (C.21) interpolates between the no-jump evolution at $\zeta = 0$ and the original Lindblad master equation in Eq. (C.1) at $\zeta = 1$. Note that the trace term in Eq. (C.21) stems from the factor $Z_\zeta(t)$ in Eq. (C.20) and $\partial_t Z_\zeta(t) = Z_\zeta(t)\,\mathrm{Tr}[\mathcal{L}_\zeta \rho_\zeta(t)]$. This trace term ensures the trace-preserving property of the dynamics of $\rho_\zeta(t)$ and makes the ζ-deformed Lindblad master equation non-linear.

However, the density matrix in the ζ-deformed theory can be linearly related to the initial density matrix of the non-deformed theory via

$$\rho_\zeta(t) = \frac{1}{Z_\zeta(t)} e^{\mathcal{L}_\zeta t} \rho(0) \tag{C.23}$$

Equation (C.23) may be checked by direct substitution into Eq. (C.21) and implies a re-expression of the ζ-deformed partition function as

$$Z_\zeta(t) = \mathrm{Tr}[e^{\mathcal{L}_\zeta t} \rho(0)] \tag{C.24}$$

Moreover, Eq. (C.23) shows that the operator $\rho_\zeta(t)$ inherits its Hermiticity property from $\rho(0)$. The positive semi-definite property of $\rho_\zeta(t)$ is ensured by the probabilistic interpretation of $\rho_n(t)$ in terms of quantum trajectories discussed in Eq. (C.13). Alternatively, this can be seen by recasting the infinitesimal evolution operator $1 - \mathcal{L}\delta t$ in a Kraus form and using the Kraus theorem. Therefore, $\rho_\zeta(t)$ has all the expected properties of a well-defined density matrix. Importantly, when evolving with the ζ-deformed Liouvillian, the non-negative quantity $\zeta^n \,\mathrm{Tr}\, \rho_n(t)$ is precisely the probability of having experienced n quantum jumps from time $t = 0$ to t. This interpretation is equivalent to the imperfect detection scheme that was discussed in Ref. [138].

C.2 Possible Implementation Schemes

C.2.1 Post-selection interpretation at $\zeta < 1$

Having established the mathematical consistency of the ζ-deformed theory, we now provide a physical interpretation of this deformation. A natural motivation arises from considering post-selection protocols based on imperfect detectors. The idea is to model the dynamics through quantum trajectories while accounting for the finite efficiency of realistic measurement devices. Figure 4.1 schematically illustrates this setting.

The scheme can be summarized as follows. Gain and loss events are monitored by realistic detectors with efficiency $1 - \zeta$. Post-selection is performed by retaining only those trajectories where the monitoring fails to register certain jump events. As a consequence, depending on the detection efficiency, some trajectories are conditionally included or discarded, leading to the effective dynamics described by the ζ-deformed Liouvillian.

To illustrate this concretely, it is useful to consider three cases, corresponding to perfect, completely faulty, and realistic detectors.

	Post-selection Rule on Trajectories	**Resulting Dynamics**
Perfect detector $\zeta = 0$	$\{0,0,0,0,0,0,0,0,0,0\} \rightarrow$ keep $\{0,0,1,0,0,1,0,0,0,0\} \rightarrow$ discard Only trajectories with no detected jumps are retained.	Non-Hermitian Hamiltonian evolution
Completely faulty detector $\zeta = 1$	$\{0,0,0,0,0,0,0,0,0,0\} \rightarrow$ keep $\{0,0,1,0,0,1,0,0,0,0\} \rightarrow$ keep All trajectories are retained regardless of detected jumps.	Standard Lindblad dynamics
Realistic detector $0 < \zeta < 1$	$\{0,0,0,0,0,0,0,0,0,0\} \rightarrow$ keep $\{0,0,1,0,0,1,0,0,0,0\} \rightarrow$ keep with probability ζ^2 Trajectories containing jumps are kept probabilistically according to detector imperfection.	ζ-Deformed Liouvillian dynamics

Table C.1: Summary of the post-selection protocols corresponding to different detector efficiencies ζ. The symbols $\{0,1\}$ represent the occurrence of no jump or a quantum jump, respectively, at discrete times along a trajectory.

This interpretation highlights how the ζ-deformation can be physically realized through controlled detector inefficiency and appropriate post-selection. It provides not only a consistent theoretical construction but also a potential route for experimental implementation using realistic measurement protocols.

C.2.2 Another Scheme

Here, we provide another possible implementation that was recently proposed in Ref. [138]. Let us consider the original system, evolving with the original Liouvillian $\mathcal{L}$. Each dissipation channel can always be thought of as coupling the system to baths. Consider each channel coupled to two identical baths with coupling strengths $\sqrt{\zeta}$ and $\sqrt{1-\zeta}$, respectively. This amounts to formally rewriting

the original Liouvillian as

$$\mathcal{L}\star = -\mathrm{i}[H,\star] + \underbrace{\zeta\sum_{\alpha=1}^{M}\mathcal{D}[O_\alpha]\star}_{\text{non-monitored}} + \underbrace{(1-\zeta)\sum_{\alpha=1}^{M}\mathcal{D}[O_\alpha]\star}_{\text{monitored}} \tag{C.25}$$

Instead of system-bath couplings, such a decomposition can also be seen as coupling each of the dissipation channels to a beam splitter which sends the particle into two detectors with probability ζ and $1-\zeta$, respectively. The post-selection protocol consists of constantly monitoring the latter bath/detector only. The results of this monitoring are used to post-select the quantum trajectories with no-jump with respect to the monitored bath/detector. The resulting dynamics is equivalent to erasing the jump term from the second Lindblad term in Eq. (C.25). It is now described by

$$\mathcal{L}_\zeta = -\mathrm{i}\,[H,\star] + \sum_\alpha\left[\zeta O_\alpha \star O_\alpha^\dagger - \frac{1}{2}\left\{O_\alpha^\dagger O_\alpha,\star\right\}\right] \tag{C.26}$$

After normalizing observables with respect to the number of post-selected trajectories, in the limit of a large number of these, the results will match the ones computed from the dynamics governed by the trace-preserving Eq. (C.21).

C.3 Connection to full counting statistics

In this Section, we exploit the connection of the ζ-deformed theory to full counting statistics to relate the imbalance to an analog of a thermodynamic quantity, namely the activity.

In the limit $\zeta = 1$, the partition function introduced in Eq. (C.20) can be seen as a moment generating function for the number of quantum jumps, or the activity in the language of full counting statistics, with ζ serving as the counting field. The time-dependent free energy, or the cumulant generating function, is defined as

$$F_\zeta(t) := \ln Z_\zeta(t) = \ln\left(\sum_{n=0}^{\infty}\zeta^n\,\mathrm{Tr}[\rho_n(t)]\right) \tag{C.27}$$

Consequently, one gets

$$\frac{\partial}{\partial\ln\zeta}F_\zeta(t) = \langle\mathcal{R}(t)\rangle_\zeta =: \zeta\,\mathcal{A}(t) \tag{C.28}$$

where $\langle\mathcal{R}(t)\rangle_\zeta$ is the average number of quantum jumps in the ζ-deformed theory,

$$\langle\mathcal{R}(t)\rangle_\zeta = \sum_{n=0}^{\infty} n\,\zeta^n\,\mathrm{Tr}[\rho_n(t)] \geq 0 \tag{C.29}$$

and $\mathcal{A}(t)$ is the so-called dynamical activity. Taking another derivative with respect to $\ln \zeta$ yields

$$\frac{\partial}{\partial \ln \zeta}\langle \mathcal{R}(t)\rangle_\zeta = \langle \mathcal{R}(t)^2\rangle_\zeta - \langle \mathcal{R}(t)\rangle_\zeta^2 \geq 0 \tag{C.30}$$

implying that the average number of quantum jumps between time $t = 0$ and t is a non-decreasing function of ζ. Naturally, the number of quantum jumps is also a non-decreasing function of t. The associated rate of quantum jumps is directly related to the rate of dynamical activity, given by

$$\dot{\mathcal{A}}(t) = \frac{1}{\zeta}\,\partial_t \langle \mathcal{R}(t)\rangle_\zeta \geq 0 \tag{C.31}$$

$\dot{\mathcal{A}}(t)$ can be computed by first taking the derivative of $F_\zeta(t)$ with respect to ζ and subsequently taking another derivative with respect to t

$$\dot{\mathcal{A}}(t) = \frac{\partial^2}{\partial t\,\partial \zeta} F_\zeta(t) \tag{C.32}$$

The former yields

$$\frac{\partial}{\partial \zeta} F_\zeta(t) = \frac{1}{Z_\zeta(t)} \int_0^t \mathrm{d}\tau\ \mathrm{Tr}\left[\mathrm{e}^{\mathcal{L}_\zeta (t-\tau)} \mathcal{L}_\mathrm{J} \mathrm{e}^{\mathcal{L}_\zeta \tau} \rho(0)\right] \tag{C.33}$$

and the latter yields

$$\begin{aligned}\dot{\mathcal{A}}(t) &= \mathrm{Tr}\left[\mathcal{L}_\mathrm{J}\rho_\zeta(t)\right] \\ &- \frac{1-\zeta}{Z_\zeta(t)} \int_0^t \mathrm{d}\tau\ \mathrm{Tr}\left[\left(\mathcal{L}_\mathrm{J} - \mathrm{Tr}\left[\mathcal{L}_\mathrm{J}\rho_\zeta(t)\right]\right) \mathrm{e}^{\mathcal{L}_\zeta (t-\tau)} \left(\mathcal{L}_\mathrm{J} - \mathrm{Tr}\left[\mathcal{L}_\mathrm{J}\rho_\zeta(\tau)\right]\right) \mathrm{e}^{\mathcal{L}_\zeta \tau} \rho(0)\right]\end{aligned} \tag{C.34}$$

This equation can finally be rewritten as,

$$\dot{\mathcal{A}}(t) = \left\langle \mathcal{L}_\mathrm{J}(t)\right\rangle - (1-\zeta) \int_0^t \mathrm{d}\tau\ \left\langle \left[\mathcal{L}_\mathrm{J}(t) - \langle \mathcal{L}_\mathrm{J}(t)\rangle\right] \left[\mathcal{L}_\mathrm{J}(\tau) - \langle \mathcal{L}_\mathrm{J}(\tau)\rangle\right] \right\rangle \tag{C.35}$$

where in Eq. (C.35) we introduced the notation

$$\langle \cdots \rangle := \frac{1}{Z_\zeta(t)} \mathrm{Tr}\left[\mathcal{T}\, \mathrm{e}^{\int_0^t \mathrm{d}\tau\, \mathcal{L}_\zeta} \cdots\ \rho(0)\right] \tag{C.36}$$

with the time-ordering operator $\mathcal{T}$ and $Z_\zeta(t)$ is given in Eq. (C.24). The Eq. (C.35) shows that for the standard Lindblad evolutions ($\zeta = 1$), the rate of dynamical

activity can be simply expressed in terms of a single-time observable. In the generic case $\zeta < 1$, the rate of dynamical activity is reduced by additional contributions which can be expressed as a two-time connected correlation function of the jump operators.

In our specific model, the term $\langle \mathcal{L}_{\mathrm{J}}(t) \rangle$ is related to imbalance via

$$\langle \mathcal{L}_{\mathrm{J}}(t) \rangle = \sum_{i=1}^{L} \langle O_i^\dagger(t) O_i(t) \rangle = 2\gamma \left[\frac{L}{2} - \sum_{i=1}^{L} (-1)^{i+1} \langle b_i^\dagger(t) b_i(t) \rangle \right] = 2\gamma \left(\frac{L}{2} - \langle I(t) \rangle \right) \tag{C.37}$$

where we used the hard-core boson anti-commutation relations $\{b_n, b_n^\dagger\} = 1$ and $\langle I(t) \rangle$ is the numerator of the imbalance introduced in the main manuscript,

$$\mathcal{I}(t) := \frac{\langle I(t) \rangle}{\langle N(t) \rangle} \tag{C.38}$$

with

$$\langle I(t) \rangle := \sum_{i=1}^{L} (-1)^{i+1} \mathrm{Tr} \left[b_i^\dagger b_i \rho_\zeta(t) \right] \text{ and the total number } \langle N(t) \rangle := \sum_{i=1}^{L} \mathrm{Tr} \left[b_i^\dagger b_i \rho_\zeta(t) \right] \tag{C.39}$$

At $\zeta = 1$, the two-time quantum jump correlator does not participate, and one obtains $\dot{\mathcal{A}}(t) = 2\gamma \left(L/2 - \langle I(t) \rangle \right)$. In the limit $t \to \infty$, we have $\langle N(t \to \infty) \rangle = L/2$ (see Sect. C.5), and the rate of dynamical activity is directly related to the imbalance as

$$\dot{\mathcal{A}}(t \to \infty) = \gamma L \left(1 - \mathcal{I}(t \to \infty) \right), \qquad \zeta = 1 \tag{C.40}$$

If we further assume that the disorder is strong enough to be in the localized regime, $\mathcal{I}(t \to \infty) \to 1$ (see Sect. C.5) and $\dot{\mathcal{A}}(t \to \infty) \to 0$. The numerical results presented in Fig. 4 of the main manuscript are in perfect agreement with the identity in Eq. (C.40).

C.4 Symmetries of $\mathcal{L}_\zeta$ in the gain-loss model

In this Secion, we discuss the symmetries of the ζ-deformed Liouvillian $\mathcal{L}_\zeta$ defined in Eq. (C.22) with the Hamiltonian introduced in the main manuscript that reads

$$H = \sum_{i=1}^{L} h_i b_i^\dagger b_i - J \sum_{i=1}^{L-1} \left[b_i^\dagger b_{i+1} + b_{i+1}^\dagger b_i \right] + U \sum_{i=1}^{L-1} b_i^\dagger b_i b_{i+1}^\dagger b_{i+1} \tag{C.41}$$

where the b_i's are hard-core bosons and the jump operators

$$O_i = \begin{cases} \sqrt{2\gamma}\, b_i^\dagger & \text{if } i \text{ is odd} \\ \sqrt{2\gamma}\, b_i & \text{if } i \text{ is even} \end{cases} \tag{C.42}$$

The isolated Hamiltonian given in Eq. (C.41) is $U(1)$-symmetric, corresponding to a conservation of the total particle number $N = \sum_{i=1}^{L} b_i^\dagger b_i$, that is $[H,\, N] = 0$. On the other hand, the ζ-deformed Liouvillian in Eq. (C.22) has a weak-$U(1)$ symmetry,

$$[\mathcal{L}_\zeta,\, \mathcal{N}_-] = 0\,, \text{ where } \mathcal{N}_- \star := [N,\, \star] \tag{C.43}$$

The operator $\mathcal{N}_-$, when acting on a state $|n, \alpha\rangle\langle m, \beta|$ where n, m are the quantum numbers associated to the $U(1)$ symmetry and α, β account for all other quantum numbers defining the state, counts the number difference on the ket and bra side of the state, *i.e.* $n - m$. The weak symmetry translates into conserving this number difference upon acting with $\mathcal{L}_\zeta$, and therefore along the dynamics generated by $\mathcal{L}_\zeta$.

Let us now explicitly show the weak symmetry in Eq. (C.43) using a generic state ρ. For the sake of simplicity, let's only consider a single dissipative channel with jump operator $O = \sqrt{2\gamma}\, b^\dagger$, and the general case follows immediately. Expanding the commutators gives,

$$\begin{aligned} [\mathcal{L}_\zeta,\, \mathcal{N}_-]\rho &= \mathcal{L}_\zeta(N\rho - \rho N) - \left[N\mathcal{L}_\zeta(\rho) - \mathcal{L}_\zeta(\rho)N\right] \\ &= \mathcal{L}_0(N\rho - \rho N) - \left[N\mathcal{L}_0(\rho) - \mathcal{L}_0(\rho)N\right] \\ &+ \zeta\left\{\mathcal{L}_\mathrm{J}(N\rho - \rho N) - \left[N\mathcal{L}_\mathrm{J}(\rho) - \mathcal{L}_\mathrm{J}(\rho)N\right]\right\} \\ &= -\frac{1}{2}\left\{O^\dagger O(N\rho - \rho N) + O^\dagger O(N\rho - \rho N)\right\} \\ &+ \zeta\left\{\mathcal{L}_\mathrm{J}(N\rho - \rho N) - \left[N\mathcal{L}_\mathrm{J}(\rho) - \mathcal{L}_\mathrm{J}(\rho)N\right]\right\} \\ &= \zeta\left\{\mathcal{L}_\mathrm{J}(N\rho - \rho N) - \left[N\mathcal{L}_\mathrm{J}(\rho) - \mathcal{L}_\mathrm{J}(\rho)N\right]\right\} \\ &= \zeta\left\{O(N\rho - \rho N)O^\dagger - \left[NO\rho\, O^\dagger - O\rho\, O^\dagger N\right]\right\} \\ &= 0 \end{aligned} \tag{C.44}$$

where we used $[H, N] = 0$ in the third line, and in the fourth line we used the fact that our choice of jump operators obeys $[O^\dagger O, N]$. In the sixth line, we used the commutation relations $[O, N] = -O$ and $[O^\dagger, N] = O^\dagger$.

For the special case $\zeta = 0$, $\mathcal{L}_{\zeta=0} = \mathcal{L}_0$ has an additional weak $U(1)$ symmetry

$$[\mathcal{L}_0,\, \mathcal{N}_+] = 0\,, \text{ where } \mathcal{N}_+ \star := \{N,\, \star\} \tag{C.45}$$

Indeed,

$$[\mathcal{L}_0, \mathcal{N}_+]\rho = \mathcal{L}_0(N\rho + \rho N) - \left[N\mathcal{L}_0(\rho) + \mathcal{L}_0(\rho)N\right] \tag{C.46}$$

$$= -\frac{1}{2}\left\{O^\dagger O(N\rho + \rho N) + (N\rho + \rho N)O^\dagger O\right\} \tag{C.47}$$

$$+ \frac{1}{2}\left\{N(O^\dagger O\rho + \rho O^\dagger O) + (O^\dagger O\rho + \rho O^\dagger O)N\right\}$$

$$= 0$$

where we also used $[H, N] = [O^\dagger O, N] = 0$. For this $\zeta = 0$ case, one can form linear combinations of the two weak $U(1)$ symmetry generators as $\mathcal{N}_{\text{ket/bra}} = \frac{\mathcal{N}_+ \pm \mathcal{N}_-}{2}$, which count particle number on the ket and bra sides, respectively.

C.5 Equation of motion for population and imbalance

In this Section, we present the equations of motion under the evolution generated by Eq. (C.21) for the average total number of particles

$$\langle N(t)\rangle := \mathrm{Tr}\left[\sum_{i=1}^{N} b_i^\dagger b_i\, \rho(t)\right] \tag{C.48}$$

and

$$\langle I(t)\rangle := \mathrm{Tr}\left[\sum_{i=1}^{N} (-1)^{i+1} b_i^\dagger b_i\, \rho(t)\right] \tag{C.49}$$

that are, respectively, the numerator and the denominator of the imbalance $\mathcal{I}(t)$ introduced in Eq. (C.38). Defining the average bond current between sites i and $i+1$ as

$$\mathcal{J}_i(t) := -\mathrm{i}J\,\mathrm{Tr}\left[(b_i^\dagger b_{i+1} - b_{i+1}^\dagger b_i)\rho(t)\right] \tag{C.50}$$

We obtain the set of equations

$$\frac{\langle \dot{I}\rangle}{2\gamma} = (1-\zeta)\left(\langle I^2\rangle - \langle I\rangle^2\right) + \zeta\left(\frac{L}{2} - \langle I\rangle\right) - \frac{1}{\gamma}\sum_{i=1}^{L-1}(-1)^{i+1}\mathcal{J}_i \tag{C.51}$$

$$\frac{\langle \dot{N}\rangle}{2\gamma} = (1-\zeta)\left(\langle NI\rangle - \langle N\rangle\langle I\rangle\right) + \zeta\left(\frac{L}{2} - \langle N\rangle\right) \tag{C.52}$$

Once the steady state is reached, the left-hand sides of these equations vanish. This implies, notably, that in the standard Lindblad evolution ($\zeta = 1$), the steady state is half-filled, *i.e.* $\langle N(t\to\infty)\rangle = L/2$ and its imbalance $\mathcal{I}(t\to\infty) \to 1$ deep in the localized regime where one expects the staggered current in the right-hand

side of Eq. (C.51) to vanish. Since our initial state $|1,0,\ldots,1,0\rangle$ is maximally imbalanced (with charge $L/2$) we have $\mathcal{I}(t) = 1$ for all $t \geq 0$ deep in the localized regime. On the other hand, in the non-Hermitian limit ($\zeta = 0$), Eq. (C.52) implies that the steady state is a pure Fock state of the form, *e.g.*, $|1,1,\ldots,0,1\rangle$. Deep in the localized regime where the staggered current is expected to vanish, the dynamics of $\langle I\rangle$ is completely arrested, *i.e.* $\langle \dot{I}\rangle = 0$ for all $t \geq 0$, since the initial state $|1,0,\ldots,1,0\rangle$ is an eigenstate of imbalance and of the non-Hermitian Hamiltonian. This implies that the imbalance $\mathcal{I}(t) = 1$ for all $t \geq 0$ deep in the localized regime in both the $\zeta = 1$ and $\zeta = 1$ regimes.

D

Filling an empty lattice by local injection of quantum particles

D.1 Analytical forms for local density profile $n_i(t)$ and total occupation $N(t)$

In this appendix, we present the details of the derivation of the analytical forms for local density profile $n_i(t)$ given in Eq. (5.40) and total occupation $N(t)$ given in Eq. (5.50). We start with the equations of motion for the correlation function,

$$\frac{dC_{i,j}}{dt} = \mathrm{i}\, g\,(C_{i-1,j} - C_{i,j+1} + C_{i+1,j} - C_{i,j-1}) - (\Gamma_L \mp \Gamma_G)(\delta_{im} + \delta_{jm})\, C_{i,j} + 2\,\Gamma_G \delta_{mi}\delta_{mj} \quad \text{(D.1)}$$

where $\mp$ stands for bosons and fermions, respectively. Note that Γ_G and Γ_L are defined in Eq. (5.38). We will closely follow Refs. [308, 309] to derive the analytical form for the density profile. For the sake of brevity, we define

$$\Gamma' = \Gamma_L \mp \Gamma_G \quad \text{(D.2)}$$

where $\mp$ stands for bosons and fermions, respectively. It is easy to see from Eq. (5.38) that the following inequality holds for both bosons and fermions, $\Gamma' > 0$. Therefore, Eq. (D.1) can be rewritten as, Note that Eq. (D.1) is an inhomogeneous equation. Given that the lattice is initially in a vacuum, the following initial condition is satisfied

$$C_{i,j}(t=0) = 0 \quad \text{(D.3)}$$

To solve Eq. (D.1) along with the initial condition in Eq. (D.3), we consider the following auxiliary problem. We will first solve Eq. (D.1) without the inhomogeneous

piece $2\Gamma_G \delta_{mi}\delta_{mj}$. Let us write down the homogeneous equation as,

$$\frac{d\tilde{C}_{i,j}}{d\tau} = \mathrm{i}\, g\, (\tilde{C}_{i-1,j} - \tilde{C}_{i,j+1} + \tilde{C}_{i+1,j} - \tilde{C}_{i,j-1}) - \Gamma'(\delta_{im} + \delta_{jm})\, \tilde{C}_{i,j} \tag{D.4}$$

where the symbol tilde indicates an auxiliary function satisfying the homogeneous equation, and we have used the symbol τ to differentiate the time variable from that of the actual problem. Closely following Refs. [308, 309], we make the following ansatz,

$$\tilde{C}_{i,j}(\tau) = \tilde{S}_i(\tau)\tilde{S}^*_j(\tau) \tag{D.5}$$

Plugging the ansatz given in Eq. (D.5) into Eq. (D.4), we can show that $\tilde{S}_i(t)$ satisfies the following differential equation,

$$\frac{d\tilde{S}_i}{d\tau} = \mathrm{i}g\left[\tilde{S}_{i+1} + \tilde{S}_{i-1}\right] - \Gamma'\, \delta_{im}\tilde{S}_i \tag{D.6}$$

where the time dependence on $\tilde{S}_i(\tau)$ in Eq. (D.6) has been dropped for the sake of brevity. One can show that solving the original inhomogeneous differential equation in Eq. (D.1) along with the initial condition in Eq. (D.3) can be achieved by solving the auxiliary homogeneous equation in Eq. (D.4) with the initial condition

$$\tilde{C}_{i,j}(\tau = 0) = \delta_{im}\delta_{jm} \tag{D.7}$$

This auxiliary initial condition [Eq. (D.7)] translates into

$$\tilde{S}_i(\tau = 0) = \delta_{im} \tag{D.8}$$

Without loss of generality, we henceforth consider the point of contact to be at $m = 0$. Furthermore, we take the lattice size L to be infinity, i.e., the lattice is now extended from $-\infty$ to $+\infty$. Since the system is expected to be symmetric about the point of contact, we consider only the positive side of the lattice chain in the analysis presented below. Now our goal is to analyze Eq. (D.6) along with the initial condition given by Eq. (D.8). One can solve Eq. (D.6) along with the initial condition Eq. (D.8) using a combination of Laplace and Fourier transformations [308] and the solution is given as

$$\tilde{S}_i(\tau) = J_i(2\, g\, \tau) - \Gamma' \int_0^\tau d\bar{t}\, e^{-\Gamma'\bar{t}} \left(\frac{\tau - \bar{t}}{\tau + \bar{t}}\right)^{i/2} J_i\left[2\, g\, \sqrt{\tau^2 - \bar{t}^2}\right] \tag{D.9}$$

where $J_i(z)$ denotes the Bessel function of the first kind. Note that the local density at a particular site i at time t is given as,

$$n_i(t) = 2\,\Gamma_G \int_0^t d\tau\, |\tilde{S}_i(\tau)|^2 \tag{D.10}$$

Notice that simplifying Eq. (D.10) requires using Eq. (D.9), which itself involves an integral, making direct simplification of $n_i(t)$ in Eq. (D.10) complicated. However, $n_i(t)$ can admit an interesting scaling form. To do so, let us take the following limits,

$$i \to \infty, \quad t \to \infty, \quad v = \frac{i}{2\,g\,t} \sim O(1) \tag{D.11}$$

where $v \sim O(1)$ is the scaled variable that will be used later. Owing to the scaling limit described in Eq. (D.11), the upper limit of the integral can be set to ∞. Moreover, the contribution of the integral in Eq. (D.10) largely comes when the integrand is evaluated at large τ. This can be checked numerically, although it is not entirely obvious from Eq. (D.9). Therefore, it is justified to simplify Eq. (D.9) in the large τ limit. To do so, we use the following relation that holds for large τ.

$$\left(\frac{\tau - \bar{t}}{\tau + \bar{t}}\right)^{i/2} \approx e^{-\frac{i\bar{t}}{\tau}} \tag{D.12}$$

Using Eq. (D.12) in Eq. (D.9), we obtain

$$\tilde{S}_i(\tau) = \frac{i\,J_i(2\,g\,\tau)}{i + \tau\Gamma'} \tag{D.13}$$

Using the simplified form of $\tilde{S}_i(\tau)$ and substituting in Eq. (D.10), the local density at a particular site is given as

$$n_i(t) = 2\,\Gamma_G \int_0^t d\tau\, \frac{i^2\left[J_i(2\,g\,\tau)\right]^2}{(i + \tau\,\Gamma')^2} \tag{D.14}$$

where we recall that Γ_G is defined in Eq. (5.38) and $\tilde{S}_i(\tau)$ is given in Eq. (D.13). Note that i in Eq. (D.14) stands for lattice index. Eq. (D.14) is a compact analytical expression for the local density profile under the condition given in Eq. (D.11). We now proceed to analytically derive the scaling form. To do so, we need to use the appropriate asymptotic expansion for the Bessel function that appears in Eq. (D.14). Now making a change of variable $\tau = t\,s$ and recalling $i = 2\,g\,v\,t$, we rewrite Eq. (D.14) as

$$n_i(t) = 8\,\Gamma_G\,g^2\,v^2\,t \int_0^1 ds\, \frac{\left[J_{2gvt}(2\,g\,t\,s)\right]^2}{(2\,g\,v + s\,\Gamma')^2} \tag{D.15}$$

To facilitate the implementation of the asymptotic form of the Bessel function, it is convenient to introduce

$$\mu = 2\,g\,v\,t, \quad \text{and} \quad z = \frac{s}{v} \tag{D.16}$$

which simplifies Eq. (D.15) as,

$$n_i(t) = 8\,\Gamma_G\,g^2\,\nu\,t\int_0^{\frac{1}{\nu}} dz\,\frac{\left[J_\mu(\mu\,z)\right]^2}{(2\,g+z\,\Gamma')^2} \tag{D.17}$$

In the large μ limit (for a fixed z) the asymptotic expansion of $J_\mu(\mu z)$ is given by [329, 330]

$$J_\mu(\mu\,z) \sim \left(\frac{4\,\zeta(z)}{1-z^2}\right)^{\frac{1}{4}}\,\frac{1}{2\sqrt{\mu\,\pi}}\,\frac{1}{|\zeta(z)|^{\frac{1}{4}}}\,\mathcal{T}_\mu(\mu\,z) \tag{D.18}$$

where $\mathcal{T}_\mu(\mu\,z)$ is given by,

$$\mathcal{T}_\mu(\mu\,z) = \begin{cases} \exp\left[-\frac{2}{3}\mu\,\zeta(z)^{\frac{3}{2}}\right] & \text{for} \quad 0 < z \leq 1 \\ 2\cos\left[\frac{2}{3}\mu\,\left(-\zeta(z)\right)^{\frac{3}{2}} - \frac{\pi}{4}\right] & \text{for} \quad 1 < z \leq \infty \end{cases} \tag{D.19}$$

with

$$\zeta(z) = \begin{cases} \left(\frac{3}{2}\right)^{2/3}\left(\log\left(\frac{\sqrt{z^2+1}+1}{z}\right) - \sqrt{1-z^2}\right)^{2/3} & \text{for} \quad 0 < z \leq 1 \\ -\left(\frac{3}{2}\right)^{2/3}\left(\sqrt{z^2-1} - \sec^{-1}(z)\right)^{2/3} & \text{for} \quad 1 < z \leq \infty \end{cases} \tag{D.20}$$

We split Eq. (D.17) as follows

$$n_i(t) = 8\,\Gamma_G\,g^2\,\nu\,t\left[\int_0^1 dz\,\frac{\left[J_\mu(\mu\,z)\right]^2}{(2\,g+z\,\Gamma')^2} + \int_1^{\frac{1}{\nu}} dz\,\frac{\left[J_\mu(\mu\,z)\right]^2}{(2\,g+z\,\Gamma')^2}\right] \tag{D.21}$$

To evaluate Eq. (D.21), we use the appropriate forms in Eqs.(D.18)-(D.20) depending on the range of integration over z. It is easy to notice that the first integral in Eq. (D.21) is exponentially suppressed in μ. Hence, keeping only the second term in Eq. (D.21) and performing some manipulations, we get

$$n_i(t) = \frac{2\,\Gamma_G\,g}{\pi}\int_1^{\frac{1}{\nu}} dz\,\frac{1}{\sqrt{z^2-1}}\,\frac{\mathcal{T}_\mu^2(\mu\,z)}{(2\,g+z\,\Gamma')^2} \tag{D.22}$$

We now use the expression for $T_\mu(\mu z)$ from Eq. (D.19) and get

$$n_i(t) = \frac{8\,\Gamma_G\,g}{\pi}\int_1^{\frac{1}{\nu}} dz\,\frac{\cos^2\left[\frac{2}{3}\mu\,\left(-\zeta(z)\right)^{\frac{3}{2}} - \frac{\pi}{4}\right]}{(2\,g+z\,\Gamma')^2\,\sqrt{z^2-1}} \tag{D.23}$$

For large μ, the cosine-squared term in the numerator is highly oscillatory and therefore can be approximated by 1/2. We finally obtain the following scaling form for the local density profile $n_i(t)$,

$$n_i(t) \;=\; \Phi\left(\frac{i}{2gt}\right), \tag{D.24}$$

$$\Phi(\nu) \;=\; \frac{4\,\Gamma_G\,g}{\pi}\int_1^{\frac{1}{\nu}} dz\,\frac{1}{\sqrt{z^2-1}}\,\frac{1}{(2\,g+z\,\Gamma')^2} \tag{D.25}$$

as also given in the Eq. (5.43) and Eq. (5.44). Upon performing the integral in Eq. (D.25) we obtain,

$$\Phi(\nu) = \frac{\tilde{g}\,(1+\nu\,\tilde{g})\Big[\log(1+\nu\,\tilde{g}) - \log\Big(\tilde{g}+\nu-\sqrt{(\tilde{g}^2-1)\,(1-\nu^2)}\Big)\Big] - \sqrt{(\tilde{g}^2-1)\,(1-\nu^2)}}{(\tilde{g}^2-1)^{3/2}\,(\nu\,\tilde{g}+1)}, \quad \text{for} \quad 0<\nu<1 \tag{D.26}$$

which is given in Eq. (5.45). Here we introduced the dimensionless variable $\tilde{g}$ as

$$\tilde{g} = \frac{2g}{\Gamma'} = \frac{4g}{J(0)} \tag{D.27}$$

Our result in Eq. (D.25) exactly coincides with the one obtained in Ref. [308], where a different approach was used. In a similar fashion, the total occupation number $N(t)$ is given by

$$\begin{aligned} N(t) &= \sum_{i=-\infty}^{\infty} n_i(t) = 4\,g\,t\int_0^1 d\nu\,\Phi(\nu) \\ &= \frac{16\,\Gamma_G\,g^2 t}{\pi}\int_0^1 d\nu\int_1^{\frac{1}{\nu}} dz\,\frac{1}{\sqrt{z^2-1}}\,\frac{1}{(2\,g+z\,\Gamma')^2} \end{aligned} \tag{D.28}$$

We next perform an integral by parts in Eq. (D.28) which further simplifies $N(t)$ as,

$$\begin{aligned} N(t) &= \frac{4\,\Gamma_G\,\tilde{g}^2 t}{\pi}\int_1^{\infty}\frac{dz}{z}\,\frac{1}{\sqrt{z^2-1}}\,\frac{1}{(\tilde{g}+z)^2} \\ &= -\frac{2\,\Gamma_G\,t}{\pi(1-\tilde{g}^2)}\left[2\tilde{g}-\pi(1-\tilde{g}^2)+2\big(1-2\tilde{g}^2\big)\frac{\cos^{-1}(\tilde{g})}{\sqrt{1-\tilde{g}^2}}\right] \end{aligned} \tag{D.29}$$

which is given by the expression in Eq. (5.50).